

# **Gas Adsorption and Separation Properties of Porous Materials**



Wolfson Northern Carbon Reduction Laboratories  
School of Chemical Engineering and Advanced  
Materials

**Jayne Armstrong**

A Thesis Submitted for the Degree of Doctor of  
Philosophy

May 2013

For my family

## Acknowledgements

First of all I would like to thank my supervisor, Professor Mark Thomas for providing me with the opportunity to undertake my studies in the Wolfson Northern Carbon Reduction Laboratories. I would like to convey to him my sincere gratitude for the guidance and support he has provided throughout my time here.

Thanks must also be extended to Professor Matt Rosseinsky, Professor Andrew Cooper and Dr Darren Bradshaw from Liverpool University for providing the basis for the funding from the EPSRC and for providing varied and incredibly interesting samples to work with. Thanks also to Dr James Jones, Dr Tom Hassel and Dr Kyriakos Stylianou for providing samples over the past four years.

I have been fortunate to work with a large number of excellent scientists while being a part of the Wolfson Northern Carbon Reduction Laboratories. Special thanks go to Dr Xuebo Zhao, for helping me in my very first weeks and Dr Jon Bell for always being on hand with technical advice, guidance and impromptu entertainment. Dr Rachel Gill and Dr James Holcroft, I thank them for their friendship, for making me laugh and for teaching me not to take myself too seriously.

I would like to thank my friends and family for their support, patience, understanding and love throughout my time studying, especially my Mam and Dad, for instilling me with a love of science and giving me the courage to face any hurdle with strength and pride.

Finally, thank you to my husband Andrew, my rock and the bright smile at the end of every day. I thank him for bringing balance to my life and supporting me with his never failing love and encouragement.

## Abstract

The development of new porous materials for use in applications such as gas storage and separation processes, catalysis, catalysts supports and the removal of environmentally unfriendly species has increased rapidly over the past decade. Research into the development of these new materials has been dominated by metal organic frameworks, covalent organic frameworks, nanoporous polymers and, most recently, porous organic cage molecules. This thesis describes adsorption studies of a metal organic framework, Zn (TBAPy) and a porous tetrahedral organic cage molecule of  $\sim 1$  nm diameter formed by the condensation reaction of 1,3,5-triformylbenzene with 1,2-ethylenediamine.

The development of metal organic frameworks has traditionally involved the formation of rigid network structures, analogous to that of zeolites. More recently the focus has shifted to those of dynamic, flexible framework materials, and the response of these materials to adsorption of gases and vapours. The metal organic framework Zn (TBAPy) is based on a zinc metal centre functionalised with benzoate fragments. The initial two-dimensional structure undergoes rearrangement of the paddlewheel units to form a 3D framework, Zn (TBAPy)' upon desolvation. The ability of this 3D network to separate *p*-xylene and *m*-xylene was investigated. It was found that these isomers produced different effects on the framework, with *p*-xylene producing a typical Type I isotherm, whereas *m*-xylene induced a structural change within the material, with a much slower rate of *m*-xylene adsorption at higher pressures. This could potentially lead to the equilibrium separation of these two isomers by the metal organic framework Zn (TBAPy)'.

The 1 nm diameter tetrahedral cage molecules formed by the condensation reaction of 1,3,5-triformylbenzene with 1,2-ethylenediamine can exist in a number of stable polymorphs, Cage 1 $\alpha$ , Cage 1 $\beta$  and Cage 1 $\gamma$ . These polymorphs can be interconverted by exposure to certain organic vapours/solvents. The conversion of Cage 1 $\beta$  to Cage 1 $\alpha$  by adsorption of probe molecules ethyl acetate, 2-butanone, diethyl ether, pentane and methanol was studied. Adsorption of ethyl acetate, 2-butanone and diethyl ether produced unusual adsorption isotherms, which included desorption of adsorbed vapour with increasing pressure during the adsorption isotherms. This desorption is attributed to the structural change from Cage 1 $\beta$  to

Cage 1 $\alpha$ . The unusual desorption step is not observed for methanol or pentane adsorption. The adsorption of methyl acetate was studied over a wide temperature range in order to assess the thermodynamic and kinetic characteristics of the unusual desorption step. The adsorption of dichloromethane showed the reverse transformation of Cage 1 $\alpha$  to Cage 1 $\beta$ , showing that the inter conversion produces stable polymorphs. The kinetics of the structural transformation followed an Avrami model and the mechanism is an activated process.

Cage 1 $\alpha$  has voids between the cages, which are connected by very narrow constrictions that allow the kinetic molecular sieving of oxygen, carbon dioxide and nitrogen. It was found that oxygen adsorbs approximately ten times faster than nitrogen on Cage 1 $\alpha$ , with selectivity and rate constants similar to those observed for carbon molecular sieves. The thermodynamics and kinetic results are discussed in terms of structural characteristics and diffusion into molecular cage materials. The kinetic molecular sieving is not present in the polymorph Cage 1 $\beta$ , which has wider pores.

# Contents

<b>LIST OF ABBREVIATIONS .....</b>	<b>vi</b>
<b>LIST OF NOMENCLATURE .....</b>	<b>vii</b>
<b>CHAPTER 1 ADSORPTION.....</b>	<b>1</b>
1.1 PRINCIPLES OF ADSORPTION .....	1
1.1.1 <i>Physisorption and Chemisorption</i> .....	3
1.1.2 <i>Adsorption Forces for a Gas Molecule on an Open Surface</i> .....	4
1.1.3 <i>Adsorption Forces for a Gas Molecule in Porous Materials</i> .....	6
1.1.3.1 Porosity.....	6
1.1.3.2 Adsorption Potential in Micropores .....	8
1.1.4 <i>Thermodynamics of Adsorption</i> .....	9
1.1.4.1 Molar Energy of Adsorption.....	9
1.1.4.2 The Isothermic Enthalpy of Adsorption.....	9
1.2 ADSORPTION ISOTHERMS .....	11
1.2.1 <i>Classification of Isotherms</i> .....	12
1.2.2 <i>Hysteresis</i> .....	13
1.3 INTERPRETATION OF ADSORPTION ISOTHERMS.....	15
1.3.1 <i>Henry's Law</i> .....	15
1.3.2 <i>Langmuir Equation</i> .....	16
1.3.3 <i>Brunauer Emmet Teller (B.E.T) Theory</i> .....	18
1.3.4 <i>Evaluation of Microporosity – The Dubinin-Radushkevich (DR) Model</i> .....	21
1.3.4.1 Polanyi Potential Theory.....	21
1.3.4.2 Derivation of the Dubinin-Radushkevich Equation .....	23
1.3.4.3 The Dubinin – Astakhov (DA) Equation.....	25
1.3.4.4 Application of the Dubinin – Radushkevich Equation .....	25
1.3.5 <i>Virial Equation</i> .....	27
1.4 SURFACE AREA CALCULATIONS AND PHENOMENA OBSERVED DURING ADSORPTION.....	29
1.4.1 <i>Surface Area Calculation</i> .....	29
1.4.2 <i>Phenomena Observed During Adsorption</i> .....	29
1.4.2.1 Activated Diffusion .....	29
1.4.2.2 Molecular Sieve Effects.....	31
1.4.2.3 Cooperation Effects .....	31
1.5 MECHANISM OF ADSORPTION .....	32
1.6 MODELS OF ADSORPTION KINETICS .....	34
1.6.1 <i>Empirical Description</i> .....	34
1.6.2 <i>Fickian Diffusion</i> .....	35
1.6.3 <i>Linear Driving Force Model</i> .....	37

1.6.4	<i>Combined Barrier Resistance / Diffusion Model</i> .....	39
1.6.4.1	Comparison of Diffusion Models .....	40
1.6.5	<i>Stretched Exponential (SE) Model</i> .....	40
1.6.6	<i>Double Exponential Model</i> .....	42
1.7	REFERENCES .....	43
<b>CHAPTER 2</b>	<b>POROUS MATERIALS</b> .....	<b>48</b>
2.1	POROUS MATERIALS.....	48
2.1.1	<i>Current Industrial Adsorbents</i> .....	49
2.1.1.1	Activated Carbon .....	49
2.1.1.2	Carbon Molecular Sieves .....	51
2.1.1.3	Zeolites .....	51
2.2	POROUS COORDINATION POLYMERS.....	53
2.2.1	<i>Classification of Porous Coordination Polymers</i> .....	54
2.2.1.1	Generational Classification .....	54
2.2.1.2	Classification by Spatial Dimension.....	54
2.2.2	<i>Synthesis Concepts and Design</i> .....	55
2.2.2.1	Design of Motifs.....	55
2.2.2.2	Nodes and Linkers.....	56
2.2.2.3	“Design” of Pre-Determined Frameworks .....	58
2.2.2.4	Post-Synthetic Modification .....	60
2.2.2.5	Interpenetration .....	60
2.2.2.6	Dynamic Structural Responses .....	61
2.2.3	<i>Applications of Porous Coordination Polymers</i> .....	64
2.2.3.1	Separation and Purification .....	65
2.2.3.2	Clean Energy Applications.....	65
2.2.3.3	Catalysis .....	67
2.2.3.4	Drug Delivery .....	69
2.2.4	<i>New Porous Coordination Polymers</i> .....	70
2.2.4.1	Zeolitic Imidazolate Frameworks (ZIFs).....	70
2.2.4.2	Covalent Organic Frameworks (COFs) .....	71
2.3	POROUS ORGANIC MOLECULES .....	72
2.3.1	<i>Intrinsically and Extrinsically Porous Organic Materials</i> .....	73
2.3.2	<i>Porous Organic Cage Molecules</i> .....	75
2.4	REFERENCES .....	80
<b>CHAPTER 3</b>	<b>SEPARATION OF GASES AND VAPOURS</b> .....	<b>85</b>
3.1	INTRODUCTION.....	85
3.2	AIR SEPARATION.....	86
3.2.1	<i>Cryogenic Air Separation</i> .....	87
3.2.2	<i>Membrane Separation</i> .....	88

3.2.3	<i>Separation by Adsorption Technology</i> .....	90
3.2.3.1	Pressure Swing Adsorption .....	90
3.2.3.2	Air Separation Using Metal Organic Frameworks .....	93
3.3	XYLENE SEPARATION.....	95
3.3.1	<i>Industrial Separation of Xylenes</i> .....	96
3.3.2	<i>Separation of Xylenes Using Metal Organic Frameworks</i> .....	97
3.4	REFERENCES .....	100
<b>CHAPTER 4</b>	<b>RESEARCH OBJECTIVES .....</b>	<b>103</b>
4.1	OVERALL OBJECTIVES.....	103
4.2	METAL ORGANIC FRAMEWORK $Zn_2(TBAPy)(H_2O)_2$ .....	103
4.2.1	<i>Porous Characterisation</i> .....	103
4.2.2	<i>Separation of Xylene Isomers</i> .....	103
4.3	MOLECULAR ORGANIC CAGE MATERIALS .....	103
4.3.1	<i>Porous Characterisation</i> .....	103
4.3.2	<i>Structural Responses Induced by Vapour Adsorption</i> .....	104
4.3.3	<i>Gas Separation</i> .....	104
<b>CHAPTER 5</b>	<b>EXPERIMENTAL .....</b>	<b>105</b>
5.1	MATERIALS USED.....	105
5.1.1	<i>Porous Materials</i> .....	105
5.1.1.1	Porous Organic Cages .....	105
5.1.1.2	Metal Organic Framework $Zn_2(TBAPy)(H_2O)_2$ .....	105
5.1.2	<i>Organic Vapours and Gases</i> .....	106
5.1.3	<i>Saturated Vapour Pressure (<math>P^0</math>) Calculation</i> .....	107
5.2	GAS AND VAPOUR ADSORPTION STUDIES .....	109
5.2.1	<i>Intelligent Gravimetric Analyser (IGA)</i> .....	109
5.2.1.1	Microbalance System.....	111
5.2.1.2	Pressure Regulation .....	113
5.2.1.3	Temperature Control .....	114
5.2.1.4	Typical Experimental Procedure .....	115
5.2.1.5	Vapour Adsorption .....	117
5.2.1.6	Capillary Experiments .....	118
5.2.2	<i>Additional Experimental Methodologies</i> .....	118
5.2.2.1	Thermal Gravimetric Analysis .....	118
5.2.2.2	Scanning Electron Microscopy .....	119
5.2.2.3	Fourier Transform Infrared (FTIR) Spectroscopy .....	119
5.2.2.4	Single Crystal X-ray Diffraction .....	120
5.2.2.5	Powder Diffraction.....	120
5.2.3	<i>Error Analysis</i> .....	120



5.3	REFERENCES .....	121
<b>CHAPTER 6</b>	<b>XYLENE SEPARATION BY ZN(TBAPy) 1' METAL ORGANIC FRAMEWORK .....</b>	<b>122</b>
6.1	INTRODUCTION.....	122
6.2	CRYSTAL STRUCTURE OF ZN(TBAPy) 1 .....	122
6.3	STRUCTURAL TRANSFORMATION FROM ZN(TBAPy) 1 TO ZN(TBAPy) 1' .....	123
6.4	POROUS STRUCTURE CHARACTERISATION SORPTION EXPERIMENTS OF ZN(TBAPy) 1` .....	125
6.4.1	<i>Carbon Dioxide Adsorption Zn(TBAPy) 1'</i> .....	125
6.4.1.1	Carbon Dioxide Adsorption at 195 K.....	125
6.4.1.2	Carbon Dioxide Adsorption at 273 K.....	126
6.4.2	<i>Xylene Vapour Adsorption on Zn(TBAPy) 1'</i> .....	127
6.4.2.1	Adsorption of <i>p</i> -xylene .....	127
6.4.2.2	Adsorption of <i>m</i> -xylene at 303 K .....	128
6.4.2.3	Kinetics of Xylene Adsorption .....	129
6.4.2.4	Capillary loading and PXRD Analysis .....	131
6.5	CONCLUSIONS .....	131
6.6	FIGURES.....	133
6.7	REFERENCES .....	148
<b>CHAPTER 7</b>	<b>STRUCTURAL CHANGE INDUCED BY ADSORPTION OF GASES AND VAPOURS ON POROUS CAGE MATERIALS.....</b>	<b>149</b>
7.1	INTRODUCTION.....	149
7.2	CHARACTERISATION OF CAGE 1B AND CAGE 1A .....	150
7.2.1	<i>Thermal Gravimetric Analysis</i> .....	150
7.2.2	<i>Scanning Electron Microscopy of Cage 1β and Cage 1α</i> .....	151
7.2.3	<i>Carbon Dioxide Adsorption Characterisation Isotherms of Cage 1β and Cage 1α</i> .....	151
7.2.3.1	Carbon Dioxide Adsorption at 195K.....	151
7.2.3.2	Carbon Dioxide Adsorption at 273 K.....	152
7.3	PROBE MOLECULE STUDIES CAGE 1B.....	152
7.3.1	<i>Ethyl Acetate Adsorption on Cage 1β</i> .....	153
7.3.1.1	Ethyl Acetate Adsorption Isotherm Analysis.....	153
7.3.1.2	Ethyl Acetate Adsorption on Cage 1β Desorption Step Kinetics Analysis .....	154
7.3.1.3	Ethyl Acetate Adsorption on Cage 1β and Cage 1α# Kinetic Analysis .....	155
7.3.2	<i>2-butanone and Diethyl Ether Adsorption on Cage 1β</i> .....	157
7.3.2.1	2-butanone and Diethyl Ether Adsorption Isotherm Analysis .....	157
7.3.2.2	2-butanone and Diethyl Ether Adsorption Desorption Step Kinetics Analysis.....	158
7.3.2.3	2-butanone and Diethyl Ether Adsorption Kinetic Analysis .....	158
7.3.2.4	Comparison of Ethyl Acetate, 2-butanone and Diethyl Ether Adsorption on Cage 1β ...	158
7.3.3	<i>Pentane and Methanol Adsorption on Cage 1β</i> .....	160
7.4	METHYL ACETATE ADSORPTION STUDIES ON CAGE 1B .....	162

7.4.1	<i>Methyl Acetate Adsorption on Cage 1B Isotherm Analysis</i> .....	162
7.4.2	<i>Methyl Acetate Adsorption on Cage 1B Enthalpy and Entropy Calculations</i> .....	163
7.4.3	<i>Methyl Acetate on Cage 1B Kinetic Analysis</i> .....	165
7.4.4	<i>Kinetics of Methyl Acetate Desorption Step</i> .....	165
7.5	METHYL ACETATE ADSORPTION ON CAGE 1A# .....	166
7.5.1	<i>Methyl Acetate Adsorption on Cage 1A# Isotherm Analysis</i> .....	167
7.5.2	<i>Methyl Acetate Adsorption on Cage 1A# Kinetic Analysis</i> .....	168
7.5.3	<i>Methyl Acetate Adsorption on Cage 1A# Kinetic Corrections</i> .....	169
7.5.4	<i>Comparison of Cage 1B and Cage 1A#</i> .....	170
7.6	DICHLOROMETHANE ADSORPTION ON CAGE 1A.....	171
7.7	CONCLUSIONS .....	172
7.8	FIGURES.....	175
7.9	REFERENCES .....	231
<b>CHAPTER 8</b>	<b>KINETIC MOLECULAR SIEVING OF OXYGEN AND NITROGEN BY ORGANIC CAGE</b>	
<b>MATERIALS CAGE 1A AND CAGE 1A#</b> .....		<b>232</b>
8.1	INTRODUCTION.....	232
8.2	CHARACTERISATION OF CAGE 1A#.....	233
8.3	KINETIC MOLECULAR SIEVING OF OXYGEN AND NITROGEN BY CAGE 1A# AND CAGE 1A.....	235
8.4	CAGE 1A# OXYGEN AND NITROGEN ADSORPTION .....	235
8.4.1	<i>Oxygen and Nitrogen Isotherm Analysis Cage 1A#</i> .....	235
8.4.2	<i>Oxygen and Nitrogen Kinetic Analysis Cage 1A#</i> .....	237
8.4.3	<i>Diffusion Coefficients for Oxygen and Nitrogen Adsorption on Cage 1A#</i> .....	239
8.5	COMPARISON OF O <sub>2</sub> /N <sub>2</sub> ADSORPTION KINETICS ON CAGE 1A# AND CAGE 1B .....	240
8.6	CAGE 1A OXYGEN AND NITROGEN ADSORPTION .....	240
8.6.1	<i>Oxygen and Nitrogen Isotherm Analysis Cage 1A</i> .....	241
8.6.2	<i>Oxygen and Nitrogen Kinetic Analysis Cage 1A</i> .....	241
8.6.3	<i>Diffusion Coefficients for Oxygen and Nitrogen Adsorption on Cage 1A</i> .....	242
8.7	COMPARISON OF THE KINETIC MOLECULAR SIEVING PROPERTIES OF CAGE 1A# AND CAGE 1A .....	243
8.8	CONCLUSIONS .....	244
8.9	FIGURES.....	247
8.10	REFERENCES.....	278
<b>CHAPTER 9</b>	<b>OVERALL CONCLUSIONS</b> .....	<b>279</b>
9.1	REFERENCES .....	282
<b>CHAPTER 10</b>	<b>FURTHER WORK</b> .....	<b>283</b>
<b>CHAPTER 11</b>	<b>PUBLICATIONS</b> .....	<b>285</b>
<b>CHAPTER 12</b>	<b>APPENDIX</b> .....	<b>286</b>

## List of Abbreviations

cyclam	1,4,8,11-tetraazacyclotetradecane
btc	1,3,5-benzene-tricarboxylate
pzdc	pyrazine-2,3-dicarboxylate
bpy	2,2'-bipyridine
bdc	benzene-dicarboxylate
qptc	quaterphenyl-3,3'',5,5''-tetracarboxylate
tptc	terphenyl-3,3'',5,5''-tetracarboxylate
aobtc	azobenzene-3,3',5,5'-tetracarboxylate
BTT	1,3,5-benzenetristetrazolate
bpdc	biphenyl-dicarboxylate
bpe	4,4'-trans-bis'(4-pyridyl)ethylene
TPP	tris-o-phenylenedioxycyclotriphosphazene
dabco	1,4-diazabicyclo[2.2.2]octane
mim	2-methylimidazole
EtOAc	ethyl acetate
MeOAc	methyl acetate
DCM	dichloromethane
TBAPy	1,3,6,8,-tetrakis(p-benzoic acid)
<i>p</i> -xylene	para - xylene
<i>m</i> -xylene	meta - xylene
<i>o</i> -xylene	ortho - xylene
Cage 1 $\alpha$	Polymorph of Cage 1 produced by Liverpool University
Cage 1 $\beta$	Polymorph of Cage 1 produced by Liverpool University
Cage 1 $\gamma$	Polymorph of Cage 1 produced by Liverpool University
Cage 1 $\alpha$ #	Polymorph of Cage 1 produced within the IGA under vacuum at Newcastle University

## List of Nomenclature

$A$	Arrhenius equation: pre-exponential factor
$A / \varepsilon$	Dubinin Radushkevich equation: change in energy in bringing one molecule of gas to the adsorbed phase
$A_0$	Virial equation: adsorbate - adsorbent interaction
$A_1$	Virial equation: adsorbate - adsorbate interaction
$A_1, A_2$	Double exponential equation: rate contributions of rate constants $k_1$ and $k_2$ to overall rate
$A_g$	Adsorbate in the gas phase
$A_m$	Average area occupied by one molecule of adsorbate
$a$	Radius of the particle
$a_i, b_i$	Virial equation: temperature dependent empirical parameter
$B$	Lennard Jones potential: repulsive interaction energy constant
$C$	Lennard Jones potential: attractive interaction energy constant
$C_1, C_2, etc$	Virial equation: temperature dependant parameters
$C_p$	Adsorbate concentration within the pore
$C_p^*$	Surface concentration in equilibrium with the gas phase
$c$	BET equation: constant related to adsorption energy
$D$	Dubinin Radushkevich equation: measure of of pore size distribution
$D$	Ficks Law: Diffusion coefficient
$d$	Collision diameter / half width of the pore
$E$	Interaction energy
$E_a$	Activation energy of adsorption
$F$	Flux rate
$G$	Gibbs surface free energy
$H / H_a$	Enthalpy of adsorption
$H_L$	Enthalpy of vaporisation
$\Delta_{ads}\dot{h}_0$	differential enthalpy of adsorption
$ierfc$	Ficks diffusion constants
$K$	Equilibrium rate constant

$K_H$	Henry's Law Constant
$K_n$	Knudsen number
$k_b$	Barrier resistance
$k, k_1, k_2$	Rate constants
$M$	Molecular weight
$M-A$	Adsorbed molecule on surface site
$M_e$	Mass at equilibrium
$M_t$	Mass at time t
$m$	Lennard Jones potential: exponential constant
$N_A$	Avogadro's number / $6.022 \times 10^{23}$ molecules mol <sup>-1</sup>
$N^a$	Number of adsorbed molecules
$N^s$	Number of available surface adsorption sites
$n$	Specific surface excess amount
$n_a$	Number of molecules adsorbed
$n_m$	Monolayer capacity
$P$	Pressure
$P^0$	Saturated vapour pressure
$P/P^0$	Relative pressure
$P_x$	Pressure of the gas phase
$Q_{st}$	Isosteric enthalpy of adsorption
$R$	Gas constant / $8.3145 \text{ J K}^{-1} \text{ mol}^{-1}$
$r$	Radial coordinate
$r_0$	Collision radius of the molecule
$r_c$	Radius of adsorbent
$r_e$	Separation distance between molecules
$\Delta S / S$	Change in / entropy of adsorption
$\dot{S}_a$	Differential molar entropy of the adsorbed phase
$S$	Selectivity
$S_A$	Surface area
$S_{surface}$	Surface site on the adsorbent
$T$	Temperature
$t$	Time
$\Delta_a U$	Molar energy of adsorption

$\mu_a$	Chemical potential of adsorbed phase
$\mu_g$	Chemical potential of the gas phase
$V$	Volume
$\dot{V}_a$	Differential volume of the adsorbed phase
$V_g$	Volume of the gas phase
$W$	Volume of micropores
$W_0$	Total available micropore volume
$x$	Fickian Diffusion: space coordinate measured normal to the section
$\beta$	Dubinin Radushkevich equation: similarity constant
$\beta$	Stretched exponential equation: exponential parameter
$\varepsilon$	Adsorption potential
$\theta$	Fractional surface coverage
$\lambda$	Mean free path
$\tau$	Stretched exponential material dependant parameter
$\varphi$	Interaction potential
$\varphi^*$	Interaction potential of a molecule with a freely exposed surface
$\varphi/\varphi^*$	Relative interaction potential
$\varphi(t)$	Relaxation function

## Chapter 1   Adsorption

### 1.1 Principles of Adsorption

The phenomenon of adsorption has been exploited since ancient times, with the Egyptians and Sumerians utilising the adsorbent properties of clay and wood charcoal for the treatment of disease and the purification of water.<sup>1</sup> The earliest quantitative studies of adsorption were conducted by Scheele and Fontana<sup>2,3</sup> in the late 1770s, however the term “adsorption” was not coined until research by Kayser was conducted in 1881.<sup>4</sup> Many investigations were conducted into the nature of adsorption,<sup>5,6,7</sup> with major advances in the theoretical interpretation of adsorption isotherms made in the early twentieth century. A brief historical outline of the major developments in the interpretation and analysis of adsorption isotherms is given in **Table 1-1**.

Adsorption is now defined by the International Union of Pure and Applied Chemistry (IUPAC) as the enrichment of one or more components in the interfacial layer.<sup>8</sup> The adsorption process involves the accumulation of an excess of molecules at the interface between two phases. This differs from the process of *absorption* which is the bulk penetration of mass into a solid or liquid. The general term *sorption* was proposed by McBain<sup>9</sup> in 1909 and can be applied to a system where both of these processes are occurring. The term *adsorbate* applies to the gas or vapour in the adsorbed phase, the term *adsorptive* applies to the gas or vapour that is to be adsorbed in the fluid phase and the term *adsorbent* applies to the material that the gas or vapour is adsorbing onto. Adsorption is usually classified into two types, *chemisorption* and *physisorption*. The classification is according to the types of forces acting on the surface of the material. Adsorption can also be classified according to the phases which are interacting: at the gas-liquid boundary, the liquid-solid boundary, the liquid-liquid boundary or the gas-solid boundary. In this study, only gas-solid physisorption systems are reviewed.

## Chapter 1 Adsorption

**Table 1-1:** Historical description of advances in isotherm interpretation and analysis

<b>Date</b>	<b>Name</b>	<b>Significance</b>
<b>1907</b>	Freundlich	Proposed a general mathematical relationship to describe the adsorption isotherm, now used as an empirical description. <sup>10</sup>
<b>1909</b>	McBain	Noted that the uptake of hydrogen by carbon was via two processes, <i>adsorption</i> and <i>absorption</i> , and coined the term “sorption” to cover both effects. <sup>9</sup>
<b>1911</b>	Zsigmondy	Developed the theory of capillary condensation for mesoporous carbons. <sup>11</sup>
<b>1914</b>	Polanyi	Developed the Polanyi Potential Theory – a description of the intermolecular forces involved in adsorption – now the Lennard Jones Potential is the favoured theory, but the Polanyi potential was used by Dubinin to develop the theory of micropore filling. <sup>12</sup>
<b>1916</b>	Langmuir	1916 was the start of the publication of several papers by Langmuir, bringing together all evidence to support the concept of monolayer coverage. <sup>13,14</sup>
<b>1919-1922</b>	Williams and Henry	Thermodynamic and kinetic derivations of the virial equation at low surface coverage. <sup>15,16</sup>
<b>1938</b>	Brunauer, Emmet and Teller	BET theory published – identification of an “s” shaped isotherm – recognised as multilayer formation, and the definition of “Point B” as the completion of monolayer coverage and start of multilayer coverage. <sup>17</sup>
<b>1940</b>	Brunauer, Deming, Deming, Teller	Classifications of the five principle types of isotherms into the BDDT classification. <sup>18</sup>
<b>1946</b>	Dubinin – Radushkevich	Proposed the Theory of Volume Filling of Micropores (TVFM) developed from the Polanyi Potential theory to show that physisorption in micropores is different to that of adsorption in larger pores or on the open surface.



### 1.1.1 Physisorption and Chemisorption

Physisorption is a long range interaction, based on van der Waals forces (dispersion interactions) and as such is a weak force. Physisorption is analogous with condensation within the pores of the material and as such the energy released upon physisorption is of the same order of magnitude as the enthalpy of vaporisation of the gas, typically ( $\Delta H_{\text{ads}}$ ) is 10 – 80 kJ mol<sup>-1</sup>, although this may increase if adsorption occurs in narrow pores due to favourable interactions.<sup>19</sup> Chemisorption is a shorter range reaction which involves the formation of chemical bonds between the gas molecule and the surface through the exchange of electrons. Chemisorption can be associative or dissociative, dissociative chemisorption leads to the adsorbed molecule being torn into fragments on the surface, giving rise to the use of solid surfaces as catalysts, for example the oxidation of carbon monoxide on the surface of platinum.<sup>20</sup> The energy of chemisorption is much higher than that of physisorption, with ( $\Delta H_{\text{ads}}$ ) values in the region of 200 kJ mol<sup>-1</sup>. As chemical bonds are formed with the surface, chemisorption is usually irreversible, unless severe conditions are used, physisorption may be reversed by decreasing the pressure or increasing the temperature of the system, and the adsorbed molecule will return to the fluid phase in its original composition. Chemisorption is confined to monolayer coverage, physisorption will form multiple layers, however physisorption may occur on top of chemisorbed layers. Physisorption rapidly reaches equilibrium and decreases as temperature increases, chemisorption is a slower process and increases as the temperature increases, and normally occurs at high temperatures.<sup>21</sup> The physisorption process is spontaneous, and results in a decrease in entropy due to the loss of degrees of freedom of the adsorbate molecule as it is adsorbed onto the surface of the material, and can be shown using the Gibbs free energy (equation 1.1).

$$\Delta G = \Delta H - T\Delta S \quad 1.1$$

Where:

$\Delta G$  = the surface free energy (J mol<sup>-1</sup>)

$\Delta H$  = the enthalpy of adsorption (J mol<sup>-1</sup>)

$\Delta S$  = the entropy of adsorption (J K<sup>-1</sup> mol<sup>-1</sup>)

$T$  = the temperature (K)

## Chapter 1 Adsorption

As the adsorption process is spontaneous,  $\Delta G$  is therefore negative. The reduction in entropy during adsorption, as the adsorbate molecules become more ordered on the surface of the material, leads to a more negative  $\Delta S$  on adsorption. To maintain a spontaneous reaction, with a negative  $\Delta G$ ,  $\Delta H$  must therefore be negative, and therefore adsorption is an exothermic process.

The amount adsorbed decreases with increasing temperature, by Le Chatelier's principle, as thermal energy supply to the system is reduced, the exothermic process of adsorption will be favoured and the amount of adsorbate adsorbed will increase. This is true for all adsorption systems, except those which exhibit activated diffusion effects. (See section **1.4.2.1**)

### 1.1.2 Adsorption Forces for a Gas Molecule on an Open Surface

The interaction between the gas molecules and the surface of the solid are electromagnetic in nature, and involve the interaction of the electron density surrounding the involved molecules. As the nature of the interaction is electromagnetic, there will be an attractive and repulsive component to the forces involved. Which component is involved is dependent on the separation distance of the molecules.

Attractive long range forces arise from London dispersion forces. Assuming that in the ground state the electron cloud of a gas molecule is symmetrically spherical, there will be no permanent dipole. Instantaneous dipoles may be induced in the electron cloud by neighbouring molecules, these dipoles in neighbouring molecules will be in phase, resulting in the force of attraction.<sup>22</sup> The energy of this interaction is calculated by quantum mechanical methods and is given by equation 1.2:

$$E = \frac{-C}{r^6} \quad 1.2$$

Where:  $r$  is the distance between atoms and  $C$  is a constant. This equation is representative of the interactions between a pair of atoms. When the dispersion energy is between an atom and a solid, the dispersion energy becomes equal to the sum of the interaction energy between the gas atom and the molecules of the surface of the solid, as shown by equation 1.3:

$$E = \sum E_j \quad 1.3$$

## Chapter 1 Adsorption

Where:  $E$  is the dispersion energy and  $E_j$  is the energy of the interaction between the gas atom and the  $j$ th atom of the solid. The assumption of molecules being symmetrically spherical leads to a disadvantage in this model, as molecules in a solid are rarely symmetrical.

The dispersion interactions of molecules are long range, and are responsible for the condensation of gases. Repulsive interactions occur at shorter separation distances, where the electron clouds of separate molecules interact, creating valence forces, and are responsible for chemical bond formation.

The simplest equation for modelling the repulsive interaction energy is shown in equation 1.4:

$$E = Br^{-m} \quad 1.4$$

Where:

$B$  and  $m = \text{constants}$

$r = \text{the separation distance between the centres of the atoms}$

Combination of equations 1.2 and 1.4 leads to equation 1.5, with  $m$  taking the value of 12.

$$E = -Cr^{-6} + Br^{-12} \quad 1.5$$

This equation is known as the Lennard-Jones Potential.<sup>23</sup> The Lennard Jones Potential is shown schematically in **Figure 1-1**, and describes the potential energy as two molecules in the gas phase approach each other.

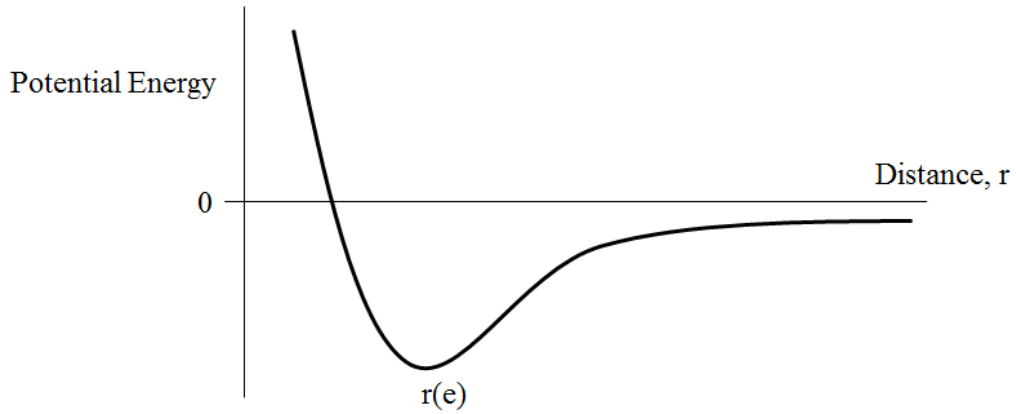


**Figure 1-1:** The Lennard-Jones Potential

Positive values of potential energy occur at short separation distance, and this is where repulsions are dominant. Negative values of potential energy occur at longer separation distances and this is where attractions are dominant. The attractive and repulsive forces of interaction between the two molecules will balance at a certain separation distance,  $r(e)$ , at this separation distance the potential energy of interaction is at a minimum.

The short and long range interactions determine if there is an electron transfer between the surface and the adsorbed gas molecule, this then determines which type of adsorption is observed, either physisorption or chemisorption.<sup>17</sup>

### 1.1.3 Adsorption Forces for a Gas Molecule in Porous Materials

#### 1.1.3.1 Porosity

The word “pore” describes a minute opening which allows gases or vapours to travel from the external surface of the material to the internal surface area. Pores provide the internal surface area on which adsorption occurs.

*The internal surface* area of a porous material is defined as the area which surrounds closed pores and all fissures and cracks which are deeper than they are wide.

*The external surface* area of a porous material is defined as the protrusions and superficial cracks which are wider than they are deep.

The total surface area of porous materials consists mainly of internal surface area; this can lead to enhanced surface areas of  $500 - 1000\text{m}^2\text{g}^{-1}$ .

The *porosity* of a material is the collective term for the pores and the pore distributions. Porosity is defined as the ratio of total pore volume to the volume of the adsorbent. Adsorption occurs in open porosity, and this is defined as the ratio of voids and open pores to the volume occupied by the adsorbent.

The sizes of pores are classified by the International Union of Pure and Applied Chemistry as in **Table 1-2** and **Table 1-3**.

**Table 1-2:** Classification of pores according to width<sup>24</sup>

<b>Pore Classification</b>	<b>Width</b>
<b>Micropores</b>	Width less than 2nm
<b>Mesopores</b>	Width between 2 and 50nm
<b>Macropores</b>	Width greater than 50nm

Macropores and mesopores are generally considered as transport pores for the adsorptive, with the micropores providing the main surface for adsorption.

Microporosity can be further defined as in **Table 1-3**.

**Table 1-3:** Classification of micropores according to width<sup>25</sup>

<b>Micropore Classification</b>	<b>Width</b>
<b>Ultramicropores</b>	Width less than 0.7nm
<b>Micropores</b>	Width between 0.7nm and 1.4nm
<b>Supermicropores</b>	Width between 1.4 and 2.0 nm

Pore size is a critical issue in the adsorption of gases into porous materials. Larger pores increase the amount of gas which can be adsorbed into the material; however larger pores pose stability issues, with structural interpenetration, where two parts of the structure interconnect and catenation, where connections of links form chains<sup>26</sup>. It is more desirable to have a larger number of small pores, which enhance the adsorption through favourable interactions.

1.1.3.2 Adsorption Potential in Micropores

At a certain pore width, the overlap of surfaces within the pore will produce a favourable minimum potential energy level, which is then occupied by the adsorbed molecule. This interaction potential is greatest in micropores, as the pore walls are in closer proximity than in wider pores, and as such the majority of adsorption occurs in micropores. This enhancement of adsorption in micropores means that a large amount of gas can be adsorbed at low values of relative pressure. This effect is not just influenced by the size of the pore, but also by the ratio of pore size to the diameter of the adsorptive. Everett and Powl calculated interaction potentials based on a slit-shaped model of micropores<sup>27</sup>. This is shown in **Figure 1-2**, where relative interaction potential  $\phi/\phi^*$  is shown plotted against the ratio  $d/r_0$  where  $d$  is the half width of the slit and  $r_0$  is the collision radius of the molecule. For large values of  $d/r_0$ , the potential curve resembles plot (a) where two minima are present. As the width of the adsorbing molecule approaches the size of the pore, the minima merge to give a single potential energy well of increasing depth, plots (b) to (c). Plot (c) is that shown in micropores, and allows enhanced adsorption.

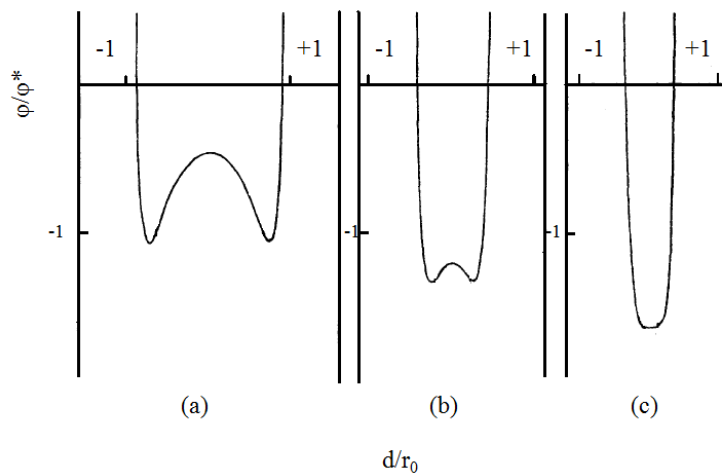


**Figure 1-2:** Enhancement of interaction potential in a slit-shaped pore<sup>27,28</sup>

1.1.4 Thermodynamics of Adsorption

1.1.4.1 Molar Energy of Adsorption

As discussed previously, the enthalpy of physisorption is exothermic due to the Gibbs free energy equation (equation 1.1). In the most simple of cases, adsorption occurs when the temperature and volume of the system are constant. This allows an expression for the molar energy of adsorption  $\Delta_a U$  shown in equation 1.6

$$\Delta_a U = -Q_{T,V} \quad 1.6$$

Where:  $-Q_{T,V}$  is the amount of heat evolved at constant temperature and volume.

In physisorption processes the adsorbent is usually an inert, stable material.<sup>29</sup> The change in molar energy is therefore brought about solely by the change in state of the adsorptive, induced by the removal of adsorptive from the gas phase by adsorption onto the surface of the material, allowing equation 1.7:

$$\Delta_a U = u_a - u_g \quad 1.7$$

Where:

$u_a$  = the molar internal energy of the adsorbed state

$u_g$  = the molar internal energy of the gas phase.

The molar energy of the adsorption system is then dependant on all adsorbate-adsorbent and adsorbate-adsorbate interactions.

1.1.4.2 The Isosteric Enthalpy of Adsorption

The change in Gibbs free energy with respect to the change in amount of substrate is known as the chemical potential,  $\mu$ , at constant pressure, temperature and constant amounts of other components. It is essential for all thermodynamic studies that the system under question reaches equilibrium.<sup>28</sup> When an adsorption is at equilibrium, the chemical potential of the gas phase will be equal to the chemical potential of the adsorbed phase:

$$\mu_a = \mu_g \quad 1.8$$

For the gas phase, the change in chemical potential energy,  $d\mu_g$  is given by:

$$d\mu_g = -S_g dT + V_g dP \quad 1.9$$

Where:

## Chapter 1 Adsorption

$S_g$  = the entropy of the gas phase ( $\text{J K}^{-1} \text{mol}^{-1}$ )

$V_g$  = the volume of the gas phase ( $\text{cm}^{-3}$ )

$P$  = the pressure (mbar)

For the adsorbed state, the change in chemical potential energy,  $d\mu_a$  is given by equation 1.10:<sup>28</sup>

$$d\mu_a = -\dot{S}_a dT + \dot{V}_a dP + \left(\frac{\delta\mu_a}{\delta n_a}\right)_{T,p} dn_a \quad 1.10$$

Where:

$\dot{S}_a$  = the differential entropy of the adsorbed phase

$\dot{V}_a$  = the differential molar volume of the adsorbed phase

$n_a$  = the number of moles adsorbed

Substituting equations 1.10 and 1.9 into 1.8, and at a constant  $n_a$  gives equation 1.11:

$$(S_g - \dot{S}_a)dT = (V_g - \dot{V}_a)dP \quad 1.11$$

Rearranging equation 1.11 gives equation 1.12:

$$\left(\frac{dP}{dT}\right)_{n_a} = \frac{(S_g - \dot{S}_a)}{(V_g - \dot{V}_a)} \quad 1.12$$

Assuming that  $V_g$  (molar volume of the gas phase) is much greater than  $V_a$  (differential molar volume of adsorbed phase) and assuming that  $V_g$  obeys the perfect gas laws, then substitute  $V_g = RT/P$ , equation 1.12 becomes equation 1.13:

$$\left(\frac{dP}{dT}\right)_{n_a} = P(S_g - \dot{S}_a)/RT \quad 1.13$$

$S_g - S_a$  represents the total change in entropy, so equation 1.13 becomes equation 1.14:

$$\left(\frac{dP}{dT}\right)_{n_a} = -P\Delta\dot{S}_a/RT \quad 1.14$$

At equilibrium, we have equation 1.15 which defines the differential molar enthalpy of adsorption,  $\Delta\dot{H}_a$ :

$$\Delta\dot{H}_a = T\Delta\dot{S}_a \quad 1.15$$

Rearranging and substituting equation 1.15 into equation 1.14 gives equation 1.16:



$$\left(\frac{dP}{dT}\right)_{n_a} = -\frac{P\Delta\dot{H}_a}{RT^2} \quad 1.16$$

Separation of variables gives equation 1.17:

$$\int \frac{dP}{P} = \frac{\Delta\dot{H}_a}{R} \int \frac{dT}{T^2} \quad 1.17$$

Integration of equation 1.17 gives the Clausius Clapeyron Equation 1.18:<sup>30</sup>

$$\ln P = -\frac{\Delta\dot{H}_a}{RT} + \frac{\Delta S}{R} \quad 1.18$$

This equation represents the relationship between pressure and temperature for a given amount adsorbed, therefore is an adsorption *isostere*. By obtaining isotherms at a series of temperatures, for a set value of amount adsorbed,  $n_a$  (mmol g<sup>-1</sup>), a plot of  $\ln P$  against  $1/T$  (K<sup>-1</sup>) may be obtained, and the value of the isosteric enthalpy of adsorption can be calculated directly from the gradient of this plot,  $\Delta H/R$ , whilst the entropy of adsorption can be calculated from the intercept,  $\Delta S/R$ . Extrapolation of the isosteric enthalpy of adsorption to zero surface coverage provides a fundamental measure of the adsorbate/adsorbent interaction.

## 1.2 Adsorption Isotherms

The extent of adsorption ( $n$  / mmol g<sup>-1</sup>) on the surface of the adsorbate is a function of the temperature ( $T$  / K) and pressure ( $P$  / mbar) of the system, and of the properties of both the adsorbate and the adsorbent:

$$n = f(P, T, \text{adsorbent}, \text{adsorbate}) \quad 1.19$$

For a given adsorbate adsorbed on a given adsorbent at constant temperature this simplifies to:

$$n = f(P)_{T, \text{adsorbent}, \text{adsorbate}} \quad 1.20$$

To allow comparison between different systems, isotherms are conventionally plotted on the basis of relative pressure  $P/P^0$  where  $P^0$  is the saturated vapour pressure of the adsorbate:

$$n = f\left(\frac{P}{P^0}\right)_{T, \text{adsorbent}, \text{adsorbate}} \quad 1.21$$

This gives a universal basis which allows graphical representation and comparison of isotherms.

1.2.1 Classification of Isotherms

Brunauer *et al*<sup>18</sup> classified physisorption isotherms into five types, with a sixth being added in 1985 by the IUPAC classification scheme.<sup>8</sup> The classification chart is shown in **Figure 1-3**. All isotherms should fit one, or a combination of two or more of these isotherms.

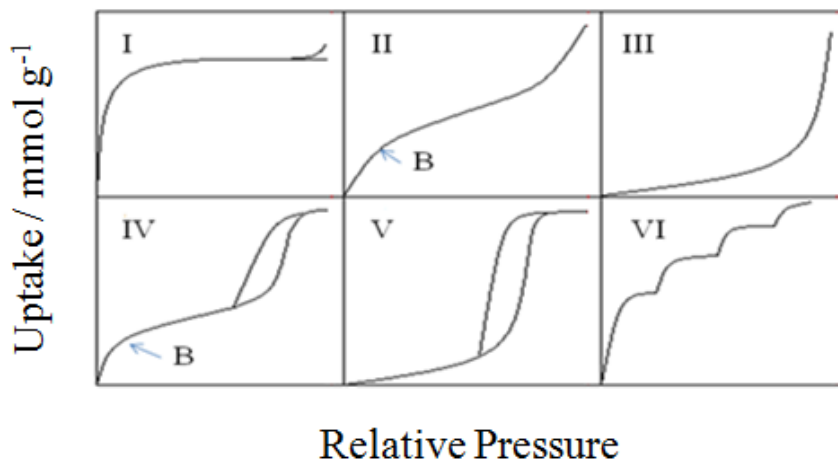


**Figure 1-3:** Isotherm classification chart

*Type I Isotherm:* As explained in **Section 1.1.3.2**, enhanced adsorption occurs in micropores which approach the diameter of the adsorbate. A decrease in the micropore width results in an increase in adsorption energy, and a reduction at the relative pressure at which maximum adsorption occurs. This leads to the production of an isotherm concave to the relative pressure axis, which rises sharply at low relative pressures and reaches a plateau at low relative pressure, giving an isotherm characteristic of microporous materials. The amount adsorbed reaches a limiting value as  $P/P^0$  approaches 1. The value of amount adsorbed at the plateau gives a good indication of the pore volume of the material.<sup>17</sup> An example is nitrogen and carbon dioxide adsorption on activated carbon at 77 K.<sup>10</sup>

*Type II Isotherm:* The isotherm follows a path which is concave to the relative pressure axis, then linear, then convex at higher relative pressure. The point B is the start of the linear section of the isotherm and represents the completion of monolayer coverage and the start of multilayer formation. The thickness of the multilayer increases as  $P/P^0$  approaches 1, with the adsorbed layer becoming bulk liquid or solid when  $P/P^0$  reaches 1. This isotherm type is typically obtained for non-porous or

macroporous materials, for example nitrogen adsorption on non-porous silica and n – butane on carbon black at 298 K.<sup>31, 32</sup>

*Type III Isotherm:* The isotherm is convex to the relative pressure axis over the entire pressure range. It is characteristic of weak adsorbate-adsorbent interactions, leading to low uptakes at low relative pressure. Once an adsorbate molecule has been adsorbed onto an adsorption site the interactions become stronger, which becomes the driving force for adsorption, leading to larger uptakes at higher relative pressure.<sup>33</sup> An example of this type of isotherm is water adsorption on active carbon BAX950.<sup>34</sup>

*Type IV Isotherm:* The isotherm follows a similar path to that of the Type II isotherm; however a plateau is reached at high relative pressure rather than the continued uptake. The most characteristic feature is the hysteresis loop, which shows the adsorption section on the lower branch and a different desorption section on the upper branch. The extent of the hysteresis is dependent on the system, and can be attributed to capillary condensation in mesoporous materials such as activated carbon and to structural change in microporous materials such as metal organic frameworks, both of which result in different adsorption and desorption mechanisms. An example of this adsorption isotherm is water adsorption on silica.<sup>35</sup>

*Type V Isotherm:* The isotherm follows a similar path to the Type III isotherm, with a plateau at higher relative pressure rather than continued uptake. This type of isotherm is uncommon, but has been seen for water vapour adsorption on activated carbon.<sup>36</sup>

*Type VI Isotherm:* The isotherm was initially introduced as a hypothetical isotherm but was included in the 1985 International Union of Pure and Applied Chemistry classification system. The isotherm shows stepwise multilayer adsorption on a highly uniform surface, and has been shown with krypton adsorption on carbon black at 77 K.<sup>37</sup>

### 1.2.2 Hysteresis

The desorption section of an isotherm often follows the same pathway as the adsorption isotherm. When the desorption isotherm deviates from the path of the adsorption isotherm, as in isotherm Types IV and V, this is known as hysteresis. It is

well known that mesoporous materials produce distinctive hysteresis loops, and these were first classified into three types by de Boer.<sup>38</sup> A further fourth type was added in 1985 by Sing *et al.*,<sup>2</sup> and these hysteresis types are shown in **Figure 1-4**. The variety in the shapes of the hysteresis loops can be associated with specific pore structures.

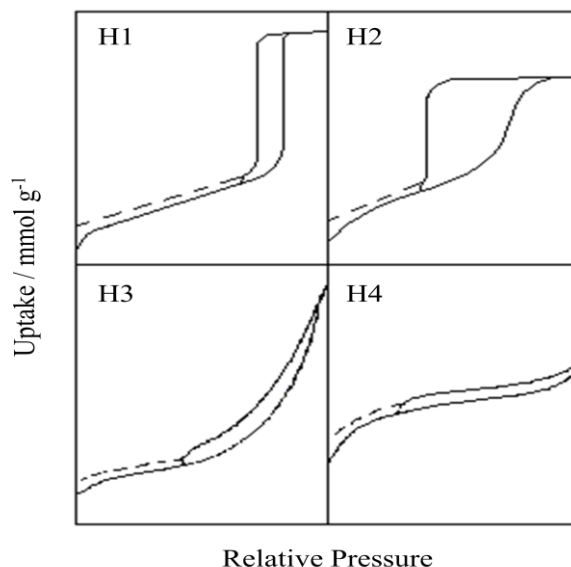


**Figure 1-4:** Types of adsorption – desorption hysteresis loops<sup>17</sup>

The H1 hysteresis loop has very steep adsorption and desorption branches which are very narrow. This hysteresis is often given by porous materials with a narrow distribution of mesopores. H1 hysteresis contains a plateau, as does the H2 hysteresis. The H2 loop is broad with the desorption branch showing a long flat plateau before the steep desorption section, and is characteristic of complex pore structures. Hysteresis types H3 and H4 show no plateau at high relative pressure and convergence of the two hysteretic branches does not occur until the system approaches the saturation vapour pressure. H3 and H4 are usually given by adsorbents with slit shaped pores, as seen in activated carbons; however H4 is also given by adsorbents with a size distribution in the micropore range.

In order to provide interpretation of the much studied Type IV isotherm hysteresis, the theory of capillary condensation was put forward by Zsigmondy<sup>11</sup>, who described adsorption as the multilayer formation within a pore, with desorption being the evaporation of the adsorbate from the surface of the pore, two different mechanisms, giving rise to different shapes for the adsorption and desorption isotherm. In

mesoporous carbon based materials the hysteresis is based on this theory of pore filling and emptying difference. As the equilibrium pressure approaches saturation pressure there will be a spontaneous condensation of the gas molecules onto the pore walls, with multilayer formation until the pore is filled. The desorption process then follows from a changed meniscus, as seen in **Figure 1-5**, leading to an altered desorption isotherm.

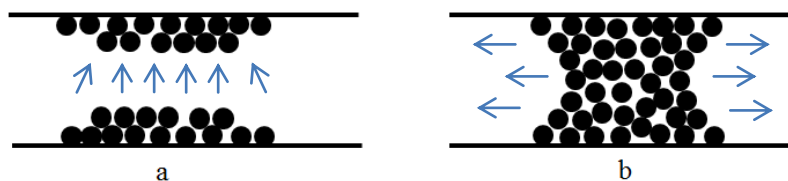


**Figure 1-5:** Hysteresis in a column-like pore, (a) adsorption (b) desorption

Capillary condensation does not account for all occurrences of hysteresis, for example, in metal organic frameworks the hysteresis may be based on structural change, as metal organic frameworks are mostly microporous, and as such capillary condensation does not occur as the pores are too narrow. The hysteretic adsorption of hydrogen by a nanoporous metal organic framework was observed by Zhao *et al*<sup>39</sup> and Fletcher *et al*<sup>40</sup> where microporous metal organic frameworks showed hysteresis based on kinetic trapping effects through structural flexibility.

### 1.3 Interpretation of Adsorption Isotherms

#### 1.3.1 Henry's Law

The simplest interpretation of the behaviour of adsorbed molecules at the low surface coverage region of the isotherm is that the adsorbed molecules have no interaction with each other.<sup>16</sup> This is Henry's Law and can be expressed as in 1.22:

$$n = K_H P \quad 1.22$$

Where:

$n$  = the specific surface excess amount

$P$  = the pressure (mbar)

$K_H$  = Henry's law constant

This shows a linear relationship between amount adsorbed at the gas equilibrium pressure, at low pressure and high temperatures, at low uptakes.

The differential enthalpy of adsorption at zero surface coverage can be calculated from equation 1.23 by plotting  $\ln K_H$  against  $1/T$ .

$$\Delta_{ads} \dot{h}_0 = RT^2 \left( \frac{\partial(\ln K_H)}{\partial T} \right)_n \quad 1.23$$

All isotherms should obey this relationship at low pressure, however in the cases where there is deviation from this, a virial treatment may be adopted. Virial analysis is also useful for analysis of adsorption where the adsorptive are above their critical temperature.<sup>41, 42</sup>

### 1.3.2 Langmuir Equation

The Langmuir model is the simplest description of an adsorption isotherm, and is generally used for the analysis of Type I isotherms. Although classically developed for analysis of adsorption on an open surface, the equation describes the limiting value shown on the plateau of the Type I isotherm, which is the isotherm characteristic of adsorption in microporous materials.<sup>13,14</sup> The Langmuir isotherm is based on several assumptions<sup>43</sup>:

- i. Adsorption in the Type I isotherm is monolayer; the attractive forces of the surface are shielded by the monolayer and multilayers of adsorbate are not formed
- ii. The surface of the adsorbing surface is uniform and all adsorption sites are energetically homogenous
- iii. The adsorbed molecules and the molecules in the bulk gas phase are in dynamic equilibrium
- iv. Collisions between a molecule in the bulk gas phase and a vacant adsorption site on the adsorbent result in adsorption
- v. Once adsorbed, the molecules become localised, and do not migrate across unfilled surface sites

The Langmuir equation is derived from the kinetic theory of gases. Assuming that the adsorbate in the gas phase is in dynamic equilibrium with the surface of the adsorbent, this gives equation 1.24 for associative adsorption.

## Chapter 1 Adsorption



Where:

$A_g$  = the adsorbent in the gas phase

$S_{surface}$  = the surface site of the adsorbent

$k_a$  and  $k_d$  = the rate constants of adsorption and desorption, respectively ( $s^{-1}$ )

$M - A$  = adsorbed molecule on a surface site

The adsorption surface is comprised of  $N^s$  independent and energetically homogenous adsorption sites, which can be occupied by  $N^a$  adsorbed molecules, this fractional surface coverage,  $\theta$ , is given by equation 1.25:

$$\theta = \frac{N^a}{N^s} \quad 1.25$$

The rate of adsorption is dependent on pressure  $P$  of the system and the fraction of unoccupied surface sites on the adsorbent  $1 - \theta$  as shown in equation 1.26:

$$\text{rate of adsorption} = k_a P (1 - \theta) \quad 1.26$$

Where:  $k_a$  = the rate constant of adsorption ( $s^{-1}$ ). Equation 1.26 shows that if the pressure and rate constant are large, and the fraction of unoccupied sites is small, then the adsorption will be fast.

The rate of desorption is independent of pressure, but is dependent on the fraction of occupied surface sites as shown in equation 1.27:

$$\text{rate of desorption} = k_d \theta \quad 1.27$$

Where:  $k_d$  = the rate constant of desorption ( $s^{-1}$ ).

At equilibrium, the rates of adsorption and desorption are equal, and equations 1.26 and 1.27 combine to give equation 1.28:

$$k_a P (1 - \theta) = k_d \theta \quad 1.28$$

This can be rearranged to equation 1.32 via the following rearrangement:

$$k_a P = \theta(k_d + k_a P) \quad 1.29$$

$$\theta = \frac{k_a P}{(k_d + k_a P)} \quad 1.30$$

$$\theta = \frac{\left[\left(\frac{k_a}{k_d}\right)P\right]}{\left[1 + \left(\frac{k_a}{k_d}\right)P\right]} \quad 1.31$$

$$\theta = \frac{KP}{1+KP} \quad 1.32$$

Where  $K$  = the equilibrium rate constant (not the thermodynamic equilibrium constant) and is defined as:

$$K = \frac{k_a}{k_d} \quad 1.33$$

As the fractional surface coverage is a difficult dimension to measure, it is re-defined as the relative mass, and is given by:

$$\theta = \frac{n}{n_m} \quad 1.34$$

Where:

$n$  = the amount adsorbed (g)

$n_m$  = the monolayer capacity of the material ( $\text{mmol g}^{-1}$ )

Combination of equations 1.32 and 1.34, rearrangement and simplification give the Langmuir equation used for isotherm analysis:

$$\frac{P}{n} = \frac{P}{n_m} + \frac{1}{Kn_m} \quad 1.35$$

A plot of  $P/n$  against  $P$  should give a linear graph of gradient  $1/n_m$ , the reciprocal of which will give the monolayer capacity of the material. At very low pressures the isotherm is linear and reduces to Henry's Law. The equilibrium constant,  $K$ , represents the strength of interaction between the adsorbate and the adsorbent.

### 1.3.3 Brunauer Emmet Teller (B.E.T) Theory

Although Langmuir put forward an isotherm equation to model monolayer adsorption, he also recognised that the kinetic theory used to derive his equation could be applied to second and higher layers of adsorbed molecules. The model Langmuir arrived at for multilayer adsorption was too complex, and was not adopted. By introducing further assumptions to the Langmuir theory, Brunauer, Emmet and Teller were able to arrive at their famous equation now commonly used to calculate the surface area of many porous materials.<sup>44</sup> The assumptions used in forming their equation include all those used by Langmuir and the following additions:



## Chapter 1 Adsorption

- i. Unrestricted multilayer formation may take place
- ii. Only the uppermost layers of molecules in the multilayer system are in dynamic equilibrium with the vapour
- iii. Enthalpies of adsorption of the second and higher layers are equal to the enthalpy of condensation
- iv. Desorption can only occur from the uppermost exposed layer

The B.E.T equation is associated with Type II and Type IV isotherms, discovered by Brunauer and Emmet in 1937, during their work studying nitrogen adsorption on a synthetic iron ammonia catalyst.<sup>45</sup> Type II isotherms show unrestricted multilayer formation, whereas Type IV isotherms show restricted multilayer formation.

The B.E.T equation in its linear form is shown in equation 1.36:

$$\frac{p}{n(p^0-p)} = \frac{1}{n_m C} + \frac{(c-1)}{n_m C} \cdot \frac{p}{p^0} \quad 1.36$$

Where:

$p$  = pressure (mbar)

$p^0$  = saturation vapour pressure (mbar)

$n$  = uptake at pressure  $p$  (mmol g<sup>-1</sup>)

$n_m$  = monolayer capacity (mmol g<sup>-1</sup>)

$c$  = dimensionless constant, related to adsorption energy, as shown in equation 1.37:

$$c = \exp\left[\frac{\Delta H_A - \Delta H_L}{RT}\right] \quad 1.37$$

Where:

$\Delta H_A$  = enthalpy of adsorption of first layer

$\Delta H_L$  = enthalpy of vaporisation of molecules present in the second and higher multilayer

$R$  = the gas constant

$T$  = the temperature

When  $C$  is large, indicating that the enthalpy of adsorption of the monolayer is large compared to the enthalpy of adsorption of the second and higher layers, there will be greater adsorption than when  $C$  is small. The value of  $C$  taken will affect the shape

of the isotherm produced, with larger values of  $C$  giving Type I shaped isotherms, and smaller values giving Type III shaped isotherms. Middle range values, from  $\sim 10 - 100$  will give Type II shaped isotherms. The effect of changing values of  $C$  on the shape of the isotherms is shown in **Figure 1-6**.

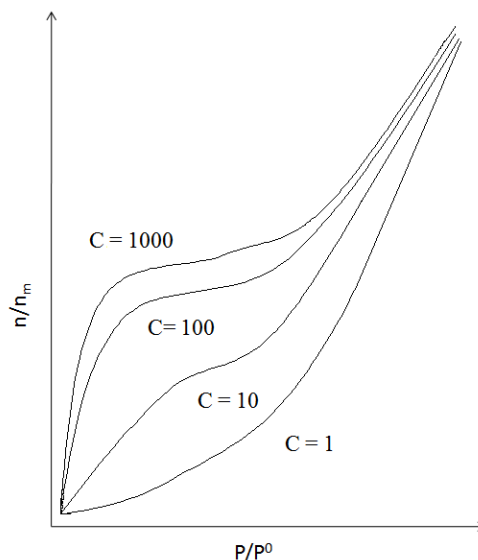


**Figure 1-6:** B.E.T isotherm plots showing change in isotherm with changing  $C$  values

Plotting  $p/n (p^0 - p)$  against  $p/p^0$  will give a straight line, gradient  $(c - 1)/n_m c$  and intercept  $1/n_m c$  in the region of  $0.05 - 0.3$  on the relative pressure axis. From this monolayer coverage and  $C$  values can be calculated, and from this the apparent surface area.

The B.E.T model is the most widely used model for the determination of surface area of porous materials, with nitrogen being the standard adsorptive at 77 K. Nitrogen molecules at low temperature tend to fill the entire porosity, with packing only depending on the size of the nitrogen molecule, independent of the adsorbent structure<sup>46</sup> making this the optimum adsorptive for determining B.E.T surface area.

Although the B.E.T equation is commonly used to describe the porosity of many materials, there are fundamental problems with the equation, which have been recognised since its development. The assumptions used in deriving the equation do not take into account several important features. Not all surface sites are energetically homogenous; almost all adsorbents have energetically heterogeneous surfaces. The model does not take into account the horizontal interactions of

molecules in the layers, which must be prominent when surfaces are approaching completion due to the proximity of the molecules on the surface. When used to study the surface area of microporous carbons, the B.E.T equation can give unreasonably high surface areas.

### 1.3.4 Evaluation of Microporosity – The Dubinin-Radushkevich (DR) Model

The Dubinin Theory of the Volume Filling of Micropores (TVFM) equation is based on earlier theories developed by de Saussure<sup>47</sup>, Eucken<sup>48</sup> and Polanyi<sup>49</sup>. It is widely used for assessing the volume of micropores in activated carbons and other porous materials.<sup>14, 50, 51, 52, 53, 54, 55, 56, 57, 58, 59, 60</sup> The DR model is based upon the Polanyi Potential Theory, which assumes that the monolayer does not shield the attractive forces of the surface of the material; instead they can reach beyond the dimensions of a monolayer and form a potential energy gradient. This is fundamentally different to the Langmuir derivation as this assumes monolayer formation only, with no influence beyond the monolayer.

#### 1.3.4.1 Polanyi Potential Theory

The adsorption potential was defined by Polanyi as the work involved in bringing a molecule of gas or vapour from the gas phase to a point within the adsorbed phase.<sup>49</sup>

**Figure 1-7** illustrates schematically the basic ideas involved in the Polanyi Potential Theory of adsorption.

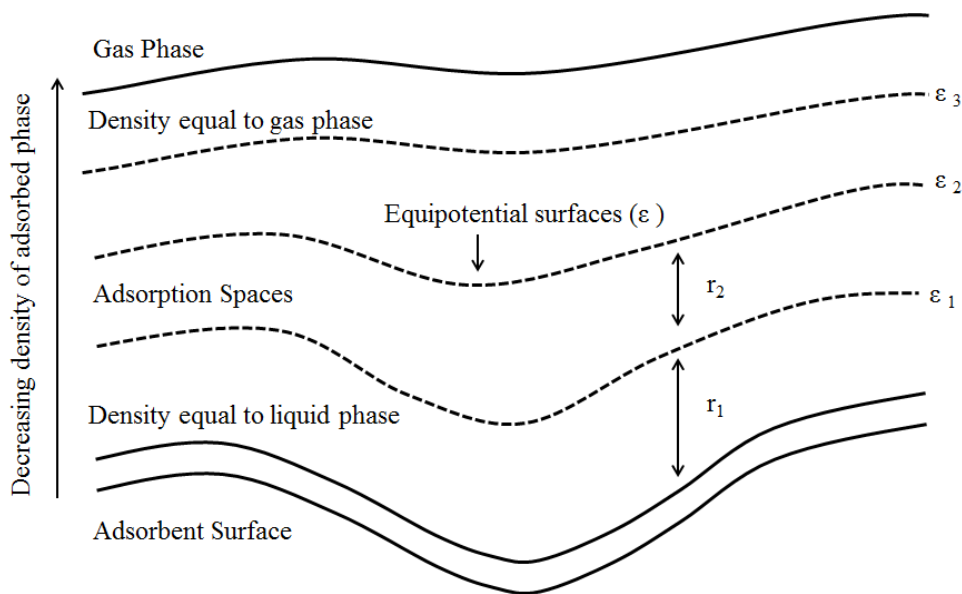


**Figure 1-7:** Polanyi Potential Theory – cross-section of the adsorbed phase

## Chapter 1 Adsorption

The adsorbent surface emanates a strong attractive force, and is responsible for the formation of multilayers of adsorbed gas or vapour. The layers are compressed due to the strong attractive force, and by compression from higher layers. This results in a density gradient, with the adsorbed gas closest to the adsorbed surface being denser than higher layers, with density approximating the liquid phase. The density decreases with increasing distance from the surface until it reaches that of the gas phase. The work done in compressing the gas is given by equation 1.38.<sup>61</sup>

$$\varepsilon_i = \int_{\rho_x}^{\rho_i} V dP \quad 1.38$$

Where:

$\varepsilon_i$  = the adsorption potential when the density of the gas is  $\rho_i$

$\rho_x$  = the density of the gas phase ( $\text{g cm}^{-3}$ )

$V = M/\rho$  where  $M$  is the molecular weight of the adsorbate

The forces of attraction at any given point between the adsorbent surface and the gas phase form layers, or equipotential surfaces, shown in the diagram as  $\varepsilon_1, \varepsilon_2, \varepsilon_3$  and  $\varepsilon_4$ , at a distance  $r_1, r_2$ , etc. Each equipotential surface therefore encloses a volume,  $v_1, v_2$ , etc.  $V_{\text{max}}$ , the total volume is that encompassed by the adsorbed surface and the adsorbed phase/gas phase boundary. The maximum adsorption potential is found at the adsorbent surface, the minimum adsorption potential is found at the gas phase boundary. The adsorption potential ( $\varepsilon$ ) is a function of the volume ( $V$ ) it encompasses, shown by equation 1.39, and as such can be considered as an isotherm equation as both  $\varepsilon$  and  $V$  can be expressed in terms of temperature and pressure.

$$\varepsilon = f(V) \quad 1.39$$

The curve produced from this relationship is known as a “characteristic curve”, as the adsorption potential is postulated to be independent of temperature, the curve produced becomes characteristic for a given gas at any temperature.

The Polanyi theory was not developed from kinetic or thermodynamic approaches, instead a characteristic curve was calculated from experimental isotherm data, and all other isotherms were calculated from this analysis. When calculating the characteristic curve the following assumptions were followed:

## Chapter 1 Adsorption

- i. The vapour present in the gas phase behaves as an ideal gas ( $PV = nRT$ )
- ii. The liquid in the adsorbed phase is incompressible

The Polanyi equation is given in equation 1.40:

$$\varepsilon_i = \int_{\rho_x}^{\rho_i} \frac{RT}{P} = RT \ln \frac{P^0}{P_x} \quad 1.40$$

Where:

$\varepsilon_i$  = described as the work done in compressing an ideal gas from the gas phase at pressure  $P_x$  to the saturated gas pressure  $P^0$

$R$  = the gas constant ( $8.314 \text{ J K}^{-1} \text{ mol}^{-1}$ )

$T$  = temperature (K)

This allows the temperature dependency of physisorption to be taken into account in this adsorption model.

### 1.3.4.2 Derivation of the Dubinin-Radushkevich Equation

While interpreting the Polanyi potential Dubinin re-defined what Polanyi had coined the “adsorption potential” to “the change in free energy associated with reversibly bringing a molecule of gas from the gas phase to the condensed adsorbed phase” and denoted this as  $A$ , as shown in equation 1.41.<sup>62</sup>

$$\varepsilon = A = RT \ln \frac{P^0}{P_x} \quad 1.41$$

Where:

$R$  = the gas constant ( $8.314 \text{ J K}^{-1} \text{ mol}^{-1}$ )

$T$  = temperature in (K)

$P^0$  = saturated gas pressure (mbar)

$P_x$  = pressure (mbar)

The theory involves calculation of the volume filling of the micropores, therefore a second parameter, the degree of filling of the micropores,  $\theta$ , is defined as in equation 1.42.

$$\theta = \frac{W}{W_0} \quad 1.42$$

Where:

$W$  = the volume of micropores that has been filled at a relative pressure of 1

$W_0$  = the total available micropore volume

The micropore size distribution is assumed to be Gaussian<sup>63, 64, 65</sup>, and this led to the arrival at the following exponential expression:

$$\theta = \exp \left[ -k \left( \frac{A}{\beta} \right)^2 \right] \quad 1.43$$

Where:

$$A = -RT \ln(P^0/P)$$

$k$  = a characteristic parameter

$\beta$  = the similarity constant

Where  $k$  and  $\beta$  are both characteristic of the adsorbate

Combination of equations 1.42 and 1.43 results in the well-known DR equation:

$$W = W_0 \exp \left[ -k \left( \frac{RT}{\beta} \right)^2 \left( \ln \frac{P^0}{P} \right)^2 \right] \quad 1.44$$

which can be simplified to equation 1.42:

$$\frac{W}{W_0} = \exp \left[ -B \left( \frac{T}{\beta} \right)^2 \left( \log \frac{P^0}{P} \right)^2 \right] \quad 1.45$$

To plot the DR equation, equation 1.45 can be simplified to give equation 1.46

$$\log w = \log W_0 - D \log^2 \left( \frac{P^0}{P} \right) \quad 1.46$$

Where:

$$D = B \left( \frac{T}{\beta} \right)^2 = \text{a measure of the pore size distribution of the adsorbent.}$$

A graph of  $\log(W)$  against  $\log^2(P^0/P)$  should yield a straight line where the intercept is equal to the total micropore volume. In normal cases where mass uptake is measured,  $W$  and  $W_0$  can be replaced by  $n$  and  $n_0$ , which are the consecutive mass measurements, and volumes can be calculated from these values.

#### 1.3.4.3 The Dubinin – Astakhov (DA) Equation

The squared factor in the Dubinin – Radushkevich equation ( $\log P^0/P$ )<sup>2</sup>) describes a Gaussian distribution of micropore sizes. The Dubinin – Astakhov equation is simply a generalised version of this, where the square is replaced by  $n$  as shown in equation 1.47:

$$\log w = \log W_0 - D \log^n \left( \frac{P^0}{P} \right) \quad 1.47$$

The term  $n$  is referred to in the literature as the heterogeneity factor, relating to the distribution of pore sizes. Experimentally it has been shown that  $n = 2$  for activated carbons and  $n = 4 - 6$  zeolites. It allows linearization of plots by adjustments of the value of  $n$ .

The DR and DA equations are based upon the description of the distribution of the pore sizes within the structure. It has been suggested that for carbons and coals, the DR and DA equations are successful so long as the distribution of pores sizes can be described by a mathematical model.<sup>66,67,68</sup>

#### 1.3.4.4 Application of the Dubinin – Radushkevich Equation

The Dubinin – Radushkevich equation is a powerful tool in the analysis of isotherms produced by microporous materials. It can yield the following information when analysing the low relative pressure region of the isotherms by carbon dioxide adsorption at 273 K<sup>28</sup>:

- i. The amount adsorbed leading to the micropore volume
- ii. Relative pore size distributions based upon the gradient of the plots
- iii. How the pore size distributions vary from the expected Gaussian distribution

The relative pore size distributions affect the shape and degree of linearity of the plots produced by the DR analysis. This is shown in **Figure 1-8** along with how this changes the shape of the distribution from the expected Gaussian.<sup>69</sup> The dashed lines represent the expected shapes of the graphs; the solid lines show the possible deviations.

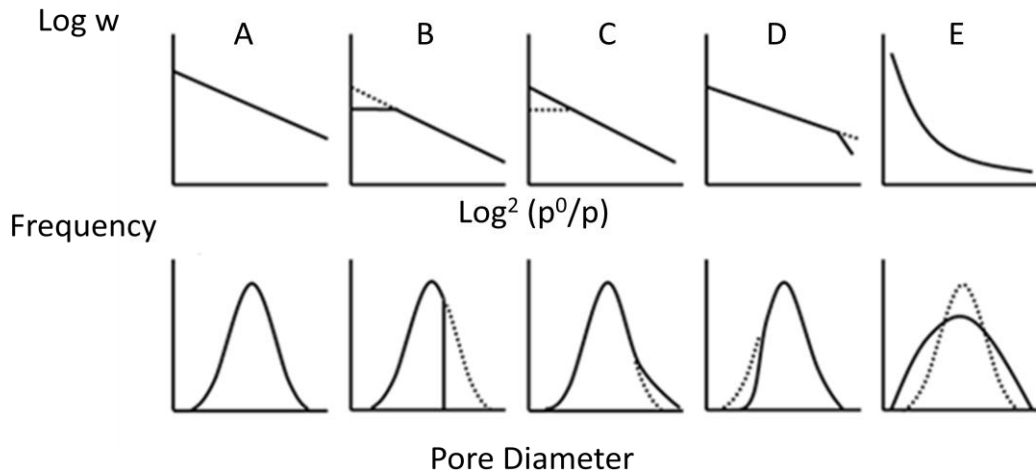


**Figure 1-8:** Possible deviations from the linear Dubinin - Radushkevich plot<sup>68</sup>

- A) Shows that the material obeys the theory of volume filling of micropores, where the micropore filling occurs from the smallest to the largest.
- B) Shows a pore distribution where the larger micropores are absent, or complete micropore filling occurs at a relative pressure less than 1.
- C) Shows an increase at higher relative pressures. This is attributed to the filling of additional porosity, for example mesoporosity, supermicropores or multilayer adsorption on the non-porous surfaces of the material.
- D) Shows a decrease in micropore filling at lower values of relative pressure, showing the smallest of micropores are not filled, this could be due to activated diffusion or molecular sieve effects.
- E) Shows that the micropore distribution is narrow and the isotherm is not at equilibrium, and cannot be analysed by the DR equation.

The gradients of the plots shown in **Figure 1-8** can be used to describe the average pore size distributions, lower values of the gradient represent a narrower distribution of micropores, higher values of the gradient represent a wider distribution of micropores, when adsorbents of similar types are compared.<sup>69</sup>



### 1.3.5 Virial Equation

The virial equation is employed as a method for analysing the low surface coverage region of adsorption isotherms. It can be applied to many systems and mechanisms, and is particularly useful when the isotherms are of gas adsorption at temperatures above the gas critical temperature.

A linear form of the virial equation was developed in the early 1900s by Williams<sup>15</sup> and Henry<sup>16</sup> and is given by equation 1.48.<sup>70</sup>

$$\ln\left(\frac{n}{p}\right) = A_0 + A_1n + A_2n^2 \dots \quad 1.48$$

In this equation  $A_0$  and  $A_1$  parameters are indicative of the interaction between the adsorbate-adsorbent at zero coverage and adsorbate-adsorbate interactions, respectively. The higher terms,  $A_2$  and above, can be ignored under circumstances of low surface coverage.<sup>71, 72</sup>

A similar virial treatment was adopted by Kiselev *et al*<sup>73</sup> to analyse the adsorption of methane, ethane and ethylene on carbon black and zeolite materials. The form of the equation used is shown as equation 1.49.

$$p = n \exp(C_1 + C_2n + C_3n^2 + C_4n^3 \dots) \quad 1.49$$

Where:

$n$  = the amount adsorbed (mol g<sup>-1</sup>)

$p$  = pressure (Pa)

$C$  = a temperature dependant parameter of the gas – solid system.

Czerpirski and Jagiello<sup>74</sup> developed equation 1.50 for virial analysis of adsorption isotherms, assuming that the isotherms obey Henry's Law at low surface coverage.

$$\ln(P) = \ln(N) + \frac{1}{T} \sum_{i=0}^m a_i N^i + \sum_{j=0}^n b_j N^j \quad 1.50$$

Where:

$P$  = pressure (Pa)

$N$  = uptake (mol g<sup>-1</sup>)

$T$  = Temperature (K)

$a_i$  and  $b_j$  = temperature independent empirical parameters.

## Chapter 1 Adsorption

This equation has been previously used by Rowsell *et al*<sup>75</sup> to describe the unique curvature of hydrogen adsorption isotherms observed on metal organic frameworks at 77 K, which were shown to be poorly described by Langmuir and other empirical isotherm equations.

The validity of the use of the linear equation 1.48 over equation 1.50 was investigated by Chen *et al* who compared the analysis of isotherms by equations 1.48 and 1.50 and also by the empirical Langmuir – Freundlich equation:

$$\left(\frac{n}{n_l}\right) = \left(\frac{KP^{1/m}}{1+ KP^{1/m}}\right) \quad 1.51$$

The greatest uncertainties in the applications of these equations occur at low pressure where there is the steepest uptake of gas. For this reason equation 1.51 was the least successful at modelling the isotherms at low pressure, as the equation does not reduce to Henry's Law. In the comparison by Chen *et al*, the linear equation 1.48, was found to have smaller errors when fit to the isotherm data than equation 1.50, and was used to model the data presented in their study.

At low surface coverage the amount adsorbed,  $n$ , approaches zero, and the linear virial equation 1.48 reduces to equation 1.52.

$$\frac{n}{p} = \exp(A_0) \quad 1.52$$

Calculation of  $A_0$  values can then yield the Henry's law constant by equation 1.53.

$$K_H = \exp(A_0) \quad 1.53$$

The specific values of  $A_0$  can be calculated by plotting  $\ln (n/P)$  against  $n$ .

The virial equation can be used to determine the isosteric enthalpy of adsorption. By plotting  $\ln (n/p)$  against  $n$  at series of temperatures, it is then possible to estimate the enthalpy of adsorption at zero surface coverage by plotting values of  $A_0$  against  $1/T$ . The gradient of this plot would be equal to  $\Delta H/R$ , allowing calculation of  $\Delta H$  in  $\text{kJ mol}^{-1}$ .

### 1.4 Surface Area Calculations and Phenomena Observed During Adsorption

Adsorption techniques are widely applied to determine the surface area of porous materials. The surface area of a porous material calculated by adsorption does not give a true representation of the actual surface area. The “equivalent” surface area that is calculated is a function of the experimental conditions and the method used to interpret the data, therefore it is a variable parameter and must be treated with caution. The calculation of surface area may also be affected by certain phenomena which exist in adsorption science, such as activated diffusion, molecular sieve effects and cooperation effects.

#### 1.4.1 Surface Area Calculation

With the calculation of monolayer capacity from either the Langmuir or B.E.T equation, the apparent surface area of the material can be calculated using equation 1.54.

$$S = A_m n_m N_A \quad 1.54$$

Where:

$S$  = the specific surface area ( $\text{m}^2 \text{g}^{-1}$ )

$A_m$  = the average area occupied by one molecule of adsorbate at monolayer coverage

$N_A$  = Avogadro's number,  $6.022 \times 10^{23}$  (molecules  $\text{mol}^{-1}$ )

$n_m$  = the monolayer capacity of the material ( $\text{mmol g}^{-1}$ )

#### 1.4.2 Phenomena Observed During Adsorption

##### 1.4.2.1 Activated Diffusion

Adsorption is an exothermic process, so by convention it is expected that as temperature is increased at a given relative pressure, the amount adsorbed should decrease. In porous systems in which ultra-microporosity is present often the contrary to this expected behaviour is observed, and a mass *increase* with increasing temperature is seen, with very slow timescales - where equilibrium may not be reached for many hours or days. **Figure 1-9** shows how activated diffusion was observed by P. Zwietering *et al.*<sup>76</sup>

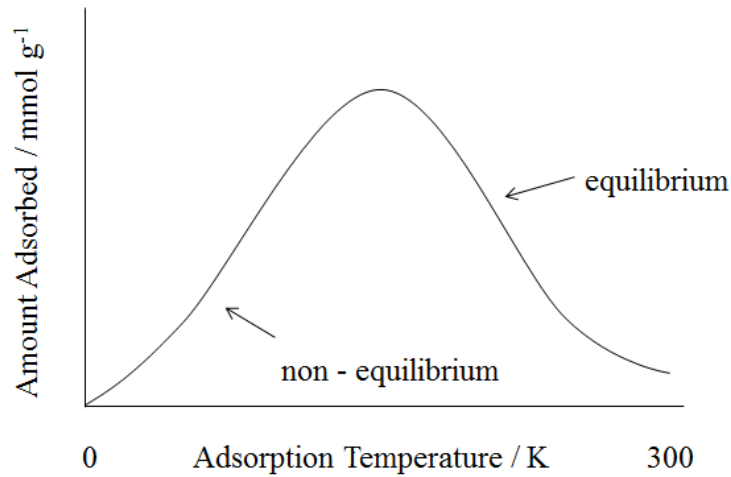


**Figure 1-9:** Activated diffusion<sup>76</sup>

**Figure 1-9** illustrates how low levels of adsorption occur at low temperatures, with equilibrium not being established. As the temperature increases, the amount adsorbed increases to a point where equilibrium is established. From this point any further increases in temperature results in mass loss, which is as expected, and has been shown many times.<sup>77,78</sup> The effect of activated diffusion is attributed to the relative sizes of the pores and the adsorbate molecules. When the size of the adsorbate approaches the size of the pores, barriers to diffusion occur which are only overcome by having enough thermal energy, as shown by the Arrhenius equation (equation 1.55).

$$k = A e^{-\frac{E_a}{RT}} \quad 1.55$$

Where:

$k$  = the rate of adsorption (s<sup>-1</sup>)

$E_a$  = the activation energy of the process (J mol<sup>-1</sup>)

$A$  = the pre exponential factor (s<sup>-1</sup>)

$R$  = the gas constant (8.314 J K<sup>-1</sup> mol<sup>-1</sup>)

$T$  = the temperature (K)

The barrier to diffusion is the activation energy required to enter the pore, and is related to the pore size. According to equation 1.55 the activation energy is related to the temperature of the system, the higher the temperature the more thermal energy the adsorbate possesses therefore the rate of adsorption increases, increasing the amount adsorbed. This temperature dependency for adsorption in porous materials

which possess the smallest and highest energy micropores may pose a problem for producing reliable surface areas, as values will change with changing temperature. This is especially a problem for nitrogen adsorption, and activated diffusion effects are often observed while attempting to gain a B.E.T nitrogen surface area value.

#### 1.4.2.2 Molecular Sieve Effects

Molecular sieve effects mainly refer to the exclusion of certain adsorbates from the porosity due to their effective diameters being larger than the entrance to the porosity. Molecules which have a smaller effective diameter will provide a larger value of surface area than those the same size, or larger than, the entrance to the porosity. This effect is explained more in **Chapter 2 – Porous Materials**.

#### 1.4.2.3 Cooperation Effects

Cooperative effects occur in larger micropores, where it is possible for more than monolayer coverage to occur. The phenomenon is illustrated in **Figure 1-10**.

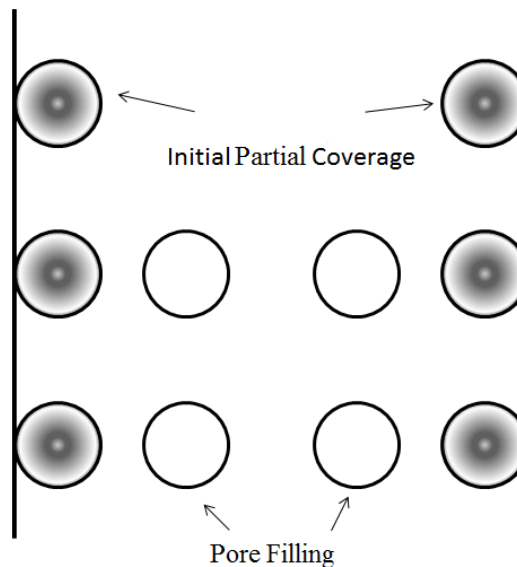


**Figure 1-10:** Cooperative effects in micropores

Initial filling of the monolayer occurs at low relative pressures. As the pressure increases, it becomes as energetically favourable to fill the middle of the pore as it is to complete the partially filled monolayer. This leads to an over – estimation of the surface area.

1.5 Mechanism of Adsorption

For the adsorption of a gas phase adsorbate onto the surface of the adsorbent to occur, the gas phase adsorbate must first diffuse to the surface of the adsorbent; this makes adsorption a two-step process, diffusion followed by adsorption. The rate of adsorption of the adsorbate onto the open surface of the solid is so great that it can be considered as instantaneous, making the rate determining step of adsorption the rate of diffusion (or how fast the molecules approach the surface of the solid).<sup>79</sup> The process of diffusion can follow four main mechanisms including: a) gas diffusion; b) Knudsen diffusion; c) surface diffusion; and d) activated diffusion. Which mechanism is followed is greatly dependent on the ratio of the dimensions of the adsorbate (in particular the mean free path of the molecule), to the size of the pore entrance.

The mean free path of the molecule is defined as the average distance the particle travels between collisions with other particles and is given by equation 1.56:

$$\lambda = \frac{RT}{\sqrt{2}\pi d^2 N_A P} \quad 1.56$$

Where:

$P$  = the pressure (Nm<sup>-2</sup>)

$T$  = the temperature (K)

$R$  = the gas constant (8.314 J K<sup>-1</sup> mol<sup>-1</sup>)

$d$  = the collision diameter (nm)

$N_A$  = Avogadro's constant (mol<sup>-1</sup>)

**Figure 1-11** illustrates the various mechanism of diffusion, and how the pore size relates to the mean free path of the molecule.

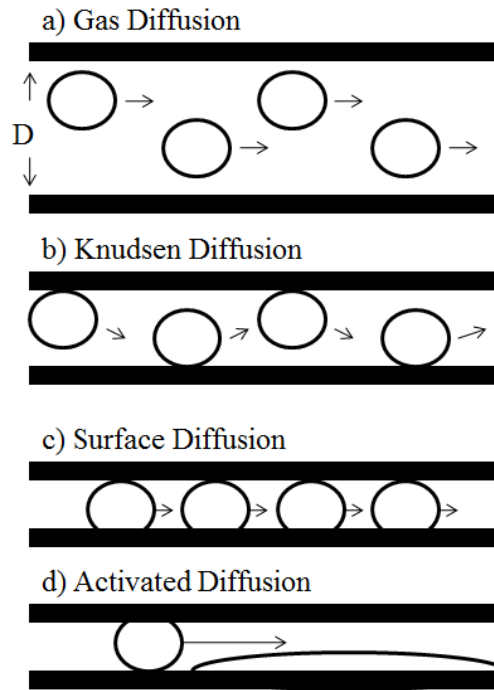


**Figure 1-11:** Mechanisms of diffusion

In gas diffusion, the molecules move through the porous structure without contact with the pore walls as the pore diameter is much greater than the mean free path of the molecules. This usually occurs in the larger macropores which have a diameter greater than 50 nm.

Knudsen diffusion can be described by the Knudsen Number, which is the ratio of the mean free path of the molecule and the diameter of the pore wall.<sup>80</sup>

$$K_n = \frac{\lambda}{d} \tag{1.57}$$

Where:

$\lambda$  = mean free path

$d$  = diameter of the pore (cm)

Free gas diffusion  $K_n \ll 1$

Knudsen diffusion  $K_n = 1$

Surface diffusion  $K_n \gg 1$

A small number indicates that the diffusion is similar to gas diffusion, and there is minimum contact with the pore walls. When the Knudsen number is large the

molecule is permanently within the influence of the surface of the pore wall, and there is more collisions with the pore walls than with other molecules.

Surface diffusion occurs when the pore diameter reaches a size smaller than the mean free path of the adsorbate, leaving the molecule constantly in contact with the pore wall, the molecule diffuses via site to site hopping along the pore wall.

Activated diffusion occurs when small molecules diffuse into high energy pores. The pore has an energy barrier that the molecule must overcome. This is common in microporous materials, as the molecule mean free path approaches the size of the pore diameter, and interactions between the molecule and the pore walls create repulsive effects.

## 1.6 Models of Adsorption Kinetics

### 1.6.1 Empirical Description

Kinetic models describe the adsorption of a gas particle into a spherical pore. Empirical adsorption is shown by equation 1.58.

$$\frac{M_t}{M_e} = kt^n \quad 1.58$$

Where:

$M_t$  = uptake at time  $t$  (s) / (g)

$M_e$  = uptake at equilibrium (g)

$k$  = rate constant ( $s^{-1}$ )

$n$  = diffusion exponent

A plot of  $\ln (M_t/M_e)$  against  $\ln (t)$  should yield a linear plot, from the gradient of which the diffusion exponent can be determined. The diffusion exponent can distinguish between different types of diffusion behaviour, determined by the value which it takes. Rao *et al*<sup>81</sup> describe the mechanisms which govern the diffusion of gaseous species into porous carbon materials.

- 1) Diffusion through a barrier at the pore entrance ( $n = 1$ )
- 2) Diffusion along the pore ( $n = 0.5$ )
- 3) Combination of diffusion through a barrier and along the pore ( $0.5 < n < 1$ )

These kinetic barriers to diffusion can be illustrated as in **Figure 1-12**.



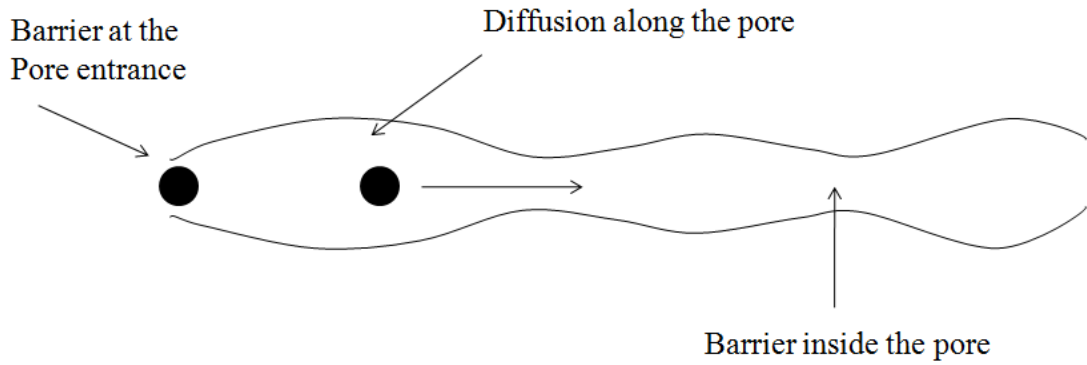


**Figure 1-12:** Kinetic barriers to diffusion

The rate at which adsorption occurs is dependent on which mechanism is controlling the diffusion of the gas into the porous system. Diffusion along the pore is described by the Fickian model, diffusion through a barrier at the pore entrance is modelled by the Linear Driving Force model (LDF) and when both types of mechanism contribute to the rate, this may be modelled by the Combined Barrier Resistance/Diffusion model (CBRD).

### 1.6.2 Fickian Diffusion

The Fickian diffusion model is concentration dependent, where the kinetics of adsorption are controlled by the transportation of the adsorbate through the pore, rather than through the rate of adsorption onto the surface. This is shown by Ficks first law of diffusion:

$$F = -D \frac{dC}{dx} \quad 1.59$$

Where:

$F$  = Flux rate ( $\text{mol cm}^{-2} \text{s}^{-1}$ )

$C$  = concentration of diffusing species ( $\text{mol cm}^3$ )

$x$  = space coordinate measured normal to the section

$D$  = diffusion coefficient ( $\text{cm}^2 \text{s}^{-1}$ )

This can be illustrated by **Figure 1-13**.

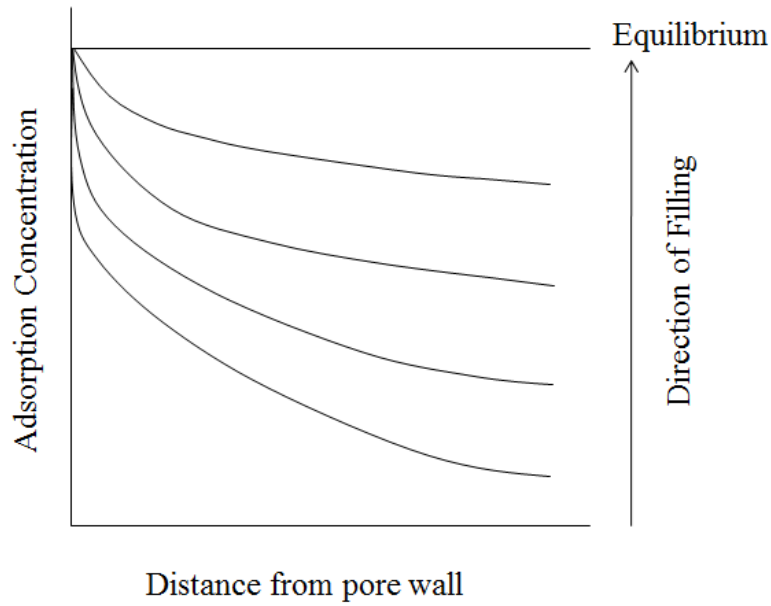


**Figure 1-13:** Representation of Fickian diffusion concentration gradient

Ficks second law of diffusion models the rate at which the concentration changes at any given point in space when the diffusion is radial into a spherical shaped pore. It is described by the partial differential equation shown in equation 1.60.<sup>82</sup>

$$\frac{\delta C}{\delta t} = D \left( \frac{\delta^2 C}{\delta a^2} + \frac{2\delta C}{r\delta a} \right) \quad 1.60$$

Equation 1.60 is a diffusion law for isothermal diffusion into a homogenous sphere. The solution of equation 1.60 is given by equation 1.61 which shows the total amount of diffusing substance entering and leaving the spherical particle.<sup>83</sup>

$$\frac{M_t}{M_e} = 1 - \frac{6}{\pi^2} \sum_{n=1}^{\infty} \frac{1}{n^2} \exp\left(\frac{-Dn^2\pi^2 t}{a^2}\right) \quad 1.61$$

Where:

$M_t$  = uptake (g) at time  $t$  (s)

$M_e$  = uptake at equilibrium (g)

$D$  = gas diffusion coefficient ( $\text{cm}^2 \text{s}^{-1}$ )

$a$  = radius of particle (cm)

Equation 1.60 can be solved for short timescales and long timescales. For small times the solution of the equation is as follows:

$$\frac{M_t}{M_e} = 6 \left(\frac{Dt}{a^2}\right)^{1/2} \left\{ \pi^{-1/2} + 2 \sum_{n=1}^{\infty} \text{ierfc} \frac{na}{\sqrt{(Dt)}} \right\} - 3 \frac{Dt}{a^2} \quad 1.62$$

Equation 1.62 approximates to:

$$\frac{M_t}{M_e} = 6 \left( \frac{Dt}{a^2} \right)^{1/2} \quad 1.63$$

Expansion of this gives

$$\frac{M_t}{M_e} = \frac{6}{\sqrt{\pi}} \cdot \frac{\sqrt{D}\sqrt{t}}{a} \quad 1.64$$

This equation is valid for small timescales where  $M_t/M_e < 25\%$ , so a plot of  $M_t/M_e$  against  $t^{1/2}$  will have a gradient equal to  $\frac{6}{\sqrt{\pi}} \cdot \frac{\sqrt{D}}{a}$ .

For long timescales equation 1.60 is solved as follows:

$$\frac{M_t}{M_e} = 1 - \frac{6}{\pi^2} \left[ \exp \left( \frac{-D\pi^2 t}{a^2} \right) \right] \quad 1.65$$

Rearranging gives:

$$1 - \frac{M_t}{M_e} = \frac{6}{\pi^2} \left[ \exp \left( \frac{-D\pi^2 t}{a^2} \right) \right] \quad 1.66$$

To illustrate the long term behaviour of diffusion, a plot of  $\ln (1 - M_t/M_e)$  against time will give a linear plot of gradient  $\frac{-D\pi^2}{a^2}$ . This equation is valid for long timescales where  $M_t/M_e > 60\%$ . This equation has been used to analysis kinetics of gas adsorption on carbon molecular sieves.<sup>84</sup>

### 1.6.3 Linear Driving Force Model

The linear driving force (LDF) model is a concentration independent model. When the mechanism of diffusion follows the LDF model, the number of available surface sites available for adsorption will decrease exponentially with time as shown in **Figure 1-14**. The rate constant is directly proportional to the displacement of the system from equilibrium.

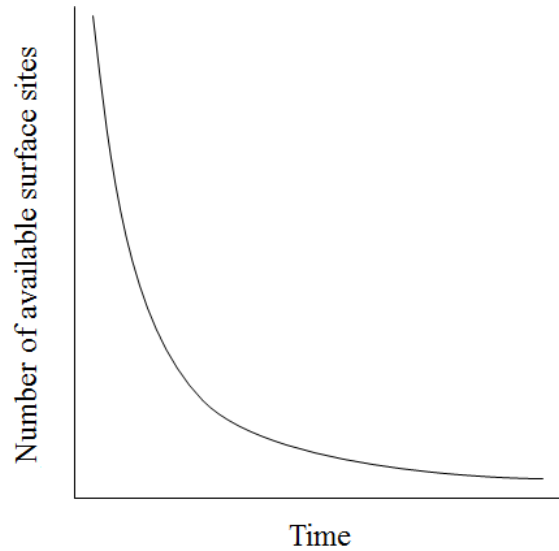


**Figure 1-14:** Exponential decay of surface adsorption sites

This is modelled by a conventional rate law:

$$\text{Rate} = k(\text{adsorbate concentration}) \times (\text{available sites})^n$$

When  $n = 1$  this implies a first order rate constant. Assuming that adsorption follows first order reaction kinetics, then the rate of change of adsorbate concentration is given by equation 1.67:

$$\frac{d[M_e - M_t]}{dt} = k[M_e - M_t] \quad 1.67$$

$M_e - M_t$  is the driving force for adsorption. Integration gives:

$$\int \frac{1}{(M_e - M_t)} d(M_e - M_t) = -k \int dt \quad 1.68$$

Giving the following conditions:

$$\int_{M_e}^{M_t} d[\ln(M_e - M_t)] = \int_0^t -k dt \quad 1.69$$

Then:

$$\ln\left(1 - \frac{[M_t]}{[M_e]}\right) = -kt \quad 1.70$$

Rearrangement gives the standard LDF equation 1.71:

$$\frac{M_t}{M_e} = 1 - e^{-kt} \quad 1.71$$

Where:

## Chapter 1 Adsorption

$M_t$  = the amount adsorbed (g) at time  $t$  (s)

$M_e$  = the equilibrium uptake (g)

$k$  = the rate constant ( $s^{-1}$ )

A graph of  $\ln(1 - M_t/M_e)$  against time  $t$  should yield a linear plot with a gradient equal to the rate constant. The linear driving force model has been used to give rate constants for various gas adsorption on activated carbon,<sup>85,86,87</sup> carbon molecular sieves<sup>88</sup> and metal organic frameworks.<sup>89</sup>

### 1.6.4 Combined Barrier Resistance / Diffusion Model

The combined barrier resistance / diffusion (CBRD) model<sup>90</sup> is used to describe the diffusion of an adsorbate when there is both diffusion through a barrier and diffusion along the pore contributing to the rate of adsorption. To analyse this mechanism of adsorption, Ficks second law is again used (equation 1.60) and an additional equation 1.72.

$$D = \frac{\delta C(r_c t)}{\delta r} = k_b \{C^*(t) - C(r, t)\} \quad 1.72$$

Where:

$D$  = crystalline diffusivity ( $cm^2 s^{-1}$ )

$k_b$  = barrier resistance ( $cm s^{-1}$ )

$r_c$  = the radius of the adsorbate (cm)

$r$  = the radial coordinate

$t$  = time (s)

$C$  = adsorbate concentration within the pore ( $mmol cm^{-3}$ )

$C^*$  = surface concentration in equilibrium with the gas phase ( $mmol cm^{-3}$ )

The useful parameters which can be derived from this equation are the barrier resistance,  $k_b$  and  $k_d = D/r_c^2$ . Although this model has been used to describe the kinetics of gas adsorption<sup>41</sup> it is difficult to use and involves complicated mathematical interpretations.

1.6.4.1 Comparison of Diffusion Models

Typical schematic plots of Fickian, LDF and CBRD analysis are shown in **Figure 1-15**. This shows the Fickian model deviating from linearity at low uptake values, whereas the LDF model obeys linearity across the entire uptake range, and the CBRD model sits between the two.

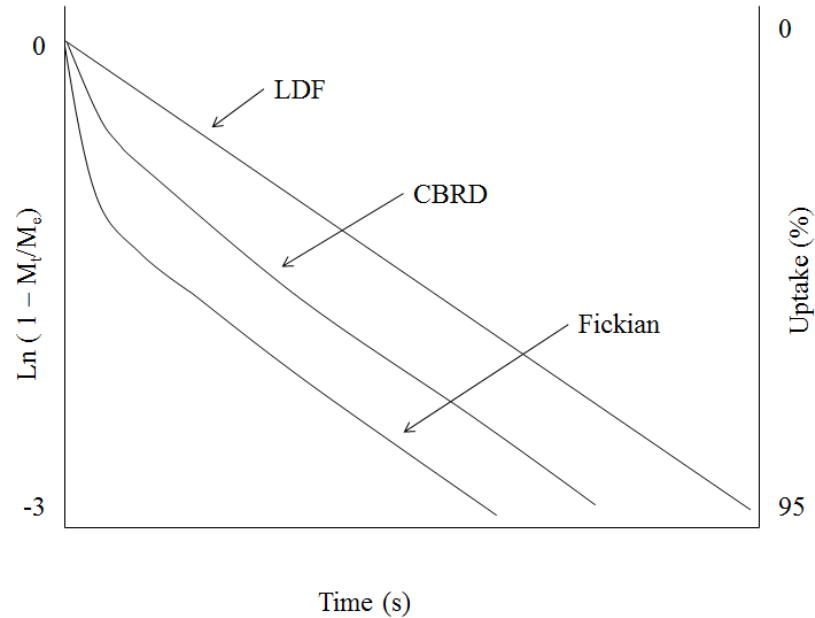


**Figure 1-15:** Schematic comparison of Fickian, LDF and CBRD models

1.6.5 Stretched Exponential (SE) Model

In 1847, Kohlrausch<sup>91</sup> first proposed the stretched exponential model to describe mechanical creep. He proposed the equation in the following form:

$$\phi(t) = \exp\left[-\left(\frac{t}{\tau}\right)^\beta\right] \quad 0 < \beta < 1 \quad 1.73$$

Where:

$\phi(t)$  = the relaxation function

$\beta$  and  $\tau$  = material dependent parameters

The equation was then used by Williams and Watts<sup>92</sup> to describe dielectric relaxation in polymers. It was shown by Klafter and Shlesinger<sup>93</sup> that this equation can be applied to many complex systems to describe relaxation decay. For example, they showed that the stretched exponential equation has underlying mathematical features which relate it to the Förster direct-transfer mechanism, which is a model of energy

transfer from a donor to an acceptor molecule, such as transfer of excitation energy between chromophore in a molecule. They also showed common mathematical features with other decay models.<sup>94,95</sup>

It is possible to use the stretched exponential equation to model diffusion into a porous material. The relaxation modelled in the adsorption of gases into porous materials is the relaxation of degrees of freedom of the adsorbate molecule as it is adsorbed onto the surface of the material. Klafter and Shlesinger also concluded that when the value of  $\beta = 0.5$ , this is indicative that the model is one dimensional, when  $\beta = 1$  this is indicative that the model is three dimensional, with the model presumably becoming two dimensional at intermediate values. The  $\beta$  values give an indication of the distribution of the relaxation times, as  $\beta$  decreases the distribution broadens. When  $\beta = 1$  there is a single relaxation time which is indicative of a rate determining step due to the diffusion through a barrier at the pore entrance. The stretched exponential equation can be used in the following form for application to adsorption kinetics:

$$y = A[1 - \exp(-(kt)^\beta)] \quad 1.74$$

Where:

$A$  = a constant

$k$  = rate constant ( $s^{-1}$ )

$t$  = time (s)

$\beta$  = the exponential parameter

The experimental data is conventionally normalised to show fractional uptake, which gives  $A$  the value 1 and reduces equation 1.74 equation 1.75.

$$\frac{M_t}{M_e} = 1 - e^{-(kt)^\beta} \quad 1.75$$

When  $\beta = 1$ , equation 1.75 reduces to a single exponential, and becomes identical to the LDF model.

### 1.6.6 Double Exponential Model

The linear driving force model is used to analysis kinetics in systems where there is a single barrier to diffusion at the pore entrance. This can be extended to incorporate systems with two kinetic processes contributing to the overall rate of adsorption, by using the double exponential model as shown in equation 1.76:

$$\frac{M_t}{M_e} = A_1(1 - e^{-k_1 t}) + A_2(1 - e^{-k_2 t}) \quad 1.76$$

Where:

$M_t$  = the amount adsorbed (g) at time  $t$  (s)

$M_e$  = the equilibrium uptake (g)

$k_1$  and  $k_2$  = the rate constants ( $s^{-1}$ )

$A_1$  and  $A_2$  = the contributions of the rate constants to the overall rate of adsorption, with the relationship  $A_1 + A_2 = 1$

This model has been used previously to describe the adsorption kinetics of gases and vapours on metal organic frameworks,<sup>96</sup> where the two different kinetic processes were found to be:

1. Slow diffusion through pore windows which have a high activation energy
2. Fast diffusion along cavities in the porous structure with low activation energies.



1.7 References

- <sup>1</sup> E. Robens, In “*Characterisation of Porous Solids III*”, J. Rouquerol, F. Rodriguez-Reinoso, J. Rouquerol, K. S. W. Sing, K. K. Unger Eds., Elsevier, Amsterdam, **1994**, 109
- <sup>2</sup> C. W. Scheele, *Chemische Abhandlung von der Luft und dem Feuer*, **1773**
- <sup>3</sup> F. Fontana, *Merorie Mat. Fi. Soc., Ital. Sci.* **1777**, *1*, 211
- <sup>4</sup> H. Kayser, *Wied. Ann.*, **1881**, *14*, 450
- <sup>5</sup> G. Gore, *Phil. Mag.*, **1894**, *37*, 306
- <sup>6</sup> L. G. Gurvich, *J. Russ. Phys. Chem.*, **1915**, *47*, 805
- <sup>7</sup> S. D. Forrester, C. H. Giles., *Chem. and Ind.*, **1972**, 318
- <sup>8</sup> K. S. W. Sing, D. H. Everett, R. W. Haul, L. Moscou, R. A. Pierotti, J. Rouquerol, T. Siemieniewska, *Pure & Applied Chem.*, **1985**, *57*, 603
- <sup>9</sup> J. W. McBain, *Phil. Mag.*, **1909**, *18*, 916
- <sup>10</sup> H. Freundlich, *Colloid and Capillary Chemistry*, Methuen, London, **1926**,
- <sup>11</sup> R. Z. Zsigmondy, *Inorg. Chem.*, **1911**, *71*, 356
- <sup>12</sup> M. Polanyi, *Verb. Deutsch Phys. Ges.*, **1914**, *16*, 1012
- <sup>13</sup> I. Langmuir, *J. Amer. Chem. Soc.*, 1916, **38**, 2219
- <sup>14</sup> I. Langmuir, *J. Amer. Chem. Soc.*, 1918, **40**, 1361
- <sup>15</sup> A. M. Williams, *Proc. Russ. Soc.*, **1919**, *96*, 287
- <sup>16</sup> D. C. Henry, *Philos. Mag.*, **1922**, *44*, 689
- <sup>17</sup> F. Rouquerol, J. Rouquerol, K. Sing, *Adsorption by Powders and Porous Solids*, Academic Press, London, **1999**
- <sup>18</sup> S. Brunauer, L. S. Deming, W. E. Deming, E. Teller, *J. Am. Chem. Soc.* **1940**, *62*, 1723
- <sup>19</sup> P. W. Atkins, *Atkins Physical Chemistry*, 7<sup>th</sup> Ed; Oxford University Press, Oxford, **2002**
- <sup>20</sup> H. Igarashi, H. Uchida, M. Suzuki, Y. Sasaki, M. Watanabe, *App. Cat. A:Gen.*, **1997**, *159*, 159
- <sup>21</sup> B. M. W. Trapnell, *Chemisorption*, Butterworths, London, **1955**

- <sup>22</sup> F. London, *Trans. Faraday. Soc.*, **1937**, 33, 8
- <sup>23</sup> J. E. Lennard-Jones, *Physica. Eindhoven* 4, **1937**, 4, 941
- <sup>24</sup> I.U.P.A.C., *Pure and Applied Chemistry*, **1972**, 31, 578
- <sup>25</sup> J. Rouquerol, D. Avnir, C. W. Fairbridge, D. H. Everett, J. H. Haynes, N. Pericone, J. D. F. Ramsey, K. S. W. Sing, K. K. Unger, *Pure and Applied Chemistry*, **1994**, 66, 1739
- <sup>26</sup> J. Rowsell, O. Yaghi, *Microporous and Mesoporous Materials*, **2004**, 73, 3 – 14
- <sup>27</sup> D. H. Everett, J. C. Prowl, *J. Chem. Soc. Farad. Trans.*, **1976**, 72, 619
- <sup>28</sup> S. J. Gregg, K. S. W. Sing, *Adsorption, Surface Area and Porosity*, Academic Press, **1982**
- <sup>29</sup> S. Ross, J. P. Olivier, *On Physical Adsorption*, Interscience, New York, **1964**
- <sup>30</sup> J. R. Barrante, *Applied Mathematics for Physical Chemistry*, Pearson Education Ltd, London, **2004**
- <sup>31</sup> M. R. Bhambhani, P. A. Cutting, K. S. W. Sing, D. H. Turk, *J. Chem. Phys.*, **1972**, 38, 109
- <sup>32</sup> J. Tóth, F. Berger, I. Dékány, *J. Colloid. Interface Sci.*, **1999**, 212, 411
- <sup>33</sup> A. J. Fletcher, PhD Thesis, Newcastle University, **2000**
- <sup>34</sup> A. J. Fletcher, K. M. Thomas, *Langmuir*, **2000**, 16, 6253
- <sup>35</sup> L. Cossarutto, T. Zimny, J. Kaczmarczyk, T. Siemieniewska, J. Bimer, J. V. Weber, *Carbon*, **2001**, 39, 2339
- <sup>36</sup> N. Qi, M. D. LeVan, *Carbon*, **2005**, 43, 2258
- <sup>37</sup> H. Clark, *J. Phys. Chem.*, **1955**, 59, 1068
- <sup>38</sup> J. H. de Boer, In “*The Structure and Property of Porous Materials*” (D. H. Everett and F. S. Stone Eds.), Butterworths, London, **1958**
- <sup>39</sup> X. Zhao, B. Xiao, A. J. Fletcher, K. M. Thomas, D. Bradshaw, M. J. Rosseinsky, *Science*, **2004**, 306
- <sup>40</sup> A. J. Fletcher, K. M. Thomas, M. J. Rosseinsky, *J. Solid State Chem.*, **2005**, 178, 2491
- <sup>41</sup> C. R. Reid, K. M. Thomas, *Langmuir*, **1999**, 15, 3206

- <sup>42</sup> C. R. Reid, K. M. Thomas, *J. Phys. Chem. B*, **2001**, *105*, 10619
- <sup>43</sup> G. Attard, C. Barnes, *Surfaces*, Oxford University Press, New York, **1998**
- <sup>44</sup> S. Brunauer, P. H. Emmett, E. Teller, *J. Am. Chem. Soc.*, **1938**, *60*, 309
- <sup>45</sup> S. Brunauer, P. H. Emmet, *J. Am. Chem. Soc.*, **1937**, *59*, 2682
- <sup>46</sup> K. Sing, *Colloids and Surfaces A: Physicochem. Eng. Aspects.*, **2001**, *187*, 3
- <sup>47</sup> T. d. Saussure, *Gilbert's Ann. Phys.* **1814**, *47*, 113
- <sup>48</sup> A. Eucken, *Verhandlungen der Deutschen Physikalischen Gesellschaft* **1914**, *16*, 345
- <sup>49</sup> M. Polanyi, *Verhandlungen der Deutschen Physikalischen Gesellschaft* **1914**, *16*, 1012
- <sup>50</sup> B. P. Bering, M. M. Dubinin, V. V. Serpinsky, *Journal of Colloid and Interface Science*, **1966**, *21*, 378
- <sup>51</sup> M. M. Dubinin, *Journal of Colloid and Interface Science*, **1967**, *23*, 487
- <sup>52</sup> M. M. Dubinin, *Journal of Colloid and Interface Science*, **1974**, *49*, 5
- <sup>53</sup> M. M. Dubinin, *Carbon*, **1980**, *18*, 355
- <sup>54</sup> M. M. Dubinin, V. V. Serpinsky, *Carbon*, **1981**, *19*, 402
- <sup>55</sup> M. M. Dubinin, V. V. Serpinsky, *Carbon*, **1982**, *20*, 136
- <sup>56</sup> M. M. Dubinin, *Carbon*, **1984**, *22*, 221
- <sup>57</sup> M. M. Dubinin, *Carbon*, **1985**, *23*, 373
- <sup>58</sup> M. M. Dubinin, *Carbon*, **1987**, *25*, 593
- <sup>59</sup> M. M. Dubinin, O. Kadlec, *Carbon*, **1987**, *25*, 321
- <sup>60</sup> M. M. Dubinin, *Carbon* **1989**, *27*, 457
- <sup>61</sup> G. N. Lewis, M. Randall, *Thermodynamics*, New York, U. S. A., **1923**
- <sup>62</sup> M. M. Dubinin, *Uspekhi Khimii*, **1952**, *21*, 513
- <sup>63</sup> F. Stoeckli, *Carbon*, **1998**, *36*, 363
- <sup>64</sup> K. J. Masters, B. McEnaney, *Journal of Colloid and Interface Science*, **1983**, *95*, 340

- <sup>65</sup> S. G. Chen, R. T. Yang, *Langmuir*, **1994**, *10*, 4244
- <sup>66</sup> H. Marsh, T. Siemieniewska, *Fuel*, **1967**, *46*, 441
- <sup>67</sup> H. Marsh, T. E. O'Hair, *Fuel*, **1966**, *45*, 301
- <sup>68</sup> E. M. Freeman, T. Siemieniewska, H. Marsh, B. Rand, *Carbon*, **1967**, *8*, 7
- <sup>69</sup> H. Marsh, *Carbon*, **1987**, *25*, 49
- <sup>70</sup> J. H. Cole, D. H. Everett, C. T. Marshall, A. R. Paniego, J. C. Powl, F. Rodriguez – Reinoso, *J. Chem. Soc. Faraday Transactions*, **1974**, *70*, 2154
- <sup>71</sup> C. R. Reid, I. P. O'Koye, K. M. Thomas, *Langmuir*, **1998**, *14*, 2415
- <sup>72</sup> I. P. O'Koye, M. Benham, K. M. Thomas, *Langmuir*, **1997**, *13*, 4045
- <sup>73</sup> N. N. Avgul, A. G. Bezuz, E. S. Dobrova, A. V. Kiselev, *J. Chem. Phys.* **1973**, *42*, 486
- <sup>74</sup> L. Czerpirski, J. Jagiello, *Chem. Eng. Sci.*, **1989**, *44*, 797
- <sup>75</sup> J. L. C. Rowsell, O. M. Yaghi, *J. Am. Chem. Soc.*, **2006**, *28*, 1304
- <sup>76</sup> P. Zweitering, D. W. Von Krevelen, *Fuel*, **1954**, *33*, 331
- <sup>77</sup> F. A. P. Maggs, *Research*, London, **1953**, *6*, 513
- <sup>78</sup> H. Marsh, W. F. K. Wynn – Jones, *Carbon*, **1964**, *1*, 269
- <sup>79</sup> S. Brunauer, *The Adsorption of Gases and Vapours*, Oxford University Press, London, UK, **1943**
- <sup>80</sup> D. D. Do, *Adsorption Analysis: Equilibria and Kinetics*, Imperial College Press, London, **1998**
- <sup>81</sup> M. B. Rao, R. G. Jenkins, W. A. Steele, *Langmuir*, **1985**, *1*, 137
- <sup>82</sup> J. Crank, *The Mathematics of Diffusion*, Clarendon Press, Oxford, **1975**
- <sup>83</sup> H. K. Chagger, F. E. Ndaji, M. L. Sykes, K. M. Thomas, *Carbon*, **1995**, *33*, 1405
- <sup>84</sup> C. R. Reid, K. M. Thomas, *Langmuir*, **1999**, *15*, 3206
- <sup>85</sup> N. J. Foley, P. L. Forshaw, K. M. Thomas, D. Stanton, P. R. Norman, *Langmuir*, **1997**, *13*, 2083
- <sup>86</sup> A. W. Harding, N. J. Foley, P. R. Norman, D. C. Francis, K. M. Thomas, *Langmuir*, **1998**, *14*, 3858

- <sup>87</sup> A. J. Fletcher, K. M. Thomas, *Langmuir*, **2000**, *16*, 6253
- <sup>88</sup> T. A. Braymer, C. G. Coe, T. S. Farris, T. R. Gaffney, J. M. Schork, J. N. Armor, *Carbon*, **1994**, *32*, 445
- <sup>89</sup> A. J. Fletcher, E. J. Cussen, T. J. Prior, M. J. Rosseinsky, C. J. Kepert, K. M. Thomas, *J. Am. Chem. Soc.* **2001**, *123*, 10001
- <sup>90</sup> K. F. Loughlin, M. M. Hassan, A. I. Fatehi, M. Zahur, *Gas. Sep. Purif.*, **1993**, *7*, 264
- <sup>91</sup> R. Kohlrausch, *Ann. Phys.* **1847**, *12*, 393
- <sup>92</sup> G. Williams, D. C. Watts, *Trans. Faraday. Soc.*, **1970**, *66*, 80
- <sup>93</sup> J. Klafter, M. F. Shlesinger, *Proc. Natl. Acad. Sc., USA*, **1986**, *83*, 848
- <sup>94</sup> R. G. Palmer, D. Stein, E. S. Abrahams, P. W. Anderson, *Phys. Rev. Letters.* **1984**, *53*, 958
- <sup>95</sup> S. H. Glarum, *J. Chem. Phys.*, **1960**, *33*, 1371
- <sup>96</sup> A. J. Fletcher, E. J. Cussen, D. Bradshaw, M. J. Rosseinsky, K. M. Thomas, *J. Am. Chem. Soc.*, **2004**, *126*, 9750

## Chapter 2      Porous Materials

### 2.1 Porous Materials

The success of the adsorption process lies fundamentally with the adsorbent used. In principle any microporous material can adsorb gases or vapour; however, to be industrially viable, the adsorbent must have a good capacity for adsorption, and must complete adsorption at an acceptable rate. Historically, there have been many porous materials applied to a variety of uses, and these have developed continually, with new porous materials approaching the forefront of recent research.<sup>1</sup> **Table 2-1** illustrates briefly the historical development of porous materials.

**Table 2-1:** Historical development of porous materials

<b>Date</b>	<b>Name</b>	<b>Significance</b>
<b>1773</b>	Scheele	Investigation of the uptake of gases by charcoal and clays. <sup>2, 3</sup>
<b>1814</b>	De Saussure	Started the systematic analysis of various adsorbents such as cork and charcoal, and discovered the exothermic nature of adsorption. <sup>4,5</sup>
<b>1901</b>	Von Ostrejko	Activated carbons become commercial developed through the process of incorporating metallic chlorides. <sup>6</sup>
<b>1903</b>	Tswett	Selective adsorption by silica gels was observed during the separation of chlorophyll and other plant pigments. <sup>7</sup>
<b>1904</b>	Dewar	Observed the selective adsorption of oxygen during air uptake by carbon. <sup>8</sup>
<b>1911</b>	NORIT Factory, Amsterdam	Founded as one of the international manufacturers of activated carbon.
<b>1956</b>	Breck	North American Linde Company started to produce zeolites on a commercial scale. <sup>9</sup>
<b>1959</b>	Milton	Synthetic zeolite molecular sieves discovered – allowing shaped based gas separation. <sup>10</sup>
<b>1990</b>	Hoskins and Robson	Identification of Metal Organic Frameworks. <sup>11</sup>

### 2.1.1 Current Industrial Adsorbents

There are several adsorbents used in industry which satisfy the criteria of good capacity and fast kinetics. These include alumina, silica gel, activated carbons, carbon molecular sieves and zeolites. Alumina and silica gel are predominately used for gas drying, whereas activated carbons, carbon molecular sieves and zeolites have applications in gas purification and separation.

#### 2.1.1.1 Activated Carbon

Activated carbons are a classic rigid adsorbent, commonly used in industry for applications including: trace impurity removal, gas separation and removal of CO<sub>2</sub> from flue gas.<sup>12</sup> They are porous, amorphous materials which can have extremely high internal surface areas, up to 3000m<sup>2</sup> g<sup>-1</sup>.

#### Structure

The structure of activated carbon consists of graphene layers, which contain a regular hexagonal arrangement of carbon atoms, with varying degrees of perfection. These layers are randomly stacked within the structure, with the varying gaps between the stacks giving rise to the microporous nature of the material, which has a pore size distribution of macropores, mesopores and micropores.<sup>13</sup>



**Figure 2-1:** Structure of activated carbon<sup>14</sup>

The pores in activated carbon can be classified into four main types as described in **Figure 2-2**.

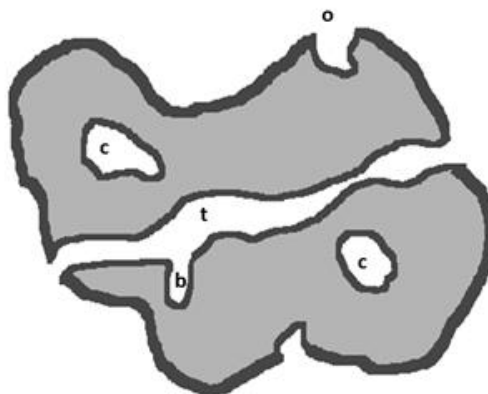


**Figure 2-2:** Pore classification in activated carbons<sup>15</sup>

*Open* - connected to external surface allowing passage of adsorbate

*Closed* - isolated void within solid, not connected to external surface

*Transport* - connects parts of external surface to inner porosity

*Blind* – not isolated but not leading to other pores/surface

The microporous nature and high surface area of the activated carbons leads to their use in industry as an adsorbent. The adsorption potential of activated carbons is also modified by the presence of functional groups, which are found at the edge of the graphene layers within the structure, where there are unsaturated carbon atoms. The most important functional groups are oxygen based, which gives hydrophilic nature in addition to the hydrophobic nature of the graphene layers. The dual nature of activated carbons allows a wide range of chemical species to be adsorbed into the material.

### Production

Activated carbons are made from coals, cokes, wood, coconut shells and pecan shells, along with other carbonaceous agricultural by-products.<sup>16</sup> To make an activated carbon, a char must first be formed from the source material. Pyrolysis in an inert atmosphere at temperatures below 1000 K results in thermal decomposition leading to the loss of impurities such as water, carbon dioxide and a wide range of organic molecules. This carbonaceous precursor is then activated by either physical methods, such as partial gasification using carbon dioxide, steam or air at 1073 – 1223 K to develop the porous structure, or chemical methods, by adding reagents before or after the carbonisation process, such as  $\text{ZnCl}_2$ ,  $\text{KOH}$  or  $\text{CaCl}_2$ . These compounds act as dehydrating agents, preventing the formation of tars and increasing



the yield of activated carbon. Chemical activation often yields higher surface areas than physical activation.<sup>17, 18</sup>

#### 2.1.1.2 Carbon Molecular Sieves

Molecular sieves are substances which can separate mixtures of species based on the size of the species in relation to the pore size of the sieve. The term “molecular sieve” was first coined by McBain in 1932 for materials which “exhibit selective sorption properties”.<sup>2</sup> Carbon molecular sieves (CMS) are a special type of activated carbon, where the main difference is in the separation properties of the two carbon types. Activated carbons are utilised in separation on the basis of the difference in equilibrium adsorption capacity of the carbon, whereas CMS separates mixtures based on the rate of adsorption, or the kinetic differences. One of the most useful separations achieved by CMS is the separation of nitrogen from air; this will be discussed in more detail in **Chapter Three – Separation of Gases and Vapours**.

#### 2.1.1.3 Zeolites

Zeolites are crystalline hydrated aluminosilicates which contain regular discrete pores and cavities which extend into three dimensions, differentiating zeolites from the irregular and amorphous carbon molecular sieves. Zeolites consist of connected tetrahedral sites formed by oxygen ions. Within each tetrahedral oxygen sites sits a cation, either Si<sup>4+</sup> or Al<sup>3+</sup>, forming SiO<sub>4</sub> or AlO<sub>4</sub> tetrahedra. These primary tetrahedral building units form the extended 3D network of the zeolite framework. Due to the negative charge of the AlO<sub>2</sub><sup>-</sup> which makes up the tetrahedra, zeolites are negatively charged. This negative charge is balanced by the inclusion of positively charged cations within the non-framework positions. These cations are typically group I or group II, such as Na<sup>+</sup> and Ba<sup>2+</sup>.<sup>19</sup> Water molecules are also found within the non-framework positions. A typical equation to describe zeolites is shown as:



Where  $n+$  represents the charge on the guest cation,  $x$  and  $y$  represent the number of aluminium and silicon tetrahedra,  $x-$  represents the negative charge of the zeolite and  $w$  represents the extent of hydration of the zeolite. The dimensions of the cavities found in zeolites are dependent on the structure, with the sizes of the openings ranging from 3 to 7 Å across various zeolites. An example of a commercial zeolite is shown in **Figure 2-3**.

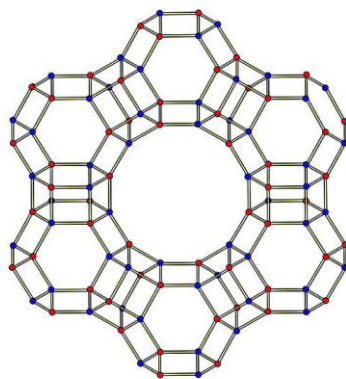


**Figure 2-3:** Faujasite zeolite

Zeolites were first commercialised in 1954, where they were exploited for their hydrophilic nature by being utilised as refrigerant desiccants and in the drying of natural gas.<sup>20</sup> The first exploitation of the molecular sieve properties of zeolites occurred in 1959 with the ISOSIV process, which separates branched and linear hydrocarbons on the basis of their molecular cross-sectional areas, with branched isomers having a larger cross sectional area than linear isomers. The smaller pore openings allow the passage of linear hydrocarbons, but prevent the entry of the bulkier branched and cyclic structures, as shown in **Figure 2-4**.

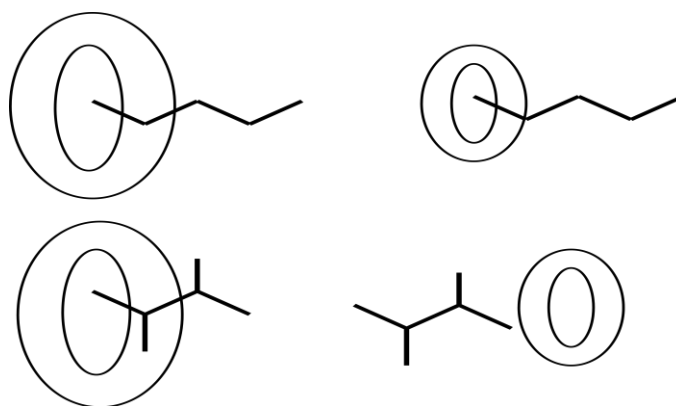


**Figure 2-4:** Molecular sieve effect

This property can be used to separate other hydrocarbons,<sup>21</sup> and in separating metallic impurities from water.<sup>22</sup> Zeolites can also be applied to air separation. This will be discussed in more detail in **Chapter Three – Separation of Gases and Vapours**.

## 2.2 Porous Coordination Polymers

Coordination polymers<sup>23</sup> date back to the 1960s, but it was not until the research by Hoskins and Robson<sup>11</sup> in the early 1990s that research truly engaged, producing a vast amount of research papers and porous materials. Porous coordination polymers are crystalline porous materials, bearing similarities to zeolites through their scaffold-like, rigid structures. However they contain both inorganic and organic components, allowing the manipulation of surfaces within the frameworks to enhance adsorption.<sup>24</sup> The inorganic fragments are *nodes* and these are found at “corner” sections of the scaffold. The organic fragments are *linkers*, joining the nodes together to form the extended network, as shown in **Figure 2-5**.

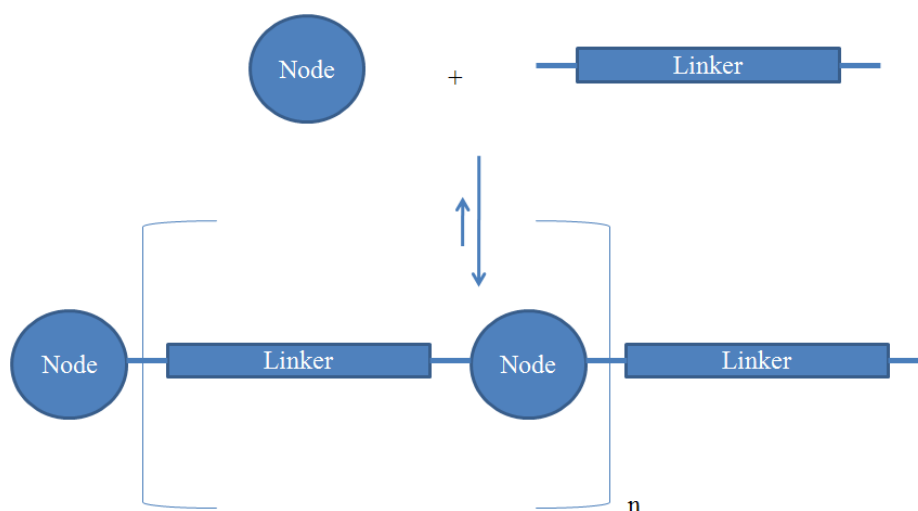


**Figure 2-5:** Schematic of porous coordination polymer assembly

Porous coordination polymers may also include additional components, such as counter-ions, guest/template molecules, within the voids formed by the frameworks. Permanent porosity is exhibited when the guest/templating molecules can be removed, with the framework retaining structural integrity. The template molecules are often from the solvent used in synthesis to dissolve the starting materials, they will have a weak interaction with the framework itself and this allows easy removal at low temperatures, under the correct conditions this will quickly yield accessible porosity. This then leaves an open space within the framework, which may then be able to adsorb other guest materials, leading to interesting applications in clean energy applications, gas separation, drug delivery and catalysis.

### 2.2.1 Classification of Porous Coordination Polymers

Kitigawa *et al*<sup>25</sup> classified porous coordination polymers by two main features: the interaction with guest molecules and the spatial dimensions of the pores.

#### 2.2.1.1 Generational Classification

The generational classification scheme is based upon the interaction of the guest molecules with the framework:

*1<sup>st</sup> Generation:* microporous frameworks which irreversibly collapse upon removal of guest/templating molecules.

*2<sup>nd</sup> Generation:* microporous frameworks which retain robust stability upon removal of the guest/templating molecules.

*3<sup>rd</sup> Generation:* stable, flexible, dynamic frameworks which respond to guests and other external stimuli.

#### 2.2.1.2 Classification by Spatial Dimension

Porous coordination polymers can exist in 0, 1, 2 or 3 dimensions. The spatial dimension classification is based upon the space created during synthesis which then yields the porosity of the solid on desolvation.

*0D Dots:* these are isolated voids within the structure which are impenetrable by guest molecules.

*1D Channels:* regular 1D channels which extend through the porous structure. Size and functionality of these pores can be modified by changing the linker molecule to give wider pores or to enhance interaction with the guest molecules.

*2D Layers:* Channels extending in two dimensions to create layers, between which guest molecules can be incorporated. Often weakly held together by hydrogen bonds, this type of structure can have a flexible response to guest adsorption.

*3D Intersecting Channels:* This structure frequently occurs in zeolites, formed by the interconnection of 1D channels. These structures have high porosity, but are rare due to the inherent instability of the frameworks due to the high porosity.

### 2.2.2 Synthesis Concepts and Design

The design and synthesis of porous coordination polymers relies on careful selection of nodes, linkers and guest molecules/solvents as well as temperatures and synthetic methods and conditions. Synthesis methods include hydro/solvothermal techniques and slow diffusion methods. Typically porous coordination polymers are characterised first by single crystal X-ray diffraction, and as such a crystalline product is desirable. Due to the nature of the reagents typically used in synthesis, reactions can occur quickly and produce amorphous products, which are difficult to characterise. As such, techniques such as slow-diffusion and hydro/solvothermal synthesis have been developed, these techniques slow the reaction time and allow the thermodynamically more stable and crystalline product to form, rather than the amorphous kinetic product. Due to the insolubility of the frameworks, they must be produced in single step reactions. Solvothermal synthesis involves dissolving reagents in a suitable solvent, placing the solution mixture into a Teflon lined high pressure autoclave, and heating at 60 - 150°C for a varying amount of time, from hours to days. Solvothermal techniques are more prevalent when the framework is to be forced to form around a specific templating molecule, with the high pressure inside the autoclave and the high temperature, the length of time which the solvent remains in the liquid phase increases, whilst reacting at a higher temperature, drastically reducing the time taken for crystallisation.

#### 2.2.2.1 Design of Motifs

The motifs which can be produced vary with the coordination mode of the metal node, as shown in **Figure 2-6**. These include a) honeycomb b) ladder c) cubic d) hexagonal diamondoid e) square grid and f) zigzag chain.

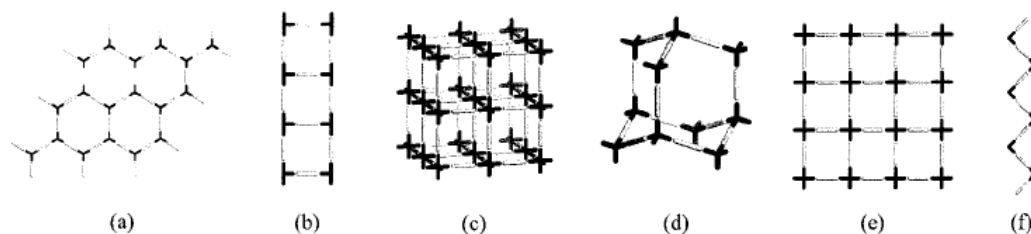


**Figure 2-6:** Various simple motifs available to porous coordination polymers<sup>26</sup>

There are several types of bonding interactions found within the motifs, from simple coordination bonds between the nodes and linkers, to hydrogen bonding and  $\pi$ - $\pi$

stacking, which help to aggregate lower dimensional polymers to more complex 3-dimensional frameworks.

### 2.2.2.2 Nodes and Linkers

#### Nodes

Nodes and linkers are most often the starting materials that are used in the synthesis of the polymer, and are the principal construction elements of the network. Nodes are typically metal cations, requiring anionic organic linkers to charge balance the network. Transition metals are typically used as nodes as they have labile coordination bonds, the advantage of a range of readily accessible oxidation states, and also a range of possible coordination numbers, from two to seven. This allows a wide range of geometries; linear, T or Y shaped, tetrahedral, square planar, square pyramidal, trigonal bipyramidal and all distorted forms of these.<sup>25,27</sup> The most commonly used transition metals are first row transition metals, such as copper, cobalt, nickel, manganese and zinc. Recently, lanthanide ions have also been used to produce coordination polymers.<sup>28,29</sup> Lanthanide metals have photo-luminescent properties, enhanced when combined with organic chromophore linkers.<sup>30</sup> This makes the incorporation of Lanthanide metal ions into metal organic frameworks a very interesting avenue of research, the luminescence could be exploited in sensor technology, with a luminescent reaction to guest molecules.

#### Linkers

As the linker molecules are required to bridge between two metal ions, they must normally be bi- or multi- dentate (with two or more donor binding sites). The most common linker molecules currently used are those which contain multiple oxygen or nitrogen donor sites, as these lead to be structurally stable polymers which are able to withstand the loss of guest molecules. Typically donors are carboxylates and heterocyclic nitrogen donors. Examples of typical oxygen donors are shown in **Figure 2-7** and examples of typical nitrogen donors are shown in **Figure 2-8**. Traditionally, rigid linkers are used, leading to thermally stable frameworks; however there are also flexible ligands which can be used, as shown in **Figure 2-9**.

## Chapter 2 Porous Materials

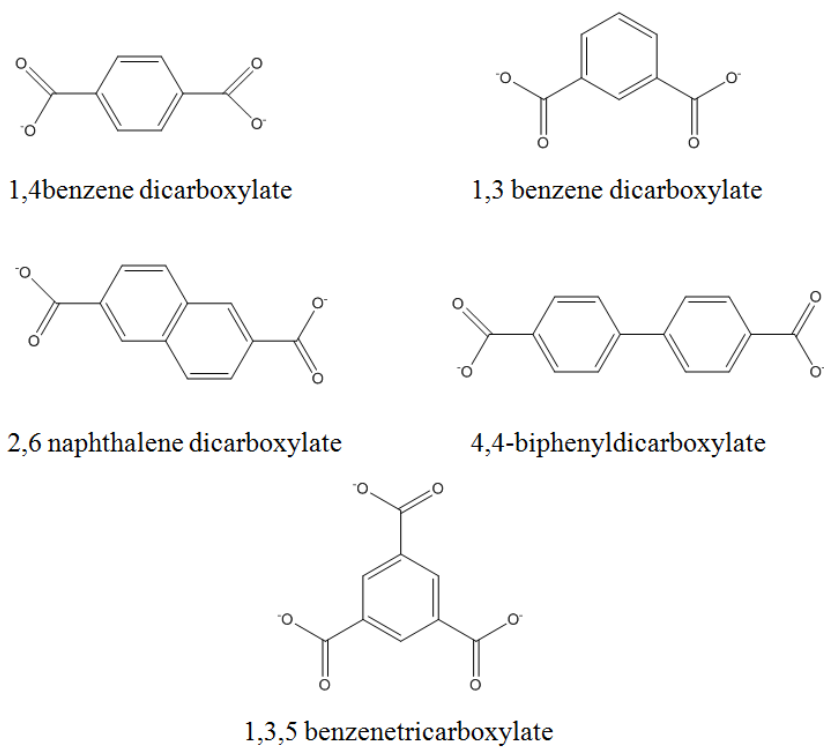
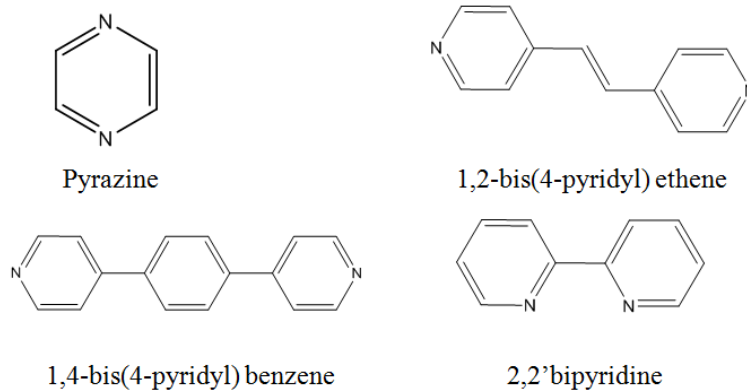


**Figure 2-7:** Oxygen donors

1D and 2D Structures:



3D Structures:

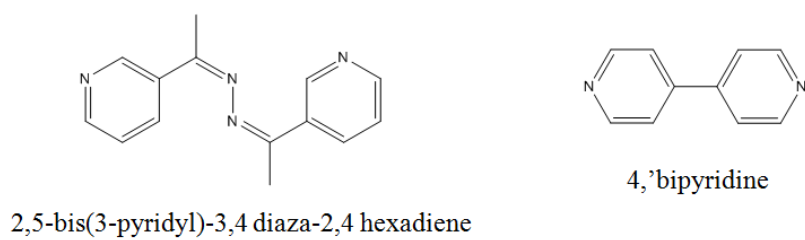
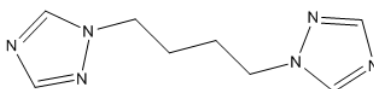
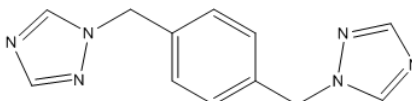


**Figure 2-8:** Nitrogen donors producing 1, 2 and 3D structures



1,4-bis(1,2,4-triazol-1-yl)butane (and any other alkane chains)



1,4-bis(1,2,4-triazol-1-ylmethyl)benzene

**Figure 2-9:** Flexible linkers<sup>31,32</sup>

### 2.2.2.3 “Design” of Pre-Determined Frameworks

Yaghi *et al* have coined the term *reticular* synthesis to describe the conceptual formation of three dimensional framework materials by the means of *secondary building units* (SBUs).<sup>33</sup> Secondary building units are fragments of inorganic or organic components that can be generated by organic synthesis or *in situ*. These secondary building units are used to define geometrical shapes, which can then be used to predict the structures of the frameworks. This is important as attempts to produce structures simply by mixing reagents together often results in a large number of possible structures, with a lack of control over pore size and functionality. The knowledge of which reaction conditions give particular shaped secondary building units, and then how these units to form an extended network allows the control over the topology of the network. An example of the use of secondary building units to produce a porous framework is MOF-5, the structure of which is shown in **Figure 2-10**.<sup>34</sup> MOF-5 is part of a series of structures produced by Yaghi *et al*, the IR – MOF (iso-reticular metal organic framework) series. This series contains the Zn<sub>4</sub>O tetrahedra and carboxylate carbon atoms, forming the octahedral SBU, all linked by varying length dicarboxylic acids, produces frameworks of varying size, all with the same topology. This series is shown in **Figure 2-11**.



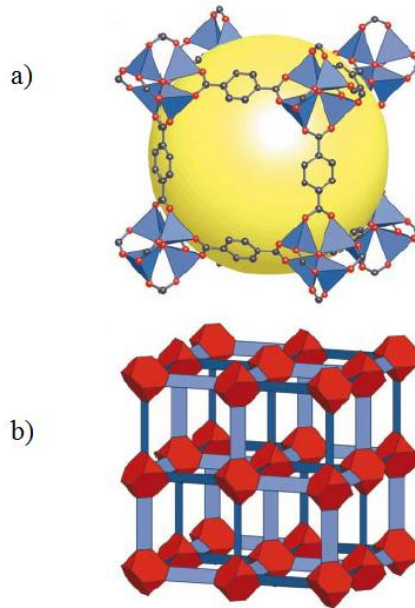


**Figure 2-10:** MOF-5 a) shows  $Zn_4O$  tetrahedra SBU linked by benzene dicarboxylate linkers b) shows MOF-5 represented schematically – red polyhedra represent inorganic SBU blue polyhedra represent linkers<sup>33</sup>

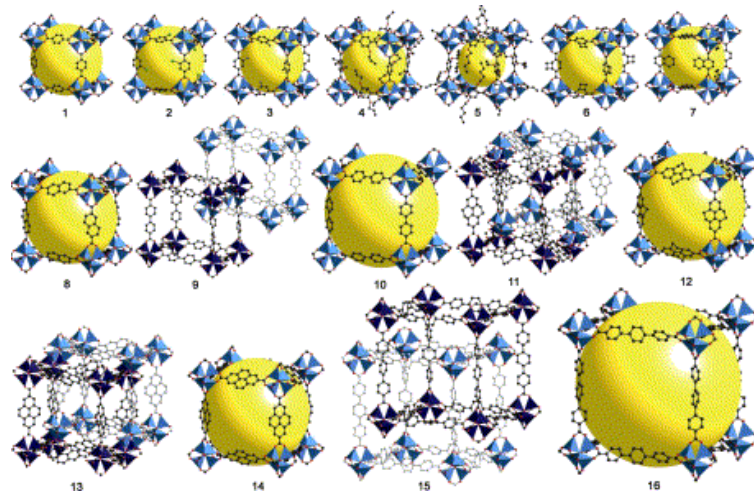


**Figure 2-11:** IR-MOF Series

Yellow spheres represent void space<sup>33</sup>

#### 2.2.2.4 Post-Synthetic Modification

The range of functionality available to porous coordination polymers through modification of linker molecules is a major advantage as the chemical nature of the surface of the pores controls the overall pore environment, and can be achieved by simple chemical modification of the linker molecule. A new approach, “Post Synthetic Modification” is being applied; this is a two-step approach which involves the initial framework synthesis followed by functional group transformation. For example, IR - MOF 3, a metal organic framework from the IR – MOF series synthesised by Yaghi *et al* can be modified post synthetically by the transformation of amine functionality to salicylidene functionality.<sup>35</sup> The functional groups that are to be modified must not have a structure defining role during framework synthesis. The advantages of post synthetic modification are that functional groups can be incorporated which may not survive the temperature and pH conditions required during framework synthesis, and which may interfere with the donor group on the bridging ligand during synthesis.<sup>36</sup>

#### 2.2.2.5 Interpenetration

The incorporation of larger linker molecules to provide larger pores, as in the IR – MOF series can cause problems with respect to stability of the framework, and although used to increase pore size, can result in reduced pore size due to interpenetration. Networks which have long linker molecules can result in the penetration of one framework into the void space in a second framework, in **Figure 2-12** this is shown by the interpenetration of two diamondoid networks.

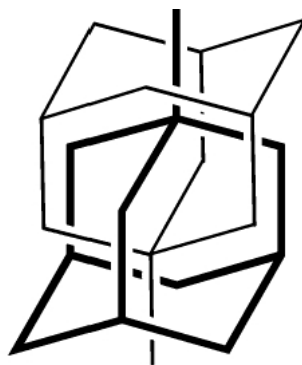


**Figure 2-12:** Schematic representation of the interpenetration of diamondoid frameworks

This can be avoided if anions are required for synthesis, as these will tend to fill the pores, or if guest/template molecules are used which have stronger interactions with the framework, than other framework networks.<sup>27</sup>

### 2.2.2.6 Dynamic Structural Responses

3<sup>rd</sup> generation polymers have the ability to exhibit dynamic structural responses to guest molecules. These were categorised by Kitigawa *et al* as one of two structural changes<sup>25</sup>:

- 1) Guest-induced crystal to amorphous deformation - the framework collapses on removal of guests but can be reformed by exposure to original conditions.
- 2) Guest-induced crystal to crystal change – the framework structure changes but long-range crystalline structure is retained.

Structural change can be brought about by submersion in a liquid or by exposure to vapour.

#### Crystal to Amorphous Deformation

Pores which collapse on removal of guest species can be reformed by re-exposure to the original guest/template molecule. An example of this is by Choi *et al*, and their framework  $\{[\text{Ni}(\text{cyclam})(\text{H}_2\text{O})_2]_3[\text{btc}]_2 \cdot 24\text{H}_2\text{O}\}_n$  where  $\text{btc} = 1,3,5$  benzenetricarboxylate. In this compound the structure is held together by hydrogen bonds between the Ni (II) macrocycle and  $\text{btc}$  via water molecules. Removal of the water provides an amorphous solid, which re-crystallises to the original structure on suspension in water.

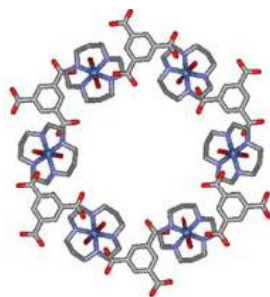


**Figure 2-13:** Crystal structure of  $\{[\text{Ni}(\text{cyclam})(\text{H}_2\text{O})_2]_3[\text{btc}]_2 \cdot 24\text{H}_2\text{O}\}_n$  (in the presence of water)<sup>37</sup>

Crystal to Crystal Deformations

There are many examples of structural change where the crystalline structure is retained, for example, induced fit, breathing of pores, and deformation by exchange of guests.

Induced Fit

Induced fit occurs when the pore shrinks to fit tightly around the guest molecule. An example of this is by Kondo *et al*, who used the compound  $[\text{Cu}_2(\text{pzdc})_2(\text{bpy})]$  where pzdc = pyrazine-2,3-dicarboxylate and bpy = 4,4'-bipyridine. This compound shows a reversible structural change on the adsorption and desorption of benzene. In the absence of benzene the pores are rectangular in shape, when benzene is adsorbed the pores shrink around the benzene to form a “z” shaped pore, as shown in **Figure 2-14**.

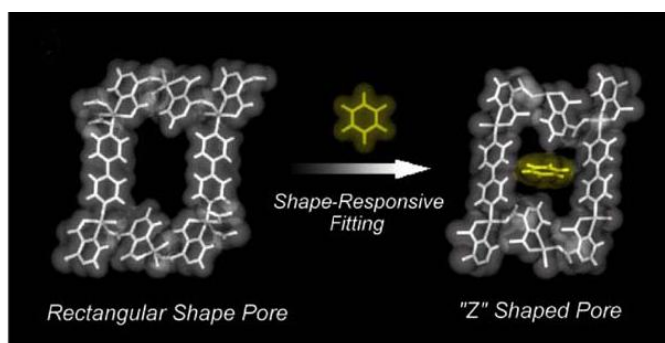


**Figure 2-14:** The shrinkage of a pore on adsorption of a benzene molecule<sup>38</sup>

A structural change also occurs around copper metal centre, in which the arrangement of the ligands changes from a square pyramidal geometry to a square planar on adsorption of the benzene.

Breathing of Pores

When the size of the pore is too small to hold the guest molecule, the pore will expand to the correct size to hold the guest tightly. This effect was shown by Soldatov *et al*, and their compound  $[\text{Cu}(\text{L}_1)_2]$  where  $\text{L}_1 = \text{CF}_3\text{COCH}_2\text{COC}(\text{OMe})\text{Me}_2$ . This compound forms two different structures. When the initial non porous form is exposed to the guest molecules, the oxygen of the methoxy group coordinates to the copper axial sites to form six-membered cyclic structures, hence opening up the porosity, as shown in **Figure 2-15**. The key to this transformation is the lability of the copper – methoxy bond.

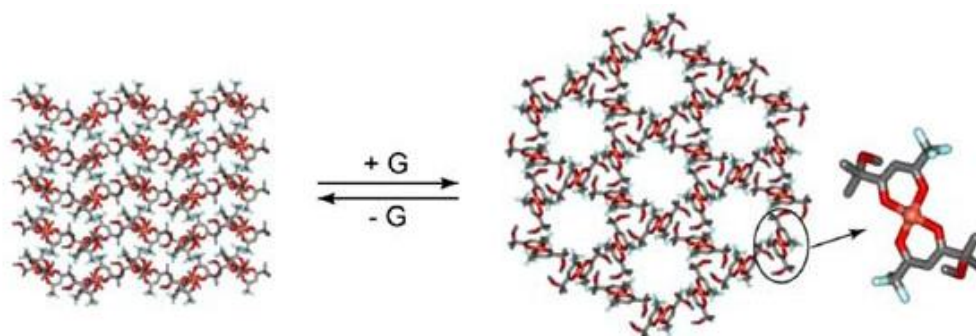


**Figure 2-15:** Expansion of the framework to incorporate a guest molecule<sup>39,40</sup>

#### Guest Exchange Deformation

Guest exchange deformation occurs when the simultaneous exchange of guest molecules induces a structural change. This was observed by Biradha *et al*, and their compound  $\{[\text{Ni}(\text{L}_2)_2(\text{NO}_3)_2] \cdot 4(o\text{-xylene})\}_n$  where  $\text{L}_2 = 4,4'$ -bis(4-pyridyl)biphenyl. The compound is structured as 2D layers with a short interlayer separation of 4.1 Å, held together by weak interlayer aromatic and hydrogen bonds. These weak bonds allow sliding of the layers, during which time the bonds are broken and reformed. When the *o*-xylene guest is exchanged with mesitylene, the extent of the sliding between the layers gives rise to channels which are larger than when the guest is *o*-xylene. This transformation appears to be limited to mesitylene, attempts with benzene, *m*-xylene and 1,2- and 1,3- dimethoxybenzene failed.

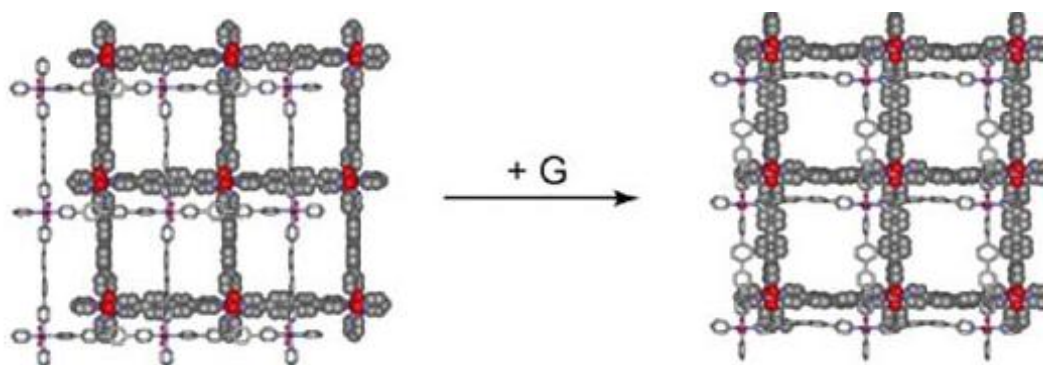


**Figure 2-16:** Structural change observed on exchange of *o*-xylene and mesitylene guests.<sup>41,42</sup>

#### Crystal to Crystal Transformation

Deformations by the expansion and collapse of pores, where structural changes occur without the breaking or forming of bonds have been shown many times. Transformations in which bonds are broken and different bonds are formed, whilst retaining crystallinity, are much rarer. For transformations of this nature to occur

within metal organic frameworks with only one metal centre and one type of linker, then the linker must possess dual functionality, allowing the formation of strong bonds and weaker bonds. This would allow cleavage of weaker bonds, whilst stronger bonds remain intact, retaining crystallinity. An example of a linker with dual functionality is 5-sulfoisothalate, which contains two strongly binding carboxylate groups and one weaker sulfonate group, allowing rearrangement through the sulfonate group without cleaving the metal-carboxylate bonds.<sup>43</sup> An example of the use of this linker in a metal organic framework is that of Cu-SIP-3.3H<sub>2</sub>O by Xiao *et al.*<sup>44</sup> Xiao *et al* showed that upon dehydration, the bound water molecules coordinated to the copper centre are removed at 405 K, allowing the previously unbounded oxygen of the sulfonate to bind to the copper centre. Cooling down under a moist atmosphere shows the rehydration of the copper centre and the reversibility of the transformation. During both of these processes, no change occurs to the stronger carboxylate connectivity. The dehydrated form of this material shows selective adsorption of NO at sub ambient pressures over any other common gases up to a pressure of 10bar. On exposure of the NO-loaded material to water, the original hydrated phase is reformed and NO is released. Xiao *et al* also show that the transformation can be stopped using a “blocking” ligand, in this case pyridine, which replaces the coordinated water molecule and prevents formation of an open metal centre, blocking the coordination of the sulfonate group.

### 2.2.3 Applications of Porous Coordination Polymers

Several possible applications of porous coordination polymers have been discussed in the literature during their development, including gas separation and purification, clean energy applications, catalysis; for which zeolites and carbon molecular sieves are already utilised in industry. The ability to tailor the surface chemistry, size of the pores and the ability to introduce flexibility within porous coordination polymers towards specific processes makes them highly significant materials in the improvement and development of these applications.

### 2.2.3.1 Separation and Purification

This is the main application to be investigated within this study and as such is covered in more detail in **Chapter 3 – Separation of Gases and Vapours**.

### 2.2.3.2 Clean Energy Applications

Hydrogen has long been seen as a clean energy source, the only by-product of hydrogen use in an engine is water, and the way forward as a greener alternative to fossil fuels to be used in motor vehicles. The challenges involved with the storage of hydrogen for use in motor vehicles are the safety, efficiency and economic value of on-board hydrogen storage systems.<sup>45</sup> Hydrogen can be stored via a number of methods, by storage in tanks as compressed gas or as a cryogenic liquid or through the absorption and adsorption of the gas into porous materials. In 2009, the US Department of Energy (DOE) released revised targets for on-board hydrogen storage for light-duty vehicles, as an update to previous targets which were deemed unobtainable. These revised targets are shown in **Table 2-2**.

**Table 2-2:** US DOE targets for hydrogen storage for 2010 and 2017<sup>46</sup>

Storage Parameter	2010	2017	Ultimate
Gravimetric Capacity / (kgH <sub>2</sub> / kg system)	0.045	0.055	0.075
Volumetric Capacity / (kgH <sub>2</sub> / L system)	0.028	0.040	0.070
Min/Max Delivery Temp / (°C)	-40/85	-40/85	-40/85
Cycle life / (cycles)	1000	1500	1500

Along with these targets, the materials must have fully reversible hydrogen adsorption, refuelling times should be within minutes to compete with current fuel loading systems and both loading and unloading of hydrogen should occur at ambient pressures and temperatures. The majority of research into hydrogen storage has been conducted at 77 K, across a pressure range of 20 – 80 bar. Examples of porous coordination polymers which have displayed hydrogen adsorption properties are shown in **Table 2-3**, with calculated enthalpy of adsorption at 77 K. Adsorption properties and enthalpy of hydrogen adsorption data for selected other porous materials are given in **Table 2-4**. At cryogenic temperatures the uptake volume of hydrogen is low due to the low enthalpy of adsorption, even at high pressures. It is predicted that for viable storage at ambient temperature, the enthalpy of hydrogen

adsorption should be approximately 20kJ/mol. The ability to alter the surface functionality of porous coordination polymers could lead to the enhancement of the interaction between the hydrogen on the surface of the material, for example by including open metal centres within the framework. This is important at lower pressures, where having a larger enthalpy of adsorption is important for maximizing the adsorption potential. At higher pressures, the adsorption potential is determined more by the available pore space, larger pores are more desirable as the volume available is what limits the capacity for hydrogen loading.

**Table 2-3:** High pressure adsorption data, porous structure characterisation and enthalpies of adsorption for porous coordination polymers (adapted from ref.45)

Porous Material	Surface Area / $\text{m}^2 \text{g}^{-1}$	Pore Volume / $\text{cm}^3 \text{g}^{-1}$	Amount adsorbed at 77K (wt%)	Amount adsorbed at ambient temperature (wt%)	Enthalpy of Adsorption, $Q_{\text{st}} / \text{kJ mol}^{-1}$
Zn <sub>4</sub> O(BDC) <sub>3</sub> MOF-5 <sup>47,48</sup>	2296 <sup>B</sup>	1.19	5.1 (65 bar)	0.28 (65 bar)	4.9 – 4.4 (77 – 87 K)
Cu <sub>3</sub> (btc) <sub>2</sub> HKUST - 1 <sup>49,48</sup>	1154 <sup>B</sup>	0.75	3.6 (30 bar)	0.35 (65 bar)	6.6- 6.0 (77 – 87 K)
Cu <sub>2</sub> (qptc) NOTT-102 <sup>50</sup>	2932 <sup>B</sup>	1.138	6.07 (20 bar)	-	5.3 (77 K)
Cu <sub>2</sub> (tpc) NOTT-101 <sup>50</sup>	2247 <sup>B</sup>	0.886	6.06 (20 bar)	-	5.4 (77 K)
Cu <sub>2</sub> (abtc) PCN-10 <sup>51</sup>	1779 <sup>L</sup>	0.67	4.33 (20 bar)	0.25 (46 bar)	7 – 4 (77 – 300 K)
Mn <sub>3</sub> [(Mn <sub>4</sub> Cl) <sub>3</sub> (BTT) <sub>8</sub> ] <sub>2</sub> Mn-BTT <sup>52</sup>	2100 <sup>B</sup>	0.795	5.1 (40 bar)	0.95 (90 bar)	10.1 (77 K)
Zn(mim) <sub>2</sub> ZIF-8 <sup>53</sup>	1810 <sup>L</sup>	0.663	3.1 (55 bar)	-	4.5 (30 – 300 K)

<sup>B</sup> BET surface area <sup>L</sup> Langmuir surface area



**Table 2-4:** High pressure adsorption data and porous structure characterisation for selected porous materials (adapted from ref. 45)

Porous Material	Surface Area / m <sup>2</sup> g <sup>-1</sup>	Pore Volume / cm <sup>3</sup> g <sup>-1</sup>	Amount adsorbed at 77K (wt%)	Amount adsorbed at ambient temperature (wt%)
Porous carbons <sup>54</sup>	22 – 2564 <sup>B</sup>	0.0065 – 0.75	0 – 4.4	0 – 0.54
COFs <sup>55</sup>	3472 <sup>B</sup>	-	8.8 (80 bar) <sup>GCMC</sup>	-
Zeolites <sup>56</sup>	-	-	1.02 – 2.07 (16 bar)	0.42 – 0.49 (60 bar)
Ion-exchanged zeolites <sup>57</sup>	384 – 725 <sup>B</sup>	-	1.32 – 2.19 (15 bar)	-

<sup>B</sup> BET surface area <sup>GCMC</sup> Grand canonical Monte Carlo simulation data

**Table 2-5:** High pressure enthalpies of adsorption for selected porous materials (adapted from ref. 45)

Porous Material	Enthalpy of Adsorption, Q <sub>st</sub> / kJ mol <sup>-1</sup>	Temperature range of enthalpy of adsorption calculation / K
Functionalised activated carbons <sup>58</sup>	5.2 – 3.9	77 – 114
Zeolites 4A, 5A, 13X <sup>59</sup>	7.9 – 5.9	75 – 90
COFs <sup>55</sup>	8.8 – 2.7 <sup>GCMC</sup>	-

<sup>GCMC</sup> Grand canonical Monte Carlo simulation data

### 2.2.3.3 Catalysis

Catalysis is a major part of industrial process, with porous materials employed as supports, such as platinum loaded on activated carbon and as catalysts in their own right, such as zeolites. The ability to fine tune the structural components of porous coordination polymers makes them a highly attractive material for use as catalysts. MOF-5 [ZnO<sub>4</sub>(BDC)<sub>3</sub>] has been extensively investigated as a catalyst support for various nanoparticle catalysts, as outlined in **Table 2-6**.

**Table 2-6:** Selected examples of the catalytic activity of MOF – 5 derivatives

MOF-5 Variant	Reaction	Reference
Pd – MOF-5	Sonogashira coupling reaction	60
Ni – MOF-5	Hydrogenation	61
Ag – MOF-5	Epoxidation	62
Pt – MOF-5	H <sub>2</sub> O <sub>2</sub> Synthesis	63

MOF-5 is readily utilised due to its high surface area, thermal stability and ease of synthesis, with these features being comparable to that of classical catalyst supports such as activated carbon and zeolites.

Incorporation of active sites within the building units of porous coordination polymers can help to develop catalysts which have similar properties to zeolite catalysts, with size and shape selectivity and fixed areas of catalytic activity. (*R,R*)-(2)-1,2-cyclohexanediamino-*N,N'*-bis(3-*tert*-butyl-5-(4-pyridyl)salicylidene)Mn<sup>III</sup>Cl is a chiral ligand which was incorporated into a zinc based framework, Zn<sub>2</sub>(bpdc)<sub>2</sub> by Cho *et al.*<sup>64</sup> The chirality of the manganese ligand makes this framework an effective asymmetric catalyst for olefin epoxidation, with enhanced catalytic behaviour attributed to the fixation of the active site within the linkers, allowing a highly stable and size-selective catalyst to be formed.

Lewis and Brønsted acid sites within catalysts have been reported for a number of porous coordination polymers. The material [Cu<sub>3</sub>(btc)<sub>2</sub>(H<sub>2</sub>O)<sub>3</sub>] also known as HKUST-1 (Hong Kong University of Science and Technology)<sup>65</sup> reveals an open Cu(II) site upon desolvation of coordinated water molecules. This Lewis acid site has been shown to catalyse the cyanosilylation of benzaldehyde or acetone.<sup>66</sup> Chemisorption of the benzaldehyde activates the aldehyde for the cyanosilylation, and produces a high yield of product. A copper based framework produced by Ingleson *et al.*<sup>67</sup> with amino acid linkers, Cu(asp)bpe<sub>0.5</sub>, allows the confinement of an aspartate group within the framework. Post synthetic modification of the framework can occur by protonation of one of the two carboxylate groups available in the aspartate. Only one carboxylate in the aspartate can be protonated due to the coordination of the aspartate to the metal centre. The carboxylate acid group formed

binds to the Cu metal centre, producing a Brønsted acid site, which can be used to facilitate the ring-opening methanolysis of small epoxides.<sup>67</sup>

### 2.2.3.4 Drug Delivery

Effective control over the size, loading, release kinetics and surface properties are crucial for the development of therapeutic agents for effective biological applications.<sup>68</sup> Over the past five years there has been extensive research conducted into the use of porous coordination polymers for drug delivery, with the high surface areas, large pores and tuneable surface functionality being the major advantages exploited for the use of these materials as drug carriers. A major disadvantage for using porous coordination polymers is that of the inherent toxicity of the metal centres and the ligands used as building units within the framework, therefore careful selection of building units and complete evaluation of biocompatibility is required for each individual framework produced. Metals centres such as zinc or iron that have acceptable LD<sub>50</sub> ranges are more likely to be incorporated into metal organic frameworks for drug delivery, coupled with naturally occurring linkers such as polycarboxylates or polar compounds which have fast excretion rates from the human body. The stability of porous coordination polymers, which is an extremely important factor for applications such as gas storage and catalysis, as the system would be required to be continually regenerated, is not as great an issue for medicinal uses, providing the material retains stability long enough for the function to be completed within the biological system. Solubility in certain biological solutions in fact may be an advantage, as this would facilitate the removal of the drug carrier from the body in a reasonable timescale.

### Specific Examples

The MIL (Material of Institute Lavoisier) family of porous coordination polymers have been investigated for their ability to store and release Ibuprofen.<sup>69</sup> MIL-101 showed a loading of 1.376g Ibuprofen per gram of MIL-101, with steady release of the drug over an initial eight hour period in simulated body fluid at 37°C. MIL-101 is a framework based around a chromium metal centre, which is toxic, with an LD<sub>50</sub> range of 50 – 150 mg/kg. Chromium damages the kidneys and liver by oxidation reactions, and as such this material would be unsuitable for drug carrying purposes, however, an iron analogue to MIL-101 has been produced.<sup>70</sup> Iron is a component in haemoglobin and has a concentration of approximately 22µM in blood plasma,

therefore an iron analogue displaying the same properties as the chromium analogue would be a highly effective drug carrier, as shown by the Lin group, who incorporated both a cisplatin pro-drug for chemotherapy treatment and a bodipy fluorophore bulk into MIL-101(Fe).<sup>71</sup> This opens up the potential for using both an active cancer treatment and an imaging reagent in the same drug delivery system, allowing real time monitoring of cancer treatment.

Porous coordination polymers have also shown an ability to store nitric oxide (NO) gas by utilising unsaturated metal centres within the framework.<sup>25</sup> Materials such as HKUST-1<sup>65</sup> adsorb significant volumes of NO, with a marked hysteresis, indicating a trapping effect.<sup>72</sup> This allows little release of NO from the HKUST structure, which, although for storage application is useful, for small release into biological systems it is not. M-CPO-27 (where M=Ni or Co) has been shown to adsorb 7mmol NO per gram of material, and release the adsorbed NO on exposure to moisture.<sup>73</sup> The NO which is released from the material is pure, and has been shown to promote vasodilation and inhibit platelet formation, thus reducing thrombosis occurrence.<sup>74</sup>

### 2.2.4 New Porous Coordination Polymers

Metal organic frameworks have been dominant in research into porous coordination polymers for the past decade, however new porous coordination polymers are being developed, such as zeolite imidazole frameworks and covalent organic frameworks.

#### 2.2.4.1 Zeolitic Imidazolate Frameworks (ZIFs)

Zeolites have an advantage over other porous materials due to the rigid, stable and highly predictable topologies. The drive to incorporate this into new porous materials, with the added extra of functionalised organic links has been the force behind the development of zeolitic imidazolate frameworks (ZIFs). ZIFs are porous crystalline materials which contain tetrahedral topologies resembling that of zeolites, however the tetrahedral coordinated atoms in the zeolites, for example silicon, are replaced by a transition metal, and the oxygen bridges are replaced by the imidazole molecule. The key in developing ZIFs was the realization that the metal – imidazole – metal linkage retains an angle close to 145°, which is comparable to that of the silicon – oxygen – silicon bridge found in zeolites, as shown in **Figure 2-17**.

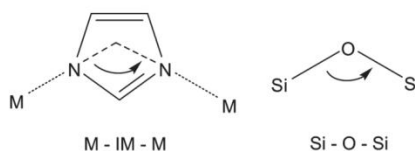
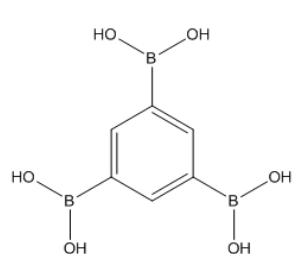


**Figure 2-17:** Bond angles in ZIFs and in zeolites<sup>53</sup>

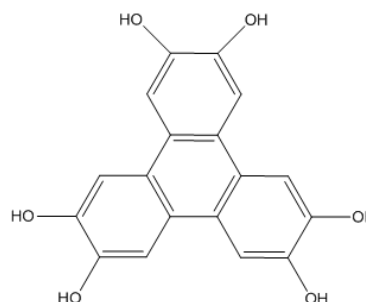
The synthesis of two ZIFs was recently reported by Yaghi *et al*, which show potential for the separation and storage of carbon dioxide. ZIFs 95 and 100 both show thermal stability to 500°C and show large Langmuir surface areas, up to 1, 240 m<sup>2</sup> g<sup>-1</sup>. The ZIFs have small apertures opening into large cages, leading to the ability to separate due to size exclusion principles and to store a large capacity of gas. Both of these ZIFs show a high affinity for carbon dioxide when compared with adsorption of methane, carbon monoxide and nitrogen. This is attributed to the slit width to the entrance to the porosity being similar to that of the dimensions of carbon dioxide, and also due to the quadrupole interactions between the carbon dioxide and the nitrogen in the imidazolate linkers. Using breakthrough curves, Yaghi *et al* showed that carbon dioxide is retained selectively when flowed through the ZIF with mixtures of carbon monoxide, methane and nitrogen.<sup>53</sup>

#### 2.2.4.2 Covalent Organic Frameworks (COFs)

Covalent organic frameworks are a new class of porous material, based on strong C-O, C-C and C-B bonds, which are being investigated for their potential application in storage of gases pertinent to obtaining clean energy and a greener environment. The group led by Yaghi *et al* has synthesised a number of covalent organic frameworks as shown in **Figure 2-18**.<sup>75</sup>



1, 3, 5 benzenetriboronic acid



2, 3, 6, 7, 10, 11 hexahydroxytriphenyl

**Figure 2-18:** Examples of secondary building units used in COF synthesis

COFs are formed by either the self or co-crystallisation of a number of starting materials. The basic synthesis involves the heating of reaction mixture consisting of either the self-condensing or the two co-condensing starting materials.<sup>75</sup>

The hydrogen uptake for COF-102 is 72.4mg g<sup>-1</sup>, this is comparable to one of the highest performing MOFs, MOF-5, placing COFs high up among the ranks of porous materials approaching the guidelines of 45g of hydrogen per litre, as sent out by the US Department of Energy.<sup>55,76,77</sup>

### 2.3 Porous Organic Molecules

Porous coordination polymers and zeolites all display *conventional porosity* – they are permeable and generally unaffected by guest uptake and removal. These materials all are fixed two dimensional or three dimensional frameworks with clearly defined channels giving access to voids and cavities into which gas molecules can be adsorbed. A second type of porosity, *porosity “without pores”*, was discussed by L. J. Barbour in relation to molecular crystals.<sup>78</sup> Molecular species tend to pack in the crystal state at distances which maximise the attractive intermolecular forces between the units of the crystal, therefore it is unusual to encounter molecular crystals which possess the channel and voids as a functional analogue of zeolites and metal organic frameworks. The lack of conventional porosity within the material does not mean there are no voids within the crystal structure - there are crystal lattice voids, which, when connected by crystal lattice channels, allow the permeation of guest molecules into the lattice porosity – hence the term porosity “without pores”. Molecular materials which display this porosity “without pores” have been shown recently to display porosity in the solid state. The porosity displayed by these non – conventionally porous organic molecules has been defined by Cooper *et al*<sup>79</sup> as either being *intrinsic* or *extrinsic*. Intrinsic porosity is that which results from the discrete molecular subunits within the crystal structure, guest molecules are adsorbed into the discrete unit. Extrinsic porosity is that which results from the inefficient packing of the molecules in the crystal lattice, and is not a result of the discrete units themselves, with guest molecules being adsorbed between the discrete units. These terms are illustrated in **Figure 2-19**.

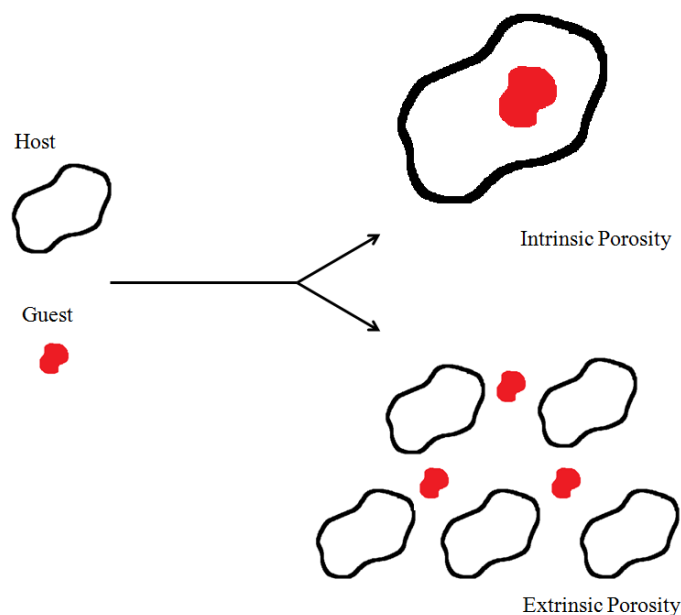


**Figure 2-19:** Diagram illustrating the difference between intrinsic and extrinsic porosity

### 2.3.1 Intrinsically and Extrinsically Porous Organic Materials

The spatial dimension classification applied to porous coordination polymers can also be applied to porous organic materials.<sup>80</sup> An example of an intrinsically porous molecule which is also 0D is that of calix[n]arenes. Calix[n]arenes are macrocyclic polyphenol compounds where the n denotes the number of phenol groups in the macrocycle.<sup>81,82</sup> There is a large number of calix[n]arene derivatives, with structures varying in the number of phenol groups in the ring, and in the functional groups attached to the phenol ring. One particular example of a calix[n]arene which shows promising interactions with guest molecules is *p-tert*-butylcalix[4]arene, shown in **Figure 2-20**. Thallapally *et al*<sup>83</sup> have shown that a high density guest-free form of *p-tert*-butylcalix[4]arene can be converted to the lower density form and vice versa by gas induced transformation upon exposure to carbon dioxide at 3.5MPa at room temperature. This transformation occurs despite the high density form being devoid of pores or cavities. It is thought that the gas molecules diffuse through the solid into small lattice voids produced by inefficient packing of the crystal lattice. Adsorption of carbon dioxide results in 10% increase in the volume of the crystal lattice.

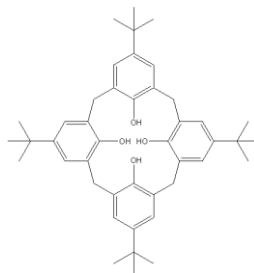


**Figure 2-20:** *p*-*tert*-butylcalix[4]arene<sup>83</sup>

One dimensional channel forming organic crystals have been seen as analogues to zeolites due to their structural similarity. One of the compounds which paved the way in the development of these one dimensional zeolite analogues is that of *tris*-*o*-phenylenedioxycyclotriphosphazene (TPP), **Figure 2-21**.

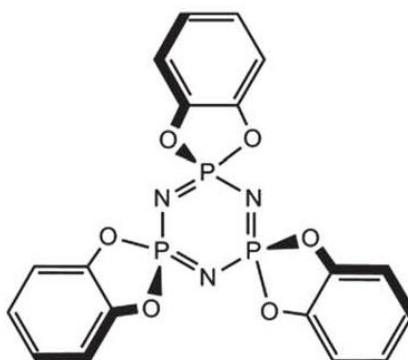


**Figure 2-21:** Structure of *tris*-*o*-phenylenedioxycyclotriphosphazene (TPP)<sup>84</sup>

The channels form a hexagonal array which often collapses upon the removal of the guest solvent molecules present in the channels. The TPP molecule with guest benzene molecules was successfully desolvated to reveal empty nano-channels within the hexagonal array, which are 4.6Å in diameter.<sup>84</sup> This desolvated TPP is stable to 150°C and is accessible to carbon dioxide and methane molecules.

A calix[n]arene functionalised to form 1,2-dimethoxy-*p*-*tert*-butylcalix[4]-dihydroquinone has been shown to form two distinct types of porosity, interconnecting channels forming a 3D network and discrete units formed by the calix[n]arene molecules.<sup>85,86</sup> After removal of water molecules the structural integrity was retained, giving a BET surface area of 230 m<sup>2</sup>g<sup>-1</sup>. The dehydrated molecule was shown to selectively adsorb carbon dioxide and methane over

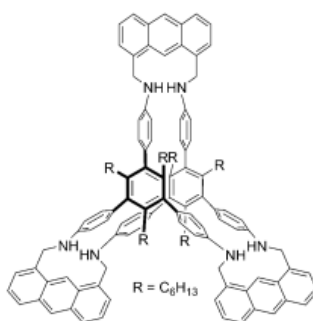


hydrogen, and recent studies have shown that the adsorbed methane resides within the interconnecting channels of the 3D network.<sup>87</sup>

### 2.3.2 Porous Organic Cage Molecules

Porous organic cage molecules are examples of compounds which can show both intrinsic and extrinsic porosity. The composition of cage molecules is similar to that of covalent organic frameworks (COFs) as they contain C-C, C-H, N-H and C-N bonds. The cages are assembled without the use of the directional covalent bonding used in COFs, instead using weaker intermolecular interactions, giving the potential for flexibility within the materials through both reorientation and complete relocation of the individual discrete units. A number of cage molecules have been reported in the literature over the past five years with research lead by Zhang, Mastalerz and Cooper.

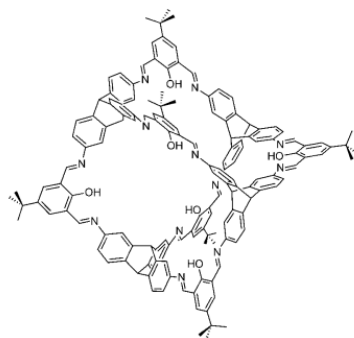
Zhang *et al* produced a trigonal-prismatic cage from the imine condensation of a triamine and a dialdehyde, Zhang cage-6 is shown in **Figure 2-22**.<sup>88</sup>



**Figure 2-22:** Zhang Cage-6<sup>88</sup>

The cages pack together in offset layers the provided channels of diameter 4.6 – 10.6 Å. The well-ordered 3D structure, plus the secondary amine groups present within the pores allows the preferential adsorption of carbon dioxide over nitrogen at 293 K, which is an essential feature for carbon capture from flue gas. Further cage structures have been produced by Zhang *et al* by varying the triamine and dialdehyde used in the synthesis of Zhang cage-6.<sup>89</sup>

Mastalerz *et el* produced a cage compound which has an exceptionally high surface area of 1566 m<sup>2</sup>g<sup>-1</sup> which compares well with covalent organic frameworks, and is one of the highest reported for a porous organic cage, **Figure 2-23**.<sup>90</sup>

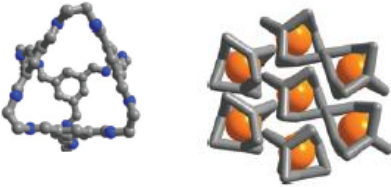
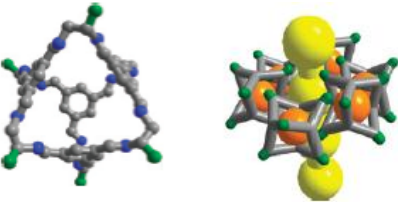
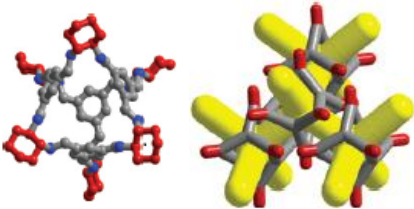


**Figure 2-23:** Mastalerz cage-3<sup>90</sup>

This cage was produced via the imine condensation of a triamine and salicylbisaldehyde. This compound was shown to adsorb 9.4wt % of carbon dioxide, compared to 0.94wt% of methane, showing a much higher selectivity for carbon dioxide. Mastalerz *et al* have shown that salicylbisimine cage compounds can be functionalised at the periphery, and a series of cages have been produced, one of which, cage-3a, shows a BET surface area of 2071 m<sup>2</sup>g<sup>-1</sup>.<sup>91</sup>

Cooper *et al* have reported the synthesis of three organic cages,<sup>92</sup> via the [4 + 6] condensation of 1, 3, 5-triformylbenzene with three different diamines. The cages were isolated as crystalline solids when recrystallized from various solvents. The various packing motifs and the porosity produced in these materials is a direct result of the symmetry of the individual cage units and the functional groups bound at the vertices of the cages as shown in **Table 2-7**.

**Table 2-7:** Cage structures with synthesis, structure, porosity and adsorption details. Yellow and orange space filling represents Connolly Surface area.<sup>92</sup>

Cage	Synthesis	Structure and Porosity	Adsorption
Cage One	1,2ethylenediamine Crystallised from ethyl acetate	 <p>Intrinsic Porosity with isolated void volume</p>	<p>Little hydrogen or nitrogen at 77K</p> <p>Larger quantities of methane and carbon dioxide at ambient temperature.</p>
Cage Two	1,2propylenediamine Crystallised from acetonitrile	 <p>Intrinsic and Extrinsic Porosity with isolated void volume as in Cage 1 – methyl groups attached to arene gives inefficient packing providing 1D pore channels</p>	<p>Type I nitrogen adsorption at 77K</p> <p>Langmuir surface area: 600m<sup>2</sup>g<sup>-1</sup></p> <p>BET surface area: 533m<sup>2</sup>g<sup>-1</sup>.</p>
Cage Three	(R,R)-1,2diaminocyclohexane Crystallised from dichloromethane	 <p>Interconnected diamondoid network</p>	<p>Type I nitrogen adsorption at 77K</p> <p>Langmuir surface area: 730m<sup>2</sup>g<sup>-1</sup></p> <p>BET surface area: 624m<sup>2</sup>g<sup>-1</sup>.</p>

### Cage One

Cage one will form the basis of the majority of the research conducted in this thesis. Cage one was prepared and fully characterised by single crystal X-ray diffraction and powder X-ray diffraction by the research group led by Andrew Cooper at Liverpool University. The following information is provided from the paper published in 2010<sup>93</sup>, and is not claimed as the authors own.

Cage one is synthesised by the [4 + 6] condensation of 1, 3, 5-triformylbenzene with 1, 2 ethylenediamine, the product of which is crystallized from ethyl acetate as a solvate, 1α•2.5EtOAc. The cage itself is around 1nm in size. Cage one has been

shown to interconvert between a number of stable polymorphs upon exposure to certain chemical triggers.<sup>93</sup> The conversion between polymorphs  $1\alpha$  and  $1\beta$  are shown in **Figure 2-24**.

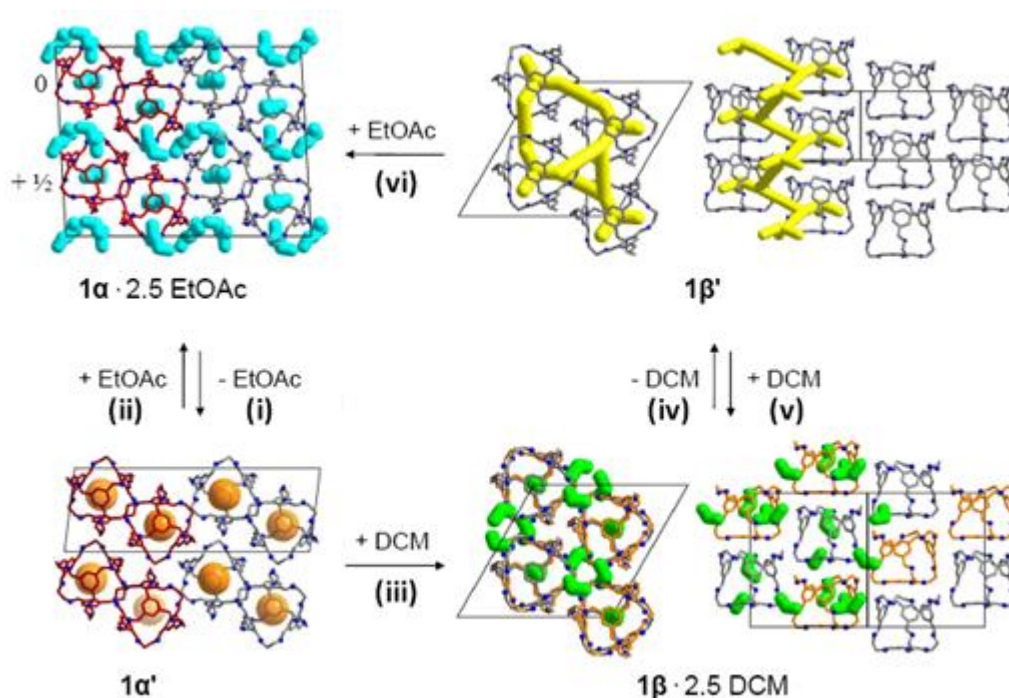


**Figure 2-24:** Conversion between various polymorphs ( $1\alpha$  and  $1\beta$ ) accessible to the cage one structure, where  $1\alpha'$  and  $1\beta'$  indicate desolvated structures. Yellow, blue, green and orange space filling represents Connolly Surface area.<sup>93</sup>

Desolvation of  $1\alpha \cdot 2.5 \text{ EtOAc}$  leads to  $1\alpha'$  (step i), which can reform the solvated structure on exposure to ethyl acetate (step ii). Exposing  $1\alpha'$  to dichloromethane solvent converts  $1\alpha'$  to  $1\beta \cdot 2.5 \text{ DCM}$  (step iii). Removal of DCM solvent produces  $1\beta'$  (step iv), which can be converted to  $1\alpha \cdot 2.5 \text{ EtOAc}$  upon exposure to ethyl acetate (step vi), or can be reconverted to  $1\beta \cdot 2.5 \text{ DCM}$  by exposure to dichloromethane (step v).  $1\beta \cdot 2.5 \text{ DCM}$  exists in a state which contains two conformers,  $1^T$  and  $1^{C^3}$ .  $1^T$  is a tetrahedral conformer, and  $1^{C^3}$  is non-tetrahedral. These conformers exist in a 1:1 ratio within the  $1\beta \cdot 2.5 \text{ DCM}$  structure, stacking alternately in a window to arene fashion to give a helical channel structure, which is occupied by the dichloromethane molecules. On desolvation of the dichloromethane molecules, the  $1^{C^3}$  conformer converts to  $1^T$  via rotation around the C-C bond of the imine to arene connection, forming a homochiral crystal of  $1\beta'$ , containing only one enantiomer of the  $1^T$  conformer. Exposure of  $1\beta'$  to ethyl acetate causes the transformation to the  $1\alpha \cdot 2.5 \text{ EtOAc}$  phase through the incompatibility of the ethyl acetate and the helical

pore channel structure of  $1\beta'$ , resulting in a structure consisting of disconnected cage voids. Conformational conversion causes the formation of a racemic crystal by the production of both R and S enantiomers of the  $1^T$  conformer. The  $1^T$  conformers in  $1\alpha \cdot 2.5\text{EtOAc}$  stack in parallel layers, on desolvation these layers move closer together, reducing the pore volume by 12%. The narrow porosity restricts adsorption and at 77 K  $1\alpha'$  is non-porous to nitrogen and hydrogen. Exposing  $1\alpha'$  to dichloromethane results in the transformation of  $1\alpha'$  to  $1\beta \cdot 2.5\text{DCM}$ , converting  $1^T$  conformers to  $1^{C3}$  producing the helical channel structure. Although non-porous to nitrogen and hydrogen at 77 K, exposure to dichloromethane opens the structure of  $1\alpha'$  in a cooperative diffusion mechanism. There is no conversion from one polymorph to another over time, or with application of heat, indicating a stable system which only converts when exposed to the trigger molecules of ethyl acetate and dichloromethane. The conversion has been shown to be as a result of conformational change of the tetrahedral cage units and the reorganization of the discrete cages within the crystal lattice.<sup>93</sup>

2.4 References

- <sup>1</sup> D. D. Do, *Adsorption Analysis: Equilibria and Kinetics*, Imperial College, London, **1998**
- <sup>2</sup> J. W. McBain, *The Sorption of Gases and Vapours by Solids*, Rutledge and Sons, London, **1932**
- <sup>4</sup> T. De Saussure, *Ann. Phil.*, **1814**, 47, 113
- <sup>5</sup> T. De Saussure, *Ann. Phys.*, **1815**, 6, 241
- <sup>6</sup> R. Von Ostrejko, *Patent*, German, 136 792, **1901**
- <sup>7</sup> M. S. Tswett, *Tswett Chromatographic Adsorption Analysis: Selected Work.*, Elis Horwood Ltd., **1990**
- <sup>8</sup> J. Dewar, *Proc. R. Soc.*, **1904**, 74, 127
- <sup>9</sup> R. M. Breck, *Zeolites and Clay Materials*, Academic Press, **1978**
- <sup>10</sup> R. M. Milton, *Patent*, US, 2882243 and 2882244., **1959**
- <sup>11</sup> B. F. Hoskins, R. Robson., *J. Am. Chem. Soc.*, **1990**, 112, 1546
- <sup>12</sup> S. Sircar, T. C. Golden, M. B. Pao, *Carbon*, **1996**, 34, 1
- <sup>13</sup> A. W. Harding, N. J. Foley, P. R. Norman, D. C. Francis, K. M. Thomas, *Langmuir*, **1998**, 14, 3858
- <sup>14</sup> H. F. Stoeckli, *Carbon* **1990**, 28, 1
- <sup>15</sup> B. McEnaney, J. J. Mays, *In Introduction to Carbon Science*, Marsh H., Ed.; Butterworths, **1989**, 153
- <sup>16</sup> W. Heschel, E. Klose, *Fuel*, **1995**, 74, 1786
- <sup>17</sup> M. Molina-Sabio, F. Rodriguez-Reinoso, F. Caturla, M. J. Selles, *Carbon*, **1995**, 33, 1105
- <sup>18</sup> J. Laine, S. Yunes, *Carbon*, **1992**, 30, 601
- <sup>19</sup> P. Feng, X. Bu, G. D. Stucky, *Nature*, **1997**, 388, 735
- <sup>20</sup> R. Szostak, *Molecular Sieves – Principles of Synthesis and Identification.*, 2<sup>nd</sup> Ed. Blackie Academic and Professional, London, **1998**
- <sup>21</sup> H. H. Funke, M. G. Kovalchick, J. L. Falconer, R. D. Noble, *Ind. Eng. Chem. Res.*, **1996**, 35, 1575

- <sup>22</sup> L. C. Oliveira, D. I. Petkosicz, A. Smaniotto, S. B. Pergher, *Water Res.*, **2004**, *38*, 3699
- <sup>23</sup> J. C. Bailar, Jr. *Jr. Prep. Inorg. React.*, **1964**, *1*, 1
- <sup>24</sup> C. Janiak, *Dalton Transactions* **2003**, *14*, 2781
- <sup>25</sup> S. Kitigawa, R. Kitaura, S. Noro, *Angew. Chem. Int. Ed.*, **2004**, *43*, 2334
- <sup>26</sup> B. Moulton, M. J. Zaworotko, *Chem. Rev.* **2001**, *101*, 1620
- <sup>27</sup> S. L. James, *Chem. Soc. Rev.*, **2003**, *32*, 276
- <sup>28</sup> M. D. Allendorf, C. A. Bauer, R. K. Bhaktaa, R. J. T. Houka, *Chem. Soc. Rev.*, **2009**, *38*, 1330
- <sup>29</sup> B. L. Chen, Y. Yang, F. Zapata, G. D. Qian, Y. S. Luo, J. H. Zhang, E. B. Lobkovsky, *Inorg. Chem.* **2006**, *45*, 8882
- <sup>30</sup> F. J. Steemers, W. Verboom, D. N. Reinhoudt, E. B. Van der Tol, J. W. Verhaven, *J. Am. Chem. Soc.*, **1995**, *117*, 9408
- <sup>31</sup> A. X. Tion, J. Ying, J. Peng, J. Q. Sha, Z. G. Hon, J. F. Ma, Z. M. Su, N. H. Hu, H. Q. Jia, *Inorg. Chem.*, **2008**, *47*, 3274
- <sup>32</sup> X. Liu, H. Ge, Y. Zhang, L.HU, B. Li, *J. Mol. Structures*, **2006**, *796*, 129
- <sup>33</sup> O. M. Yaghi, M. O'Keefe, N. W. Ockwig, H. K. Chae, M. Eddaoudi, J. Kim, *Nature*, **2003**, *423*, 705
- <sup>34</sup> H. Li, M. Eddaoudi, M. O'Keefe, O. M. Yaghi, *Nature*, **1999**, *402*, 276
- <sup>35</sup> M. J. Ingleson, J. P. Barrio, J. B. Guilbaud, Y. Z Khimiyak, M. J. Rosseinsky, *Chem. Commun.* **2008**, 2680
- <sup>36</sup> A. D. Burrows, C. G. Frost, M. F. Mahon, C. Richardson, *Angew. Chemie. Int. Ed.* **2008**, *47*, 8482
- <sup>37</sup> H.J. Choi, T.S. Lee, M.P. Suh, *Angew. Chem. Int. Ed.* **1999**, *38*, 1405
- <sup>38</sup> M. Kondo, T. Okuba, A. Asami, S. I. Noro, T. Yoshitomi, S. Kitigawa, T. Ishii, H. Matsuzaka, K. Seki, *Angew. Chem. Int. Ed.* **1999**, *38*, 140
- <sup>39</sup> D.V. Soldatov, J.A. Ripmeester, S.I. Shergina, I.E. Sokolov, A.S. Zanina, S.A. Gromilov, Y.A. Dyadin, *J. Am. Chem. Soc.* **1999**, *121*, 4179
- <sup>40</sup> A.Y. Manakov, D.V. Soldatov, J.A. Ripmeester, J. Lipkowski, *J. Phys. Chem. B.* **2000**, *104*, 12111.

- <sup>41</sup> K. Biradha, Y. Hongo, M. Fujita, *Angew. Chem. Int. Ed.*, **2002**, *41*, 3395
- <sup>42</sup> K. Biradha, Y. Hongo, M. Fujita, *Angew. Chem. Int. Ed.*, **2000**, *39*, 3843
- <sup>43</sup> D. S. Kim, P. M. Forster, R. Le Toqui, A. K. Cheetham, *Chem. Commun.* **2004**, 2148
- <sup>44</sup> B. Xiao, P. J. Byrne, P. S. Wheatley, D. S. Wragg, X. Zhao, A. J. Fletcher, K. M. Thomas, L. Peters, J. S. O. Evans, J. E. Warren, W. Zhou, R. E. Morris, *Nature*, **2009**, *1*, 289
- <sup>45</sup> K. M. Thomas, *Dalton. Trans.*, **2009**, 1487
- <sup>46</sup> [http://www1.eere.energy.gov/hydrogenandfuelcells/storage/current\\_technology.html](http://www1.eere.energy.gov/hydrogenandfuelcells/storage/current_technology.html)  
04/05/2012
- <sup>47</sup> M. Latroche, S. Suble, C. Serre, C. Mellot-Draznieks, P. L. Llewellyn, J. H. Lee, J. S. Chang, S. H. Jung, G. Ferey, *Angew. Chem. Int. Ed.*, **2006**, *45*, 8227
- <sup>48</sup> B. Panella, M. Hirscher, H. Puetter, U. Mueller, *Adv. Func. Mater.*, **2006**, *16*, 520
- <sup>49</sup> J. L. C. Rowsell, O. M. Yaghi, *J. Am. Chem. Soc.*, **2006**, *28*, 1304
- <sup>50</sup> X. Lin, J. Jia, X. Zhao, K. M. Thomas, A. J. Blake, G. S. Walker, N. R. Champness, P. Hubberstey, M. Schroder, *Angew. Chem. Int. Ed.*, **2006**, *45*, 7358
- <sup>51</sup> X. S. Wang, S. Q. Ma, K. Rauch, J. M. Simmons, D. Q. Yuan, X. P. Wang, T. Yildirim, W. C. Cole, J. J. Lopez, A. d. Meijere, H. C. Zhou, *Chem. Mater.*, **2008**, *20*, 3145
- <sup>52</sup> M. Dincă, A. Dailly, Y. Liu, C. M. Brown, D. A. Neumann, J. R. Long, *J. Am. Chem. Soc.*, **2006**, *128*, 16876
- <sup>53</sup> K. S. Park, Z. Ni, A. P. Cote, J. Y. Choi, R. Huang, F. J. Uribe-Romo, H. K. Chae, M. O'Keeffe, O. M. Yaghi, *PNAS*, **2006**, *103*, 10186
- <sup>54</sup> B. Panella, M. Hirscher, S. Roth, *Carbon*, **2005**, *43*, 2209
- <sup>55</sup> S. S. Han, H. Furukawa, O.M. Yaghi, W. A. Goddard, *J. Am. Chem. Soc.*, **2008**, *130*, 11580
- <sup>56</sup> J. Dong, X. Wang, H. Xu, Q. Zhao, J. Li, *Int. J. Hydrogen Energy*, **2007**, *32*, 4998
- <sup>57</sup> H. W. Langmi, D. Book, A. Walton, S. R. Johnson, M. M. Al-Mamouri, J. D. Speight, P. P. Edwards, I. R. Harris, P. A. Anderson, *J. Alloys Compd.*, **2005**, *404 – 406*, 637
- <sup>58</sup> X. B. Zhao, B. Xiao, A. J. Fletcher, K. M. Thomas, *J. Phys. Chem. B.*, **2005**, *109*, 8880



- <sup>59</sup> I. D. Basmadjian, *Can. J. Chem.*, **1960**, 38, 141
- <sup>60</sup> S. Gao, N. Zhao, M. Shu, S. Che, *Applied Catalysis A: General* **2010**, 388, 196
- <sup>61</sup> H. Zhao, H. Song, L. Chou, *Inorganic Chemistry Communications*, **2012**, 15, 261
- <sup>62</sup> U. Mueller, L. Lobree, M. Hesse, O. M. Yaghi, M. Eddaoudi, *Patent*, WO 03/101975, **2003**
- <sup>63</sup> U. Mueller, O. Metelkina, H. Junicke, T. Butz, O. M. Yaghi, *Patent*, US 2004/081611, **2004**
- <sup>64</sup> S. Cho, B. Ma, S. T. Nguyen, J. T. Hupp, T. E. Albrecht-Schmitt, *Chem. Commun.* **2006**, 2563
- <sup>65</sup> S. Y. Chui, S. M. F. LO, J. P. H. Charmant, A. G. Orpen, I. D. Williams, *Science*, **1999**, 283, 1148
- <sup>66</sup> K. Schlichte, T. Kratzke, S. Kaskel, *Micro. Meso. Mat.* **2004**, 73, 81
- <sup>67</sup> M. J. Ingleson, J. P. Barrio, J. Bacsá, C. Dickinson, H. Park, M. J. Rosseinsky, *Chem. Comm.*, **2008**, 1287
- <sup>68</sup> R. C. Huxford, J. D. Rocca, W. Lin, *Current Opinion in Chemical Biology*, **2010**, 14, 262
- <sup>69</sup> P. Horcajada, C. Serre, M. Vallet-Regi, M. Sebban, F. Taulelle, G. Férey, *Angew. Chem. Int. Ed.*, **2006**, 45, 5974
- <sup>70</sup> S. Bauer, C. Serre, T. Devic, P. Horcajada, J. Marrot, G. Férey, *Inorg. Chem.*, **2008**, 47, 7568
- <sup>71</sup> K. M. L. Taylor-Pashaw, J. D. Rocca, Z. Xie, S. Tran, W. Lin, *J. Am. Chem. Soc.*, **2009**, 131, 14261
- <sup>72</sup> B. Xiao, P. S. Wheatley, X. Zhao, A. J. Fletcher, S. Fox, A. G. Rossi, I. L. Megson, S. Bordiga, L. Regli, K. M. Thomas, R. E. Morris, *J. Am. Chem. Soc.*, **2007**, 129, 1203
- <sup>73</sup> A. C. McKinlay, B. Xiao, D. Wragg, P. S. Wheatley, I. L. Megson, R. E. Morris, *J. Am. Chem. Soc.*, **2008**, 130, 10440
- <sup>74</sup> N. J. Hinks, A. C. McKinlay, B. Xiao, P. S. Whetaley, R. E. Morris, *Micro. Meso. Mat.*, **2010**, 129, 330
- <sup>75</sup> H. Furukawa, O. M. Yaghi, *J. Am. Chem. Soc.*, **2009**, 131, 8875
- <sup>76</sup> H. M. El-Kaderi, J. R. Hunt, J. L. Mendoza-Cortes, A. P. Cote, R. E. Taylor, M. O'Keefe, O. M. Yaghi, *Science*, **2007**, 316, 268

- <sup>77</sup> A. P. Côté, H. M. El-Kaderi, H. Furukawa, J. R. Hunt, O. M. Yaghi, *J. Am. Chem. Soc.*, **2007**, *129*, 12914
- <sup>78</sup> L. J. Barbour, *Chem. Comm.*, **2006**, 1163
- <sup>79</sup> J. R. Holst, A. Trewin, A. I. Cooper, *Nature Chemistry*, **2010**, *2*, 915
- <sup>80</sup> J. Tian, P. K. Thallapally, B. P. McGrail, *Cryst. Eng. Comm.*, **2012**, *14*, 1909
- <sup>81</sup> G. D. Gutsche, *Calixarenes*, RSC, Cambridge and London, **1989**
- <sup>82</sup> G. D. Andreotti, R. Ungaro, A. Pocchini, *Chem. Commun.*, **1979**, 1005
- <sup>83</sup> P. K. Thallapally, B. P. McGrail, S. J. Dalgarno, H. T. Schaef, J. Tian, J. L. Atwood, *Nat. Mat.*, **2008**, *7*, 146
- <sup>84</sup> P. Sozzani, S. Bracco, A. Comotti, L. Ferretti, R. Simonutti, *Angew. Chem. Int. Ed.*, **2005**, *44*, 1816
- <sup>85</sup> C. Tedesco, T. Immediata, L. Gregoli, L. Vitagliano, A. Immirzi, P. Neri, *Cryst. Eng. Comm.*, **2005**, *7*, 449
- <sup>86</sup> P. K. Thallapally, B. P. McGrail, J. L. Atwood, C. Gaeta, C. Tedesco, P. Neri, *Chem. Mat.*, **2007**, *19*, 3355
- <sup>87</sup> C. Tedesco, L. Erra, M. Brunelli, V. Cipolletti, C. Gaeta, A. N. Fitch, J. L. Atwood, P. Neri, *Chem. Eur. J.*, **2010**, *16*, 2371
- <sup>88</sup> Y. Jin, B. A. Voss, R. D. Noble, W. Zhang, *Angew. Chem. Int. Ed.*, **2010**, *49*, 6348
- <sup>89</sup> Y. Jin, B. A. Voss, A. Jin, H. Long, R. D. Noble, W. Zhang, *J. Am. Chem. Soc.*, **2011**, *133*, 6650
- <sup>90</sup> M. Mastalerz, M.W. Schneider, I. M. Oppel, O. Presly, *Angew. Chem. Int. Ed.*, **2011**, *50*, 1046
- <sup>91</sup> M. W. Schneider, I. M. Oppel, H. Ott, L. G. Lechner, H. J. Hauswald, R. Stoll, M. Mastalerz, *Chem. Eur. J.* **2012**, *18*, 836
- <sup>92</sup> T. Tomokazu, J. T. A. Jones, S. I. Swamy, S. Jiang, D. J. Adams, S. Shakespeare, R. Clowes, D. Bradshaw, T. Hasell, S. Y. Chong, C. Tang, S. Thompson, J. Parker, A. Trewin, J. Bacsá, A. M. Z. Slawin, A. Steiner, A. I. Cooper, *Nat. Mat.*, **2009**, *8*, 973
- <sup>93</sup> J. T. A. Jones, D. Holden, T. Mitra, T. Hasell, D. J. Adams, K. E. Jelfs, A. Trewin, D. J. Willock, G. M. Day, J. Bacsá, A. Steiner, A. I. Cooper, *Angew. Chem. Int. Ed.*, **2010**, *50*, 749

## Chapter 3      Separation of Gases and Vapours

### 3.1 Introduction

The separation of gases and vapours is a major process in the chemical industry, from the separation of hydrocarbons to the production of nitrogen from air. Although cryogenic distillation methods still remain the most dominant separation technique used industrially, adsorptive gas separations using carbon materials and zeolites are becoming increasingly more popular. Adsorptive separation of gases and vapours can occur via three different mechanisms, these are:

- 1) Exclusion of one or more components of the mixture based solely on the size or shape of the adsorbate
- 2) Exclusion of one or more components of the mixture based on the kinetic effects produced by the difference in size or shape
- 3) Exclusion of one or more components of the mixture based on differences in the interaction of the adsorbate with the surface of the porous material<sup>1</sup>

Separation of gaseous or vapour mixtures based on the size or shape of the adsorbate was first utilised industrially in the 1960s using zeolites for the separation of linear hydrocarbons from branched and cyclic isomers. This separation takes advantage of the critical molecular diameter of the branched and cyclic isomers being significantly larger than that of the linear isomers, for example the kinetic diameter of *n*-octane is 0.43nm, which is significantly smaller than the branched isooctane with a kinetic diameter of 0.62nm.<sup>2</sup> This illustrates the simplicity of size exclusion principle, using materials of a fixed pore width; molecules of too large a critical diameter will not diffuse through the aperture, and those with a critical molecular diameter smaller than the pore width will diffuse through, therefore allowing an effective molecular sieve process. True size exclusion separations are rare as typically there is not enough of a difference between the molecular diameters of the components of the mixture.<sup>3</sup> Separations also occur due to the differences in the rates of passage through the apertures into the pores of the material, one or more components of the mixture will adsorb faster into the pores than the other components, resulting in kinetic molecular sieving. Favourable interactions between one or more components of the mixture and the surface of the adsorbent can also lead to separation through the preferential adsorption of the species with the stronger interaction with the

surface, for example the separation of carbon dioxide and methane on metal organic framework MIL-53. Carbon dioxide molecules are adsorbed into the framework, where the interaction of the quadrupole moment of the carbon dioxide with the oxygen atoms of hydroxyl groups lead to a strong interaction. In contrast methane has no specific interactions with the framework, and as such is adsorbed to a lesser extent.<sup>4</sup> There are two specific separation processes which will be investigated during this study, the separation of air and the separation of xylene isomers.

### 3.2 Air Separation

Air separation is widely used in industry as a method to produce nitrogen, oxygen and argon; three of the mostly widely used industrial gases in the world today. It is a highly cost effective process as air is a limitless raw supply. The composition of dry unpolluted air at sea level is shown in **Table 3-1**.

<b>Component</b>	<b>Volume / %</b>
<b>Nitrogen</b>	78.084
<b>Oxygen</b>	20.946
<b>Argon</b>	0.934
<b>Carbon dioxide</b>	0.0360 variable
<b>Neon</b>	0.00182
<b>Helium</b>	0.00052
<b>Methane</b>	0.00016
<b>Krypton</b>	0.00011
<b>Hydrogen</b>	0.00005
<b>Nitrous Oxide</b>	0.00003
<b>Xenon</b>	Trace

**Table 3-1:** Typical composition of unpolluted dry air at sea level<sup>5</sup>

Gaseous nitrogen is primarily utilised as an inert atmosphere, for reactions and processes such as food storage for which oxidation is a damaging process. Liquid nitrogen is a cryogenic liquid, boiling at 77 K therefore allowing uses in freezing and cooling, for example in refrigerating biological samples. Oxygen is used as a respiratory gas in the healthcare system, and also as a major component in the metals production industry. The oxidising properties of oxygen are utilised in rocket fuel

and in other combustion based processes. Argon is a noble gas and is therefore also greatly desired for use as an inert atmosphere. Noble gases are produced as by-products from cryogenic oxygen and nitrogen separation, as argon is the most abundant in the atmosphere it is readily inexpensive, and therefore highly desirable. Argon is also used in welding, in inert atmosphere production and in preserving food.

Industrially there are three major processes for separating air; cryogenic, membrane and adsorptive separation.<sup>6</sup> Cryogenic systems are the dominant industrial process with larger scale systems producing high purity gas. Membrane and adsorptive separations are non-cryogenic and often provide lower purity gases, however they require less space than cryogenic units and as such allow the separation of gases at a lower capital cost.<sup>7</sup>

### 3.2.1 Cryogenic Air Separation

Cryogenic air separation is a process which has been continually developed since its conception by Carl von Linde in the early 20<sup>th</sup> century.<sup>8</sup> A distillation process, cryogenic separation of air relies on the difference in boiling points of the various gaseous components of air. Large volumes of air are taken from the atmosphere and compressed at pressures of up to 10 atm before impurities are removed. Using an adsorbent bed, impurities such as water and carbon dioxide; which would freeze later in the cooling process; and hydrocarbons, are removed. The purified and compressed air is then cooled using a heat exchanger.<sup>9</sup> The compressed, purified and cooled air is then fed into a distillation column, separating the major components, as shown in **Figure 3-1**.

Additional distillation columns are added to separate argon from the gases found in the mid-section of the distillation column.<sup>9</sup> Although the nitrogen produced by cryogenic air separation is very high purity, the process itself incurs a high capital cost due to the utility requirements and the large on-site space required for the distillation tower. The size of the system does not allow effective scalability, so although cryogenic separation is effective for large scale high purity nitrogen production, it is often too large and of too high a capital cost for small scale on-site production of nitrogen.<sup>10</sup>

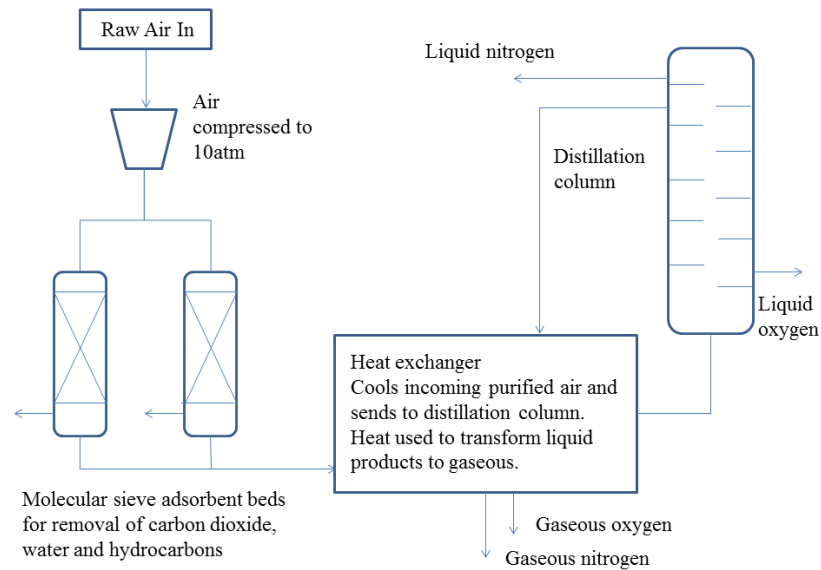


**Figure 3-1** Simplified flow diagram of a cryogenic air separation system<sup>9</sup>

### 3.2.2 Membrane Separation

Industrial separation of air by using membrane technology was first introduced by the company Generon in the 1980s.<sup>11</sup> There are a number of materials which are utilised as membranes for air separation, including carbon molecular sieves, zeolites and mixed-matrix materials.<sup>12</sup> Air separation using a membrane is based on the difference in permeation rates of the individual components of air through the particular membrane. The first polymer membranes developed allowed the generation of nitrogen with purity greater than 99%.<sup>13</sup> For a material to be efficient as a membrane separator, it must have suitable permeability and selectivity – attributes which can be tailored for the desired separation – and must have the ability to form stable and thin membranes.<sup>11</sup> For the rate of permeation to be maximised, the selective layer of the membrane must be extremely thin, 0.5 – 0.1  $\mu\text{m}$  or even thinner. This allows the formation of thin fibres, which increases the surface area to volume ratio and therefore giving a more economic process. Often the very thin films must be supported on another porous material to withstand the operating pressure of the membrane system.<sup>7</sup> The fibres can be kept as flat sheets or as hollow fibres, as shown in **Figure 3-2**. Multiple hollow fibres can be combined to form a membrane module, maximising surface area to volume for maximum economic gain.

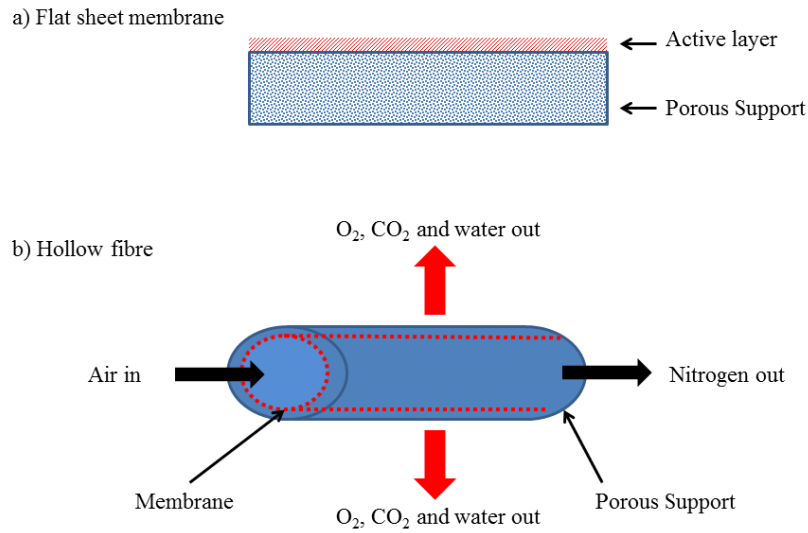


**Figure 3-2** Membrane construction a) flat sheet membrane b) hollow fibre membrane

Similar to the cryogenic systems, air is first compressed and filtered through a molecular sieve adsorbent bed to remove carbon dioxide, water and hydrocarbons. The compressed, purified air is then passed through the membrane, as depicted in **Figure 3-3**, to produce an enriched air stream. Producing pure nitrogen through membrane separations is relatively easy, as air already contains 80% nitrogen and it is a matter of allowing small volumes of oxygen to permeate through the membrane. Often nitrogen also partially permeates the membrane with the oxygen and argon, and as such it is difficult to produce pure oxygen by this method, and typically only oxygen-enriched air is produced. Producing pure oxygen by membrane separation is still a challenging field of research. In comparison with cryogenic systems, the near ambient conditions and smaller scale system leads to lower capital cost, but produces lower purity nitrogen. Membrane separation technology cannot produce nitrogen on the large scale that cryogenic systems are capable of, and membranes currently are only utilised in nitrogen production, not oxygen or argon production.<sup>11</sup>

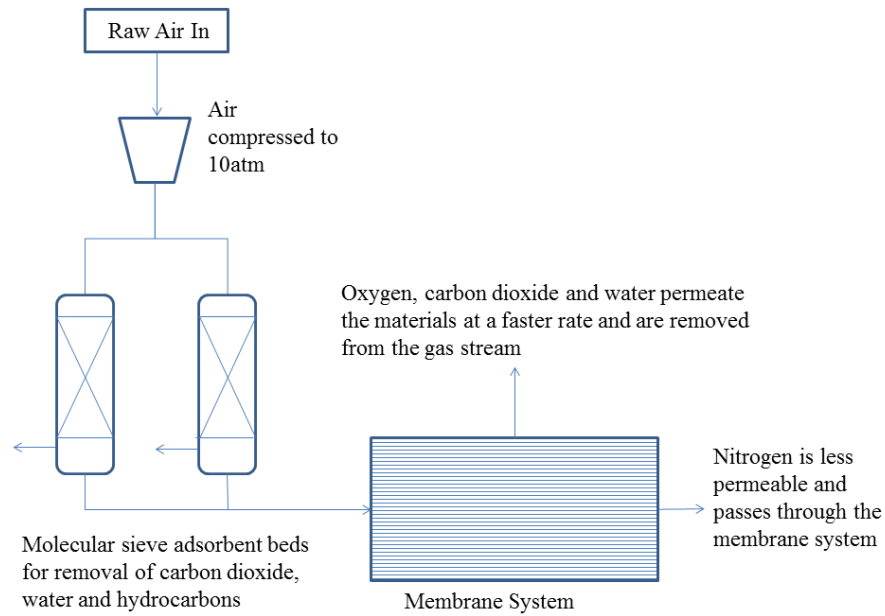


**Figure 3-3** Simplified flow diagram of a membrane air separation system<sup>10</sup>

### 3.2.3 Separation by Adsorption Technology

There are a number of materials which are utilised as adsorbents for commercial air separation, including activated carbon, carbon molecular sieves, zeolites, aluminas and silica gels. The availability of such a wide range of adsorbents, with a wide range of pore volumes, structures and pore size distribution, and the ability to use these materials in the design of novel separation processes has led to a large amount of research into their potential applications in the separation industry. Activated carbons are a leading material in gas separation technologies along with zeolites. The varying precursors, methods of production and methods of activation lead to a large variety of activated carbons, which can be tailored to specific separation processes. Carbon molecular sieves, a class of activated carbon, are used for commercial scale air separation.<sup>14</sup>

#### 3.2.3.1 Pressure Swing Adsorption

Pressure swing adsorption (PSA) was first introduced by Skarstrom in 1960.<sup>15</sup> The basic pressure swing adsorption system contains two adsorbents beds, typically containing either carbon molecular sieve or zeolite, depending on which gas is required as the main product. Air is compressed and pre-filtered and a valve controls the flow of the air into one of the adsorbent beds, where the adsorbed component is



removed from the air stream. The adsorbent bed is then regenerated by lowering the partial pressure of the system to remove the adsorbed species. While the first adsorbent bed is being regenerated, the valve directs the air flow to the second bed, so a continuous feed process is created. A simplified flow diagram of this process is shown in **Figure 3-4**.

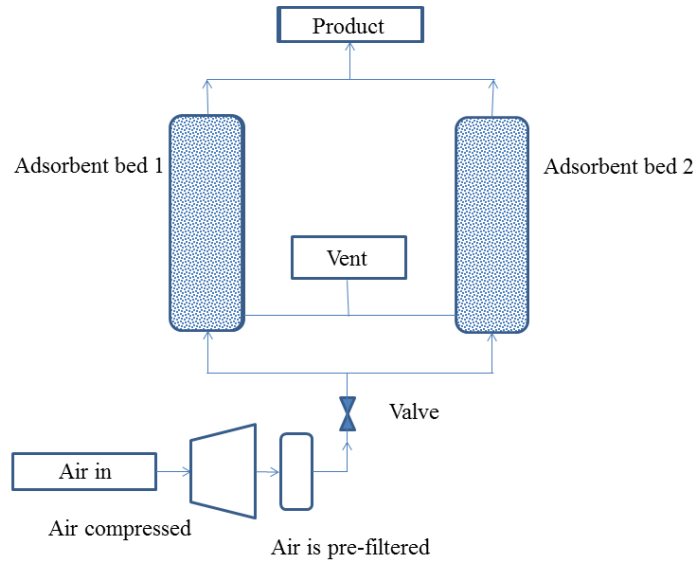


**Figure 3-4** A simplified flow sheet of a pressure swing adsorption process<sup>16</sup>

Pressure swing adsorption is a well-developed method used industrially to separate nitrogen from air. A subset of pressure swing adsorption, vacuum swing adsorption (VSA) is used to produce oxygen from air.

### Nitrogen Production

In the pressure swing adsorption process to produce nitrogen, carbon molecular sieves make up the adsorbent bed. Carbon molecular sieves contain pores which have a size of a similar order of magnitude to that of the molecules in air. The slightly smaller oxygen molecules are adsorbed at a faster rate into the cavities of the carbon molecular sieve than nitrogen making this a kinetically selective separation.<sup>17</sup> The selectivity has been previously explained by the difference in kinetic diameter of oxygen and nitrogen, (3.46 and 3.64 Å, respectively). However, it is more likely that the molecular width of these molecules (2.8 and 3.0 Å, respectively) is the rate determining factor into the adsorption of these molecules into the slit shaped pore of

carbon materials. Oxygen and nitrogen have similar thermodynamic properties, so after time there will be equal amounts of both gases adsorbed into the system, therefore the separation is a time-dependant process. Oxygen adsorbs at  $114 \times 10^{-4} \text{ s}^{-1}$ , whereas nitrogen adsorbs approximately twenty five times slower at  $3.23 \times 10^{-4} \text{ s}^{-1}$  at 293 K and 99 kPa, leading to 80% adsorption of oxygen within the first few minutes of exposure, but only 5% adsorption of nitrogen.<sup>18</sup> Pressure swing adsorption processes have a lower capital cost than cryogenic processes for nitrogen production, but there is a limit in the scalability to large scale productivity as more adsorbent beds would need to be added to the process, subsequently increasing the capital cost.<sup>9</sup> A comparison of techniques for nitrogen production is shown in **Figure 3-5**.

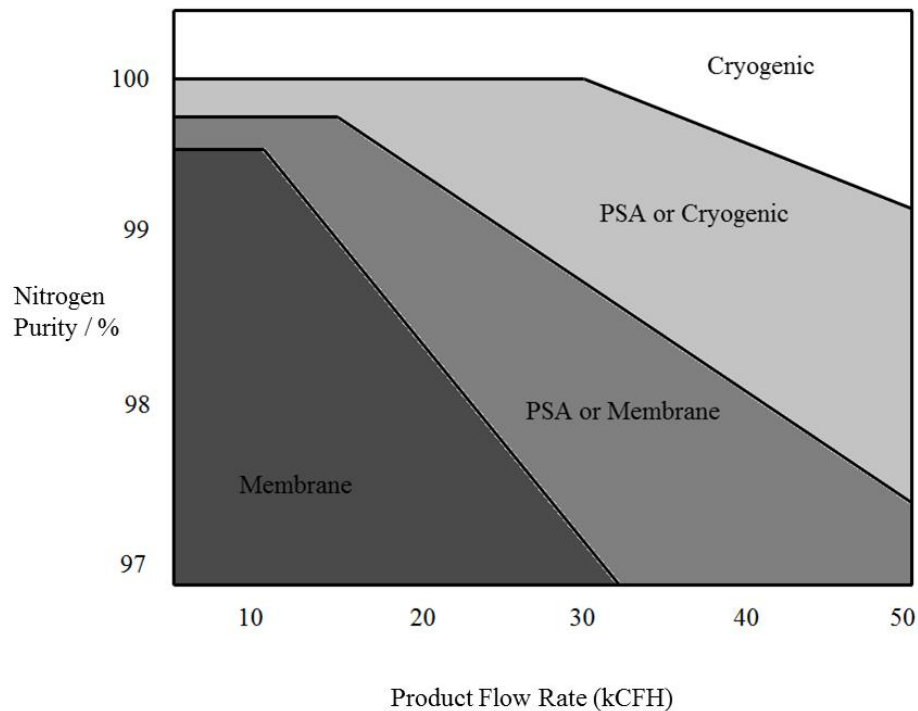


**Figure 3-5** Comparison of cryogenic, PSA and membrane technology<sup>19</sup>

Pressure swing adsorption processes produce higher purity nitrogen than membrane technology, but not as a high purity as that produced by cryogenic processes.

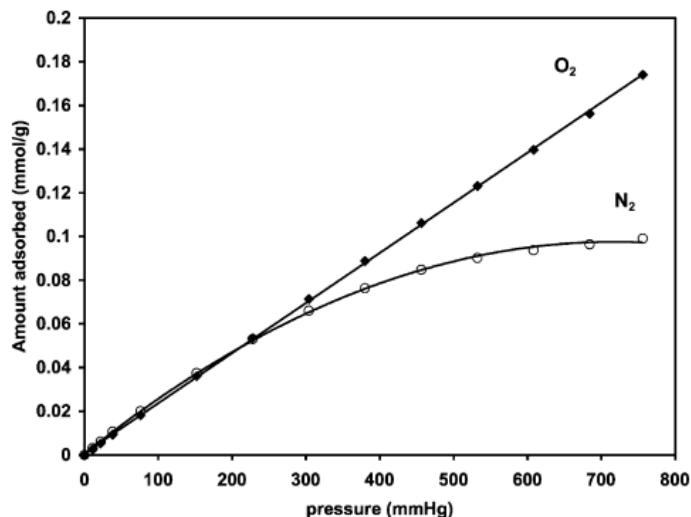
### Oxygen Production

In the vacuum swing adsorption process to produce oxygen, zeolites are utilised in the adsorbent bed due to their equilibrium selectivity for the adsorption of nitrogen over oxygen and argon.<sup>20</sup> The selectivity for nitrogen arises from the interaction of

the quadrupole in nitrogen with the electric field generated inside the zeolite pores formed by the presence of cations.<sup>21</sup> Vacuum swing adsorption operates in a similar way to pressure swing adsorption, the difference is that while pressure swing adsorption regenerates the adsorbent bed at atmospheric pressure, vacuum swing adsorption has an additional vacuum stage to more completely purge the adsorbent bed.<sup>22</sup> Synthetic zeolites are typically used in oxygen production. Zeolites A (LTA) and X (FAU) and Y (FAU) have all previously been used, with cations such as sodium, calcium and lithium present in the pores.<sup>23</sup> The choice of zeolite and cation can improve the ability to adsorb nitrogen; lithium cations in zeolite X have showed a significant improvement over zeolite X with sodium cations.<sup>24, 25</sup>

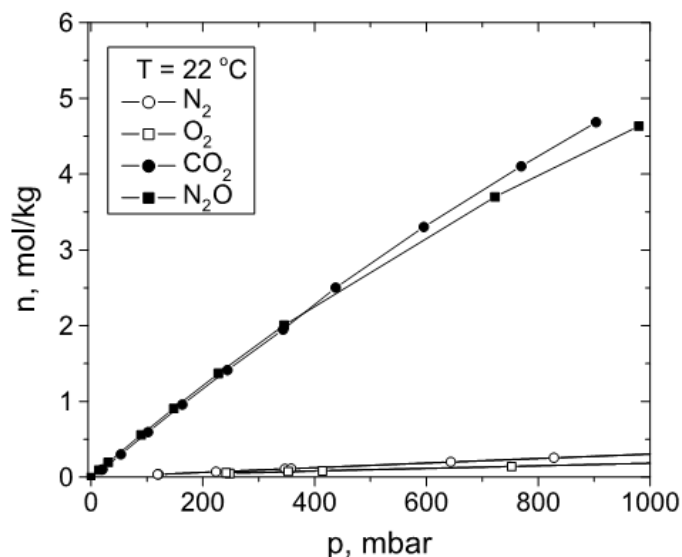
### 3.2.3.2 Air Separation Using Metal Organic Frameworks

Metal organic frameworks have been utilised in a number of gas separations, including separating methane and carbon dioxide, carbon dioxide capture and some exploration into removal of other toxic and environmentally hazardous compounds.<sup>26</sup> MOF-177  $Zn_4O(1,3,5\text{-benzenetricarboxylate})_2$  has been shown to preferentially adsorb oxygen over nitrogen at low pressures and at 298 K as shown in **Figure 3-6**, with unique behaviour. As shown in the isotherms the oxygen uptake is linear with pressure whereas the nitrogen plateaus in a Type 1 isotherm shape, showing that oxygen is adsorbed more favourably on the framework at higher pressure. Traditionally separation isotherms display the same shape and uptake for oxygen and nitrogen separation on carbon molecular sieves. This difference in uptake volume at low pressure indicates that a larger separation factor would be seen at higher pressure, allowing the possibility of using this metal organic framework in the production of nitrogen at high pressure.<sup>27</sup> Separation of air by the adsorption of oxygen is more desirable as oxygen is less abundant, so less work would be required to remove it from the air stream.



**Figure 3-6:** Nitrogen and oxygen adsorption isotherms on MOF-177 at 298 K.<sup>27</sup>

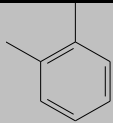
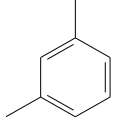
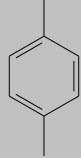
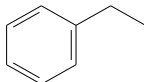
Cu-BTC (copper (II) benzene-1,3,5-tricarboxylate) is a 3D porous metal organic framework which has shown preferential adsorption of nitrous oxide and carbon dioxide over both nitrogen and oxygen at 295 K, as shown in **Figure 3-7**.<sup>28</sup> Although not suitable for direct separation of oxygen and nitrogen, this material could be readily utilised in an air pre-purification unit such as the ones found within a cryogenic separation system.



**Figure 3-7:** N<sub>2</sub>O, CO<sub>2</sub>, O<sub>2</sub> and N<sub>2</sub> adsorption isotherms on Cu-BTC at 295 K<sup>28</sup>

3.3 Xylene Separation

Xylene is the collective term for a mixture of several C<sub>8</sub> alkyl aromatic hydrocarbons including *o*-xylene, *m*-xylene, *p*-xylene and traces of ethyl benzene as an impurity. The mixed xylenes are produced from crude oil, via the catalytic reforming of petroleum naphtha. The structures of each isomer and some data are given in **Table 3-2**. The *p*-xylene constituent of the mixed xylenes is the most important in industry, where it is used to form purified terephthalic acid, which is a major component in the polyester production chain. The major growth in demand for polyester is currently in Asia, where it is used in textile production, and in Europe and North America where polyethylene terephthalate (PET) industry is growing to meet demand for resins for soft drinks and mineral water bottles. *O*-xylene is the next most important xylene isomer used in industry. The major use of *o*-xylene is in the manufacture of phthalic anhydride, which is used to make plasticisers and resins, the largest demand for which is to make poly vinyl chloride (PVC) resins. *M*-xylene is used to produce isophthalic acid, which can be used in PET resin blends and ethyl benzene is used to obtain styrene.

Xylene	Structure	Boiling Point	Melting Point
<i>o</i> -xylene		144.4°C	-24°C
<i>m</i> -xylene		139.1°C	-48°C
<i>p</i> -xylene		138.4°C	13°C
Ethyl benzene		136.2°C	-95°C

**Table 3-2:** Xylene isomers: structures and data<sup>29</sup>

### 3.3.1 Industrial Separation of Xylenes

The major challenge in industrial processes is the separation of these isomers. *O*-xylene can be separated by fractional distillation, as it has a higher boiling point, however, fractional distillation cannot separate *p*- and *m*-xylene due to the similarity in boiling point.<sup>30</sup> Currently in industry there are two methods employed to separate *p*-xylene from the xylene mixtures, *fractional crystallisation* and *adsorption*. Fractional crystallisation constitutes 40% of industrial *p*-xylene production, whereas adsorption methods constitute 60% of *p*-xylene production.<sup>31</sup> In fractional crystallisation, the variation in melting points of the xylene isomers leads to the separation of *p*-xylene. The mixture is cooled to -75°C at which point the *p*-xylene precipitates as a crystalline solid, as this has the highest melting point.<sup>32</sup>

There are multiple adsorption methods which have been developed to separate *p*-xylene, such as the Universal Oil Products (UOP) Parex process,<sup>33</sup> Toray's Aromax<sup>34</sup> and IFP's Eluxyl process.<sup>35</sup> These processes use a solid ion exchanged Faujasite zeolite adsorbent which is shape selective for *p*-xylene over the other xylene isomers. The adsorbed *p*-xylene is then removed by displacement by a desorbent, such as toluene or *p*-diethyl benzene, at purities above 99.7%.<sup>36</sup> The adsorption processes are based on a Simulated Moving Bed (SMB) separation,<sup>37</sup> which uses a continuous counter current flow of the liquid phase adsorbate against the solid phase adsorbent bed. As it would be technically difficult to physically move the solid bed of adsorbent, the continuous flow is simulated by periodically moving the position of the inlet stream (which consists of the feed and the desorbent) and the outlet stream (consisting of the high purity *p*-xylene and the remaining fluid raffinate). The three processes all differ in the way that the inlet and outlet streams are rotated. A simplified flow diagram of the Parex process is shown in **Figure 3-8**.

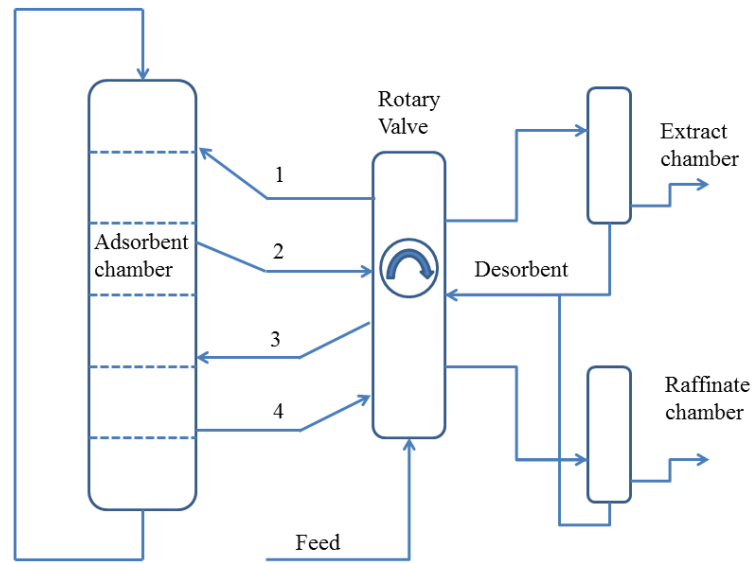


**Figure 3-8:** A simplified flow sheet of the UOP Parex simulated moving bed (SMB) xylene separation process

1 = desorbent feed 2 = extract 3 = mixed feedstock 4 = raffinate (gas stream with adsorbed component removed)

### 3.3.2 Separation of Xylenes Using Metal Organic Frameworks

Several metal organic frameworks have been shown to selectively adsorb one of the constituents of the mixture of xylene isomers and ethyl benzene. MIL-47 and MIL-53 have been extensively investigated by Alaerts *et al.*<sup>38,39</sup> MIL-47 is a 3D microporous framework consisting of infinite chains of  $V^{4+}O_6$  octahedra linked together with terephthalate linkers to produce one-dimensional diamond shaped channels.<sup>40</sup> Analysis of xylene separation is conducted by breakthrough experiments.

During breakthrough experiments, a known concentration of adsorbent is flowed in a carrier gas through a hollow tube which has been packed with adsorbent. A concentration front is formed which moves down the packed bed, and due to the kinetics of adsorption, the shape of the front will change. The concentration front eventually breaks through the edge of the bed, and a plot of relative vapour or gas concentration leaving the bed against time is produced. Keeping the concentration and carrier gas flow constant and assuming adsorption occurs by physisorption, an s-shaped breakthrough curve will be produced. From this curve the amount of gas or

vapour adsorbed can be calculated through integration over time, and the shape of the curve can give an indication about the kinetics of adsorption.

Through breakthrough, Finsy *et al* have shown that MIL - 47 selectively adsorbs *p*-xylene over *m*-xylene due to the more efficient packing of *p*-xylene into the porous structure of the framework at a lower energy cost in comparison to *m*-xylene.<sup>41</sup> Finsy *et al* and Loiseau *et al* showed the separation of ethyl benzene and ortho xylene using the aluminium analogue of MOF-53.<sup>39,42</sup> MIL-53 is constructed of chains of  $\text{AlO}_4(\text{OH})_2$  octahedra held together by terephthalate linkers, giving a three dimensional polymer with one dimensional diamond shaped channels. Experimentally it is shown that within the contracted form there is a single line arrangement of guests, as the gateway pressure is reached, the uptake doubles within a very small pressure window, showing the molecules reorganising into a paired row. This is shown in **Figure 3-9**.

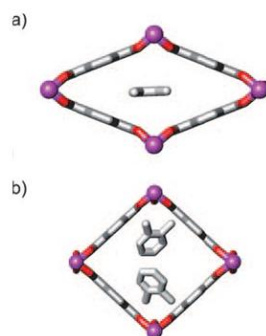


**Figure 3-9:** a) the contracted form of MIL-53, containing a single row of *o*-xylene  
 (b) the reformed form of MIL-53 containing two rows of *o*-xylene<sup>39</sup>

This effect is strongest for ortho xylene, as this has the strongest interaction with the framework at full occupancy, as both methyl groups can interact with the framework. The results of these initial adsorption experiments were tested by performing breakthrough experiments, showing that at a pressure of 0.056 bar complete separation of *o*-xylene and ethyl benzene was achieved, with pure ethyl benzene eluted from the column.

Both of these materials show that pore filling effects have an impact on the adsorption potential and selectivity of the metal organic frameworks. This was also shown by Nicolau *et al* in their investigation into the vapour phase separation of the xylene isomers on MOF-1  $[\text{Zn}(\text{BDC})(\text{Dabco})_{0.5}]$ , where BDC = benzene



### Chapter 3 Separation of Gases and Vapours

dicarboxylate and Dabco = 1,4-diazabicyclo[2.2.2]octane.<sup>43</sup> Preferential adsorption of *o*-xylene was observed over *m*-xylene and *p*-xylene due to more favourable interactions and therefore more efficient packing of the *o*-xylene molecules within the porous framework.

The separation characteristics as well as the stability, and cost of the materials are all major factors in the application of these new materials in commercial separations.

3.4 References

- <sup>1</sup> R. T. Yang, *Gas Separation by Adsorption Process*, Butterworths, Boston, **1987**
- <sup>2</sup> H. H. Funke, M. G. Kovalchick, J. L. Falconer, R. D. Noble, *Ind. Eng. Chem. Res.*, **1996**, 35, 1575
- <sup>3</sup> D. M. Ruthven, *Chemie Ingenieur Technik.*, **2011**, 83, 44
- <sup>4</sup> V. Finsy, L. Ma, L. Alaerts, D. E. De Vos, G. V. Baron, J. F. M. Denayer, *Microp. Mesop. Mater.* **2009**, 120, 221
- <sup>5</sup> P. Brimblecombe, *Air Composition and Chemistry*, Cambridge University Press, **1986**
- <sup>6</sup> Air Products online air properties database 03/10/2012  
<http://www.airproducts.com/products/gases.aspx>
- <sup>7</sup> R. M. Thorogood, *Gas. Sep. Pur.*, **1991**, 5, 83
- <sup>8</sup> R. Agrawal, R. M. Thorogood, *Gas. Sep. Pur.*, **1991**, 5, 203
- <sup>9</sup> W. F. Castle, *Int. Journal. Refridge.* **2002**, 25, 158
- <sup>10</sup> A. R. Smith, J. Klosek, *Fuel Process. Tech.* **2001**, 70, 115
- <sup>11</sup> R. W. Baker, *Ind. Eng. Chem. Res.*, **2002**, 41, 1393
- <sup>12</sup> P. Bernardo, E. Brioli, G. Golemme, *Ind. Eng. Chem. Res.*, **2009**, 48, 4638
- <sup>13</sup> E. Sanders, D. O. Clark, J. A. Jensvold, H. N. Beck, G. G. Lipscomb, F. L. Coan, *Patent*, US, 4772392, **1988**
- <sup>14</sup> S. Sircar, T. C. Golden, M. B. Rao, *Carbon*, **1996**, 34, 1
- <sup>15</sup> C. W. Skarstrom, *Patent*, US, 2944627, **1960**
- <sup>16</sup> A. M. M, Mendes, C. A. V. Costa, A. E. Rodrigues, *Sep. Purif. Tech.*, **2001**, 24, 173
- <sup>17</sup> T. R. Gaffney, *Solid State and Materials Science*, **1996**, 1, 69
- <sup>18</sup> I. P. O'Koye, M. Benham, K. M. Thomas, *Langmuir*, **1997**, 13, 4054
- <sup>19</sup> W. J. Koros, G. K. Fleming, *J. Membrane. Tech.*, **1993**, 83, 1
- <sup>20</sup> G. Reiss, *Gas Sep. and Purif.*, **1994**, 8, 95
- <sup>21</sup> D. W. Breck, *Zeolite Molecular Sieves*, Wiley, New York, **1974**

- <sup>22</sup> Z. Budner, J. Dula, W. Podstawa, A. Gawdzik, *I. Chem. E.*, **1999**, 77, 405
- <sup>23</sup> M. W. Ackley, S. U. Rege, H. Saxena, *Microp. Mesop. Mater.*, **2003**, 61, 25
- <sup>24</sup> A. Jayaraman, R. T. Yang, *Adsorption*, **2002**, 8, 271
- <sup>25</sup> S. Yoshida, N. Ogawa, K. Kamioka, S. Hirano, T. Mori, *Adsorption*, **1999**, 5, 57
- <sup>26</sup> S. T. Meek, J. A. Greathouse, M. D. Allendorf, *Adv. Mater.*, **2011**, 23, 249
- <sup>27</sup> Y. Li, R. T. Yang, *Langmuir*, **2007**, 23, 12937
- <sup>28</sup> Q. M. Wang, D. Shen, M. Bulow, M. L. Lau, S. Deng, F. R. Fitch, N. O. Lemcoff, J. Semanscin, *Microp. Mesop. Mater.*, **2002**, 55, 217
- <sup>29</sup> D. Ruthven, *Principles of Adsorption and Adsorption Processes*, Wiley, New York, **1984**
- <sup>30</sup> R. Meyers, *Handbook of Petroleum Refining Processes 3<sup>rd</sup> Edition*, McGraw-Hill, New York, 203
- <sup>31</sup> M. Minceva, A. E. Rodrigues, *AIChE. J.*, **2007**, 53, 138
- <sup>32</sup> H. A. Mohameed, B. A. Jdayil, K. Takrouri, *Chem. Eng. Proc.*, **2007**, 46, 25
- <sup>33</sup> D. B. Broughton, R. W. Neuzil, J. M. Pharis, C. S. Brearley, *Chem. Eng. Proc.*, **1970**, 66, 70
- <sup>34</sup> S. Otani, T. Iwamura, K. Sando, M. Kanaoka, K. Matsumura, S. Akita, T. Yamamoto, I. Takeuchi, T. Tsuchiya, Y. Noguchi, T. Mori, *Patent*, US, 3761533, **1973**
- <sup>35</sup> G. Ash, K. Barth, G. Hotier, L. Mank, P. Renard, *Revue de l'Institut Francaise du Pétrole*, **1994**, 49, 541
- <sup>36</sup> C.L. Cavalcante, *Latin American Applied Research*, **2000**, 30, 357
- <sup>37</sup> D. B. Broughton, C. G. Gerhold, *Patent*, US, 2985589, **1961**
- <sup>38</sup> L. Alaerts, C. E. A. Kirschhock, M. Maes, M. A. Van der Veen, V. Finsy, A. Depla, J. A. Maten, G. V. Baron, P. A. Jacobs, J. F. M. Denayer, D. E. De Vos, *Angew. Chem. Int. Ed.*, **2007**, 46, 4293
- <sup>39</sup> V. Finsy, C. E. A. Kirschhock, G. Vedts, M. Maes, L. Alaerts, D. E. De Vos, G. V. Baron, J. F. M. Denayer, *Chem. Eur. J.*, **2009**, 15, 7724
- <sup>40</sup> K. Barthelet, J. Marrot, D. Riou, G. Férey, *Angew. Chemie., Int. Ed.*, **2002**, 41, 281

### Chapter 3 Separation of Gases and Vapours

<sup>41</sup> V. Finsy, H. Verelst, L. Alaerts, D. De Vos, P. A. Jacobs, G. V. Baron, J. F. M. Denayer, *J. Am. Chem. Soc.*, **2008**, *130*, 7110

<sup>42</sup> T. Loiseau, C. Serre, C. Huguenard, G. Fink, F. Taulelle, M. Henry, T. Bataille, G. Férey, *Chem. Eur. J.* **2004**, *10*, 1373

<sup>43</sup> M. P. M. Nicolau, P. S. Bárcia, J. M. Gallegos, J. A. C. Silva, A. E. Rodrigues, B. Chen, *J. Phys. Chem. C.*, **2009**, *113*, 13173

## Chapter 4      Research Objectives

### 4.1 Overall Objectives

The overall objectives of this research are to evaluate porous materials synthesised by the research groups led by Professors M. J. Rosseinsky and A. I. Cooper at Liverpool University. The porous materials to be evaluated include a metal organic framework and a new branch of porous materials – porous organic cages. Initial porous structure characterisation will be conducted followed by the evaluation of the materials with regard to gas separation properties and in the case of the porous organic cages, also the evaluation of the structural response upon exposure to certain organic vapours.

### 4.2 Metal Organic Framework $Zn_2(TBAPy)(H_2O)_2$

#### 4.2.1 Porous Characterisation

- To characterise the porous structure of the framework using carbon dioxide adsorption at 195 K and 273 K including pore volume and surface area determination

#### 4.2.2 Separation of Xylene Isomers

- To evaluate the adsorption of *p*-xylene adsorption on the framework, including thermodynamic and kinetic analysis
- To evaluate the adsorption of *m*-xylene adsorption on the framework, including thermodynamic and kinetic analysis
- To compare the kinetic analysis of *p*- and *m*- xylene adsorption on the framework to evaluate the ability of the framework to separate the xylene isomers on a kinetic basis
- To evaluate the powder X-ray diffraction data by sealing samples of  $Zn_2(TBAPy)(H_2O)_2$  in capillaries at set vapour pressures

### 4.3 Molecular Organic Cage Materials

#### 4.3.1 Porous Characterisation

- To characterise the porous structure of the Cage 1 $\alpha$  using carbon dioxide adsorption at 195 K and 273 K including pore volume and surface area determination

## Chapter 4 Research Objectives

- To characterise the porous structure of the Cage 1 $\beta$  using carbon dioxide adsorption at 195 K and 273 K including pore volume and surface area determination

### 4.3.2 Structural Responses Induced by Vapour Adsorption

- To investigate the structural response of Cage 1 $\beta$  upon exposure to various organic vapours
- To investigate the structural rearrangement of Cage 1 $\beta$  to Cage 1 $\alpha$ # upon exposure to ethyl acetate and methyl acetate
- To determine the kinetics of adsorption for ethyl acetate and methyl acetate on Cage 1 $\beta$  – including investigation of the kinetics of the unprecedented mass loss during adsorption
- To determine the isosteric enthalpy and entropy of adsorption of methyl acetate adsorption for the structural rearrangement of Cage 1 $\beta$  to Cage 1 $\alpha$ #
- To determine the kinetics of adsorption of methyl acetate on Cage 1 $\alpha$ #
- To determine the isosteric enthalpy and entropy of adsorption for methyl acetate adsorption on Cage 1 $\alpha$ #
- To investigate the structural rearrangement cycle of Cage1 $\beta$   $\rightarrow$  Cage1 $\alpha$   $\rightarrow$  Cage1 $\beta$   $\rightarrow$  Cage 1 $\alpha$  through exposure to methyl acetate and dichloromethane

### 4.3.3 Gas Separation

- To compare the kinetics of adsorption of oxygen and nitrogen on Cage1 $\alpha$
- To determine the isosteric enthalpy of adsorption of oxygen and nitrogen on Cage 1 $\alpha$
- To compare the kinetics of adsorption of oxygen and nitrogen on Cage1 $\alpha$ #
- To determine the isosteric enthalpy of adsorption of oxygen and nitrogen on Cage 1 $\alpha$ #
- To compare the kinetics and isosteric enthalpy of adsorption of oxygen and nitrogen on Cage 1 $\alpha$  and Cage1 $\alpha$ #

Chapter 5      Experimental5.1 Materials Used5.1.1 Porous Materials5.1.1.1 Porous Organic Cages

Cage 1 was supplied by Professor Andrew Cooper, University of Liverpool. The synthetic method was as follows: ethyl acetate (35mL) was added to 1,3,5 triformylbenzene (50 mg, 0.31 mmol) in a vial at room temperature. After 5 minutes a solution of ethylene diamine (28 mg, 0.47 mmol) in ethyl acetate (5mL) was added. The resulting mixture was left covered for 60 hours with no stirring or heating. A turbid solution was observed to form within 5 minutes after the ethylene diamine solution was added to the partially dissolved trialdehyde. This was followed by precipitation of a solid after around 5 – 6 hours, and finally, pale white needles of cage 1 were observed to crystallise from solution after around 60 hours. The product obtained was a mixture of needle like crystals which formed on the sides of the reaction vial (major component) and a thin layer of amorphous material on the base of the vial (minor component). The crystals were removed from the side of the flask using a spatula without disturbing the amorphous layer; they were washed with ethyl acetate then air dried to give the ethyl acetate solvate of cage 1. Cage 1 crystallises as Cage 1 $\alpha$ •2.5EtOAc. To desolvate cage 1, the sample was heated to 373 K for 6 hours under a dry nitrogen flow, and was then evacuated at 353 K for 6 hours to give an isolated yield of 35%.<sup>1</sup> To convert between the various polymorphs, a “vial in vial” technique of vapour diffusion was utilised, where the unconverted polymorph was placed in a small vial, which was then placed in a larger vial containing the organic trigger molecule for each conversion. The large vial was then sealed and left at room temperature for three days.<sup>1</sup>

5.1.1.2 Metal Organic Framework Zn<sub>2</sub>(TBAPy)(H<sub>2</sub>O)<sub>2</sub>

Zn<sub>2</sub>(TBAPy)(H<sub>2</sub>O)<sub>2</sub> was supplied by Dr Kyriakos Stylianou, University of Liverpool. The synthetic method was as follows: Zn(NO<sub>3</sub>)<sub>2</sub>•6H<sub>2</sub>O (9 mg, 0.030 mmol) and H<sub>4</sub>TBAPy (10 mg, 0.015 mmol) were suspended in DMF followed by the addition of dioxane and H<sub>2</sub>O in a ratio of 2:1:1 respectively and 10  $\mu$ L HCl, and the resulting yellow solution was sonicated for 10 minutes. The resulting yellow suspension was heated to 120°C for 72 hours in a 12 mL sealed vial before cooling to 30°C at a rate

of 0.2 °C/min. The resulting yellow block crystals were filtered and washed with 10 mL of the same mixture of solvents used for the synthesis.<sup>2</sup>

### 5.1.2 Organic Vapours and Gases

Organic liquids used for vapour adsorption were supplied by Sigma Aldrich. The properties of these materials are listed in **Table 5-1**. Nitrogen (99.9995% purity), carbon dioxide (99.999% purity) and oxygen (99.9995% purity) were supplied by BOC, UK. The properties of these gases are listed in **Table 5-2**.

**Table 5-1:** Properties of the organic vapours used<sup>3,4</sup>

	<b>Purity</b> / %	<b>Boiling</b> <b>Point</b> <b>(initial)</b> / °C	<b>Melting</b> <b>Point /</b> <b>°C</b>	<b>Relative</b> <b>Density (at</b> <b>298K) / g</b> <b>cm<sup>-3</sup></b>	<b>Flash Point</b> <b>(closed cup)</b> / °C	<b>Molar Mass</b> / g mol <sup>-1</sup>
<b>Ethyl</b> <b>Acetate</b>	99.99	76.5	-84.0	0.9020	-3.00	88.12
<b>DCM</b>	99.99	40.0	-97.0	1.32	-	84.93
<b>Methyl</b> <b>Acetate</b>	99.99	57.0	-98.0	0.9340	-13.0	74.08
<b>Pentane</b>	99.99	35.0	-130.0	0.6260	-49.0	72.15
<b>2-butanone</b>	99+	80.0	-87.0	0.805	-3	72.11
<b>Diethyl</b> <b>ether</b>	99+	34.6	-116.0	0.706	-40.0	74.12
<b>Methanol</b>	99.8	64.7	-98	0.791	9.7	32.04
<b><i>p</i>-xylene</b>	99+	138.00	12.00	3.7000	27.00	106.16
<b><i>m</i>-xylene</b>	99+	138	48.00	3.7000	27.00	106.16



**Table 5-2:** Properties of the gases used<sup>3</sup>

	<b>Nitrogen</b>	<b>Carbon Dioxide</b>	<b>Oxygen</b>
<b>Molecular Weight / g mol<sup>-1</sup></b>	28.0134	44.01	31.99
<b>Melting Point / °C</b>	-209.86	-56.6	-219
<b>Liquid Density / kg m<sup>3</sup></b>	808.607	1032	1141
<b>Boiling Point / °C</b>	-195.8	-78.5	-183
<b>Critical Temperature / °C</b>	-147	31	-118.6
<b>Critical Pressure / bar</b>	33.999	73.825	50.43
<b>Critical Density / kg m<sup>3</sup></b>	314.03	464	436.1
<b>Gas Density / kg m<sup>3</sup></b>	4.614	2.814	4.475

### 5.1.3 Saturated Vapour Pressure ( $P^0$ ) Calculation

The saturation vapour pressure is the pressure at which the vapour is in equilibrium with its non-vapour phase, which is specific at a given temperature.

This is calculated using the Antoine equation<sup>5</sup>:

$$\log_{10}P = A - \frac{B}{T+C} \quad 5.1$$

Where:

$P^0$  = saturated vapour pressure (mmHg)

$T$  = temperature (°C)

$A$ ,  $B$  and  $C$  = constants for each adsorbate

The saturated vapour pressure can also be calculated using Yaws Equation:

$$\log P = \frac{A-B}{T} + C \log T + DT + ET^2$$

Where:

$P^0$  = saturated vapour pressure (mmHg)

$T$  = temperature (°C)

$A$ ,  $B$ ,  $C$ ,  $D$ , and  $E$  = constants for each adsorbate

This was used for carbon dioxide adsorption with the parameters as follows,  $A = 35.0169$   $B = -1511.9$   $C = -11.334$   $D = 0.0093368$   $E = 1.7136 \times 10^{-9}$ .

The Antoine equation coefficients for the various adsorbates used in this study are given in **Table 5-3**.

**Table 5-3:** Antoine equation coefficients for gases and organic compounds<sup>6</sup>

<b>Adsorbate</b>	<b>Temperature Range, K</b>	<b>A</b>	<b>B</b>	<b>C</b>
<b>Nitrogen</b>	77 - 370	6.49457	255.68	266.550
<b>Oxygen</b>	54 – 155	6.83706	339.209	268.702
<b>Ethyl Acetate</b>	190 – 523	7.25963	1338.46	228.608
<b>Dichloromethane</b>	178 – 510	7.11464	1152.41	232.442
<b>Methyl Acetate</b>	175 - 507	7.28036	1276.29	233.155
<b>Pentane</b>	144 - 470	7.00877	1134.15	237.678
<b>2-butanone</b>	188 – 535	7.20103	1325.15	227.093
<b>Diethyl ether</b>	156 - 467	7.04631	1112.55	232.657
<b>Methanol</b>	175 – 512	8.09126	1582.91	239.096
<b>p-xylene</b>	286 – 616	7.15471	1553.95	225.23
<b>m-xylene</b>	226 – 616	7.18115	1573.02	226.671

5.2 Gas and Vapour Adsorption Studies

5.2.1 Intelligent Gravimetric Analyser (IGA)

The Intelligent Gravimetric Analyser (IGA) was used to complete all sorption studies. The IGA utilises an ultra-high vacuum system which allows the determination of the mass change of a sample as it is exposed to gases or vapours at set pressure increments. A photograph of one of the five IGAs available in the Wolfson Northern Carbon Reduction Laboratories is shown in **Figure 5-1**.



**Figure 5-1:** One of several IGAs available in the Wolfson Northern Carbon Research Laboratories

A photograph of the internal layout of the IGA cabinet is shown in **Figure 5-2**.

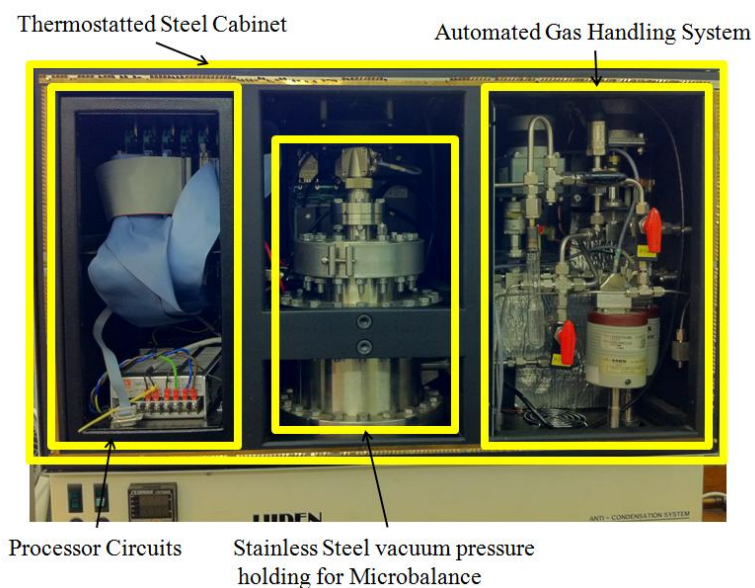


**Figure 5-2:** Internal view of IGA cabinet

## Chapter 5 Experimental

The gas handling system allows the entry of gases and vapours into the system through several valves; it houses the pressure transducers and the glass vapour reservoir. Three pressure transducers control the admitted gas/vapour pressure. The transducers have individual pressure ranges of 0-0.2 kPa, 0-10 kPa, and 0-0.1 MPa for IGA 3, while IGA 1 can reach a maximum pressure of 1 MPa. A more detailed diagram of the automated gas handling system is shown in **Figure 5-3**.

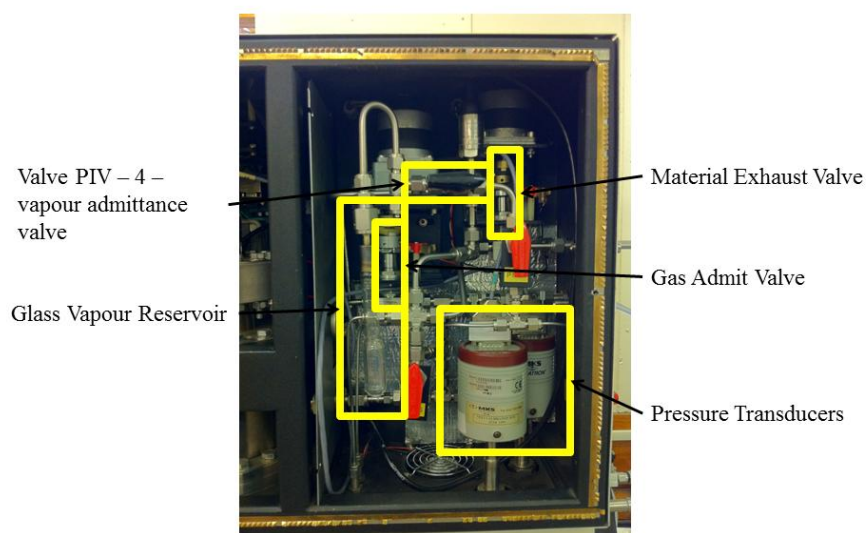


**Figure 5-3:** Automated gas handling system

The IGA is a computer controlled system which allows the simultaneous measurement and control of four processes: mass change, pressure regulation and two temperature regulation systems. Each of these processes is controlled, and data is acquired, through an integral dedicated microcomputer, using parameters and algorithms that can be controlled by the user interface in the IGA software.

5.2.1.1 Microbalance System

The mass change is measured by balance head movement. A schematic representation of the microbalance system is shown in **Figure 5-4**.

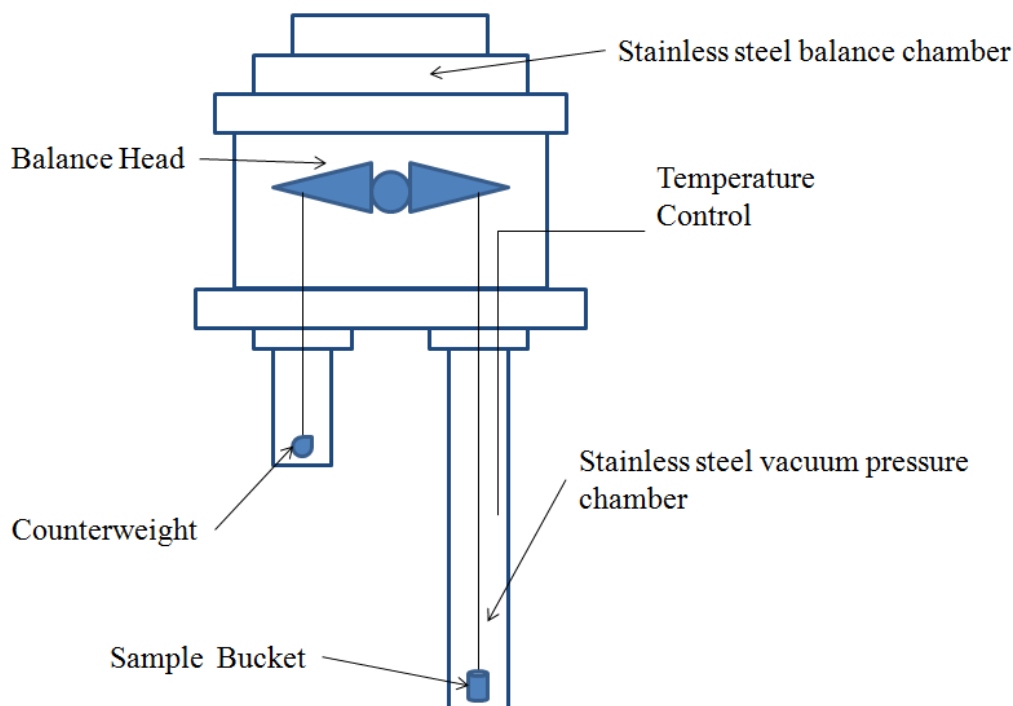


**Figure 5-4:** Schematic representation of IGA microbalance system

The system includes a balance head, which is balanced by the counterweight and the sample bucket. The microbalance has a total capacity of 5g, with 200 mg range. It has a long term stability of  $\pm 1\mu\text{g}$  and a weighing resolution of  $0.2\mu\text{g}$ . The weighing head consists of a moving coil galvanometer, with a taut band phosphor-bronze suspension and a balance beam, which is constructed from fine aluminium tubes, which have a through-beam infra-red sensing system which detects changes in balance beam position. When any change in position is detected by the infra-red sensors, the IGA computer system passes a current through the moving coil galvanometer to readjust the balance beam to the “null” position. The current needed to maintain the balance head at the null position is proportional to the weight applied by adsorption of gas or vapour. A more detailed schematic of the IGA microbalance head is shown in **Figure 5-5**.

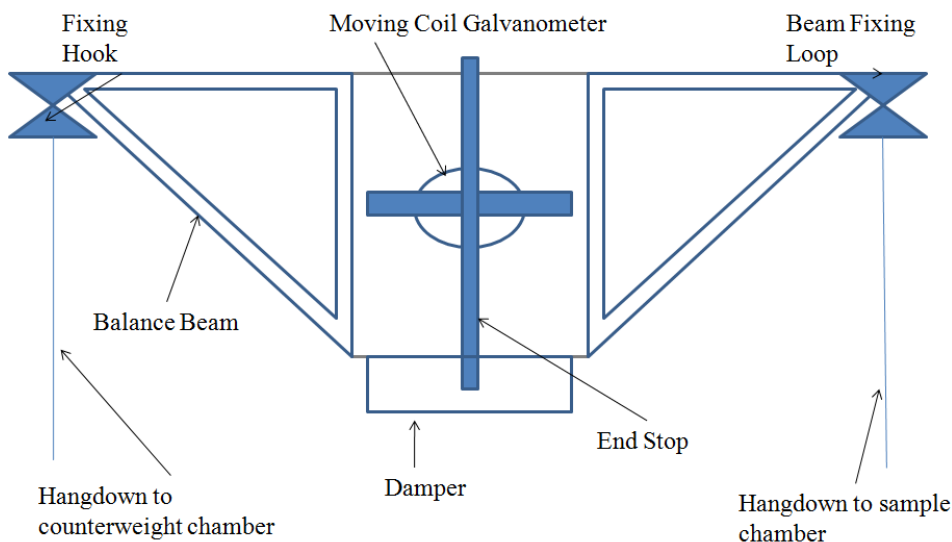


**Figure 5-5:** Schematic representation of IGA microbalance head<sup>7</sup>

The mass increase at set pressure increments was recorded by the software to produce the isotherm. The mass increase was also monitored as a function of time. The real-time processing uses non-linear least squares regression analysis to determine estimates of kinetic parameters during the adsorption/desorption process.<sup>8</sup> After the mass is equilibrated at a set pressure, the software moves the system on to the next pressure step - recording each step as a kinetic profile. The equilibrated mass value is recorded as an isothermal point. This is shown in **Figure 5-6**.

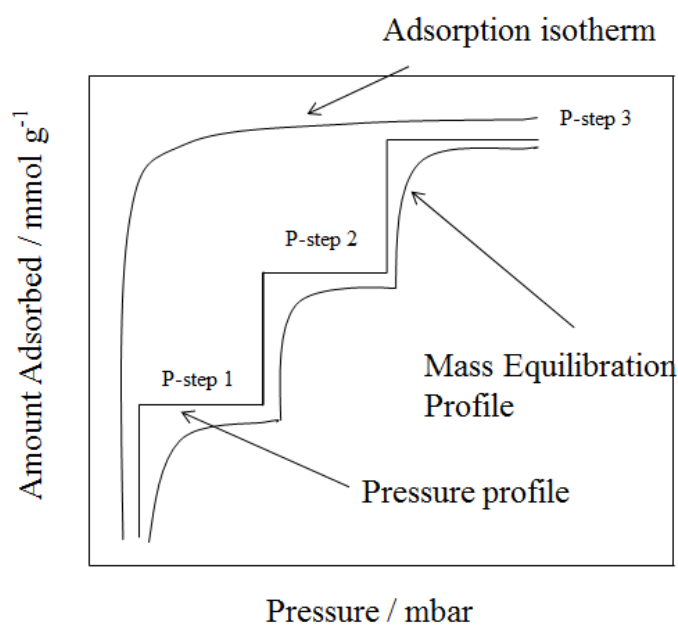


**Figure 5-6:** Typical adsorption isotherm and kinetic mass profiles

5.2.1.2 Pressure Regulation

The regulation of pressure is controlled by the IGA software algorithms. The software controls the motion of admit and exhaust valves within the automated gas handling system. These Swagelok valves are adjusted by the software using high resolution stepping motors. An example of this type of valve is shown in **Figure 5-7**.

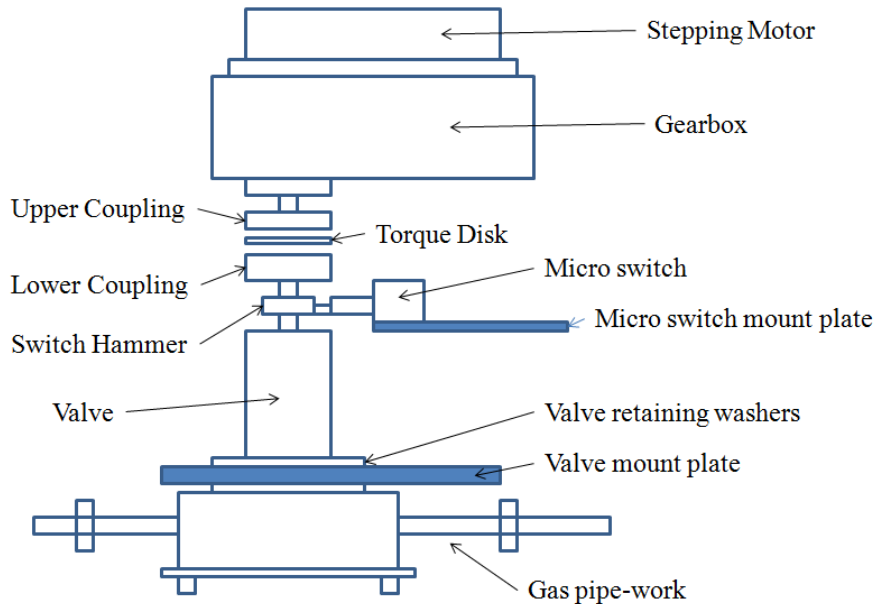


**Figure 5-7:** Schematic representation of an IGA gas admit/exhaust valve<sup>7</sup>

The computer algorithms control the stepping motor, which turns the upper and lower coupling and torque disk. This in turn rotates the switch hammer, the algorithm registers the valve as closed when the switch hammer rotates around and shuts the micro switch. The pressure controller operates over a wide range of differential pressure (the difference between the admit pressure and the system pressure). The controller can be adjusted within the software by manipulation of the proportional – integral – derivative (PID) controller process control inputs. The most important control inputs with typical values in parenthesis are: the Admit gain (4 – 6), which controls the approach to pressure set point; the Admit valve integral acceleration (0.1 – 1), which integrates the area between the set point line and the pressure set and controls the pressure once the set point is reached; the crack cycle (6 – 18) and regulation cycles (6 – 18) which control the opening of the Admit valve and the rotation limit (60 – 180 degrees), which controls the maximum angle to which the Admit valve will open. For vapours the rotation limit is usually set at a

maximum of 180 degrees. It is important to produce a good pressure set, as this allows good kinetic profiles to be obtained. Examples of good and poor pressure sets are shown in **Figure 5-8**. Adjustment of parameters helps to keep the system regulated and avoid overshoot.

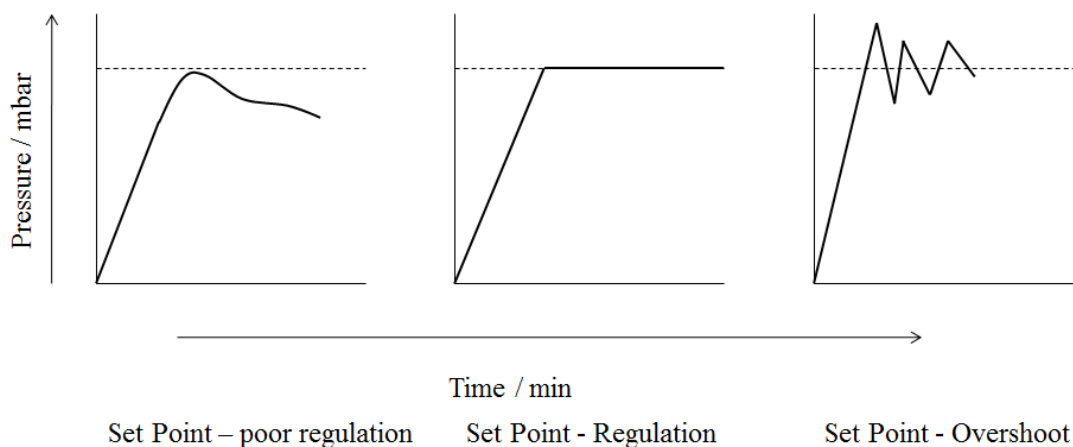


**Figure 5-8:** Pressure set point regulation

### 5.2.1.3 Temperature Control

#### Thermo-stirrers/ Cryostats / Furnaces

Thermo-stirrers and cryostats were used to control the temperature set point of the isotherm, allowing isotherms to be gathered at a variety of temperatures. Thermo-stirrers are typically an RM 6 Lauda analogue water bath, which circulates a 1:1 mixture of ethylene glycol and water. The water bath was used to set temperatures from  $-5^{\circ}\text{C}$  to  $60^{\circ}\text{C}$ . Cryostats consist of a glass-lined Dewar filled with substances to set cooler temperatures. For experiments conducted at 195 K a Dewar of dry ice and acetone was used, typically for carbon dioxide adsorption; for 77 K a Dewar was filled with liquid nitrogen, typically used for nitrogen and hydrogen adsorption. The Dewar was wrapped in a suitable insulating material and kept at 95% capacity with cooling substance as required throughout the isothermal run. Furnaces were used to bring the sample to the higher outgas temperatures to remove any volatile substances held within the porous structure, to an accuracy of  $\pm 0.3^{\circ}\text{C}$ . The sample temperature was monitored by a thermocouple 5 mm above the sample inside the steel sample chamber.



### Thermal Regulation

The thermo regulator was used to circulate air at a constant temperature around the IGA cabinet, regulating the temperature of all temperature – sensitive devices such as the microbalance. In conjunction with the anti-condensation system the thermo regulator can be used to increase range of pressure and temperature which is available to certain vapours. The air temperature was monitored using a platinum resistance thermometer and controlled also using a PID controller and a miniature fan heater to an accuracy of  $\pm 0.01^\circ\text{C}$ .

#### 5.2.1.4 Typical Experimental Procedure

A schematic diagram of the gas inlet/outlet system for the IGA is shown in **Figure 5-9**.

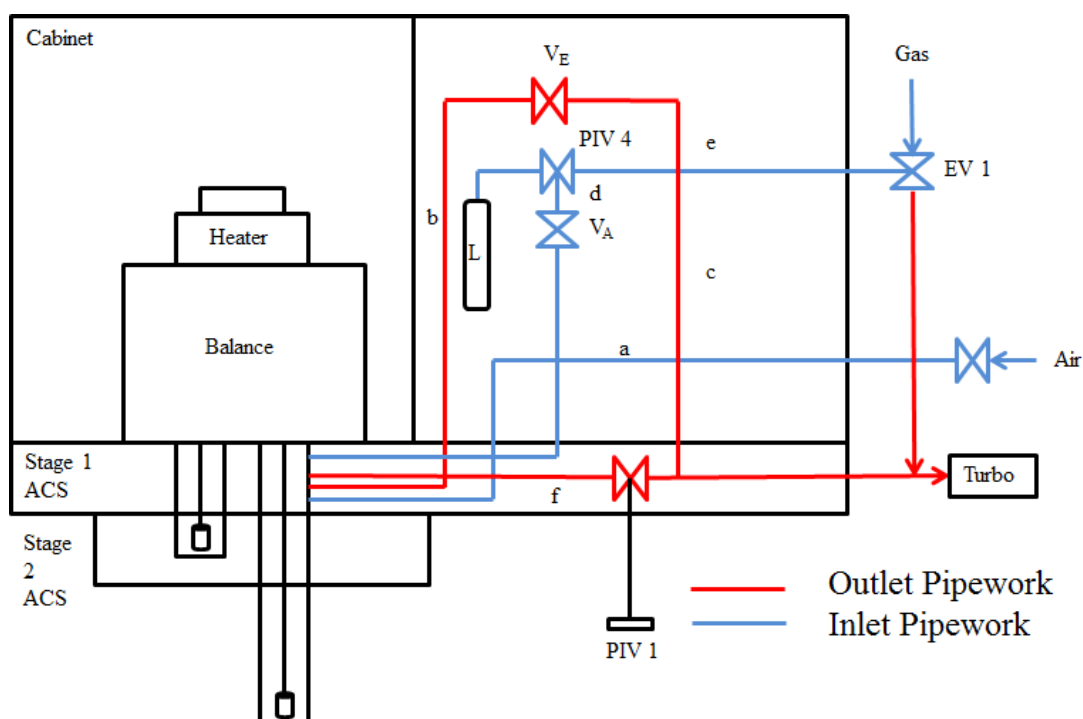


**Figure 5-9:** Schematic diagram of inlet/outlet system for gas and vapour adsorption experiments

$V_A$  – Automated Gas Admit Valve: 1/4" Swagelok connection to the computer controlled valve allowing gas/vapour into the system

$V_E$  – Automated Gas Exhaust Valve: 1/4" Swagelok connection to the computer controlled valve removing gas/vapour from the system

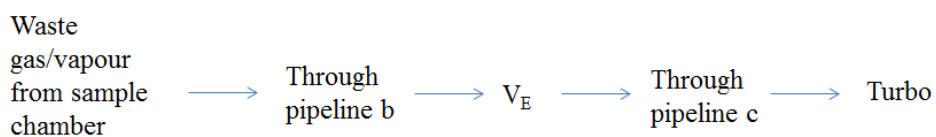
## Chapter 5 Experimental

EV1 - *External Vacuum Bleed Valve*: Switches at the automated gas admit valve between gas supply from external gas cylinders and the vacuum pump. Connection to the vacuum pump allows the decontamination of the admit pipework

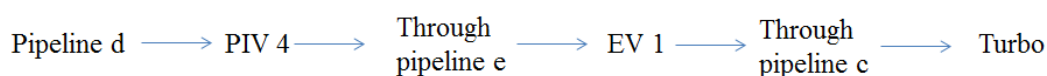
PIV 4 – *Reservoir Isolation Valve*: Switches between the vapour reservoir and the gas admittance pipework. When pointing left vapour from the reservoir is admitted to the system, when pointing right gas from the external supply is admitted to the system, when pointing upwards the system is isolated from any vapour or gas inlet

PIV 1 – *Vacuum-Pressure Isolation Valve*: Isolates the sample chamber from direct exposure to the vacuum pump. Can be slowly opened to allow an improved vacuum within the chamber

To begin an adsorption experiment, the system was first brought to atmospheric pressure by allowing air into the system using the air admit valve and pipeline a. Once pressure was at atmospheric (~1000 mbar) the steel vacuum pressure chamber was removed, any old sample disposed of and a new sample loaded. Empty sample bucket mass measurements were taken before each new sample loading to reset the “null” position of the balance beam. After the sample was loaded, the steel vacuum vessel was replaced and the system degassed. The degassing procedure removed any volatile substances from the pores of the material and removed any residual gas or vapour from the internal pipework of the IGA. To outgas the sample the following pipework system was used:

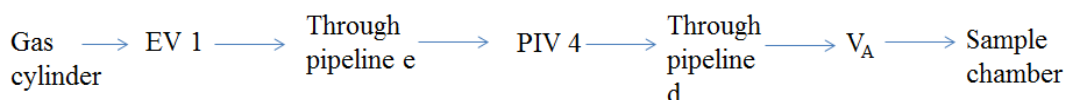


To outgas the internal pipework the following system was used:

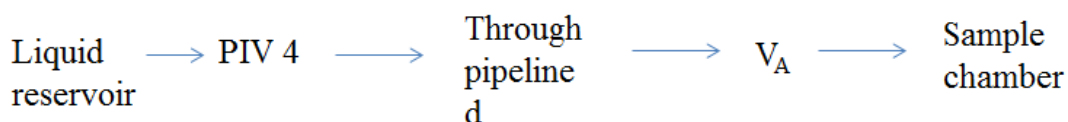


Once the pressure inside the sample chamber was below 1 mbar, valve PIV 1 was opened to expose the sample directly to the turbo pump. Outgassing at  $\times 10^{-6}$  Pa was sustained for each sample while heating was conducted. Typically samples were heated at 120°C for > 5 hours, or until a stable mass profile was obtained. At this point the samples were fully outgassed and prepared for adsorption studies. This outgas procedure was followed after every adsorption isotherm experiment to ensure all adsorbed gases from previous experiments were removed from the sample and the pipework. The experimental temperature was then set using either the water bath or Dewar containing cooling liquid.

For gas adsorption experiments, gas was introduced into the sample chamber from a cylinder via the following system:



For vapour experiments, vapour was introduced into the sample chamber via:



#### 5.2.1.5 Vapour Adsorption

Liquid adsorbate is injected into a glass reservoir using a pipette; the reservoir is then attached to the IGA within the automated gas handling section. The temperature within the IGA cabinet is held high enough to induce vapour formation from the liquid within the reservoir. The liquid in the reservoir is fully degassed using a procedure known as “blocking and bleeding” to remove any air from the liquid. In the first step, “blocking”, the vapour reservoir is isolated from the rest of the system by turning the vapour admit valve to the vacuum. This evacuates the internal pipework up to the gas admit valve. In the next step, “bleeding”, the vapour admit valve

is turned to the reservoir, so it is open to the internal pipe-work, and vapour formation is induced to fill the vacuum found within the internal pipe-work.

### 5.2.1.6 Capillary Experiments

Glass capillaries of diameter 0.3, 0.5 and 0.7mm (supplied from Capillary Tube Supplies Ltd.) were used to seal a sample at a set pressure and vapour/gas loading, so as to assess changes to the structure of the material induced by pressure and vapour exposure. The IGA sample chamber was modified to include a valve and outlet for a capillary connection. The capillary connection was sealed with Apiezon W hard wax vacuum sealant, and vacuum tested to ensure that the system was leak free. The capillary adaptation is shown in **Figure 5-10**.

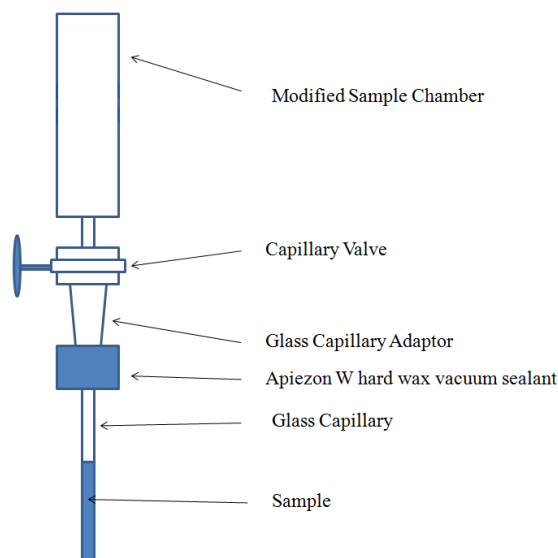


**Figure 5-10:** Capillary adaptor

The sample is outgassed as normal, using a water bath to achieve high temperatures, then vapour / gas is admitted at a set pressure, the pressure and mass is left for a pre-determined time from previous isotherms to ensure equilibration, the capillary is then sealed using a hydrogen/oxygen mix fine welding torch.

## 5.2.2 Additional Experimental Methodologies

### 5.2.2.1 Thermal Gravimetric Analysis

The Thermal Gravimetric Analysis machine used is a Stanton Redcroft STA 780 thermo-balance, which consists of an electronic microbalance with a hang down suspended down to the centre of a furnace, cooled by a water jacket. Thermal gravimetric analysis is used to determine the thermal stability of samples.

Approximately 10 mg of sample is needed to determine thermal stability. The sample is loaded into a ceramic bucket, the furnace is raised around the sample and heated at 5°C/min to temperatures of typically 500°C under a constant flow of nitrogen (50cm<sup>3</sup> min<sup>-1</sup>), while mass loss is recorded by computer software. A typical TGA analysis plot is shown in **Figure 5-11**.

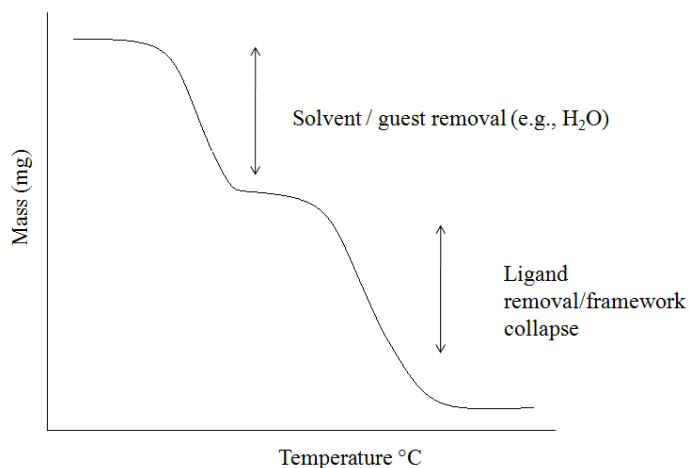


**Figure 5-11:** Typical TGA profile

#### 5.2.2.2 Scanning Electron Microscopy

Size and sample morphology were obtained using a scanning electron microscope JEOL 5300 LV fitted with Rontec and Si (Li) energy dispersive X-ray detector (EDX). Both detectors were cooled by liquid nitrogen. The EDX instrument was run with an operating voltage of 25 kV under vacuum for qualitative elemental analysis. The samples were coated with gold and imaged with secondary electrons in high vacuum mode. This analysis was carried out by the Materials Analytical Unit, Newcastle University.

#### 5.2.2.3 Fourier Transform Infrared (FTIR) Spectroscopy

FTIR spectra were collected across the wavelength range 400 – 4000 cm<sup>-1</sup> for samples of Cage 1β, Cage 1α and Cage 1α#. Spectra were collected on a Digilab SCIMITAR series FTIR Spectrometer in the Department of Chemistry, Newcastle University. A small amount of powder (~2mg) was placed on the disc press assembly for analysis. Samples were analysed for 16 scans with a resolution of 4cm<sup>-1</sup>.

### 5.2.2.4 Single Crystal X-ray Diffraction

X-ray diffraction data for the analysis of the single crystals of both the metal organic framework and the cages were completed at Liverpool University. Single crystal structures were collected on a Bruker D8 diffractometer using MoK $\alpha$  radiation. The crystal structures were solved with Direct Methods and refined with full-matrix least squares regression using SHELX.<sup>1</sup>

### 5.2.2.5 Powder Diffraction

All powder X-ray diffraction data was collected by researchers at Liverpool University.

The Zn (TBAPy) MOF samples loaded with xylene were analysed by powder X-ray diffraction collected in transmission using a STOE Stadi-P diffractometer with CuK $\alpha$  radiation at 298 K.<sup>2</sup>

The Cage materials powder X-ray diffraction analysis was carried out on a PANalytical X'pert pro multi-purpose diffractometer in transmission Debye-Scherrer geometry with a Cu anode.<sup>1</sup>

### 5.2.3 Error Analysis

Random errors may occur within the IGA measurements, such as small changes in pressure which the IGA is not sensitive enough to control. These errors appear as numerical values when a model is used to describe the dataset.

The  $\pm$  errors on calculated parameters are generated from the standard error of the fit of the models to the raw data gathered from the IGA experiments. They are at first calculated from parameters obtained from the fit of either the linear regression (such as Langmuir or DR analysis) or the curve fitting (such as kinetic analysis), and propagated through the calculations of the various stated values or parameters through combining the uncertainty for each step in the calculation.

How far the models used to analyse the kinetic profiles vary from the original data points is displayed as residuals underneath each kinetic point. The model is considered a good fit if the residuals are less than 4% and acceptable fit will have residuals up to 10%. Above that the model does not provide an accurate description of the raw data and cannot be used.

5.3 References

- <sup>1</sup> J. T. A. Jones, D. Holden, T. Mitra, T. Hasell, D. J. Adams, K. E. Jelfs, A. Trewin, D. J. Willock, G. M. Day, J. Bacsa, A. Steiner, A. I. Cooper, *Angew. Chem. Int. Ed.*, **2010**, *50*, 749
- <sup>2</sup> K. C. Stylianou, J. Rabone, S. Y. Chong, R. Heck, J. Armstrong, P.V. Wiper, K. E. Jelfs, S. Zlatogorsky, J. Bacsa, A. G. McLennan, C. P. Ireland, Y. Z. Khimiyak, K. M. Thomas, D. Bradshaw, M. J. Rosseinsky, *J. Am. Chem. Soc.*, **2012**, *134*, 20466
- <sup>3</sup> [www.sigmaaldrich.com/MSDS](http://www.sigmaaldrich.com/MSDS) November **2012**
- <sup>4</sup> *CRC Handbook of Chemistry and Physics*, 74<sup>th</sup> Edition, CRC Press, Boca Ratan, FL, **1993**
- <sup>5</sup> *Lange's Handbook of Chemistry*, 15<sup>th</sup> Edition, McGraw – Hill, New York, **1999**
- <sup>6</sup> L. C. Yaws, P.K. Narasimhan, C. Gabbula, *Yaws' Handbook of Antoine Coefficients for Vapour Pressure*, (2nd Electronic Edition), Knovel, **2009**
- <sup>7</sup> IGA Systems Guide, Hiden Analytical, **1996**
- <sup>8</sup> M. J. Benham, D. K. Ross, *Z. Phys. Chem. Neue Folge*, **1989**, *163*, 25

## Chapter 6      Xylene Separation by Zn(TBAPy) 1' Metal Organic Framework

### 6.1 Introduction

A metal organic framework has been synthesised in which flexibility is produced though changing the structural dimensions from two dimensional to three dimensional by the reconfiguration of paddlewheel units. The material was synthesised by Dr Kyriakos Stylianou in the Rosseinsky research group at Liverpool University. The metal organic framework is based on zinc metal centres and a pyrene based ligand functionalised with benzoate fragments. The initial structure produced is a two dimensional layered structure, Zn(TBAPy) 1, and upon desolvation the layers cross link to form a three dimensional framework Zn(TBAPy) 1'. The compound contains the pyrene based ligand TBAPy (1,3,6,8,-tetrakis(p-benzoic acid) pyrene (**Figure 6-1**).

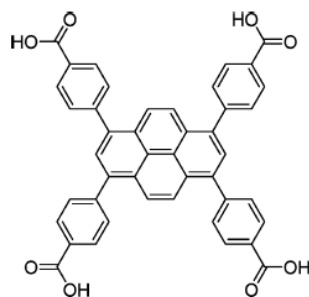


**Figure 6-1:** Structure of the fluorophore ligand TBAPy (1,3,6,8,-tetrakis(p-benzoic acid) pyrene)

The pyrene core of this molecule is a fluorophore, and has been previously shown in indium based frameworks to rotate around the benzoate functional groups to allow framework distortion and the fluorescent properties are shown to be guest responsive.<sup>1</sup> On adsorption of toluene,  $\pi - \pi$  stacking effects were also observed, showing strong interaction between the toluene and pyrene. The synthesis of Zn(TBAPy) 1 was outlined in **Chapter 5 – Experimental.**<sup>2</sup>

### 6.2 Crystal Structure of Zn(TBAPy) 1

The pyrene ligands attach to the two zinc metal centres to form a paddlewheel motif, with square based pyramidal coordination geometry, as shown in **Figure 6-2 (a)**. The carboxylate groups of four TBAPy ligands are attached in the equatorial plane of the square pyramidal geometry, with a water molecule attached in the axial position.



This allows the formation of two distinct channels within the framework as shown in **Figure 6-2 (b)**, where the channels including the axial water molecule are hydrophilic and the channel lined by the pyrene ligands are hydrophobic.

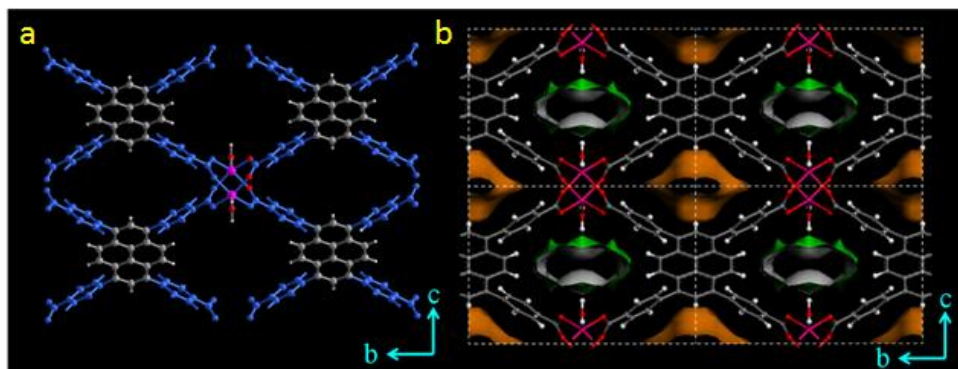


**Figure 6-2:** (a) Coordination of four different TBAPy ligands around Zn paddlewheel units (b) View along *a*-axis showing that the stacking of the 2D layered framework affords a porous network with the formation of two types of pores; the hydrophilic in which coordinated H<sub>2</sub>O molecules reside within this channel (green) and the hydrophobic (orange). Image provided by Dr D. Bradshaw (Liverpool University).

### 6.3 Structural Transformation from Zn(TBAPy) 1 to Zn(TBAPy) 1'

The structural transformation of Zn(TBAPy) 1 to Zn(TBAPy) 1' was noticed after stability of Zn(TBAPy) 1 was evaluated by outgassing for 12 hours at 110°C under dynamic vacuum ( $10^{-6}$  mbar). The colour of the crystals change from pale yellow to dark yellow, PXRD indicated a less crystalline material was formed, with SEM images showing an apparent delaminating of crystals after desolvation. In order to establish the exact nature of the structural changes, extensive molecular dynamics simulations were completed. The simulations indicate that the zinc metal centres undergo a coordination geometry change, from square pyramidal to tetrahedral upon the loss of the axial water molecule. The loss of the axial water molecule forces the formation of a four coordinate zinc complex which then forces the formation of the more sterically stable tetrahedral coordination sphere. The proposed mechanism for this change then leading to the formation of a three dimensional framework relies upon the flexibility of the benzoate fragments attached to the pyrene ligand. Cleavage of one zinc-carboxylate bond allows the rotation of the benzoate fragment,

allowing the formation of a bond between zinc atoms in adjacent layers of the paddlewheel unit. This criss-crossing of layers leads to the formation of the three dimensional framework. The reorientation of the ligands and the distortion of the framework lead to two different sized pores – one circular and one ellipsoid. Both of these pores are now hydrophobic due to the loss of the axial water molecule. The channel dimensions are 9.0 and 8.0 Å (circular channel) and 5.8 and 5.3 Å (ellipsoidal channel). Due to the specific size and shape of the channels in Zn(TBAPy) 1', and the nature of the ligand used, the adsorption properties of the sample when exposed to xylene isomers was investigated. This separation is a major industrial separation and it is outlined in **Chapter 3 – Separation of Gases and Vapours**. The dimensions of *m*-xylene and *p*-xylene are given in **Table 6-1**.

**Table 6-1:** Molecular dimensions of *m*-xylene and *p*-xylene in Å<sup>3</sup>

	<i>x</i>	<i>y</i>	<i>z</i>	MIN-1	MIN-2
<i>m</i> -xylene	8.994	3.949	7.315	3.949	7.258
<i>p</i> -xylene	6.618	3.810	9.146	3.810	6.618

**Table 6-1** gives the molecular dimensions of the xylene molecules along the *x*, *y* and *z* symmetry axis of the molecule. MIN-1 and MIN-2 are the minimum dimensions determined by rotating the molecules to find the axis which represents the minimum distance through the molecule. MIN-1 and MIN-2 are the dimensions which determine the entry into the pore. A slit shaped pore will require only MIN-1 as the limiting dimension. A cylindrical pore will rely upon two dimensions to allow entry of the molecule. Due to the meta- position of the methyl groups in *m*-xylene, as shown in **Figure 6-3**, *m*-xylene has larger MIN-1 and MIN-2 values.

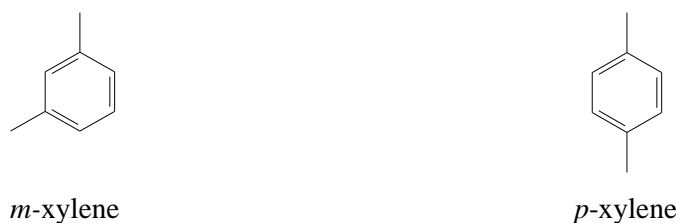


**Figure 6-3:** Structure of *m*-xylene and *p*-xylene

The MIN-1 values for both xylene isomers are similar, with *m*-xylene being slightly larger. The ellipsoidal channels in Zn(TBAPy) 1' are 5.8 and 5.3 Å, which are larger than the MIN-1 dimensions. The MIN-2 dimension of 7.258 for *m*-xylene

approaches the dimensions of the circular channel (9.0 and 8.0 Å), which could lead to the slower adsorption of *m*-xylene into the circular pores. The shape of *p*-xylene and *m*-xylene may also induce different  $\pi$ - $\pi$  stacking interactions within the framework when the aromatic nature of the xylenes interacts with the polyaromatic pyrene core.<sup>4</sup> This could potentially lead to a separation process for the two isomers.

#### 6.4 Porous Structure Characterisation Sorption Experiments of Zn(TBAPy) 1'

A sample of Zn(TBAPy) 1 was provided by Kyriakos Stylianou at Liverpool University. The main problem associated with this material is that when Zn(TBAPy) 1' is formed, it can readily destabilise to (Zn(TBAPy) 1'a, which gives (Zn<sub>2</sub>(TBAPy)(H<sub>2</sub>O)<sub>3.6</sub>, on exposure to atmospheric water. A fresh batch of sample was used for each gas / vapour adsorption experiment to ensure no conversion to (Zn(TBAPy) 1'a. Desolvation in the IGA occurred by exposing the sample to vacuum (10<sup>-6</sup> mbar) and heating to 373 K for five hours, until a stable mass profile was reached. Typical mass loss was around 22.5%. This desolvation process formed Zn(TBAPy) 1'.

##### 6.4.1 Carbon Dioxide Adsorption Zn(TBAPy) 1'

Nitrogen adsorption did not occur on Zn(TBAPy) 1' at 77 K due to activated diffusion effects. Therefore, the main characterisation isotherms were completed using carbon dioxide at 195 K and 273 K. Carbon dioxide adsorption experiments were conducted over the pressure range 100 – 1000 mbar.

##### 6.4.1.1 Carbon Dioxide Adsorption at 195 K

Carbon dioxide adsorption at 195 K was used to estimate to total pore volume of the material by using the Langmuir equation (6.1).<sup>5,6</sup>

$$\frac{P}{n} = \frac{P}{n_m} + \frac{1}{Kn_m} \quad 6.1$$

Where:

$p$  = pressure (mbar)

$n$  = amount adsorbed (g)

$n_m$  = the monolayer capacity of the material (mmol g<sup>-1</sup>)

$K$  = equilibrium constant

The mass of sample used was 30.9233mg. **Figure 6-4** shows the carbon dioxide adsorption isotherm at 195 K for Zn(TBAPy) 1'. The isotherm is a typical Type I isotherm by IUPAC classification.<sup>7</sup> The Langmuir plot is shown in **Figure 6-5**. The Langmuir equation fits the experimental data with 2.5%. The Langmuir monolayer coverage was calculated as  $6.67 \pm 0.0291$  mmol g<sup>-1</sup>, the Langmuir pore volume was calculated as  $0.287 \pm 0.00125$  cm<sup>3</sup> g<sup>-1</sup> and the apparent Langmuir surface area was calculated as  $763 \pm 3.33$  m<sup>2</sup> g<sup>-1</sup>.

#### 6.4.1.2 Carbon Dioxide Adsorption at 273 K

Carbon dioxide adsorption at 273 K was used to estimate the micropore volume of the material by using the Dubinin-Radushkevich (DR) equation (6.2).<sup>8</sup>

$$\log n = \log n_0 - D \log^2 \left( \frac{p^0}{p} \right) \quad 6.2$$

Where:

$n$  = the volume of micropores that have been filled at a relative pressure of 1

$n_0$  = the total available micropore volume

$p$  = pressure (mbar)

$p^0$  = saturated gas pressure (mbar)

$D = B \left( \frac{T}{\beta} \right)^2$  = a measure of the pore size distribution of the adsorbent.

The mass of sample used was 30.9783mg. **Figure 6-6** shows the carbon dioxide adsorption isotherm at 273 K for Zn(TBAPy) 1'. The DR plot for Zn(TBAPy) 1' is shown in **Figure 6-7**. The results show that the DR plot shows no deviation from linearity across the pressure range 5 - 950 mbar, this shows that the adsorption is consistent with micropore filling.<sup>9</sup> The micropore volume calculated at 273 K is lower than the total pore volumes calculated from carbon dioxide adsorption at 195 K, which is expected. The micropore volume is  $0.250 \pm 0.00468$  g<sup>-1</sup> cm<sup>3</sup> and the total pore volume is  $0.287 \pm 0.00125$  cm<sup>3</sup> g<sup>-1</sup>. The micropore volume accounts for 87% of the total porosity. The total pore volume compares well with the calculated PLATON pore volume of  $0.2929$  cm<sup>3</sup> g<sup>-1</sup>.

## 6.4.2 Xylene Vapour Adsorption on Zn(TBAPy) 1'

### 6.4.2.1 Adsorption of *p*-xylene

The first *p*-xylene isotherm was investigated at 303 K. Repeat isotherms were measured on different samples to ensure repeatability. The mass of samples 1 and 2 were 32.0666 mg and 39.0539 mg respectively. The isotherms were measured within the pressure range 0.02 – 14.5 mbar. The isotherm measured for sample 1 is shown in **Figure 6-8**, and shows high repeatability by sample 2 as shown in **Figure 6-9**. The isotherms measured were Type I by IUPAC classification<sup>7</sup>, the plateau is reached at 2 mbar with a slight increase in uptake at a higher pressure of 14.5 mbar. Both isotherms were reversible. At the start of the plateau, at 2 mbar pressure, the framework uptakes 1.53 *p*-xylene molecules per formula unit, whereas the framework takes up approximately 1.70 *p*-xylene molecules uptake per formula unit at 14.5 mbar, showing a slight increase towards the end of the isotherm. The isotherm was analysed using the Langmuir equation, equation 6.1. The Langmuir plot is shown in **Figure 6-10**. The Langmuir monolayer coverage for samples 1 and 2 were calculated as  $2.068 \pm 0.0180 \text{ mmol g}^{-1}$  and  $2.071 \pm 0.0193 \text{ mmol g}^{-1}$ , the Langmuir pore volume was calculated as  $0.252 \pm 2.20 \times 10^{-3} \text{ cm}^3 \text{ g}^{-1}$  and  $0.253 \pm 2.35 \times 10^{-3} \text{ cm}^3 \text{ g}^{-1}$  respectively, showing good agreement. At 2 mbar the uptake was  $1.89 \text{ mmol g}^{-1}$  which corresponds to a pore volume of  $0.231 \text{ cm}^3 \text{ g}^{-1}$ . The *p*-xylene uptake fills approximately 80% and 87% of the total pore volume at 2 mbar and 14.5 mbar, respectively. The incomplete filling of the pores can be attributed to the bulky nature of *p*-xylene. The reversibility of the *p*-xylene isotherm suggests that the pores of the 3D structure, Zn (TBAPy) 1', are large enough to accommodate the "linear" *p*-xylene possibly introducing weak  $\pi$ - $\pi$  stacking interactions with the TBAPy ligand during the adsorption process.

Attempts were made to calculate an enthalpy of adsorption for *p*-xylene adsorption. A sequence of four temperatures was investigated: 303, 313, 318 and 323K. The isotherms are shown in **Figure 6-11**. All isotherms are Type I by IUPAC classification. All isotherms reach the plateau at a relative pressure of 0.1, and show a slight further uptake at a relative pressure of 0.8. These data are unusable to calculate the enthalpy of adsorption for *p*-xylene. The isotherms do not follow the expected trend of a decrease in amount adsorbed as temperature increases, which is expected for physisorption isotherms. The isotherms all lie within expected

experimental error. There are time constraints upon the experiments which can be conducted at temperatures below 303 K the isotherms become very slow, and due to the saturated vapour pressure of *p*-xylene, to obtain an isotherm above 323 K the vapour reservoir must be held at a higher temperature, which is beyond the capabilities of the equipment.

#### 6.4.2.2 Adsorption of *m*-xylene at 303 K

Adsorption isotherms for *m*-xylene adsorption were measured on two samples to check repeatability. The mass of samples 1 and 2 were 37.7035 mg and 37.7203 mg respectively. The isotherms were measured within the pressure range 0.02 – 14.5 mbar. The isotherms measured for the two samples are shown in **Figure 6-12**. The isotherms measured initially start as Type I by IUPAC classification<sup>7</sup> until 4 mbar, where a second step occurs in the isotherm, up to 14.5 mbar. The isotherms are not reversible, they exhibit a large hysteresis, the majority of desorption starts to occur at 1 mbar in the desorption profile. The framework can uptake 1.45 *m*-xylene molecules per formula unit at 2 mbar, which is comparable with the uptake observed for *p*-xylene at 2 mbar. At 14.5 mbar the framework adsorbs 2.71 *m*-xylene molecules per formula unit, which is considerably more uptake than what is observed for *p*-xylene. The pore volume for *m*-xylene adsorption was estimated from the uptake at the end of the isotherm, and is calculated as 3.37 mmol g<sup>-1</sup>, giving a pore volume of 0.411 cm<sup>3</sup> g<sup>-1</sup>. This corresponds to filling 143% of the total pore volume. This indicates a structural change or the compression of *m*-xylene molecules which were trapped within the pores during the adsorption process. The differences between the *p*-xylene and *m*-xylene isotherms are shown in **Figure 6-13**, and in **Figure 6-14** on a relative pressure basis.

6.4.2.3 Kinetics of Xylene Adsorption

The kinetic data of each xylene isotherm were fitted using the stretched exponential (SE) model (**Chapter 1 – Adsorption**), equation 6.3:

$$\frac{M_t}{M_e} = 1 - e^{-(kt)^\beta} \quad 6.3$$

Where:

$M_t$  = the amount adsorbed (g) at time  $t$  (s)

$M_e$  = the equilibrium uptake (g)

$k$  = rate constant ( $s^{-1}$ )

$t$  = time (s)

$\beta$  = the exponential parameter

When the value of  $\beta = 0.5$ , this is indicative that the model is one dimensional, when  $\beta = 1$  this is indicative that the model is three dimensional, with the model presumably becoming two dimensional at intermediate values. The  $\beta$  values give an indication of the distribution of the relaxation times, as  $\beta$  decreases the distribution broadens. When  $\beta = 1$  there is a single relaxation time which is indicative of a rate determining step due to the diffusion through a barrier at the pore entrance.<sup>10</sup>

All kinetic plots can be found in **CD Appendix A – Xylene Separation by Zn(TBAPy) 1' Metal Organic Framework**. The differences in the kinetics of adsorption allow the potential for separation. Up to 2 mbar the kinetics for both *p*- and *m*-xylene are similar, corresponding to the similarity in the shapes of the isotherms. At 4 mbar, the shapes of the isotherms change, with *m*-xylene showing a large uptake. This corresponds to a dramatic decrease in the rate of uptake. The comparison of rate constant with adsorption of *p*-xylene is shown in **Figure 6-15**. The rate constant remains of the same order of magnitude across the entire pressure range of adsorption, which is consistent with the isotherm showing a plateau region from 2 mbar to the completion of the isotherm. In contrast, the rate of *m*-xylene adsorption is significantly slower after the plateau. The rate constants for *m*-xylene decrease at pressures above 4 mbar, which is consistent with the point of inflection in the *m*-xylene adsorption isotherm at 4mbar, as shown in **Figure 6-16**. A comparison of  $\ln(\text{rate constant})$  against pressure shows the difference in magnitude between the two xylene isomers, as shown in **Figure 6-17**. **Figure 6-18** shows a direct

comparison between the  $\ln$  (rate constant) and the adsorption isotherms for both *p*- and *m*-xylene isotherms. It is clear that below 2 mbar the rate constant values are of similar magnitude, and above 4 mbar there is a dramatic decrease in rate constant for *m*-xylene. The kinetic profile with stretched exponential analysis for *p*-xylene for the step 6.0 – 8.0 mbar is shown in **Figure 6-19**. The time taken to reach equilibrium for this point was under 2 minutes. The corresponding step for *m*-xylene is shown in **Figure 6-20**, the time taken to reach equilibrium was much longer, 39 hours for this one kinetic point. Details of stretched exponential kinetic analysis parameters are given in **Table 6-2** for *p*-xylene and **Table 6-3** for *m*-xylene. Kinetic analysis using the stretched exponential equation gives  $\beta$  values of 1 for the majority of the *p*-xylene adsorption isotherm (see **Table 6-2**). Stretched exponential  $\beta$  values of 1 indicate that the diffusion of the vapour into the porous structure is following the linear driving force (LDF) model. This model has also been used to fit the kinetic data for *p*-xylene adsorption, and the graphs of the SE and LDF analysis for 0.08 – 0.10 mbar are shown in **Figure 6-21** and **Figure 6-22**, respectively. The LDF graphs show good linear correlation, showing that the LDF model is a good description of the kinetic profiles.

Kinetic analysis of *m*-xylene shows that before the point of inflection in the plateau is reached, the SE  $\beta$  values are close to 1, indicating that the linear driving force model of diffusion is also being followed for *m*-xylene adsorption at low pressure, as shown by the graphs of SE and LDF analysis shown in **Figure 6-23** and **Figure 6-24**, respectively. At the point of inflection in the plateau, the rate of *m*-xylene adsorption slows significantly, and the  $\beta$  values lower to  $\sim 0.7$  for the remainder of the isotherm (see **Table 6-3**). According to Klafter and Schlesinger,  $\beta$  values of 1 indicates a three dimensional model, with a single relaxation time, and that the rate determining step is due to diffusion through a barrier at the pore entrance.<sup>10</sup>  $\beta$  values of 0.5 indicate a one dimensional model with a distribution of relaxation times. Values between 1 and 0.5 indicate a two dimensional model. The reduction in  $\beta$  from 1 to 0.7 after the point of inflection in the *m*-xylene isotherm indicates that the linear driving force model is no longer describing the diffusion of *m*-xylene into the material, and the diffusion process has changed from three dimensional to two dimensional. The change of  $\beta$  with the adsorption of *m*-xylene is shown in **Figure 6-25**. This change shows that the rate determining step of diffusion of *m*-xylene is



no longer solely based upon diffusion through a constriction at the pore entrance, indicating that a structural change has occurred.

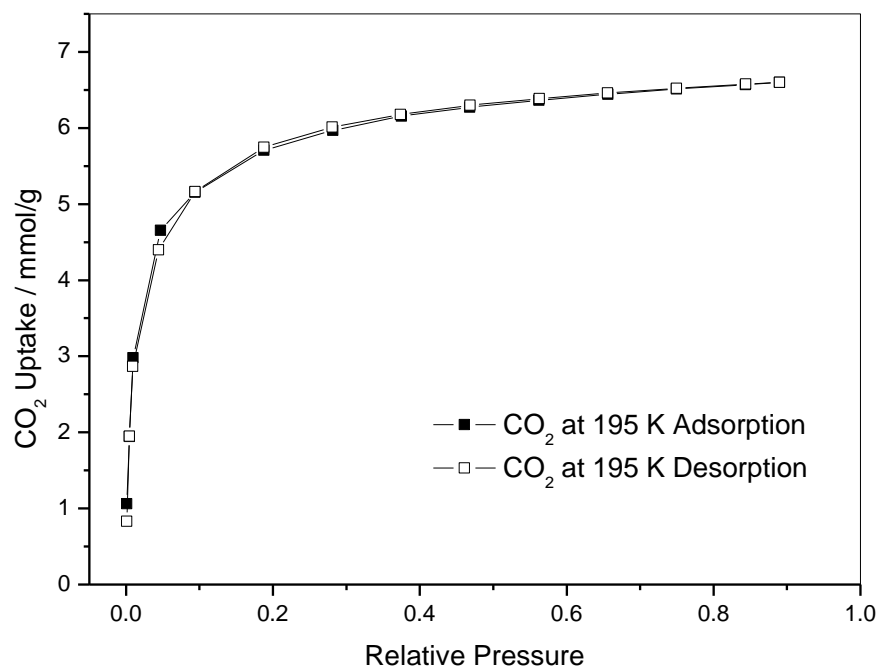
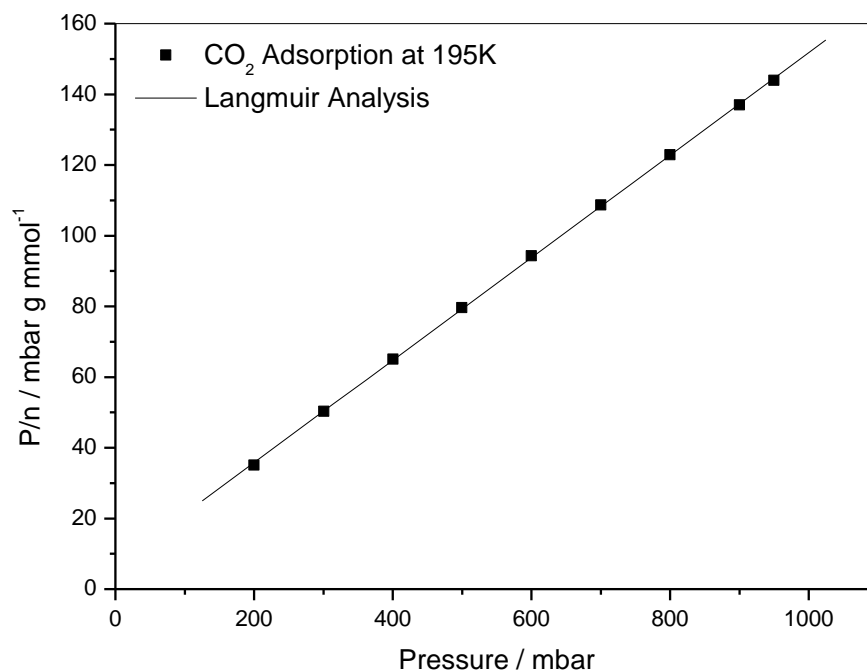
### 6.4.2.4 Capillary loading and PXRD Analysis

In order to determine any structural changes induced by the different xylene isomers, glass capillaries of 0.5 mm diameter were filled with Zn (TBAPy) 1 for powder X-ray diffraction analysis. The capillaries were sealed onto the modified IGA sample chamber (see **Chapter 5 – Experimental section 5.2.1.6**) and outgassed at 373 K for 18 hours, to form Zn(TBAPy) 1' (**Figure 6-26**). The samples were partially loaded with vapour at selected pressures at room temperature (293 K). Pressures were selected which corresponded to the relative pressure at 303 K. The relative pressures used were 0.23 which is 2.030 mbar for *p*-xylene and 2.293 mbar for *m*-xylene mbar at 293 K, corresponding to 4 mbar at 303 K; this is the point up to which the two isomers produce the same shape in the isotherm. The second relative pressure used was 0.93 which is 8.210 mbar for *p*-xylene and 7.898 mbar for *m*-xylene at 293K, corresponding to 14 mbar, the end of the isotherm for both isomers. The time allowed for equilibration was 18 hours. After this time the capillaries were sealed using a hydrogen/air flame and sent to Liverpool University for PXRD analysis. The PXRD patterns for the xylene isomer loadings at 8.210 mbar for *p*-xylene and 7.898 mbar for *m*-xylene are shown in **Figure 6-27**. The powder diffraction shows slight shifts in the peaks for *m*-xylene, and the pattern contains sharper peaks, which indicate increased crystallinity of the material as the empty cavities are filled with *m*-xylene molecules resulting in increased order and the smaller unit cell. The sample loaded with *p*-xylene is comparable with the samples loaded with *m*-xylene, as shown in **Table 6-4**. The unit cell volume for *m*-xylene is higher than that of *p*-xylene, with values of 2493 and 2457 Å<sup>3</sup>, respectively.

## 6.5 Conclusions

A 2D zinc / pyrene based metal organic framework was synthesised, which on desolvation rearranges to form a 3D framework by loss of water inducing a coordination change around the metal centre, facilitated by the flexibility of the carboxylate groups which functionalise the pyrene core of the ligand.<sup>1</sup> Due to the specific size and shape of the channels in the 3D structure and the nature of the polyaromatic ligand used, the sorption characteristics of aromatic molecules of *m*-xylene and *p*-xylene were investigated.<sup>4</sup> The isomers showed similar isotherms up

to 2 mbar, after which the *p*-xylene continued along a plateau in a standard Type I isotherm, and the *m*-xylene continued to uptake to 143% of total pore volume, producing a hysteretic desorption isotherm. The differences in the shape of isotherms were accompanied by a vast difference in rate of adsorption above 4 mbar, with *m*-xylene showing very slow adsorption kinetics. The isotherm shapes and rate constants for both *p*-xylene and *m*-xylene adsorption are similar until the 2 mbar step, this could be the pressure to which neither xylene has an effect on the framework. The  $\beta$  values for *p*-xylene adsorption remain at 1 and follow a linear driving force model for the duration of the isotherm, with similar rate constants, showing that the *p*-xylene molecules induce no structural change within the material. During *m*-xylene adsorption, a plateau is reached, then a point of inflection occurs, where the rate of adsorption decreases, the volume of *m*-xylene adsorbed increases, and the  $\beta$  parameter changes from 1 to 0.7, a value which is retained for the duration of the isotherm. These three observations show that a structural rearrangement is occurring. The larger volume of *m*-xylene adsorbed shows that the structural change leads to an increase in pore volume to a value of  $0.411 \text{ cm}^3 \text{ g}^{-1}$ , compared to  $0.231 \text{ cm}^3 \text{ g}^{-1}$  for *p*-xylene. This increased pore volume is also shown by the PXRD analysis of loaded samples of Zn(TBAPy) 1', where the unit cell volume for *m*-xylene is higher than that of *p*-xylene, with values of  $2493$  and  $2457 \text{ \AA}^3$ , respectively. This increase in pore volume is coupled with an increase in the size of the constriction at the entrance of the pore – as shown by the changing  $\beta$  values in the stretched exponential kinetic analysis. The change from  $\beta = 1$  to  $\beta = 0.7$  shows that diffusion through a barrier at the entrance to the pore is no longer the rate determining step and the rate of diffusion is also coupled with diffusion across the surface of the pore, producing a distribution of relaxation times.<sup>10</sup> The hysteretic nature of the *m*-xylene desorption is also indicative of a structural change as the *m*-xylene is desorbing from the material via a different mechanism to the adsorption.<sup>11,12</sup> This shows that *m*-xylene is adsorbed at a slower rate at higher pressures than *p*-xylene, indicating a potential separation capability at high pressures.

6.6 Figures**Figure 6-4:** Zn (TBAPy) 1' CO<sub>2</sub> adsorption isotherm at 195 K**Figure 6-5:** Langmuir analysis of Zn (TBAPy) 1' CO<sub>2</sub> adsorption at 195 K

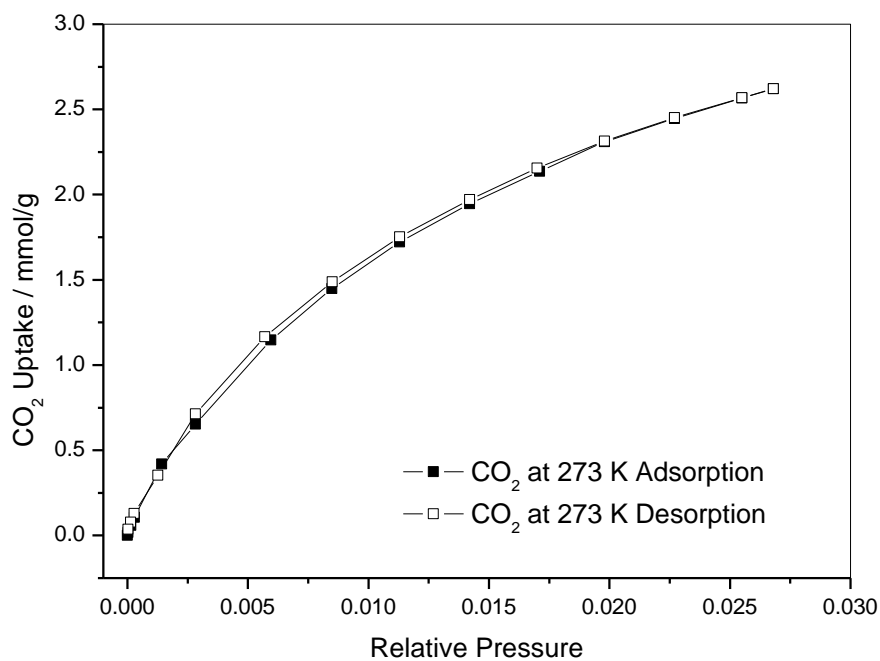


Figure 6-6: Zn (TBAPy) 1' CO<sub>2</sub> adsorption isotherm at 273 K

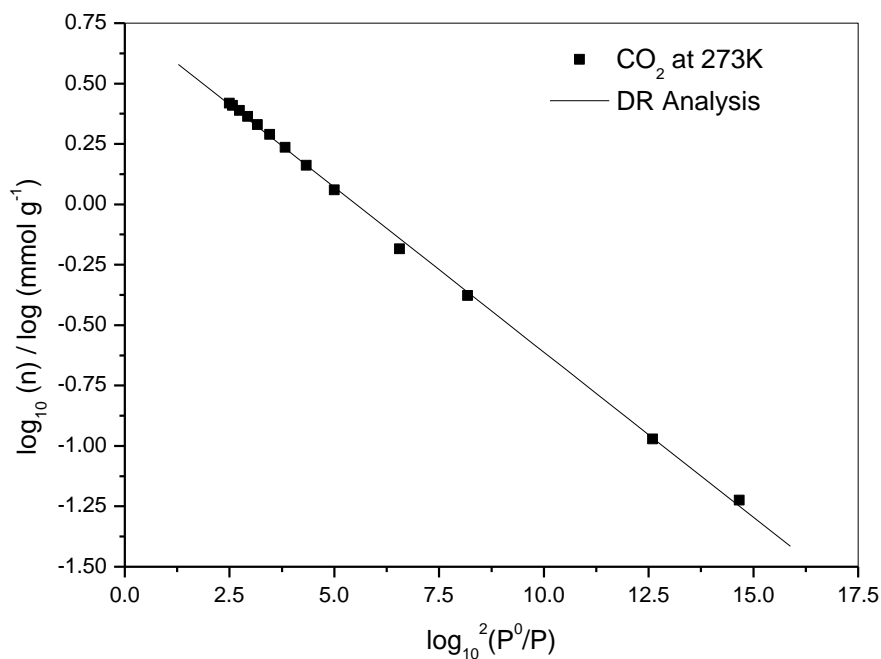
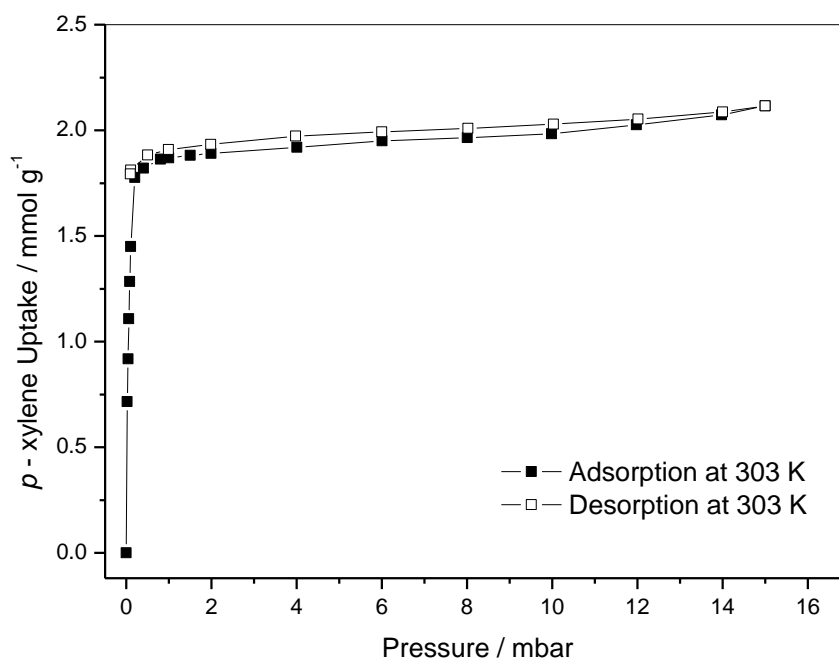
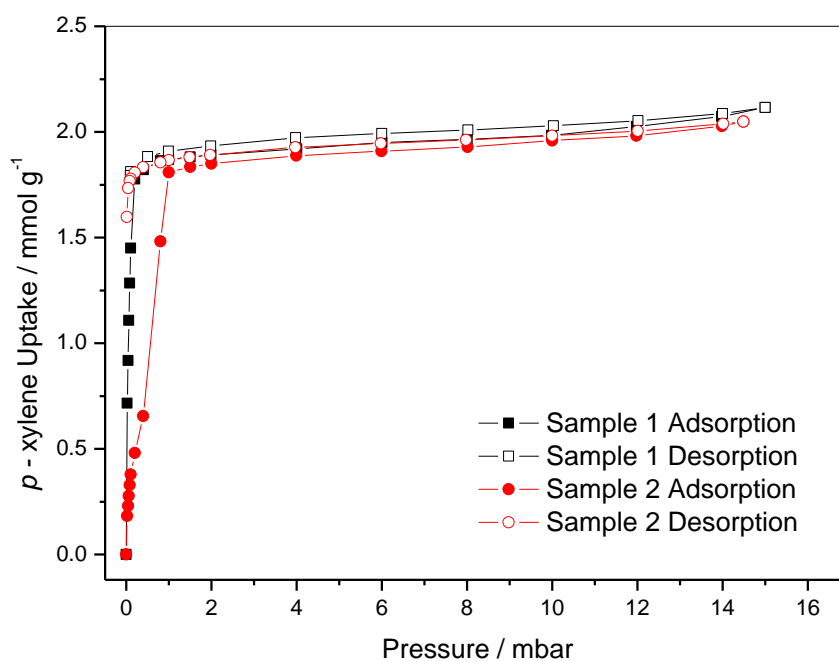


Figure 6-7: DR analysis of Zn (TBAPy) 1' CO<sub>2</sub> adsorption at 273K



**Figure 6-8:** Zn (TBAPy) 1' *p*-xylene isotherm at 303 K



**Figure 6-9:** Zn (TBAPy) 1' *p*-xylene adsorption isotherms for samples 1 and 2 at 303 K

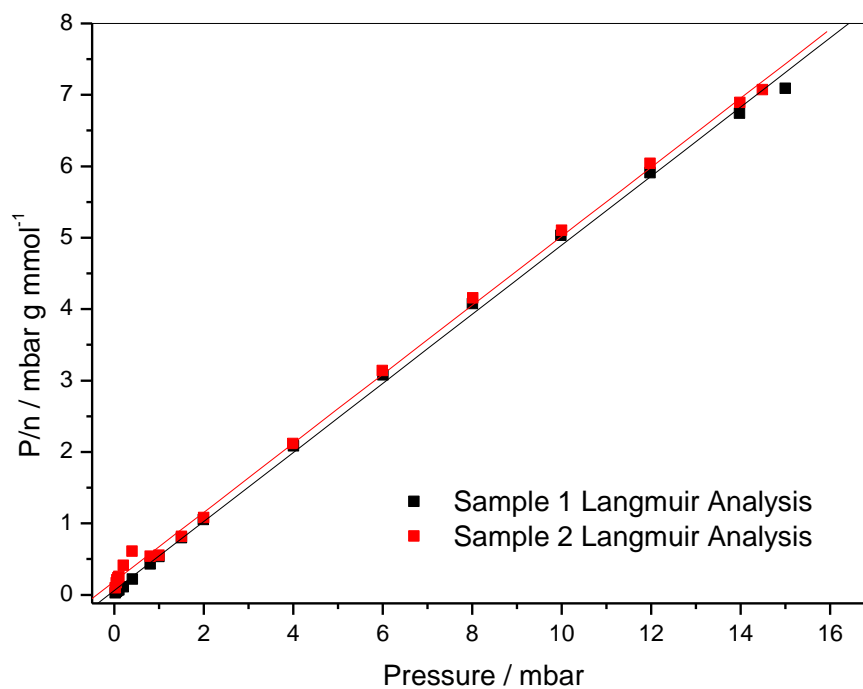


Figure 6-10: Langmuir analysis of Zn (TBAPy) 1' *p*-xylene adsorption at 303 K samples 1 and 2

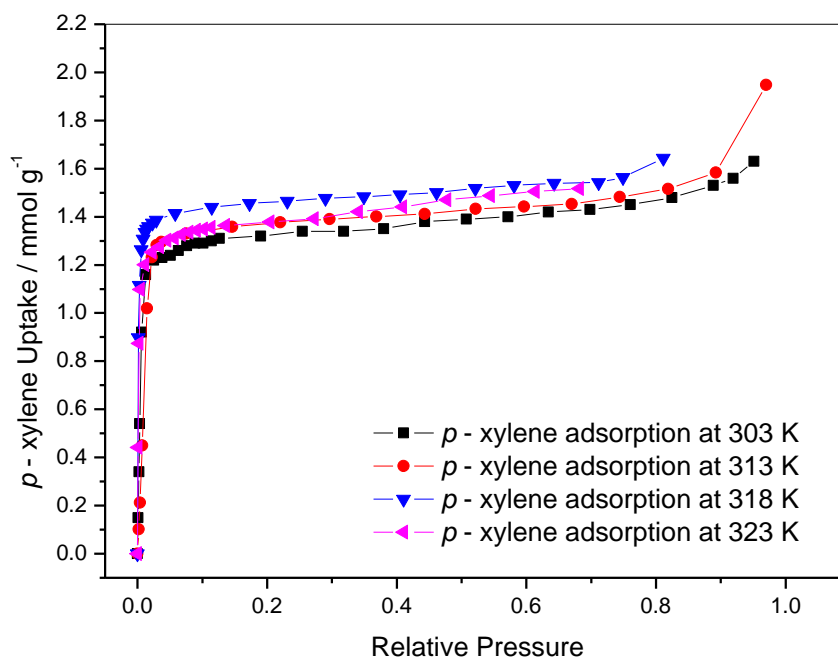


Figure 6-11: Zn (TBAPy) 1' *p*-xylene adsorption isotherms at 303, 313, 318 and 323 K

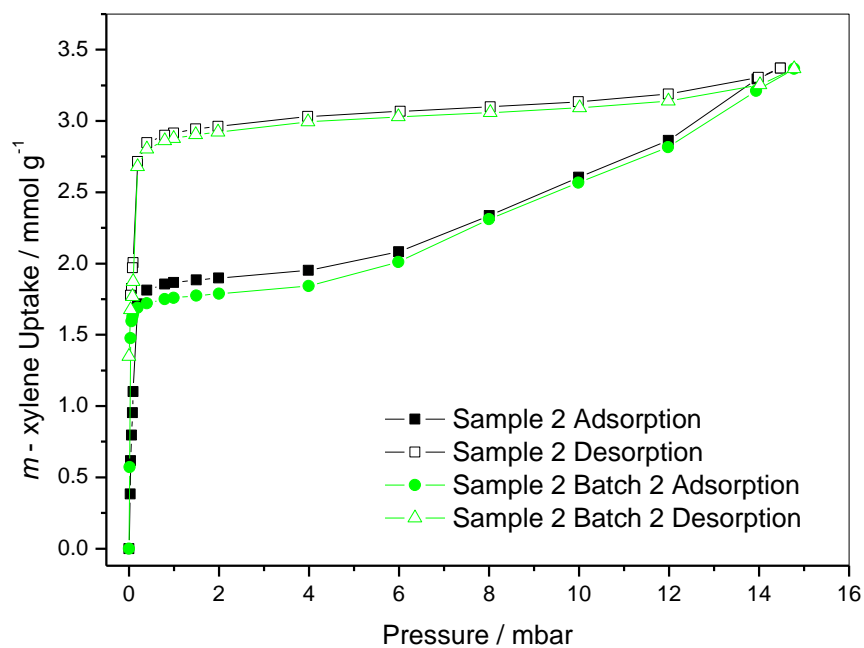


Figure 6-12: Zn (TBAPy) 1' *m*-xylene isotherm at 303 K

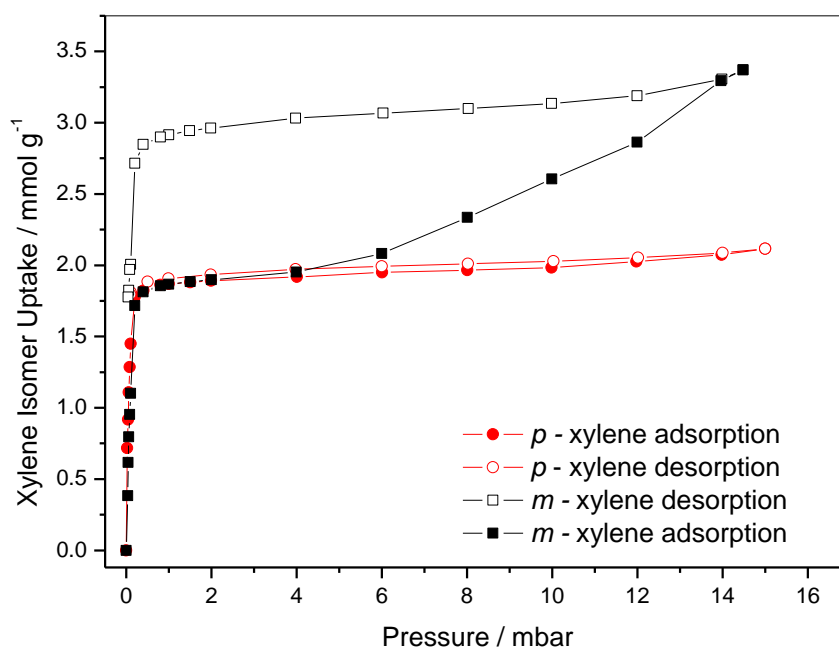
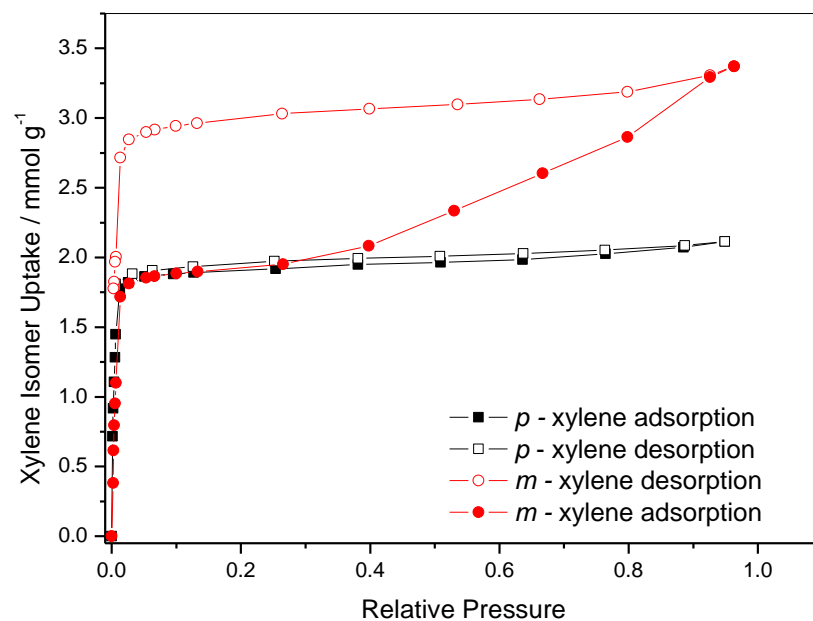
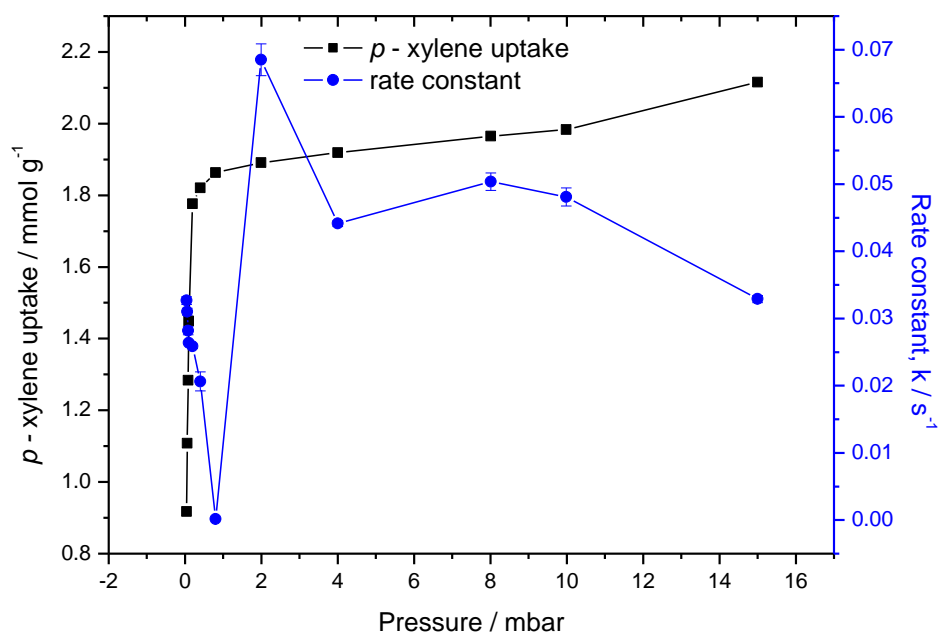


Figure 6-13: Zn (TBAPy) 1' *m*- and *p*-xylene isotherm comparisons at 303 K



**Figure 6-14:** Zn (TBAPy) 1' *m*- and *p*-xylene isotherm comparisons at 303 K on a relative pressure basis



**Figure 6-15:** Comparison of Zn (TBAPy) 1' *p*-xylene adsorption isotherm and rate constant / s<sup>-1</sup> at 303 K



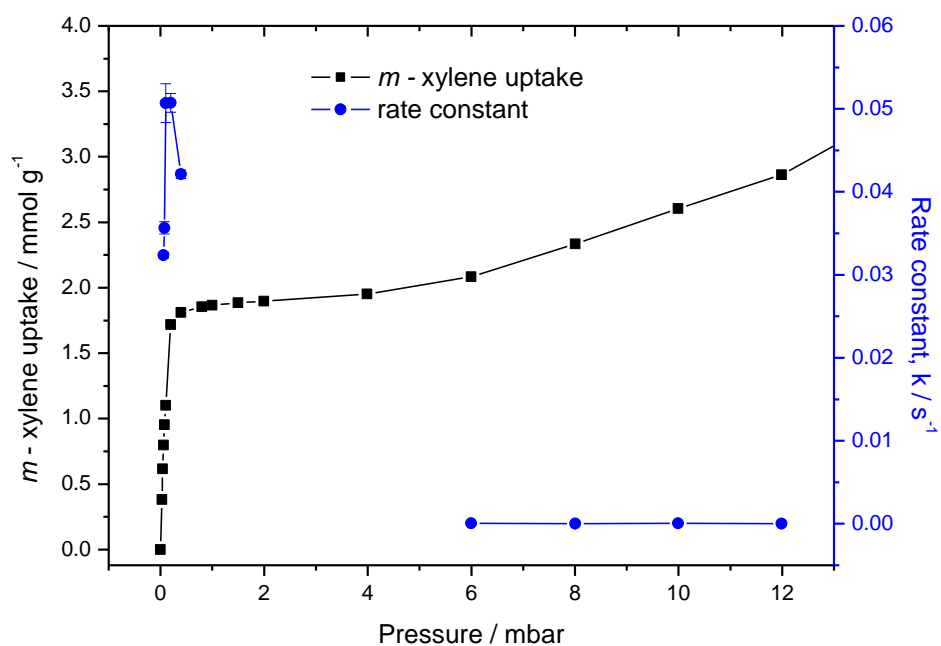


**Figure 6-16:** Comparison of Zn (TBAPy) 1' *m*-xylene adsorption isotherm and rate constant / s<sup>-1</sup> at 303 K

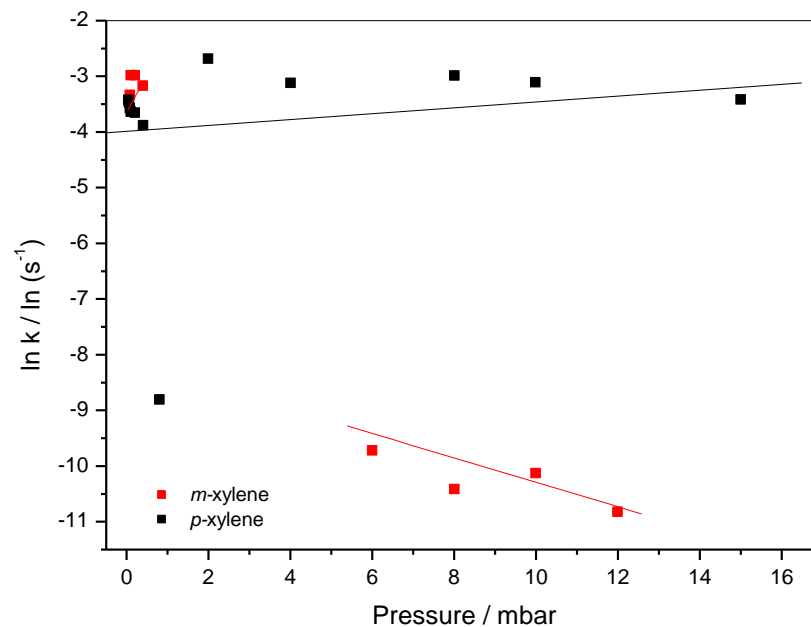


**Figure 6-17:** Comparison of ln(rate constant) for Zn (TBAPy) 1' *m*- and *p*-xylene isomers at 303 K

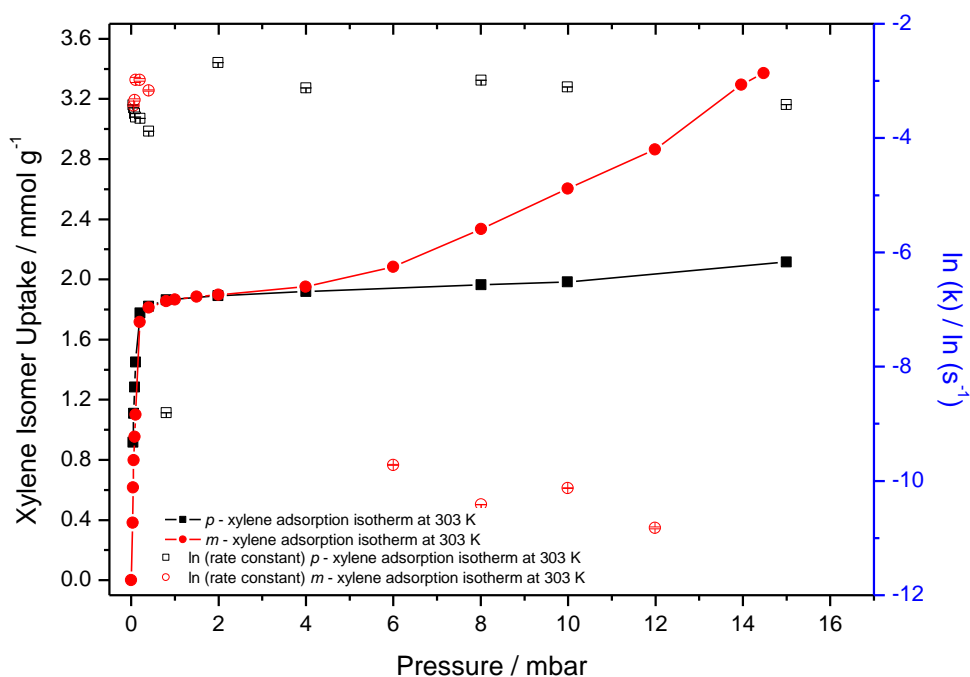


**Figure 6-18:** Comparison of  $\ln(\text{rate constant})$  for Zn (TBAPy) 1' adsorption *m*- and *p*-xylene isotherms at 303 K

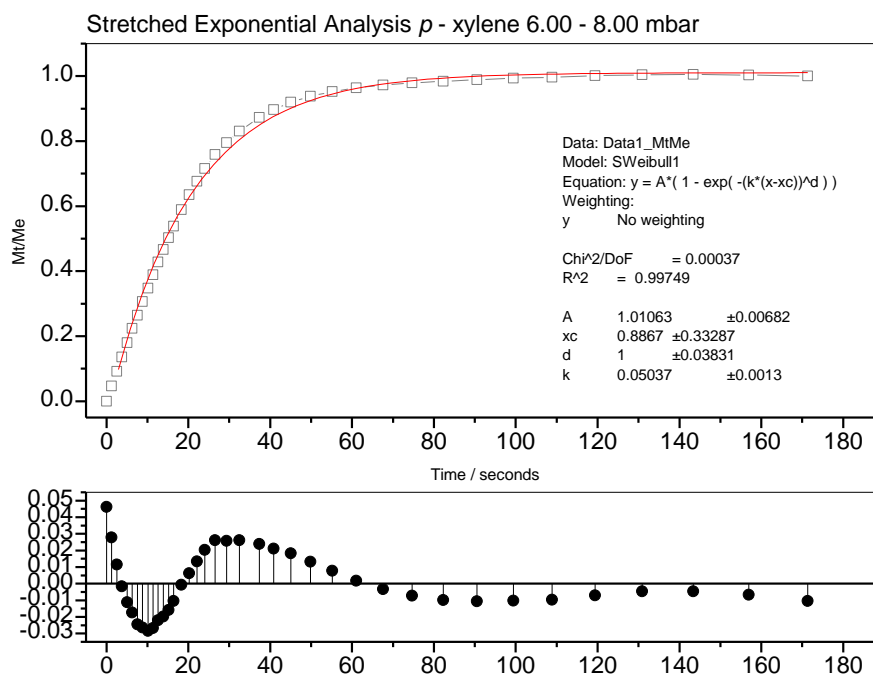


**Figure 6-19:** Zn (TBAPy) 1' *p*-xylene adsorption kinetic step 6.0 – 8.0 mbar SE kinetic analysis at 303 K

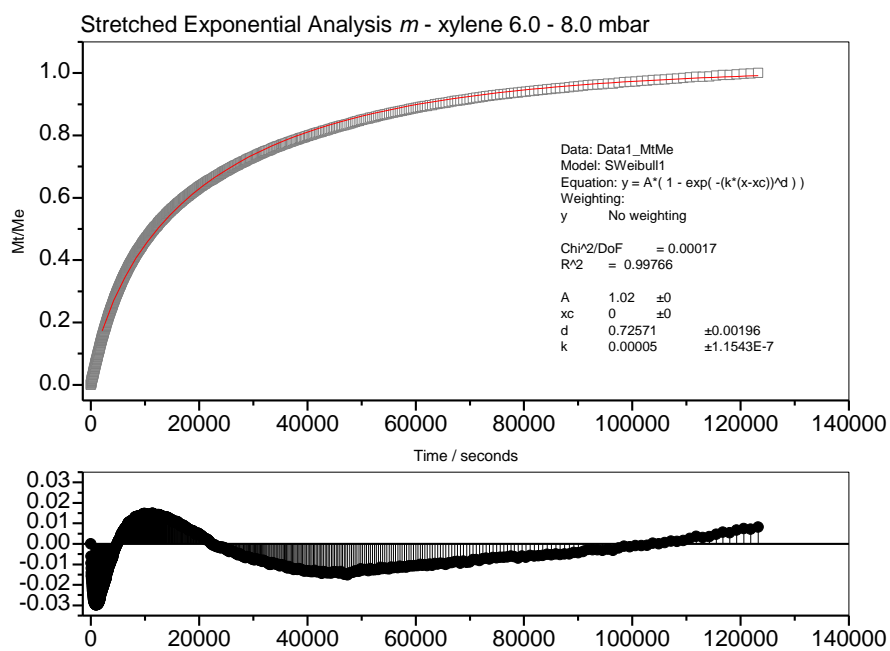


**Figure 6-20:** Zn (TBAPy) 1' *m*-xylene adsorption kinetic step 6.0 – 8.0 mbar SE kinetic analysis at 303 K

**Table 6-2:** Exponent and rate constant, k values for *p*- xylene adsorption SE kinetic analysis

Pressure / mbar	Conc. / mmol g <sup>-1</sup>	R <sup>2</sup>	Exponent	Rate Constant / s <sup>-1</sup>	ln (rate constant) / ln (s <sup>-1</sup> )
<b>0.039</b>	0.917	0.9813	1.000 ± 0.023	0.0327 ± 5.9 x 10 <sup>-4</sup>	-3.422 ± 0.0181
<b>0.059</b>	1.108	0.99703	1.000 ± 0.017	0.0310 ± 5.9 x 10 <sup>-4</sup>	-3.473 ± 0.0164
<b>0.079</b>	1.284	0.99604	1.000 ± 0.021	0.0282 ± 6.2 x 10 <sup>-4</sup>	-3.569 ± 0.022
<b>0.099</b>	1.449	0.99951	1.000 ± 0.010	0.0264 ± 1.8 x 10 <sup>-4</sup>	-3.635 ± 0.00682
<b>0.199</b>	1.776	0.98752	1.000 ± 0.021	0.0259 ± 3.3 x 10 <sup>-4</sup>	-3.655 ± 0.01276
<b>0.403</b>	1.821	0.9957	0.656 ± 0.025	0.0206 ± 1.4 x 10 <sup>-3</sup>	-3.881 ± 0.06883
<b>0.8</b>	1.863	0.99748	0.500 ± 0.0064	0.00015 ± 6.6 x 10 <sup>-7</sup>	-8.805 ± 0.00443
<b>1.99</b>	1.891	0.99845	0.994 ± 0.048	0.0685 ± 2.4 x 10 <sup>-3</sup>	-2.681 ± 0.03445
<b>4.002</b>	1.919	0.99753	1.000 ± 0.017	0.0441 ± 4.5 x 10 <sup>-4</sup>	-3.121 ± 0.0102
<b>8.009</b>	1.965	0.99749	1.000 ± 0.038	0.0504 ± 1.3 x 10 <sup>-3</sup>	-2.989 ± 0.02581
<b>9.987</b>	1.984	0.99652	1.000 ± 0.045	0.04807 ± 1.4 x 10 <sup>-3</sup>	-3.106 ± 0.02808
<b>14.997</b>	2.116	0.99737	1.000 ± 0.024	0.0329 ± 5.3 x 10 <sup>-4</sup>	-3.414 ± 0.01611

**Table 6-3:** Exponent and rate constant, k values for *m*-xylene adsorption SE kinetic analysis

Pressure / mbar	Conc. / mmol g <sup>-1</sup>	R <sup>2</sup>	Exponent	Rate Constant / s <sup>-1</sup>	ln (rate constant) / ln (s <sup>-1</sup> )
<b>0.058</b>	0.7969	0.9926	1.000 ± 0.0185	0.0324 ± 3.5 x 10 <sup>-4</sup>	-3.431 ± 0.0108
<b>0.078</b>	0.9540	0.99668	0.851 ± 0.0219	0.0357 ± 7.4 x 10 <sup>-4</sup>	-3.334 ± 0.0208
<b>0.098</b>	1.101	0.99297	1.000 ± 0.0751	0.0507 ± 2.3 x 10 <sup>-3</sup>	-2.982 ± 0.0462
<b>0.198</b>	1.717	0.99645	0.906 ± 0.0272	0.0507 ± 0.00113	-2.981 ± 0.0223
<b>0.398</b>	1.812	0.99912	0.947 ± 0.0164	0.0421 ± 5 x 10 <sup>-4</sup>	-3.168 ± 0.0119
<b>5.986</b>	5.996	0.99946	0.723 ± 0.00277	6 x 10 <sup>-5</sup> ± 4.9 x 10 <sup>-7</sup>	-9.721 ± 0.00811
<b>8.001</b>	8.007	0.99766	0.726 ± 0.00196	3 x 10 <sup>-5</sup> ± 1.154 x 10 <sup>-7</sup>	-10.414 ± 0.00385
<b>9.989</b>	9.994	0.99824	0.707 ± 0.00328	4 x 10 <sup>-5</sup> ± 2.650 x 10 <sup>-7</sup>	-10.127 ± 0.00662
<b>11.981</b>	11.990	0.99828	0.702 ± 0.00544	2 x 10 <sup>-5</sup> ± 3.437 x 10 <sup>-7</sup>	-10.820 ± 0.01719

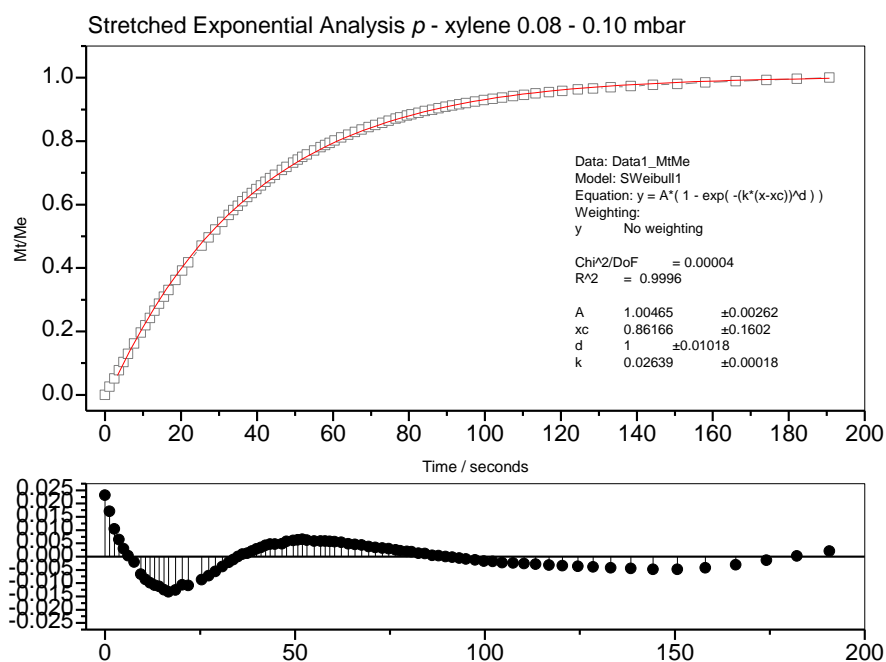


**Figure 6-21:** Zn(TBAPy) 1' *p*-xylene adsorption at 303 K 0.08 – 0.10 mbar step SE kinetic analysis

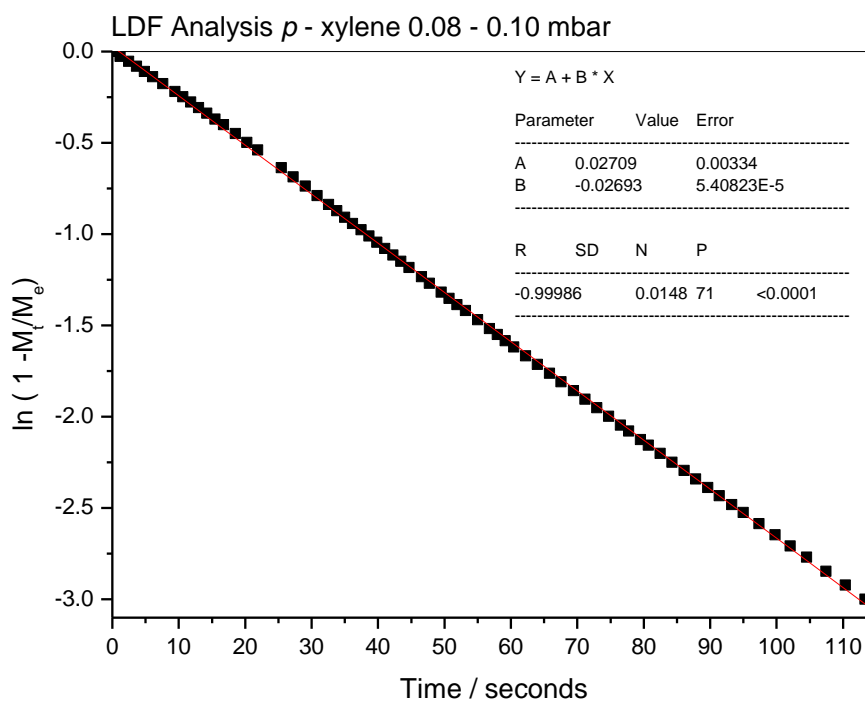


**Figure 6-22:** Zn(TBAPy) 1' *p*-xylene adsorption at 303 K 0.08 – 0.10 mbar step LDF kinetic analysis

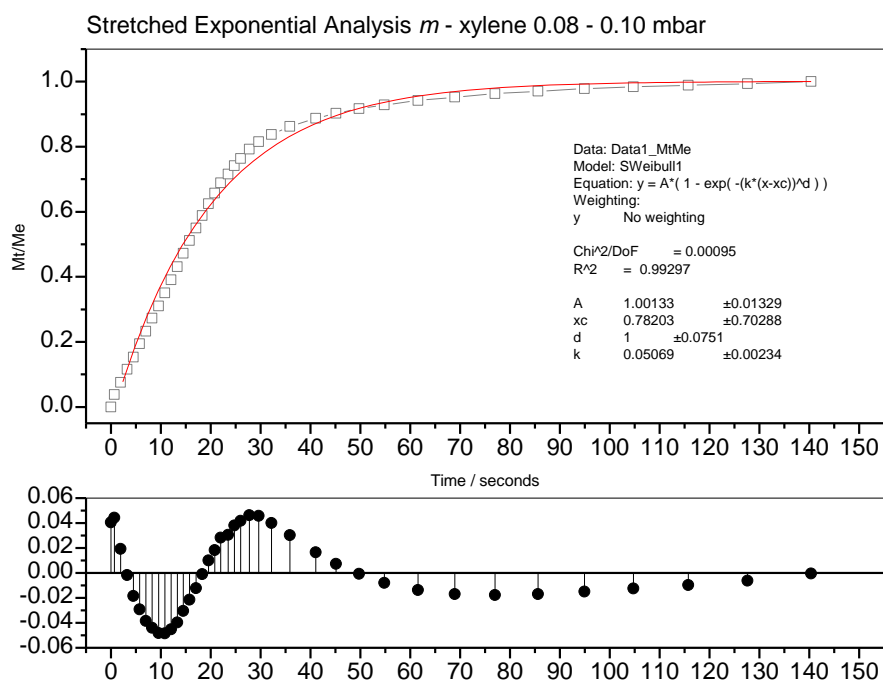


**Figure 6-23:** Zn(TBAPy) 1' *m*-xylene adsorption at 303 K 0.08 – 0.10 mbar step SE kinetic analysis

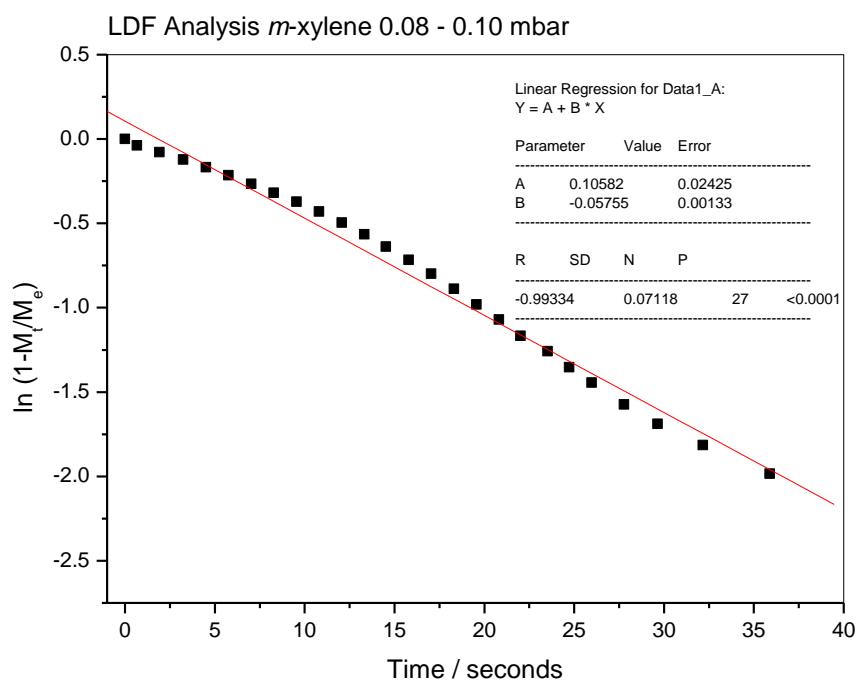


**Figure 6-24:** Zn(TBAPy) 1' *m*-xylene adsorption at 303 K 0.08 – 0.10 mbar step LDF kinetic analysis

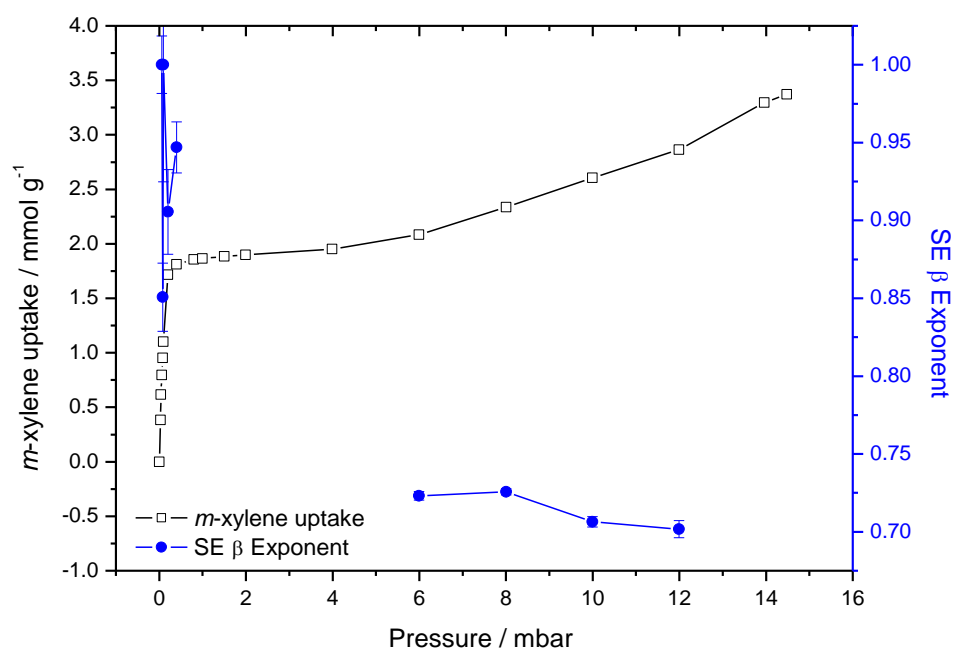


**Figure 6-25:** Zn(TBAPy) 1' *m*-xylene adsorption at 303 K comparison of adsorption isotherm and SE kinetic analysis  $\beta$  exponent



**Figure 6-26:** Capillary adapter containing a sample of Zn (TBAPy) 1'



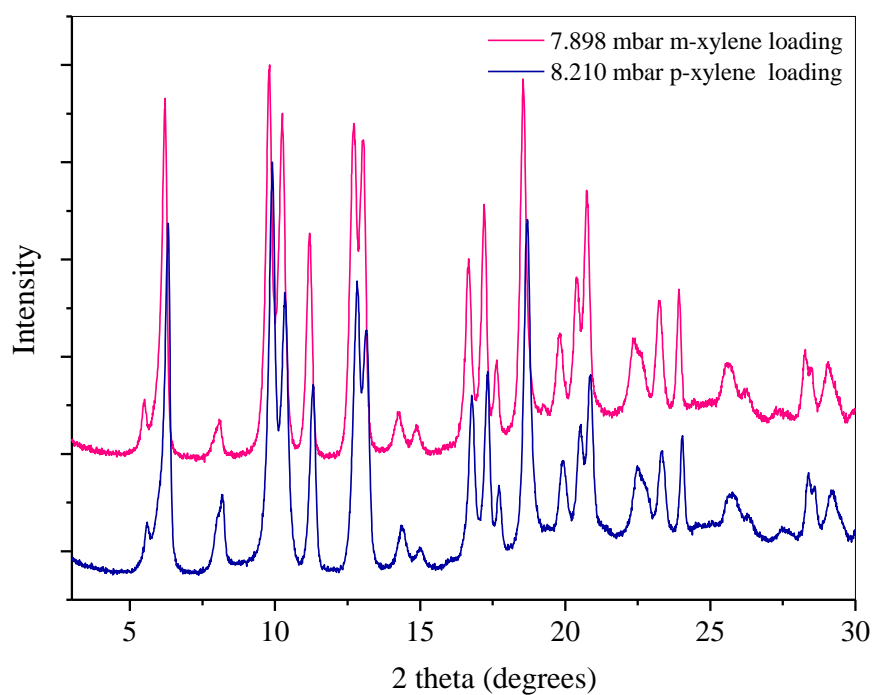


**Figure 6-27:** PXRD Patterns for *p*- and *m*-xylene loaded samples of Zn (TBAPy) 1'.

**Table 6-4:** PXRD Parameters for *p*- and *m*-xylene loaded samples of Zn (TBAPy) 1'.

Parameter	<i>m</i> -xylene at 7.898 mbar	<i>p</i> -xylene at 8.210 mbar
<b>a</b>	14.313(1)	14.188(1)
<b>b</b>	16.1199(9)	16.0557(8)
<b>c</b>	10.9660(7)	10.9439(9)
<b><math>\alpha</math></b>	95.196(4)	95.624(6)
<b><math>\beta</math></b>	93.904(4)	93.869(6)
<b><math>\gamma</math></b>	96.958(6)	96.359(6)
<b>V/Å<sup>3</sup></b>	2493(3)	2457(3)

6.7 References

- <sup>1</sup> K. C. Stylianou, R. Heck, S. Y. Chong, J. Bacsá, J. T. A. Jones, Y. Z. Khimyak, D. Bradshaw, M. J. Rosseinsky, *J. Am. Chem. Soc.*, **2010**, *132*, 4119
- <sup>2</sup> K. C. Stylianou, J. Rabone, S. Y. Chong, R. Heck, J. Armstrong, P.V. Wiper, K. E. Jelfs, S. Zlatogorsky, J. Bacsá, A. G. McLennan, C. P. Ireland, Y. Z. Khimyak, K. M. Thomas, D. Bradshaw, M. J. Rosseinsky, *J. Am. Chem. Soc.*, **2012**, *134*, 20466
- <sup>3</sup> C. E. Webster, R. S. Drago, M. C. Zerner, *J. Am. Chem. Soc.*, **1998**, *120*, 5509
- <sup>4</sup> C. Janiak, *J. Chem. Soc., Dalton Trans.*, **2000**, 3885
- <sup>5</sup> I. Langmuir, *J. Amer. Chem. Soc.*, 1916, **38**, 2219
- <sup>6</sup> I. Langmuir, *J. Amer. Chem. Soc.*, 1918, **40**, 1361
- <sup>7</sup> K. S. W. Sing, D. H. Everett, R. W. Haul, L. Moscou, R. A. Pierotti, J. Rouquerol, T. Siemieniewska, *Pure & Applied Chem.*, **1985**, *57*, 603
- <sup>8</sup> M. M. Dubinin, *Carbon*, **1989**, *27*, 457
- <sup>9</sup> E. M. Freeman, T. Siemieniewska, H. Marsh, B. Rand, *Carbon*, **1967**, *8*, 7
- <sup>10</sup> J. Klafter, M. F. Shlesinger, *PNAS, USA*, **1986**, *83*, 848
- <sup>11</sup> X. Zhao, B. Xiao, A. J. Fletcher, K. M. Thomas, D. Bradshaw, M. J. Rosseinsky, *Science*, **2004**, *306*
- <sup>12</sup> A. J. Fletcher, K. M. Thomas, M. J. Rosseinsky, *J. Solid State Chem.*, **2005**, *178*, 2491

Chapter 7      Structural Change Induced by Adsorption of Gases  
and Vapours on Porous Cage Materials

7.1 Introduction

As discussed previously (**Chapter 2 – Porous Materials**), Cage 1 was produced by the research group led by Andrew Cooper at Liverpool University.<sup>1</sup> Cage 1 has been shown to interconvert between a number of stable polymorphs. The conversion of interest in this study is the conversion of Cage 1 $\beta$  to Cage 1 $\alpha$ . The conversion was initially shown by the research group at Liverpool University, when Cage 1 $\beta$  was converted to Cage 1 $\alpha$  via vapour diffusion of ethyl acetate into a sample of Cage 1 $\beta$ . The full conversion cycle is shown in **Figure 7-1**.

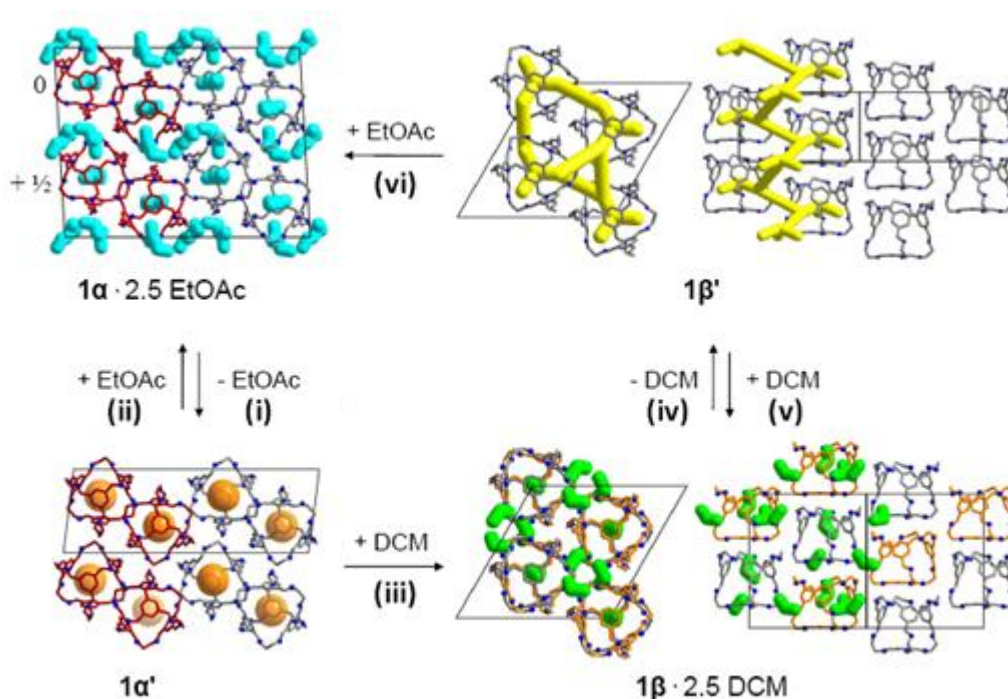


**Figure 7-1:** Conversion between various polymorphs (1 $\alpha$  and 1 $\beta$ ) accessible to the cage one structure, where 1 $\alpha'$  and 1 $\beta'$  indicate desolvated structures. Yellow, blue, green and orange space filling represents Connolly Surface area.<sup>2</sup>

The cage is initially isolated as Cage 1 $\alpha$ ·2.5EtOAc. The individual cage unit consists of four arene faces connected by six aliphatic linkers, as shown in **Figure 7-2**.

## Chapter 7 Structural Change Induced by Adsorption of Gases and Vapours on Porous Cage Materials

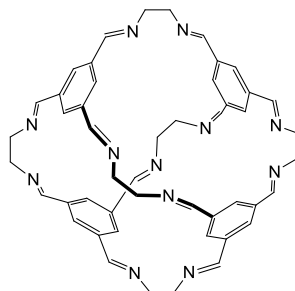


**Figure 7-2:** Individual cage units found in Cage 1

Each cage unit is around 1nm in size. On removal of ethyl acetate from Cage  $1\alpha \cdot 2.5\text{EtOAc}$  and exposure to dichloromethane, Cage  $1\beta$  is isolated. Re-exposure of desolvated Cage  $1\beta$  to ethyl acetate reforms the original Cage  $1\alpha$ . Cage  $1\beta$  and Cage  $1\alpha$ , as prepared by the research group at Liverpool University, were characterised using scanning electron microscopy, thermal gravimetric analysis and carbon dioxide adsorption at 195 and 273 K. The effects of exposing Cage  $1\beta$  to various organic triggers, starting with ethyl acetate, were investigated. The product of the exposure of Cage  $1\beta$  to ethyl and methyl acetate through vapour adsorption experiments conducted in the IGA is named Cage  $1\alpha\#$ .

### 7.2 Characterisation of Cage $1\beta$ and Cage $1\alpha$

#### 7.2.1 Thermal Gravimetric Analysis

Thermal gravimetric analysis was carried out on a 6.8 mg sample of Cage  $1\beta$  and on a 7.6 mg sample of Cage  $1\alpha$ . Cage  $1\beta$  was previously dried during synthesis by researchers at Liverpool University. The percentage mass loss profiles are shown in **Figure 7-4** and **Figure 7-5** for Cage  $1\beta$  and Cage  $1\alpha$ , respectively. Heating was carried out over the temperature range 25 - 550°C under a nitrogen flow. For Cage  $1\beta$ , a stable mass profile is observed up to a temperature of approximately 330°C, showing that the sample is very stable under increasing temperature. After this temperature the sample degrades, over the temperature range 330 - 550°C. For Cage  $1\alpha$  a stable mass profile is apparent up to 125°C, after which there is a mass loss which corresponds to approximately 15% of the total mass, which is attributable to solvent loss. A second stable plateau is present across the temperature range 230 – 330°C, which then leads to the final degradation of the sample above a temperature of 330°C.

### 7.2.2 Scanning Electron Microscopy of Cage 1 $\beta$ and Cage 1 $\alpha$

Scanning electron microscopy (SEM) images of Cage 1 $\beta$  and Cage 1 $\alpha$  crystals at 150x magnification are shown in **Figure 7-6**. The micrograph of Cage 1 $\alpha$  shows long, thin, rectangular crystals. The micrograph for Cage 1 $\beta$  shows smaller, hexagonal crystals. The Cage 1 $\alpha$  crystals are of a smaller size to Cage 1 $\beta$ , and have aggregated into clusters.

### 7.2.3 Carbon Dioxide Adsorption Characterisation Isotherms of Cage 1 $\beta$ and Cage 1 $\alpha$

#### 7.2.3.1 Carbon Dioxide Adsorption at 195K

Carbon dioxide adsorption isotherms at 195 K were analysed by the Langmuir equation (7.1).<sup>3,4</sup>

$$\frac{P}{n} = \frac{P}{n_m} + \frac{1}{Kn_m} \quad 7.1$$

Where:

$p$  = pressure (mbar)

$n$  = amount adsorbed (g)

$n_m$  = the monolayer capacity of the material (mmol g<sup>-1</sup>)

$K$  = equilibrium rate constant

The carbon dioxide adsorption isotherm for Cage 1 $\beta$  at 195 K is shown in **Figure 7-7**, and is a typical Type I isotherm by IUPAC classification.<sup>5</sup> The Langmuir plot is shown in **Figure 7-8**. The Langmuir monolayer coverage was calculated as:  $5.80 \pm 0.0570$  mmol g<sup>-1</sup>; the Langmuir pore volume was calculated as:  $0.255 \pm 2.50 \times 10^{-3}$  cm<sup>3</sup> g<sup>-1</sup>.

The carbon dioxide adsorption isotherm at 195 K for Cage 1 $\alpha$  is shown in **Figure 7-9**. The graph follows a typical Type I IUPAC classification shape until a pressure of 800 mbar, then slight deviation occurs.<sup>5</sup> Langmuir analysis for carbon dioxide adsorption up to a pressure of 800 mbar is shown in **Figure 7-10**. Analysis gave a monolayer coverage value of  $4.55 \pm 0.0445$  mmol g<sup>-1</sup>, and a pore volume of  $0.170 \pm 1.66 \times 10^{-3}$  cm<sup>3</sup> g<sup>-1</sup>.

### 7.2.3.2 Carbon Dioxide Adsorption at 273 K

Carbon dioxide adsorption at 273 K was used to estimate the micropore volume of Cage 1 $\beta$  and Cage 1 $\alpha$  using the Dubinin – Radushkevich (DR) equation (7.2).<sup>6</sup>

$$\log n = \log n_0 - D \log^2 \left( \frac{p^0}{p} \right) \quad 7.2$$

Where:

$n$  = the volume of micropores that have been filled at a relative pressure of 1

$n_0$  = the total available micropore volume

$p$  = pressure (mbar)

$p^0$  = saturated gas pressure (mbar)

$D = B \left( \frac{T}{\beta} \right)^2$  = a measure of the pore size distribution of the adsorbent.

The isotherm is shown in **Figure 7-11**, and again is typical Type I by IUPAC classification.<sup>5</sup> The DR plot for carbon dioxide adsorption on Cage 1 $\beta$  is shown in **Figure 7-12**. The plot shows that there is no deviation from linearity across the pressure range 10 – 900 mbar, showing that the material obeys micropore filling.<sup>7</sup> The micropore volume at 273 K is calculated as  $0.187 \pm 4.54 \times 10^{-4} \text{ cm}^3 \text{ g}^{-1}$  showing that the micropore volume accounts for 73% of the total porosity.

Carbon dioxide adsorption on Cage 1 $\alpha$  at 273 K is shown in **Figure 7-13**. The isotherm is a typical Type I by IUPAC classification.<sup>5</sup> The isotherm was again analysed by the DR equation, which is shown in **Figure 7-14**. The plot shows no deviation from linearity across the pressure range 200 – 1000 mbar. The micropore volume was calculated as  $0.108 \pm 1.16 \times 10^{-3} \text{ cm}^3 \text{ g}^{-1}$ . The calculation shows that Cage 1 $\alpha$  is 64% microporous. A comparison of the pore volumes and micropore volumes, calculated using Langmuir and the DR equation, of Cage 1 $\alpha$  and Cage 1 $\beta$  is given in **Table 7-1**. The data shows that Cage 1 $\alpha$  has a smaller pore volume and micropore volume than that of Cage 1 $\beta$ .

### 7.3 Probe Molecule Studies Cage 1 $\beta$

The structural transition from Cage 1 $\beta$  to Cage 1 $\alpha$ # was investigated by the adsorption of several organic trigger molecules; ethyl acetate, 2- butanone, diethyl ether, pentane, methanol and methyl acetate. These molecules were chosen as they

## Chapter 7 Structural Change Induced by Adsorption of Gases and Vapours on Porous Cage Materials

contain oxygen atoms in varying positions, and would allow the investigation of the effect of different oxygen containing functional groups, or absence of oxygen functional groups in the case of pentane, on the transition from Cage 1 $\beta$  to Cage 1 $\alpha$ #. The adsorption isotherms and kinetics of adsorption for the organic trigger molecules were investigated. The structure of the various organic trigger molecules are shown in **Figure 7-3**.

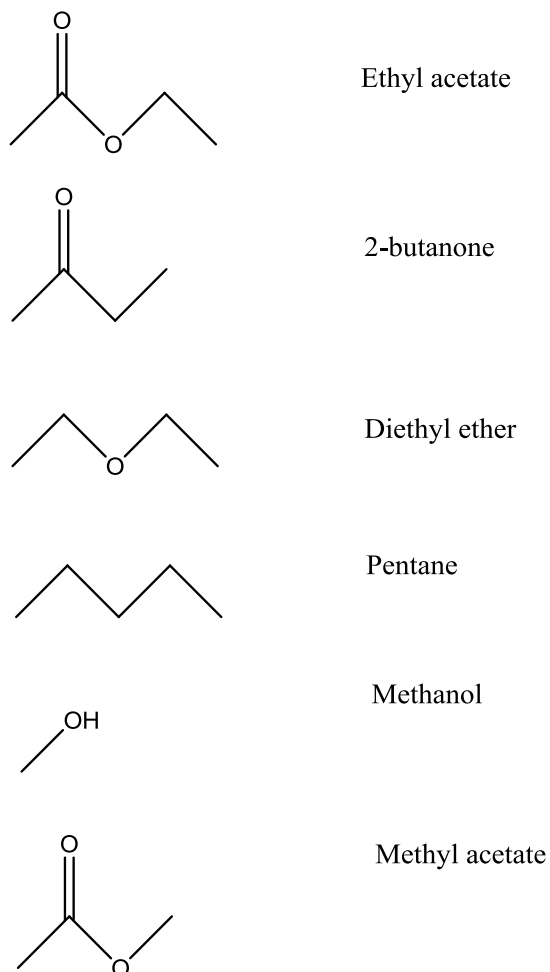


**Figure 7-3:** The structure of the organic trigger molecules used to investigate the structural change from Cage 1 $\beta$  to Cage 1 $\alpha$ #

### 7.3.1 Ethyl Acetate Adsorption on Cage 1 $\beta$

#### 7.3.1.1 Ethyl Acetate Adsorption Isotherm Analysis

The isotherm for adsorption of ethyl acetate on Cage 1 $\beta$  is shown in **Figure 7-15**, and on a relative pressure basis in **Figure 7-16**. The adsorption isotherm has an unprecedented shape. The initial section of the isotherm follows a Type I shape, up to a relative pressure of 0.150 and an ethyl acetate uptake of 1.437 mmol g<sup>-1</sup> which

## Chapter 7 Structural Change Induced by Adsorption of Gases and Vapours on Porous Cage Materials

corresponds to a volume of  $0.141 \text{ cm}^3 \text{ g}^{-1}$ , accounting for 1.14 molecules of ethyl acetate per formula unit of Cage  $1\beta$ . This is then followed by a steep uptake to a maximum ethyl acetate uptake of  $3.006 \text{ mmol g}^{-1}$  at a relative pressure of 0.219. This corresponds to a volume of  $0.295 \text{ cm}^3 \text{ g}^{-1}$  and accounting for 2.38 molecules of ethyl acetate per formula unit of Cage  $1\beta$ . After this second uptake, the isotherm then decreases to a plateau, which is an unusual feature of the adsorption isotherm. The desorption profile for the pressure step 35 – 40 mbar is shown in **Figure 7-17**. The amount of ethyl acetate adsorbed after this decrease falls to  $2.668 \text{ mmol g}^{-1}$ , which is a volume of  $0.262 \text{ cm}^3 \text{ g}^{-1}$  and corresponds to 2.16 molecules of ethyl acetate per formula unit. This mass loss is associated with the desorption of ethyl acetate molecules as the structure undergoes a change to Cage  $1\alpha\#$ , the equivalent to Cage  $1\alpha$  that is prepared by adsorption of ethyl acetate in the IGA under pressure instead of by preparation by vapour diffusion in a sample vial. The uptake at the maximum pressure used of 148 mbar (relative pressure of 0.92) was  $2.784 \text{ mmol g}^{-1}$ ; giving a total pore volume of  $0.273 \text{ cm}^3 \text{ g}^{-1}$ , assuming the density of ethyl acetate is  $0.897 \text{ g cm}^{-3}$ . The ethyl acetate desorption isotherm is hysteretic, following a Type I desorption profile.

The repeat isotherm of ethyl acetate on Cage  $1\beta$  is also shown in **Figure 7-15**. The isotherm follows the same step at a relative pressure of 0.150 and an ethyl acetate uptake of  $1.435 \text{ mmol g}^{-1}$ ; however the step is to an uptake of  $2.539 \text{ mmol g}^{-1}$  at a relative pressure of 0.167. The desorption step observed in run 1 was not present in run 2, indicating that the structural rearrangement of Cage  $1\beta$  to Cage  $1\alpha\#$  is permanent and does not reverse upon desorption of ethyl acetate. The desorption profile for run 2 is also hysteretic, and follows the same desorption path as run 1.

### 7.3.1.2 Ethyl Acetate Adsorption on Cage $1\beta$ Desorption Step Kinetics Analysis

The kinetics of crystallisation has been previously described by Avrami<sup>8,9,10</sup> and the Kolmogorov-Johnson-Mehl-Avrami or KJMA equation.<sup>11</sup> The equation is given in equation 7.3 and is apparent that it is related to the stretched exponential equation.

$$\frac{M_t}{M_e} = 1 - e^{(-kt)^\beta} \quad 7.3$$

Where:



## Chapter 7 Structural Change Induced by Adsorption of Gases and Vapours on Porous Cage Materials

$M_t$  = the amount adsorbed (g) at time  $t$  (s)

$M_e$  = the equilibrium uptake (g)

$k$  = rate constant ( $s^{-1}$ )

$t$  = time (s)

$\beta$  = the Avrami exponential parameter

Although the stretched exponential and the Avrami equations are similar, the Avrami exponent  $\beta$  should be an integer between 1 and 4, and the rate constant is independent of this parameter, whilst in the stretched exponential model the exponent is fixed as  $0.5 < \beta < 1$ . The value  $\beta$  is based upon the nucleation mechanism and the dimensionality of the growth of crystals.<sup>12</sup> The Avrami equation was used to analyse all desorption kinetics to assess the rate constant for the desorption step and to determine differences in  $\beta$  parameter values – this will give an indication to differences in the crystalline to crystalline changes. The desorption profile for the step in the ethyl acetate adsorption isotherm at 303 K is shown in **Figure 7-18**. The desorption step took approximately 45 hours to complete. The rate constant for this desorption step is  $2.00 \times 10^{-5} \pm 2.73 \times 10^{-8} s^{-1}$ , with an Avrami  $\beta$  parameter of  $1.37 \pm 0.003$ . The residuals for the fit of the Avrami equation to the data are within 2%, showing that the Avrami model is a good description of the data.

### 7.3.1.3 Ethyl Acetate Adsorption on Cage 1 $\beta$ and Cage 1 $\alpha$ # Kinetic Analysis

The ethyl acetate adsorption kinetics were analysed using the stretched exponential (SE) model in the following form (equation 7.4).<sup>13</sup>

$$\frac{M_t}{M_e} = A_0 \left( 1 - e^{-(kt)^\beta} \right) \quad 7.4$$

Where:

$M_t$  = the amount adsorbed (g) at time  $t$  (s)

$M_e$  = the equilibrium uptake (g)

$k$  = rate constant ( $s^{-1}$ )

$t$  = time (s)

$\beta$  = the exponential parameter

$A_0$  = parameter for fitting purposes ( value of 1 when data is normalised)

## Chapter 7 Structural Change Induced by Adsorption of Gases and Vapours on Porous Cage Materials

According to Klafter and Schlesinger,  $\beta$  values of 1 indicate a three dimensional model, with a single relaxation time, and that the rate determining step is due to diffusion through a barrier at the pore entrance.<sup>13</sup> Stretched exponential  $\beta$  values of 0.5 indicate a one dimensional model with a distribution of relaxation times. Values between 1 and 0.5 indicate a two dimensional model. All kinetic adsorption profiles of ethyl acetate adsorption analysed by the stretched exponential model can be found in **CD Appendix B – Molecular Cage Materials**. The kinetic profiles analysed using the stretched exponential equation for ethyl acetate adsorption on both Cage 1 $\beta$  and Cage 1 $\alpha\#$  for the pressure increment 0.5 – 1.0 mbar at 303 K are shown in **Figure 7-19** and **Figure 7-20**, respectively. It is apparent from the profiles that ethyl acetate adsorption at this pressure increment is much slower for Cage 1 $\alpha\#$  than Cage 1 $\beta$ . Equilibration is reached after approximately 2 hours for Cage 1 $\beta$  whereas Cage 1 $\alpha\#$  takes approximately 4 days for equilibration. The rate constants and SE  $\beta$  parameters for ethyl acetate adsorption on Cage 1 $\beta$  and Cage 1 $\alpha\#$  are given in **Table 7-2** and **Table 7-3**, respectively. The corresponding comparison plots of rate constant are given in **Figure 7-21** and SE  $\beta$  parameters are given in **Figure 7-22**. The rate constant for EtOAc adsorption on Cage 1 $\alpha\#$  is much smaller than for EtOAc adsorption on Cage 1 $\beta$  for the initial part of the isotherm. During the step in the adsorption isotherm on Cage 1 $\beta$ , for the pressure increments 20 – 25 mbar and 25 – 28 mbar, there is a drop in the rate constant, as shown in **Figure 7-23**. The SE  $\beta$  parameters for EtOAc adsorption on Cage 1 $\beta$  increase from 0.5 to 1 throughout the initial part of the isotherm. For EtOAc adsorption on Cage 1 $\alpha\#$  the SE  $\beta$  parameters remain at 0.5 for the duration of the isotherm. The difference in the rates of adsorption of EtOAc and the difference in the SE  $\beta$  parameters indicate that the structure of Cage 1 $\beta$  has changed, and that Cage 1 $\alpha\#$  is formed during the EtOAc adsorption on Cage 1 $\beta$ . The slow rates of adsorption on Cage 1 $\alpha\#$  are indicative of a narrowing of the porosity. Narrow pores are crucial for kinetic molecular sieving of similar sized molecules. The kinetic molecular sieving of oxygen and nitrogen by Cage 1 $\alpha\#$  is investigated in **Chapter 8 – Kinetic Molecular Sieving of Oxygen and Nitrogen by Organic Cage Materials Cage 1 $\alpha$  and Cage 1 $\alpha\#$** .

Due to the large amount of time required for equilibration of ethyl acetate adsorption, the effects of methyl acetate adsorption on Cage 1 $\beta$  were studied further,

as the smaller molecule contains the same functionality, with the decrease in size facilitating faster diffusion. The methyl acetate investigation is given in **7.4 Methyl Acetate Adsorption**.

### 7.3.2 2-butanone and Diethyl Ether Adsorption on Cage 1 $\beta$

#### 7.3.2.1 2-butanone and Diethyl Ether Adsorption Isotherm Analysis

The adsorption isotherm for the adsorption of 2-butanone on Cage 1 $\beta$  at 298 K is shown in **Figure 7-24** and on a relative pressure basis in **Figure 7-25**. This isotherm again shows an unprecedented desorption step within the adsorption isotherm. A step in the isotherm occurs at a 2-butanone uptake of 1.37 mmol g<sup>-1</sup> at a relative pressure of 0.043. This corresponds to 1.08 molecules of 2-butanone per formula unit, and a volume of 0.122 cm<sup>3</sup> g<sup>-1</sup>. At the end of the second plateau the 2-butanone uptake was 3.18 mmol g<sup>-1</sup> at a relative pressure of 0.255, corresponding to a volume of 0.285 cm<sup>3</sup> g<sup>-1</sup>, and 2.52 molecules of 2-butanone per formula unit. After the desorption step the amount of 2-butanone adsorbed reduces to 2.79 mmol g<sup>-1</sup> at a relative pressure of 0.34, with a reduced volume of 0.250 cm<sup>3</sup> g<sup>-1</sup>, and 2.21 molecules per formula unit. At the end of the isotherm at a maximum pressure of 110 mbar the amount of 2-butanone adsorbed is 2.93 mmol g<sup>-1</sup>, which is a final total pore volume of 0.263 cm<sup>3</sup> g<sup>-1</sup>.

The isotherm for the adsorption of diethyl ether on Cage 1 $\beta$  is shown in **Figure 7-26** and on a relative pressure basis in **Figure 7-27**. The adsorption isotherm again also shows a step at low relative pressure and the unusual desorption step at higher relative pressure. The first plateau occurs at a diethyl ether uptake of 1.50 mmol g<sup>-1</sup> at a relative pressure of 0.105, corresponding to 1.19 molecules of diethyl ether per formula unit and a volume of 0.156 cm<sup>3</sup> g<sup>-1</sup>. The desorption step occurs at the end of the second plateau, at a diethyl ether uptake of 3.16 mmol g<sup>-1</sup> and a relative pressure of 0.562, corresponding to a volume of 0.328 cm<sup>3</sup> g<sup>-1</sup>, and 2.50 molecules per formula unit. After this desorption the amount of diethyl ether adsorbed is 2.97 mmol g<sup>-1</sup>; corresponding to 2.35 molecules of diethyl ether per formula unit and a volume of 0.308 cm<sup>3</sup> g<sup>-1</sup>. At a maximum pressure of 700 mbar the diethyl ether uptake is 3.05 mmol g<sup>-1</sup>; corresponding to a total pore volume of 0.317 cm<sup>3</sup> g<sup>-1</sup> and 2.42 molecules of diethyl ether per formula unit. The desorption isotherm is hysteretic, following a Type I desorption profile.

### 7.3.2.2 2-butanone and Diethyl Ether Adsorption Desorption Step Kinetics Analysis

The desorption step in the 2-butanone isotherm occurs at the pressure step 30 – 40 mbar, and is shown in **Figure 7-28**. The Avrami analysis of the desorption profile of 2-butanone desorption from Cage 1 $\beta$  is shown in **Figure 7-29**. The rate constant for this desorption step is  $1.70 \times 10^{-4} \pm 7.15 \times 10^{-7} \text{ s}^{-1}$ , showing a faster desorption step than that observed for ethyl acetate desorption at 303 K.

The desorption step in the diethyl ether isotherm occurs at the pressure step 400 – 500 mbar, and is shown in **Figure 7-30**. The Avrami analysis of the desorption profile of diethyl ether desorption from Cage 1 $\beta$  is shown in **Figure 7-31**. The rate constant for this desorption step is  $2.00 \times 10^{-4} \pm 4.66 \times 10^{-7} \text{ s}^{-1}$ . This shows a similar rate of desorption to that of 2-butanone, and again a faster desorption rate than ethyl acetate.

### 7.3.2.3 2-butanone and Diethyl Ether Adsorption Kinetic Analysis

Adsorption kinetics of 2-butanone adsorption on Cage 1 $\beta$  were analysed by the stretched exponential equation. All kinetic profiles of 2-butanone adsorption analysed by the stretched exponential model can be found in **CD Appendix B – Molecular Cage Materials**. The kinetic profile for the pressure step 2.00 – 5.00 mbar analysed by the stretched exponential equation is shown in **Figure 7-32**. A table of stretched exponential parameters for the isotherm up to a pressure of 20 mbar is shown in **Table 7-4**.

Adsorption kinetics of diethyl ether adsorption on Cage 1 $\beta$  were also analysed by the stretched exponential equation. All kinetic profiles of diethyl ether adsorption analysed by the stretched exponential model can be found in **CD Appendix B – Molecular Cage Materials**. The kinetic profile for the pressure step 5.00 – 10.00 mbar analysed by the stretched exponential profile is shown in **Figure 7-33**. A table of stretched exponential parameters for the isotherm up to a pressure of 175 mbar is shown in **Table 7-5**.

### 7.3.2.4 Comparison of Ethyl Acetate, 2-butanone and Diethyl Ether Adsorption on Cage 1 $\beta$

Ethyl acetate, 2-butanone and diethyl ether adsorption on Cage 1 $\beta$  all give similar shaped isotherms, containing unprecedented desorption steps within the adsorption

## Chapter 7 Structural Change Induced by Adsorption of Gases and Vapours on Porous Cage Materials

isotherm. A comparison of the adsorption isotherms is given in **Figure 7-34**, on a vapour volume basis in **Figure 7-35** and as a comparison of the number of molecules adsorbed per formula unit in **Figure 7-36**. The data at various important sections of the isotherm are presented in **Table 7-6**. The data for the three vapours is similar, with the various sections of the isotherms occurring at slightly different relative pressures, but resulting in similar uptakes and number of molecules per formula unit. At maximum relative pressures above 0.9, ethyl acetate shows the lowest number of molecules per formula unit, with diethyl ether showing the highest number of molecules per formula unit. The similar uptake and number of molecules adsorbed per formula unit at various points along the isotherm show that the vapours are all being adsorbed into the same pore space within the material. The similar pore volumes at the end of the isotherm, after the structural transition to Cage 1 $\alpha$ # has occurred, show that the vapours induce a structural change which give a structure with similar pore volumes for each vapour, indicating that the structure formed on exposure of the Cage to these three vapours is similar.

The analysis of the adsorption kinetics of ethyl acetate, 2-butanone and diethyl ether on Cage 1 $\beta$  up to the pressure before the desorption step show similar characteristics. The graph of rate constant against vapour uptake is shown in **Figure 7-37**. For the three vapours, the rate constant increases during the initial uptake to the first plateau. This is then followed by a slow uptake during the step to the second plateau, after the plateau is reached the rate constant increases again until the desorption step due to small uptakes with increasing pressure on the plateau. The graph of stretched exponential  $\beta$  parameter against vapour uptake is shown in **Figure 7-38**. The three vapours follow the same trend, of an increase in the  $\beta$  parameter from 0.55 to 1.00 up to a vapour uptake of  $\sim 1.50 \text{ mmol g}^{-1}$ . After the second uptake step in the isotherm, the  $\beta$  parameter remains between 0.8 and 1 up to uptakes of  $\sim 3.25 \text{ mmol g}^{-1}$ , before the desorption steps occur. This indicates that the diffusion mechanism changes during the initial step of the isotherms for all three vapours, the mechanism changes from three dimensional with a distribution of relaxation times to one dimensional, with one relaxation time, indicating that the rate determining step is diffusion through constrictions at the pore entrance.

The similarity in the variation of the adsorption rate constant and stretched exponential  $\beta$  parameter with amount adsorbed shows that the vapours all have a similar effect on the framework, with the adsorption process changing from three dimensional to one dimensional across the initial parts of the isotherms. This indicates that a structural change occurs during the second step of the isotherms. Further structural rearrangement occurs during the desorption step on the plateau, where structural rearrangement forces the loss of vapour from the porous structure. The loss of ethyl acetate occurs at a slower rate than the 2 – butanone and diethyl ether, indicating that ethyl acetate has a stronger interaction with the Cage material.

### 7.3.3 Pentane and Methanol Adsorption on Cage 1 $\beta$

The pentane isotherms at 298 K for Cage 1 $\beta$  are shown in **Figure 7-40** and in **Figure 7-41** on a relative pressure basis. The isotherm is Type I to a pressure of 400 mbar where a step occurs in the isotherms. The amount of pentane adsorbed before this step is 1.43 mmol g<sup>-1</sup>; corresponding to a volume of 0.165 cm<sup>3</sup> g<sup>-1</sup> and 1.21 molecules of pentane per formula unit. After the step the amount of pentane adsorbed increases to 2.733 mmol g<sup>-1</sup>, corresponding to a pore volume of 0.315 cm<sup>3</sup> g<sup>-1</sup> and 1.54 molecules of pentane per formula unit at a maximum pressure of 700 mbar. The pentane adsorption isotherms show no desorption step in the adsorption profile. The step in the adsorption profile and the hysteretic nature of the desorption profile indicate that a structural change is occurring, however it occurs without the unprecedented loss of mass as seen for ethyl acetate, 2-butanone and diethyl ether adsorption.

The methanol isotherm at 303 K for Cage 1 $\beta$  is shown in **Figure 7-42** and on a relative pressure basis in **Figure 7-43**. The isotherm contains a point of inflection at 40 mbar. The total uptake is 7.96 mmol g<sup>-1</sup>; corresponding to a pore volume of 0.322 cm<sup>3</sup> g<sup>-1</sup> and 4.50 molecules of methanol per formula unit. The desorption profile for methanol is not hysteretic, suggesting that methanol does not induce any structural change, and there is no desorption step present within the adsorption isotherm, with increasing pressure.

A comparison of the isotherms collected for pentane, methanol and ethyl acetate adsorption on a vapour volume uptake basis on Cage 1 $\beta$  is shown in **Figure 7-44**.

## Chapter 7 Structural Change Induced by Adsorption of Gases and Vapours on Porous Cage Materials

This comparison shows that the isotherms for the three vapours are quite different. The pentane isotherm is typical Type I, with a large hysteresis. Methanol shows an isotherm with a point of inflection in the shape of the curve, and shows no hysteresis. Both pentane and methanol give the same total pore volumes, of  $0.314 \text{ cm}^3 \text{ g}^{-1}$  which is higher than the total pore volume found at the end of the ethyl acetate isotherm,  $0.273 \text{ cm}^3 \text{ g}^{-1}$ .

Examples of kinetic profiles fit to the stretched exponential model are shown in **Figure 7-45** and in **Figure 7-46** for pentane and methanol, respectively. The data from the stretched exponential analysis of all kinetic points in the pentane and methanol isotherms are given in **Table 7-7** and **Table 7-8**. A comparison of the stretched exponential rate constant for pentane, methanol and ethyl acetate adsorption is given in **Figure 7-47**. The pentane adsorption kinetics increase as the isotherm progresses to values of  $6.87 \times 10^{-3} \text{ s}^{-1}$ . At a pressure of 400 mbar the rate constant decreases significantly, to  $5.00 \times 10^{-5} \text{ s}^{-1}$ . The methanol kinetic rate constants decrease as the isotherm approaches the point of inflection, with a rate at this point of  $4.5 \times 10^{-4} \text{ s}^{-1}$ . From a pressure of 80 mbar the rate constants increase and remain at a similar value for the remainder of the isotherm. The rate of methanol adsorption is greater than the rate of pentane adsorption, due to methanol having a smaller cross sectional area than pentane.

A comparison of the stretched exponential  $\beta$  parameter for pentane, methanol and ethyl acetate adsorption is given in **Figure 7-48**. As the ethyl acetate adsorption isotherm progresses, the  $\beta$  value increases from 0.566 to values above 0.80 indicating a change from a three dimensional process to a one dimensional, indicating a change in the structure which leads to a constriction in the entrance to the porosity, so that there is a single relaxation time. The  $\beta$  parameter for pentane also starts at a lower value of 0.62; this then increases to 1, and then decreases to values between 0.60 and 0.80 for the duration of the isotherm. The methanol  $\beta$  parameter remains between 0.75 and 1.00 for the duration of the isotherm.

The powder X-ray diffraction pattern for Cage  $1\beta$  loaded with pentane compared to desolvated Cage  $1\alpha$  is shown in **Figure 7-49**. The powder diffraction patterns do not match, indicating that pentane does not induce a structural transition to Cage  $1\alpha$ .

The difference in the shapes of the isotherms for ethyl acetate, pentane and methanol adsorption, absence of the desorption step within the adsorption isotherm for pentane and the difference in rate constants and stretched exponential  $\beta$  parameters, indicates that pentane does not have the same structural effect on the framework which occurs on adsorption of ethyl acetate. Pentane instead leads to the formation of a different Cage 1 polymorph, which is supported by the difference in the powder diffraction patterns when compared with Cage 1 $\alpha$ . Methanol shows no hysteresis or significant change in  $\beta$  parameter to indicate any kind of structural effect on Cage 1 $\beta$ .

#### 7.4 Methyl Acetate Adsorption Studies on Cage 1 $\beta$

Structural rearrangement by vapour diffusion using the “vial within vial” method was achieved by researchers at Liverpool University using the diffusion of ethyl acetate. Ethyl acetate adsorption into the material is a very slow process. To investigate the structural rearrangement induced by the acetate group, the adsorption isotherms of methyl acetate adsorption on Cage 1 $\beta$  were measured. Methyl acetate is smaller than ethyl acetate, and as such produced faster kinetics, allowing a larger volume of data to be gathered for analysis.

##### 7.4.1 Methyl Acetate Adsorption on Cage 1 $\beta$ Isotherm Analysis

Methyl acetate adsorption isotherms were collected for the temperature range 268 – 313 K in 5 K intervals. The methyl acetate isotherm collected at 303 K is shown in **Figure 7-50**. The isotherm shows a step at a methyl acetate uptake of 1.59 mmol g<sup>-1</sup>. This step increases to plateau. At the end of this plateau at a pressure of 100 mbar and an uptake of 3.53 mmol g<sup>-1</sup> the desorption step occurs. This decreases to amount of methyl acetate adsorbed to 3.24 mmol g<sup>-1</sup>. The amount adsorbed, at the maximum pressure of 350 mbar, is 3.49 mmol g<sup>-1</sup> which gives a pore volume of 0.277 cm<sup>3</sup> g<sup>-1</sup>. The desorption isotherm is hysteretic. A comparison of methyl acetate and ethyl acetate adsorption isotherms is given in **Figure 7-51**. The first step in the isotherms occurs at similar uptakes, the step initiates at a lower relative pressure for methyl acetate, with methyl acetate reaching a lower maximum volume adsorbed before the desorption step. At maximum relative pressures the volume of vapours adsorbed is very similar, 0.277 cm<sup>3</sup> g<sup>-1</sup> for methyl acetate and 0.273 cm<sup>3</sup> g<sup>-1</sup> for ethyl acetate. A comparison of the number of molecule of ethyl acetate and methyl acetate is given in **Figure 7-52**. From this comparison it is apparent that there are more molecules of



methyl acetate adsorbed per formula unit of Cage 1 $\beta$ , which is expected as methyl acetate has a smaller cross sectional area, and as such more molecules can pack into the porosity than ethyl acetate. **Figure 7-53** shows the adsorption isotherms for methyl acetate on Cage 1 $\beta$  for the temperature range 268 - 313 K. The isotherms were repeatable, with deviations occurring only for the lowest temperature of 268 and 273 K and the highest temperature 313 K. The isotherms show that as temperature decreases, the relative pressure at which the desorption step occurs increases. The desorption step for the isotherm at 313 K occurs at a relative pressure of 0.211. The isotherms for 278 – 308 K show desorption steps at a relative pressure of 0.280, the desorption steps for 273 K and 268 K occur at relative pressures of 0.420 and 0.500, respectively. This shows there is some temperature dependency on the relative pressures at which desorption occurs.

#### 7.4.2 Methyl Acetate Adsorption on Cage 1 $\beta$ Enthalpy and Entropy Calculations

The isotherms for the temperature range 278 – 308 K were used to calculate the enthalpy and entropy of methyl acetate adsorption (**Figure 7-54**). The enthalpy of adsorption was calculated using the van't Hoff isochore, equation, 7.5:<sup>14</sup>

$$\ln P = - \frac{\Delta \dot{H}_a}{RT} + \frac{\Delta S}{R} \quad 7.5$$

This equation represents the relationship between pressure and temperature for a given amount adsorbed. By obtaining isotherms at a series of temperatures, for a set value of amount adsorbed,  $n_a$  (mmol g<sup>-1</sup>), a plot of  $\ln P$  against  $1/T$  (K<sup>-1</sup>) may be obtained, and the value of the enthalpy of adsorption can be calculated directly from the gradient of this plot, gradient =  $\Delta H/R$ . The value of the entropy of adsorption can be calculated from the intercept of the plot, intercept =  $\Delta S/R$ . A plot of the variation of enthalpy and entropy of methyl acetate adsorption with surface coverage on Cage 1 $\beta$  for the temperature range 278 – 303 K is shown in **Figure 7-55**. At low surface coverage the enthalpy of adsorption is close to the enthalpy of vaporisation of methyl acetate, 32.7 kJ mol<sup>-1</sup>. The plot shows an increase in enthalpy of adsorption from  $32.7 \pm 5.2$  to  $49.7 \pm 2.5$  kJ mol<sup>-1</sup>, from the initial adsorption to an amount of methyl acetate adsorbed of 1.50 mmol g<sup>-1</sup>. The enthalpy of adsorption then remains constant as the amount adsorbed increases, to 2.70 mmol g<sup>-1</sup>. As the amount adsorbed approaches the maximum, which occurs prior to the desorption step, the enthalpy of

## Chapter 7 Structural Change Induced by Adsorption of Gases and Vapours on Porous Cage Materials

adsorption begins to decrease, and then there is a sharp increase as the amount adsorbed reaches a maximum. The enthalpy of adsorption at the maximum amount adsorbed is  $58.3 \pm 1.8 \text{ kJ mol}^{-1}$ . As the isotherm approaches the desorption step, the entropy becomes more negative, from values of  $-179.2 \pm 2.5$  to  $-229.6 \pm 1.8 \text{ J K}^{-1} \text{ mol}^{-1}$ . This indicates that as the isotherm approaches the desorption step the system is ordering, through an increase in the strength of adsorbate-adsorbate interactions. After the maximum uptake is reached and the desorption occurs, the isosteric enthalpy and entropy values become unreliable due to low uptakes on the plateau and possible only partial transformation of the sample to Cage 1 $\alpha$ #.

A similar phenomenon has been observed by Buckton and Darcy during the crystallisation of lactose, during which adsorbed water in the lactose is desorbed, leading to the observation of a desorption step in the isotherm, as shown through water adsorption experiments on mixtures of amorphous and crystalline  $\alpha$ -lactose monohydrate.<sup>15</sup> The initial isotherm shows a large increase in mass as water is absorbed into the amorphous regions of the mixture as well as being adsorbed onto the surface of the crystalline component of the mixture. The water absorbed by the amorphous component causes recrystallization of the amorphous material, desorbing the water from the material and resulting in mass loss. Isotherms on this crystalline sample show no desorption of water as all amorphous components have been recrystallized.<sup>15</sup> The solid-phase crystallisation growth kinetics of dried lactose has also been investigated recently by Das and Langrish<sup>16</sup> who investigated the thermodynamic effects of loss of moisture during recrystallization of amorphous lactose. When the interaction of the monolayer and subsequent multilayer molecules decreases, the enthalpy of adsorption decreases and moisture is released during crystallisation. The experiments of Das and Langrish show that there is a steady increase in moisture content to a peak, after which there is a steady decrease in moisture content until a constant value is reached, which is a similar description to the adsorption of ethyl acetate, methyl acetate, 2-butanone and diethyl ether on Cage 1 $\beta$ . At peak moisture content in the lactose experiments, it is suggested that the particles of lactose will have sufficient activation energy to initiate the process of crystallisation, starting with the desorption of moisture from the amorphous state and then the subsequent rearrangement of the particles crystalline state.<sup>16</sup>

### 7.4.3 Methyl Acetate on Cage 1 $\beta$ Kinetic Analysis

The kinetics for the pressure steps for the adsorption of methyl acetate across the temperature range 278 – 308 K fit the shapes of the isotherms well. The variation of rate constant with methyl acetate uptake on cage 1 $\beta$  is shown in **Figure 7-56**. As the first plateau is reached, at uptakes of  $\sim 1.5 \text{ mmol g}^{-1}$ , the rate constant increases, as the uptake becomes smaller. During the second step the rate constant decreases, as the structure allows larger volumes of methyl acetate to be adsorbed. As the second plateau is reached the rate constant again increases, as the uptake becomes smaller, to the point where the desorption step occurs. The stretched exponential  $\beta$  parameters for the temperature range 268 – 313 K are shown in **Figure 7-57**, this figure shows that across the temperature range the  $\beta$  values remain between mostly in the range of 0.6 – 1.0. This indicates a two dimensional process where diffusion into the porosity can be defined by both diffusion through a barrier at the entrance to the porosity and by diffusion of the methyl acetate across the surface of the pores in a site-to-site hopping mechanism.

The  $\ln(k)$  against the amount of methyl acetate adsorbed graph is shown in **Figure 7-58**. The graph shows a slight trend with temperature, the rate constant increases with increasing temperature; however the values are all of a very similar order of magnitude, indicating that there is low activation energy for adsorption into the material. If the activation energy is significantly lower than the isosteric enthalpy of adsorption, then the diffusion of the methyl acetate molecules along the pore would be controlled by the site-to-site hopping mechanism on the surface of the pore, rather than by diffusion through a constriction into the porosity.

### 7.4.4 Kinetics of Methyl Acetate Desorption Step

The Avrami equation was again used to model the desorption step in each of the methyl acetate isotherms for the temperature range 278 – 308 K, the profiles for which are shown in **Figure 7-59** to **Figure 7-65**. The model fits all of the profiles within 8%, showing that the model is a good description of the data. The Avrami exponents for the temperature range are within the range of  $1.19 \pm 0.015$  and  $1.46 \pm 0.0078$ , as shown in **Table 7-9**.

From the desorption profiles across the temperature range 278 – 303 K, the activation energy of desorption can be calculated. The graph of  $\ln(k)$  against reciprocal temperature is shown in **Figure 7-66**. From this the activation energy for methyl acetate desorption from Cage 1 $\beta$  is calculated as  $42.5 \pm 6.2 \text{ kJ mol}^{-1}$ . This kinetic barrier is much lower than the isosteric enthalpy of adsorption indicating that diffusion from the surface of the pore is the rate determining step for the structural change.

Each desorption step is accompanied by a stable adsorption step both before and after the desorption step, as shown in **Figure 7-67**. The adsorption before and after the desorption step is always a small uptake. A comparison of the desorption profile for the different adsorbates, ethyl acetate, 2-butanone, diethyl ether and methyl acetate is shown in **Figure 7-68**. The desorption step for each vapour occurs at different relative pressures, with ethyl acetate occurring at the lowest relative pressure of 0.219, and diethyl ether occurring at the higher relative pressure of 0.562, with 2-butanone desorption occurring at 0.255. It is apparent the ethyl acetate has the longest desorption time of just over 160,000 seconds to reach stable mass, methyl acetate desorbs from Cage 1 $\beta$  at a faster rate than the other three vapours, with an equilibration time of 5,000 seconds compared to 30,000 for 2-butanone and 14,000 for diethyl ether. Parameters calculated from the Avrami analysis for the desorption kinetics are shown in **Table 7-10**. The rate constant for ethyl acetate is  $2.0 \times 10^{-5} \pm 2.7 \times 10^{-8} \text{ s}^{-1}$ , for 2-butanone is  $1.7 \times 10^{-4} \pm 7.2 \times 10^{-7} \text{ s}^{-1}$ , for diethyl ether is  $2.0 \times 10^{-4} \pm 4.7 \times 10^{-7} \text{ s}^{-1}$  and for methyl acetate is  $4.7 \times 10^{-4} \pm 7.4 \times 10^{-7} \text{ s}^{-1}$ . The rate constant decreases in the order methyl acetate  $\rightarrow$  diethyl ether  $\rightarrow$  2-butanone  $\rightarrow$  ethyl acetate.

### 7.5 Methyl Acetate Adsorption on Cage 1 $\alpha$ #

In the case of methyl acetate adsorption on Cage 1 $\beta$ , after the structural transition the isosteric enthalpy of adsorption values became unreliable due to the low uptakes for each pressure step on the plateau and partial conversion from Cage 1 $\beta$  to Cage 1 $\alpha$ #. Methyl acetate adsorption was investigated on Cage 1 $\alpha$ # after conversion and exposure to methyl acetate at  $p/p_0 = 0.98$  in order to establish thermodynamic effects on the conversion of Cage 1 $\beta$  to Cage 1 $\alpha$ # involving the unusual desorption step with increasing pressure.

### 7.5.1 Methyl Acetate Adsorption on Cage 1 $\alpha$ # Isotherm Analysis

**Figure 7-69** shows the adsorption isotherm for methyl acetate on Cage 1 $\alpha$ # at 298 K. The isotherm shows two step uptake sections during the initial part of the isotherm, which are separated by a small plateau. The small plateau occurs across the pressure range 5.00 – 30.00 mbar. After the second steep uptake section stable plateau is reached to a pressure of 250 mbar. At this point the isotherm is at high relative pressure, and condensation of methyl acetate into the pores causes a sharp increase in the amount adsorbed. The desorption path closely follows the adsorption back to a pressure of 50 mbar, where slight deviation occurs. The shape of the isotherm is repeatable at increasing temperature, as shown in **Figure 7-70** and in **Figure 7-71** on a relative pressure basis for the temperature range 298 – 313 K. The shape of the Cage 1 $\alpha$ # isotherm is similar to that of Cage  $\beta$  in having a step around 1 - 1.2 molecules of methyl acetate adsorbed per formula unit of cage.

The isotherms show a consistent shape with increasing temperature. The equilibration was good above 2.5 mmol g<sup>-1</sup>, which is the uptake range where the structural change for methyl acetate adsorption on Cage 1 $\beta$  occurs. This is the important region for understanding the thermodynamic process in the structural transition. However, despite using long equilibration times of 8 to 15 hours, the isotherm points failed to reach equilibrium on the steep part of the isotherm, where the chemical potential gradient is low. Estimates of equilibrium times from the kinetic data showed that isotherm measurements for a single temperature could take over a month or more. This is not surprising since Cage 1 $\alpha$ # exhibits kinetic molecular sieving of O<sub>2</sub> and N<sub>2</sub> (see **Chapter 8**). However on the plateau at high pressure, where the chemical potential gradient is highest, the isotherm points did equilibrate satisfactorily. This is the most important isotherm region for comparison with Cage 1 $\beta$ , where the structural change occurs from Cage 1 $\beta$  to Cage 1 $\alpha$ #, which results in the unprecedented desorption step, for a porous material, with increasing pressure.

The enthalpy and entropy of methyl acetate on Cage 1 $\alpha$ # were again calculated using the van't Hoff equation. The variation of the enthalpy and entropy of adsorption with increasing amount of methyl acetate adsorbed is shown in **Figure 7-72**. There

are large errors in the enthalpy and entropy calculations at low surface coverage, and the calculated isosteric enthalpy of adsorption is lower than that of the enthalpy of vaporisation of methyl acetate, which is  $32.67 \text{ kJ mol}^{-1}$ . This is due to failure to reach equilibration in the kinetic profiles for methyl acetate uptakes below  $2.5 \text{ mmol g}^{-1}$  and at low pressure, where equilibration is not reached even after 8 – 15 hours duration per point on the isotherm. A typical example of a kinetic profile which does not equilibrate is shown in **Figure 7-73**. This is attributed to the very narrow pores present in Cage 1 $\alpha$ #. As the surface coverage increases, the standard deviation in enthalpy and entropy decreases with increasing amounts adsorbed. These values have smaller errors and are justified in their calculation as the kinetic profiles for steps above uptakes of  $2.5 \text{ mmol g}^{-1}$  all show good equilibration, examples of which are shown in **Figure 7-74** to **Figure 7-77**, and all show linear van't Hoff plots, as shown in **Figure 7-78** for uptakes of 2.5, 2.8, 3.0 and  $3.2 \text{ mmol g}^{-1}$  of methyl acetate on Cage 1 $\alpha$ #. On the plateau of the isotherm, at  $2.6 \text{ mmol g}^{-1}$  uptake of methyl acetate, the isosteric enthalpy is  $36.69 \pm 4.66 \text{ kJ mol}^{-1}$ , and the entropy is  $-148 \pm 17 \text{ J K}^{-1} \text{ mol}^{-1}$ . At higher uptakes of  $3.0 \text{ mmol g}^{-1}$  the isosteric enthalpy increases to  $88.72 \pm 1.7 \text{ kJ mol}^{-1}$ . This indicates an increase in the strength of the interactions between the adsorbate molecules and the adsorbent structure. As the isosteric enthalpy of adsorption increases, the entropy becomes more negative, indicating an ordering of the system toward the end of the isotherm. As saturation begins to occur at maximum methyl acetate loading, the entropy becomes less negative (the system disorders) and the enthalpy decreases.

#### 7.5.2 Methyl Acetate Adsorption on Cage 1 $\alpha$ # Kinetic Analysis

**Figure 7-79** shows the variation with the rate constant for methyl acetate adsorption on Cage 1 $\alpha$ #. Up to a methyl acetate uptake of  $2.5 \text{ mmol g}^{-1}$  the rate of adsorption is very slow, with rate constants in the region of  $\sim 5.00 \times 10^{-6} \text{ s}^{-1}$ . Many kinetic points in this region did not equilibrate over twelve hours. This was especially apparent over the region of curvature, where there are estimated rate constants of  $4 \times 10^{-10} \text{ s}^{-1}$ . As the plateau is reached the rate constant increases, as less methyl acetate is adsorbed into the system. The stretched exponential  $\beta$  parameter shows variation over the extent of the isotherm. Over the steep uptake section where there is s-shaped curvature the  $\beta$  parameter drops to 0.5. This then increases to values between

0.70 and 1.00 as the plateau is approached. Above methyl acetate uptakes of 2.5 mmol g<sup>-1</sup>, after which all kinetic points have equilibrated, the  $\beta$  value decreases back to 0.5 towards the maximum uptakes of 3.5 mmol g<sup>-1</sup>, as shown in **Figure 7-80**. This indicates that the diffusion is controlled more by the diffusion of the molecules along the surface of the pore than by diffusion through a constriction at the entrance to the porosity for Cage 1 $\alpha$ #.

### 7.5.3 Methyl Acetate Adsorption on Cage 1 $\alpha$ # Kinetic Corrections

The kinetic profiles were examined in detail in order to attempt to predict the fully equilibrated isotherm in the low pressure region because the isosteric enthalpies of adsorption values were below the enthalpy of vaporisation. The profiles of zeroed original mass increase against time were analysed using the stretched exponential equation. When fitting using the stretched exponential, the parameter  $A_0$  is included in the equation. This is normally fixed at 1 during the fitting process for the normalised profile, but can be allowed to vary in order to give a multiplier to allow an indication of where equilibration would be achieved. When fitting the raw mass uptake, this parameter ( $A$ ) can be used to calculate the mass at which equilibration would be reached. From this, the equilibrium concentration can be calculated, and the isotherm corrected accordingly. This then gives corrected equilibrium isotherm points, which can be used to calculate the isosteric enthalpy of adsorption. It was possible to correct non equilibration below uptakes of 1.5 mmol g<sup>-1</sup>, or at low pressure. In the region of the steep part of the isotherm, where the chemical potential gradient is low, the equilibration corrections provided values which were unreasonably high and had large errors associated with them, and as such were unusable in the corrected isosteric enthalpy of adsorption calculations.

The first pressure steps recorded in the isotherm are the 0.5 – 1.0 mbar steps. This corresponds to ~0.5 mmol g<sup>-1</sup> uptake. Below this uptake the extrapolation and hence equilibrium isotherm points and isosteric enthalpy of adsorption data are less reliable. The successful corrections were made for the range of uptakes 0.5 – 1.4 mmol g<sup>-1</sup> for 298 and 303 K. The profiles of zeroed original mass increase against time analysed using the stretched exponential equation along with tables of corrected data can be found in **CD Appendix B – Molecular Cage Materials**. The corrected isotherms are shown in **Figure 7-81** and **Figure 7-82**, respectively. Adjustment of

the isosteric enthalpy of adsorption plots to include the corrected 298 and 303 K data show an increase in isosteric enthalpy of adsorption at low uptakes, between 0.5 and 1.4 mmol g<sup>-1</sup> bringing the isosteric enthalpies of adsorption above the value of the enthalpy of vaporisation of methyl acetate. This is shown in **Figure 7-83**. Selected improved van't Hoff plots are shown in **Figure 7-84**. A comparison of corrected isosteric enthalpy of adsorption plots with error bars omitted for clarity is shown in **Figure 7-85**. This data is tabulated in **Table 7-11** and shows, for example, that for 0.6 mmol g<sup>-1</sup> of methyl acetate adsorbed, the original isosteric enthalpy of adsorption was  $26.39 \pm 15.25$  kJ mol<sup>-1</sup>, which falls below the enthalpy of vaporisation of 32.67 kJ mol<sup>-1</sup>. The corrected isosteric enthalpy of adsorption is  $36.07 \pm 12.64$  kJ mol<sup>-1</sup>.

The corrected data shows that the isosteric enthalpy of adsorption does not change significantly until the region in the isotherm where the second plateau occurs, at similar uptakes to where the Cage 1 $\beta$  to Cage 1 $\alpha$ # structural change occurs during methyl acetate adsorption on Cage 1 $\beta$ .

#### 7.5.4 Comparison of Cage 1 $\beta$ and Cage 1 $\alpha$ #

A comparison of the methyl acetate adsorption isotherms collected at 303 K on Cage 1 $\beta$  and Cage 1 $\alpha$ # are shown in **Figure 7-86**. A comparison of the isosteric enthalpy of adsorption of methyl acetate for Cage 1 $\beta$  and Cage 1 $\alpha$ # is shown in **Figure 7-87**, and a comparison of the isosteric entropy of adsorption is shown in **Figure 7-88**. Desorption of methyl acetate from Cage 1 $\beta$  occurs at 3.5 mmol g<sup>-1</sup>. The resulting uptake after this desorption is 3.2 mmol g<sup>-1</sup>, as shown in **Figure 7-86**. After this point the isosteric enthalpy and entropy of adsorption values became unreliable on the isotherm plateau due to partial conversion from Cage 1 $\beta$  to Cage 1 $\alpha$ #. For Cage 1 $\alpha$ #, reliable isosteric enthalpy and entropy of adsorption values can be calculated up to 3.3 mmol g<sup>-1</sup>, which is the point at which saturation occurs within the pores at high relative pressures ( $P/P^0 = 0.95$ ). Comparison of the isosteric enthalpy and entropy of adsorption for Cage 1 $\beta$  at 3.5 mmol g<sup>-1</sup>, just before the desorption, and Cage 1 $\alpha$ # at 3.2 mmol g<sup>-1</sup>, which is the mass after desorption, shows that Cage 1 $\beta$  has an enthalpy of adsorption of  $58.3 \pm 1.8$  kJ mol<sup>-1</sup>, whereas Cage 1 $\alpha$ # has a higher enthalpy of adsorption, with a value of  $85.7 \pm 4.2$  kJ mol<sup>-1</sup>. The entropy of adsorption for Cage 1 $\beta$  is  $-229.6 \pm 8.2$  J K<sup>-1</sup> mol<sup>-1</sup>, with Cage 1 $\alpha$ # showing more negative entropy of  $-322.8 \pm 13.7$  J K<sup>-1</sup> mol<sup>-1</sup>.



## Chapter 7 Structural Change Induced by Adsorption of Gases and Vapours on Porous Cage Materials

The structural change which occurs during desorption of methyl acetate is an activated process driven by the enthalpy of adsorption leading to a decrease in entropy. Before the desorption step there is more methyl acetate adsorbed in the material. When a maximum amount of methyl acetate is adsorbed, the material begins to undergo a structural change from Cage 1 $\beta$  to crystalline Cage 1 $\alpha$ #. The structural change leads to desorption of methyl acetate from the porous structure, and the formation of a more ordered structure. Cage 1 $\alpha$  has narrower pores than Cage 1 $\beta$ , leading to an enhanced interaction with a greater isosteric enthalpy of adsorption, and a more ordered system, as shown by the more negative entropy of adsorption.

Above 3.3 mmol g<sup>-1</sup> adsorption of methyl acetate on Cage 1 $\alpha$ #, the enthalpy decreases and the entropy becomes less negative, which is attributed to the effects of saturation of methyl acetate into the narrow pores of Cage 1 $\alpha$ # and possible partial dissolution of Cage 1 $\alpha$ #.

### 7.6 Dichloromethane Adsorption on Cage 1 $\alpha$

Through the “vial in vial” method of vapour diffusion, the researchers at Liverpool University have shown that Cage 1 $\alpha$  can be interconverted to Cage 1 $\beta$  through exposure to dichloromethane. To investigate this, the adsorption isotherm for dichloromethane adsorption on Cage 1 $\alpha$  was collected at 298 K. The isotherm shows an increase in the amount adsorbed up to a pressure of 150 mbar where a plateau is reached. This plateau continues up to a pressure of 400 mbar, at which point a large step in the amount of dichloromethane adsorbed occurs. The isotherm is hysteretic, and is shown in **Figure 7-89**. The step and the hysteresis indicate that dichloromethane adsorption induces a structural change in Cage 1 $\alpha$ .

The adsorption kinetics for dichloromethane adsorption on Cage 1 $\alpha$  can be described by the stretched exponential equation up to a pressure of 200 mbar. An example of this is shown for the pressure step 5 – 10 mbar in **Figure 7-90**. All kinetic profiles can be found in **CD Appendix B: Molecular Cage Materials**. At 200 mbar the plateau on the isotherm is reached, and due to small fluctuations in the amount adsorbed, the kinetics cannot be analysed. The stretched exponential data for the analysis of the kinetic profiles up to a pressure of 200 mbar can be found in **Table 7-12**. The data shows that the rate of dichloromethane adsorption into Cage 1 $\alpha$  is

very slow, with equilibrium not fully reached after 8 hours, giving rate constants in the region of  $1 \times 10^{-5} \text{ s}^{-1}$ . The stretched exponential  $\beta$  parameter varies between 0.5 and 0.87, indicating a two dimensional process, where the diffusion of dichloromethane is controlled more by the diffusion along the surface of the pore than by diffusion through a constriction in the porosity. At a pressure of 400 mbar adsorption of dichloromethane is resumed. For the pressure steps 400 to 450 and 450 to 500 mbar, the stretched exponential equation no longer describes the kinetics, which are now best modelled using the Avrami equation. The Avrami analysis of these pressure steps are shown in **Figure 7-91** and **Figure 7-92**, giving Avrami parameters of  $2.68 \pm 9.4 \times 10^{-3}$  and  $2.40 \pm 1.9 \times 10^{-2}$ . The Avrami model fits the data well, with small residuals showing that the model is a good description of the data. The change in the kinetics from the stretched exponential model to the Avrami model indicates that the structural change is occurring by crystalline to crystalline transformation of Cage  $1\alpha$  through dichloromethane adsorption, to Cage  $1\beta\#$ . To assess the structural change, the Cage  $1\beta\#$  prepared by dichloromethane adsorption was degassed, and a methyl acetate adsorption isotherm was collected. This is shown in **Figure 7-93** and on a volume of vapour adsorbed basis in **Figure 7-94**. The isotherms show a good repeat of methyl acetate adsorption on Cage  $1\beta$  as prepared by researchers at Liverpool University, and shows that the adsorption of dichloromethane on Cage  $1\alpha$  induces a structural change to Cage  $1\beta\#$ , which can then be transformed back into Cage  $1\alpha\#$  through exposure to methyl acetate.

### 7.7 Conclusions

The inter conversion of Cage  $1\alpha$  and Cage  $1\beta$  can be facilitated by the adsorption of various solvent vapours.<sup>1,2</sup> Probe molecule studies show that the inter conversion from Cage  $1\beta$  to Cage  $1\alpha\#$  occurs on adsorption of ethyl acetate, methyl acetate, 2-butanone and diethyl ether. These four vapours all displayed unique adsorption isotherms, which included an unusual desorption of vapour with increasing pressure. The desorption of vapour is associated with the structural change from Cage  $1\beta$  to Cage  $1\alpha\#$ . This unique isotherm shape was not observed for methanol or pentane. Methanol adsorption showed no effect on the structure of Cage  $1\beta$ . Pentane adsorption displayed features consistent with a structural change, including a step in the isotherm and a hysteretic desorption isotherm, without the presence of the

## Chapter 7 Structural Change Induced by Adsorption of Gases and Vapours on Porous Cage Materials

unusual desorption step observed in the ethyl acetate, methyl acetate, 2-butanone and diethyl ether adsorption isotherms. Analysis of the powder X-ray diffraction of a sample of Cage 1 $\beta$  after pentane adsorption showed a diffraction pattern that did not match that of either Cage 1 $\beta$  or Cage 1 $\alpha$ , indicating that pentane may have induced the formation of another polymorph of Cage 1 or a mixed phase product.

The adsorption of methyl acetate was studied over a wide temperature range in order to assess the thermodynamic and kinetic characteristics of the conversion of Cage 1 $\beta$  to Cage 1 $\alpha$ . During the methyl acetate adsorption isotherm, at low surface coverage the enthalpy of adsorption is close to the enthalpy of vaporisation ( $32 \text{ kJ mol}^{-1}$ ) of methyl acetate. As the second plateau approaches the desorption step, the enthalpy of adsorption increases, to a value of  $58.3 \pm 1.8 \text{ kJ mol}^{-1}$ , while the entropy of adsorption becomes more negative, from values of  $-179.2 \pm 2.5$  to  $-229.6 \pm 1.8 \text{ J K}^{-1} \text{ mol}^{-1}$ , indicating an ordering of the system. At maximum methyl acetate loading Cage 1 $\beta$  has sufficient activation energy to initiate conversion to Cage 1 $\alpha$ , through desorption of vapour.

The kinetics of the desorption step of methyl acetate follow the Avrami model,<sup>8,9,10</sup> with the Avrami exponents for the temperature range 278 – 308 K falling within the range of  $1.19 \pm 0.015$  and  $1.46 \pm 0.0078$ . This is consistent with the diffusion of methyl acetate from the particle surface during the formation of Cage 1 $\alpha$ . The activation energy for methyl acetate desorption from Cage 1 $\beta$  was  $42.5 \pm 6.2 \text{ kJ mol}^{-1}$ , showing that there is a kinetic barrier to diffusion. This kinetic barrier is lower than the isosteric enthalpy of adsorption indicating that diffusion through pores to the particle surface is the rate determining step for the structural change.<sup>17</sup>

The adsorption of methyl acetate on Cage 1 $\beta$  was compared with the adsorption of methyl acetate on Cage 1 $\alpha$  in order to establish the thermodynamic effects for the conversion of Cage 1 $\beta$  to Cage 1 $\alpha$ . The adsorption of methyl acetate on Cage 1 $\alpha$  does not induce further structural change and this allowed the isosteric enthalpy and entropy of adsorption to be determined. The isosteric enthalpy for methyl acetate adsorption on Cage 1 $\alpha$  had a peak ( $90.2 \pm 3.2 \text{ kJ mol}^{-1}$  at  $3.1 \text{ mmol g}^{-1}$ ) and a corresponding minimum in the entropy of adsorption ( $-335.0 \pm 10.4 \text{ J K}^{-1} \text{ mol}^{-1}$ ). Comparison of the thermodynamic parameters for methyl acetate on Cage 1 $\beta$  just

## Chapter 7 Structural Change Induced by Adsorption of Gases and Vapours on Porous Cage Materials

before structural change ( $58.3 \pm 1.8 \text{ kJ mol}^{-1}$  and  $-229.6 \pm 8.2 \text{ J K}^{-1} \text{ mol}^{-1}$  at  $3.5 \text{ mmol g}^{-1}$ ) and Cage 1 $\alpha$ # for uptakes just after the structural change ( $85.7 \pm 4.2 \text{ kJ mol}^{-1}$  and  $-322.8 \pm 13.7 \text{ J K}^{-1} \text{ mol}^{-1}$  at  $3.2 \text{ mmol g}^{-1}$ ) showed ordering driven by the enthalpy of adsorption. Further small increases in uptake with increasing pressure on the isotherm plateau result in the decrease in isosteric enthalpy of adsorption and the entropy becomes less negative ( $40.5 \pm 4.5 \text{ kJ mol}^{-1}$  and  $-180.9 \pm 14.7 \text{ J K}^{-1} \text{ mol}^{-1}$  at  $3.5 \text{ mmol g}^{-1}$ ). These changes are attributed to the pores filling with methyl acetate leading to greater disorder in the system and possible partial dissolution of Cage 1 $\alpha$ #. Cage 1 $\alpha$ # has narrower pores, and hence, an increased interaction and ordering.

Dichloromethane adsorption facilitates the reverse conversion of Cage 1 $\alpha$  to Cage 1 $\beta$ . This transition is reversed by methyl acetate adsorption. Analysis of the kinetics of dichloromethane adsorption shows that initially the adsorption profiles fit the stretched exponential model. The isotherm step corresponding to structural change occurs at high relative pressure. The kinetic data for this step can be described by the Avrami model, giving exponent parameters of  $2.68 \pm 9.4 \times 10^{-3}$  and  $2.40 \pm 1.9 \times 10^{-2}$ . These Avrami exponents are much larger than those observed for the methyl acetate desorption from Cage 1 $\beta$ , indicating a difference in the diffusion mechanism for the two vapours.<sup>12</sup> The kinetic data show that methyl acetate drives the conversion by diffusion through pores and out of the particle surface, whereas dichloromethane drives the structural change through adsorption, which then results in an opening of the structure to facilitate structural change to form wider pores and increased adsorption capacity.

Cage 1 can interconvert between stable polymorphs  $\alpha$  and  $\beta$  on exposure to selected solvent vapours by an activated process, retaining crystallinity. The structural change is driven by the enthalpy of adsorption and subtle cage structural packing effects, which influence the mechanism of vapour diffusion in the pore structure.

7.8 Figures

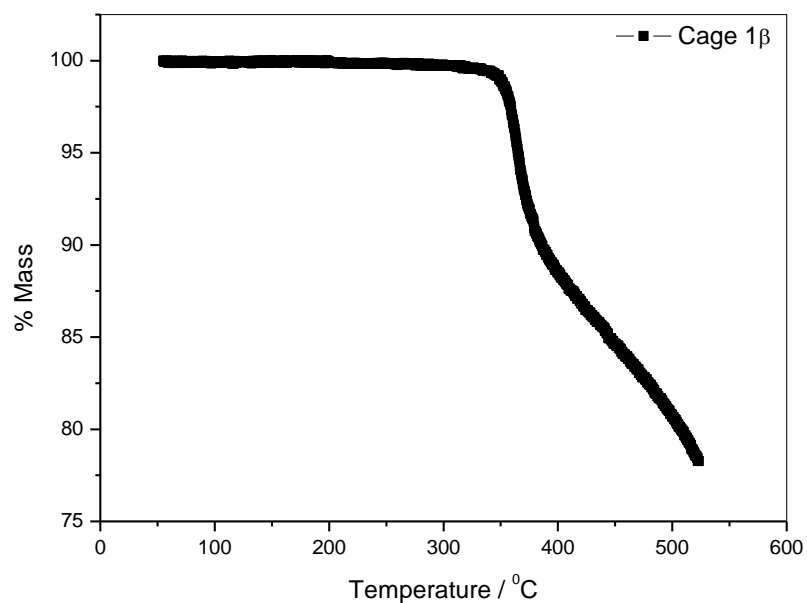


**Figure 7-4:** Thermal gravimetric analysis (TGA) of Cage 1β for the temperature range 0 – 500°C

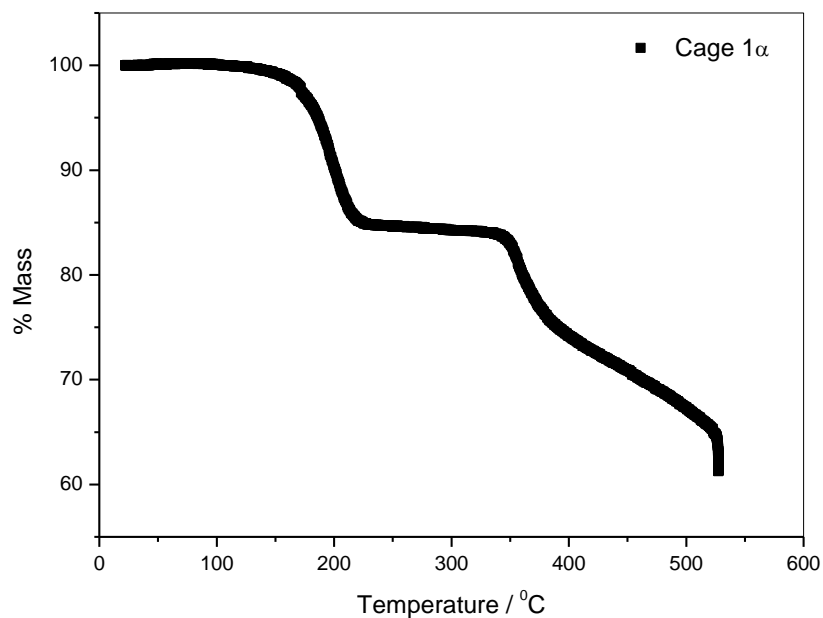
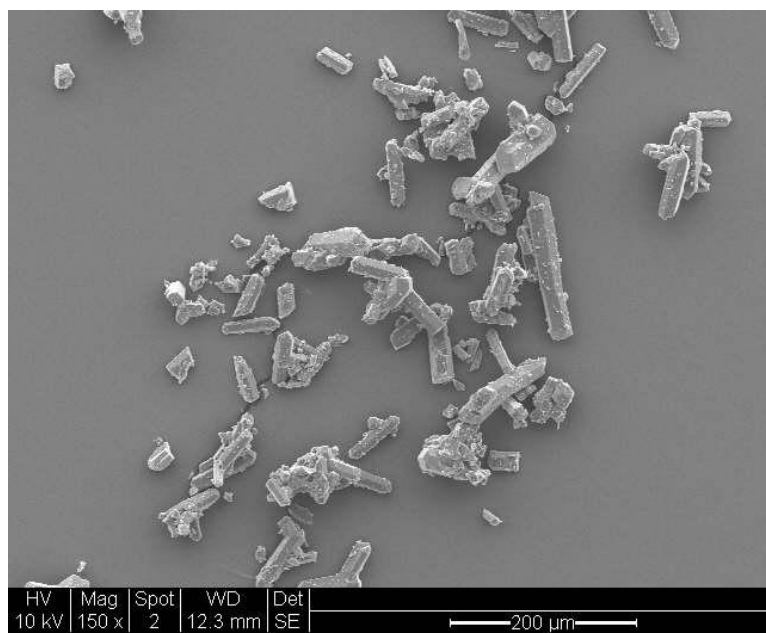
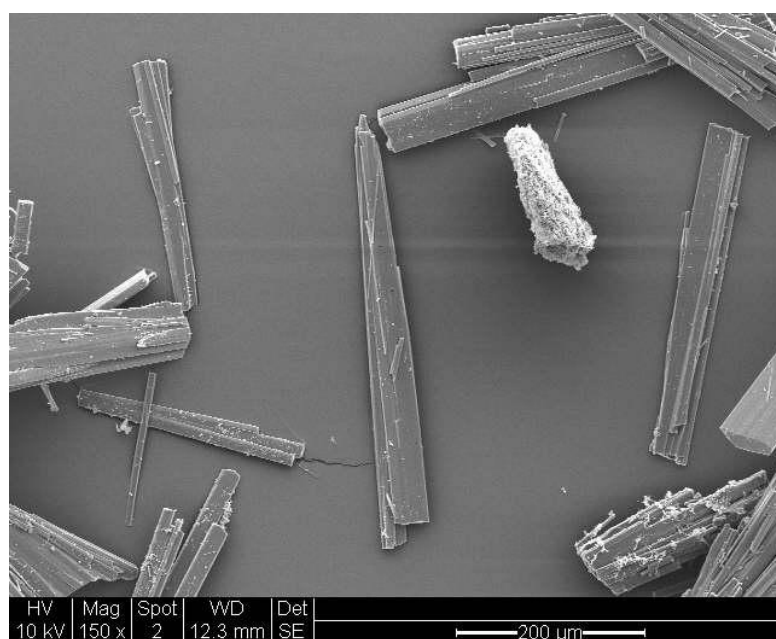


**Figure 7-5:** Thermal gravimetric analysis (TGA) of Cage 1α for the temperature range 0 – 500°C

Chapter 7 Structural Change Induced by Adsorption of Gases and Vapours on  
Porous Cage Materials



a)



b)

**Figure 7-6:** Scanning electron microscopy (SEM) image of a) Cage 1 $\beta$  crystals at 150x magnification b) Cage 1 $\alpha$  crystals at 150x magnification

Chapter 7 Structural Change Induced by Adsorption of Gases and Vapours on  
Porous Cage Materials

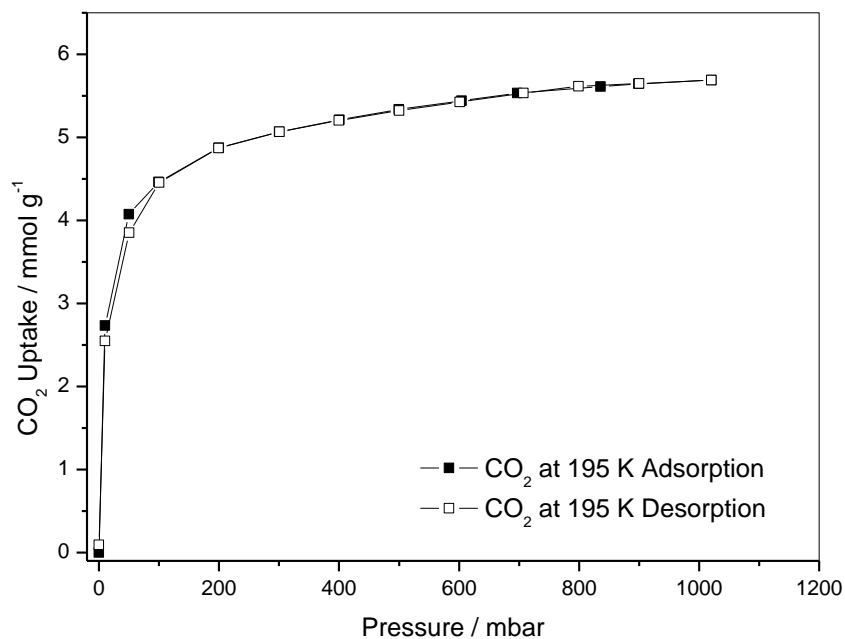


Figure 7-7: CO<sub>2</sub> isotherm for Cage 1β at 195 K

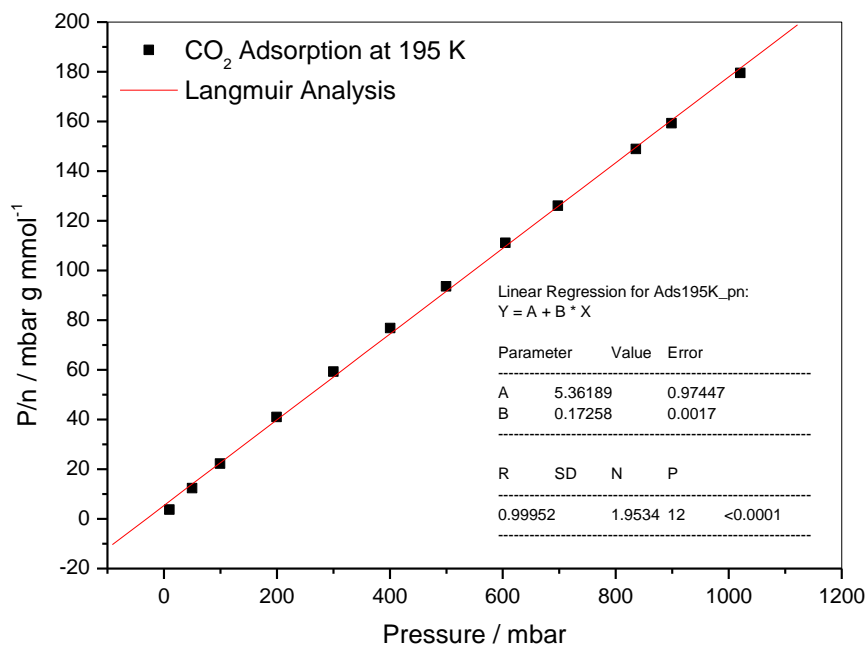
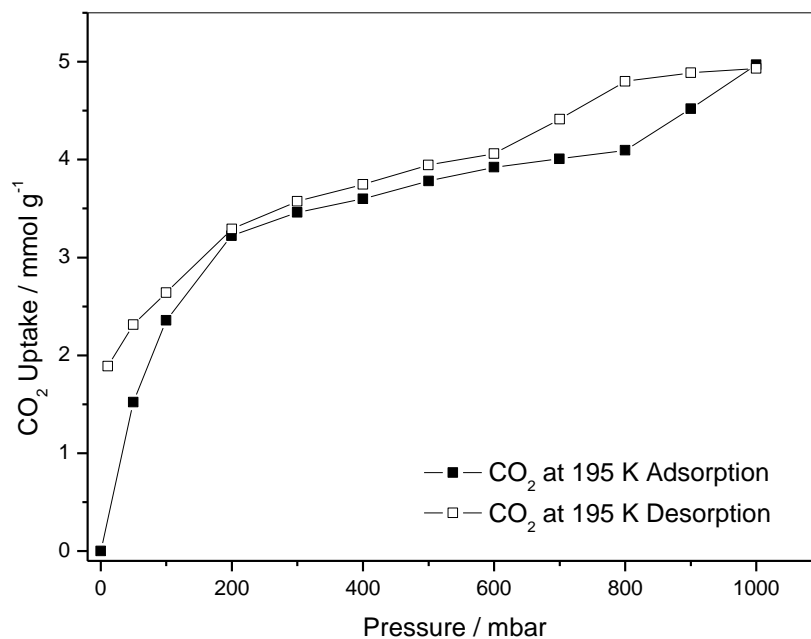
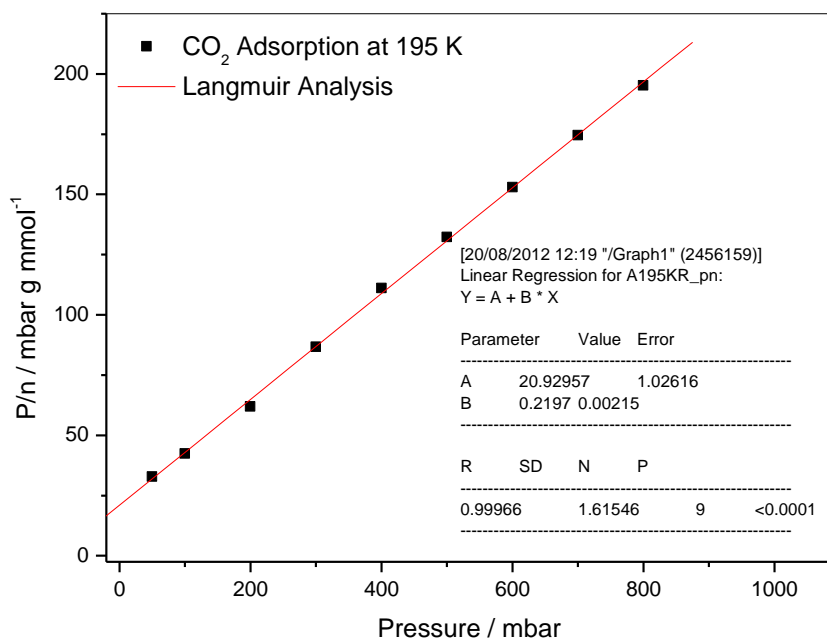


Figure 7-8: Langmuir analysis of CO<sub>2</sub> adsorption on Cage 1β at 195 K

Chapter 7 Structural Change Induced by Adsorption of Gases and Vapours on  
Porous Cage Materials



**Figure 7-9:** CO<sub>2</sub> isotherm for Cage 1α at 195 K



**Figure 7-10:** Langmuir analysis of CO<sub>2</sub> adsorption on Cage 1α at 195 K across the pressure range 10 – 800 mbar



Chapter 7 Structural Change Induced by Adsorption of Gases and Vapours on  
Porous Cage Materials

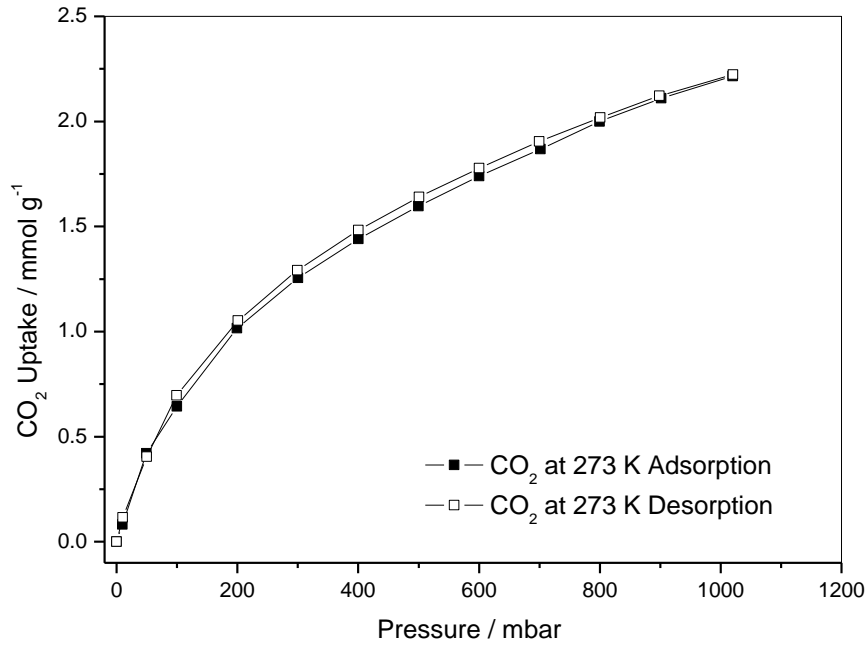


Figure 7-11: CO<sub>2</sub> isotherm for Cage 1β at 273 K

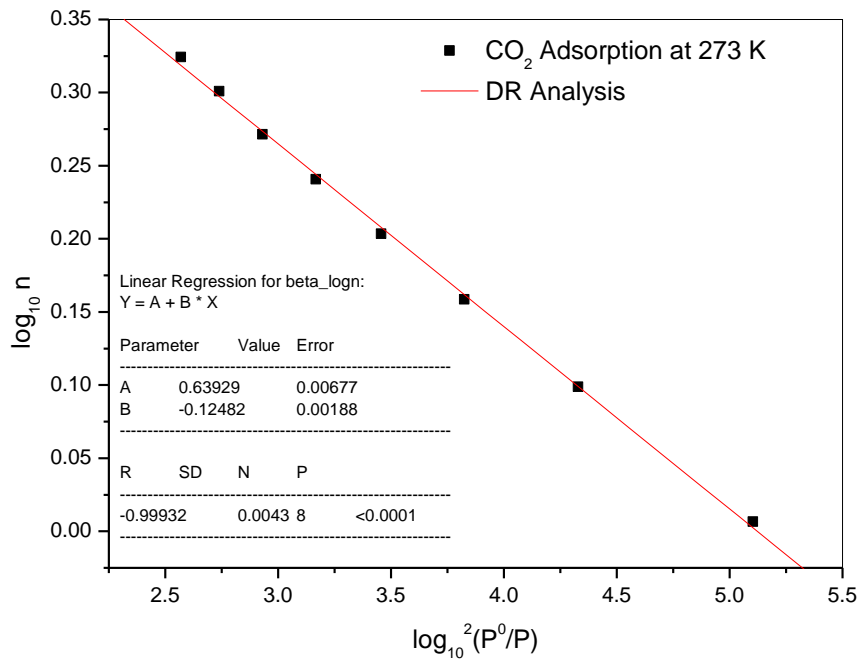
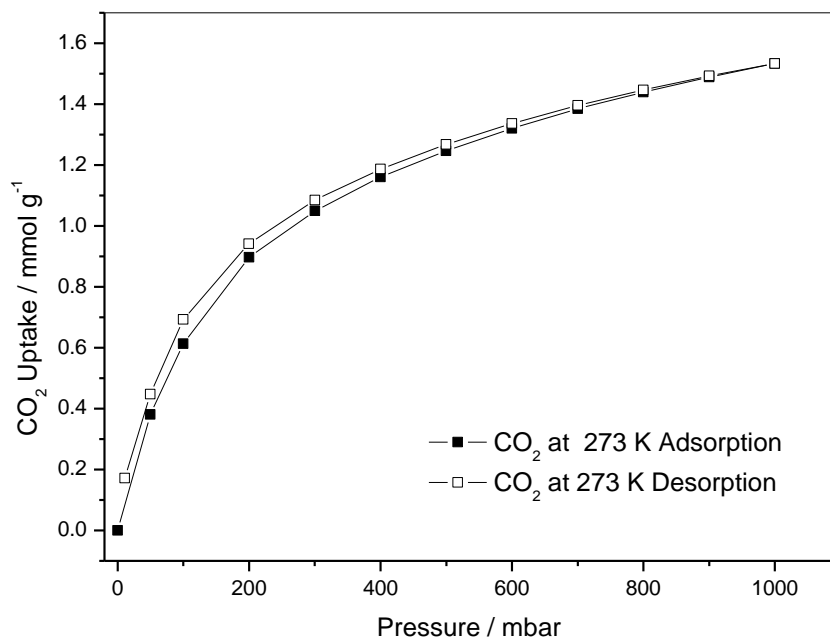
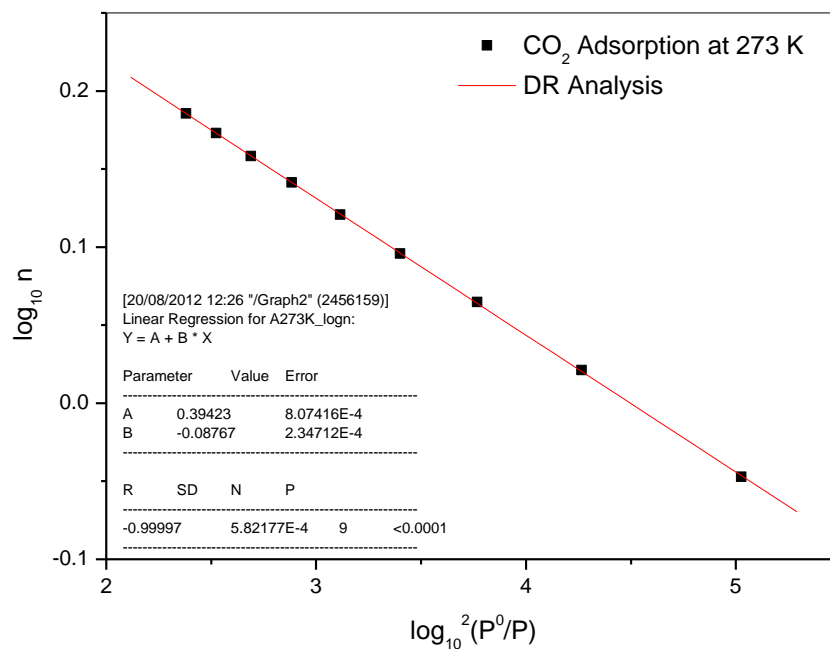


Figure 7-12: DR analysis of CO<sub>2</sub> adsorption on Cage 1β at 273 K

Chapter 7 Structural Change Induced by Adsorption of Gases and Vapours on  
Porous Cage Materials



**Figure 7-13:** CO<sub>2</sub> isotherm for Cage 1α at 273 K



**Figure 7-14:** DR analysis of CO<sub>2</sub> adsorption on Cage 1α at 273 K

Chapter 7 Structural Change Induced by Adsorption of Gases and Vapours on  
Porous Cage Materials

**Table 7-1:** Langmuir and DR data for carbon dioxide adsorption on Cage 1 $\beta$  and Cage 1 $\alpha$

Material	Langmuir Monolayer coverage / mmol g <sup>-1</sup>	Langmuir pore volume / cm <sup>3</sup> g <sup>-1</sup>	DR micropore volume / cm <sup>3</sup> g <sup>-1</sup>
Cage1 $\beta$	5.80 $\pm$ 0.0570	0.255 $\pm$ 2.50 x 10 <sup>-3</sup>	0.187 $\pm$ 4.54 x 10 <sup>-4</sup>
Cage 1 $\alpha$	4.55 $\pm$ 0.0445	0.170 $\pm$ 1.66 x 10 <sup>-3</sup>	0.108 $\pm$ 1.16 x 10 <sup>-3</sup>

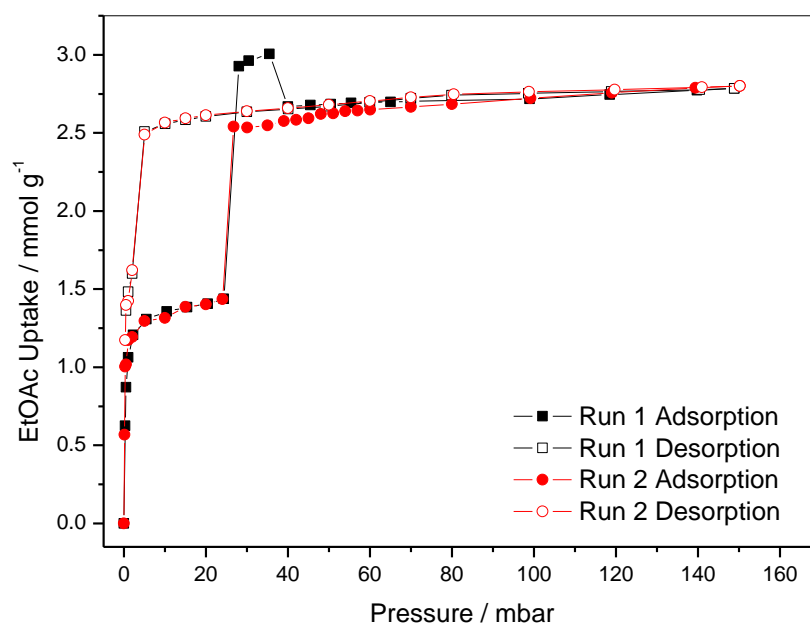


**Figure 7-15:** Ethyl acetate adsorption on Cage 1 $\beta$  at 303 K run 1 and run 2

Chapter 7 Structural Change Induced by Adsorption of Gases and Vapours on  
Porous Cage Materials

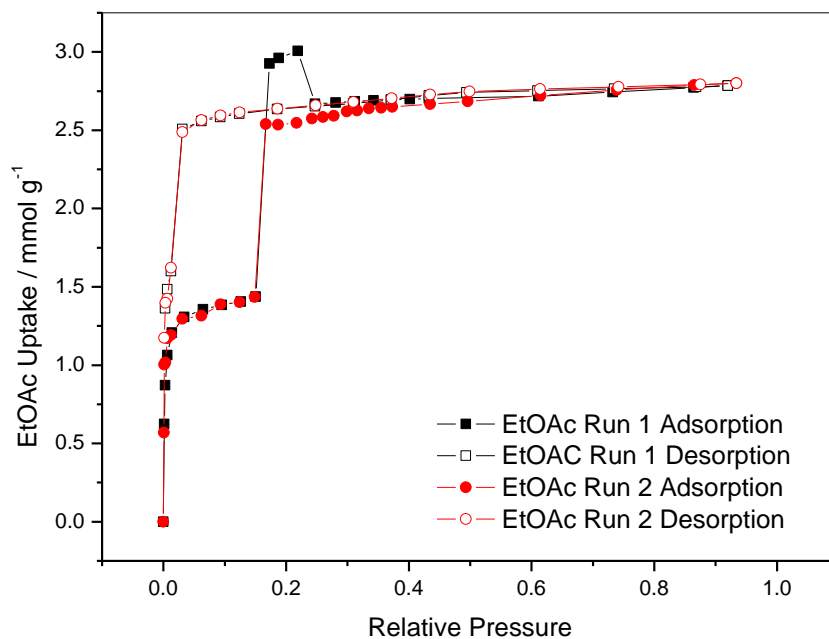


**Figure 7-16:** Ethyl acetate adsorption on Cage 1 $\beta$  at 303 K run 1 and run 2 on a relative pressure basis

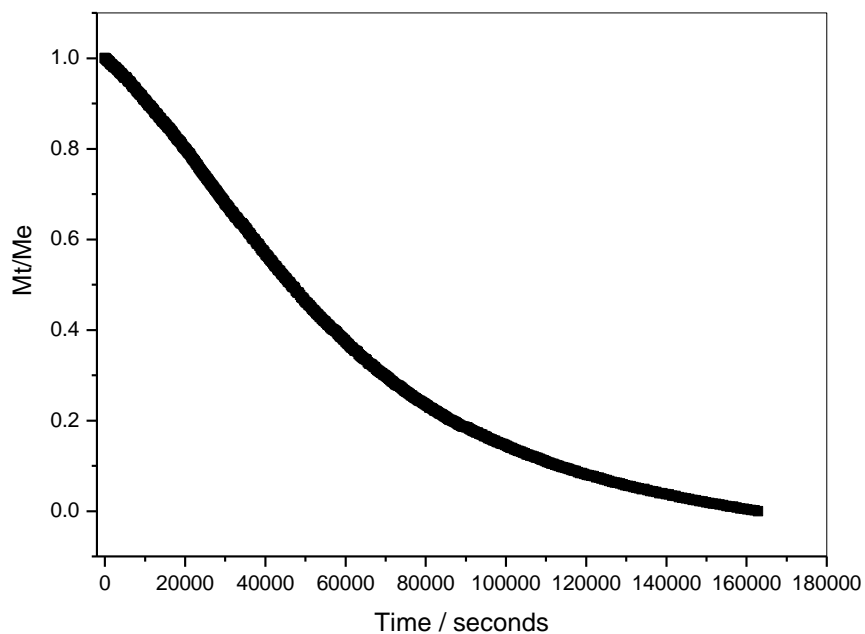


**Figure 7-17:** Desorption of ethyl acetate at the pressure step 35 to 40 mbar

Chapter 7 Structural Change Induced by Adsorption of Gases and Vapours on  
Porous Cage Materials

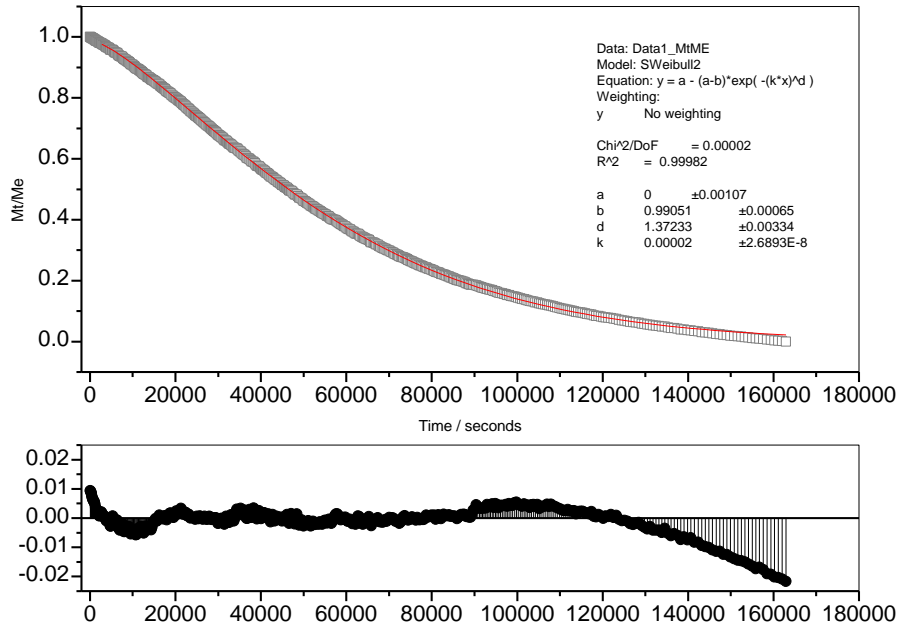


**Figure 7-18:** Cage 1 $\beta$  EtOAc desorption step at 35 – 40 mbar at 303 K, Avrami analysis

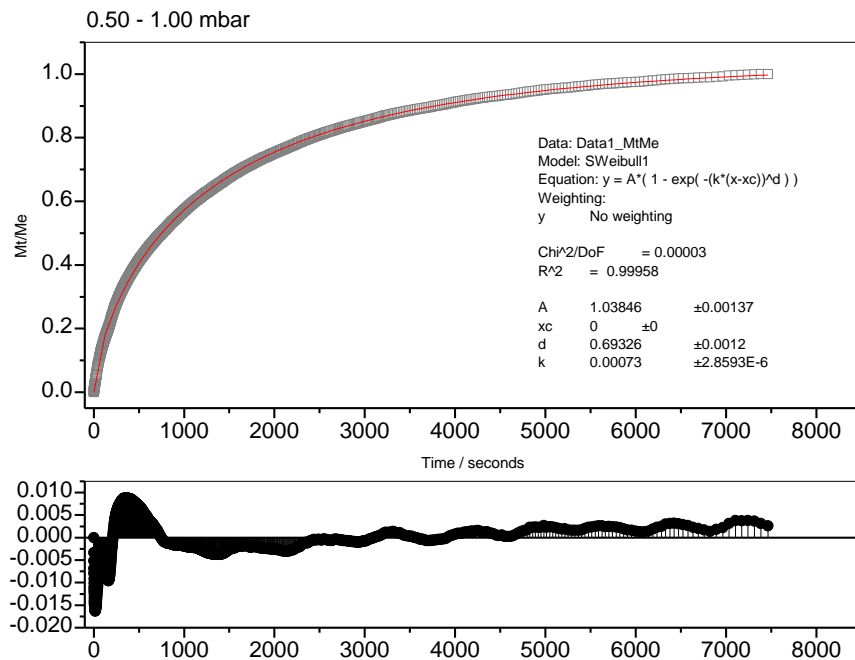


**Figure 7-19:** EtOAc adsorption on Cage 1 $\beta$  at 303 K 0.500 – 1.00 mbar step SE kinetic analysis

Chapter 7 Structural Change Induced by Adsorption of Gases and Vapours on  
Porous Cage Materials

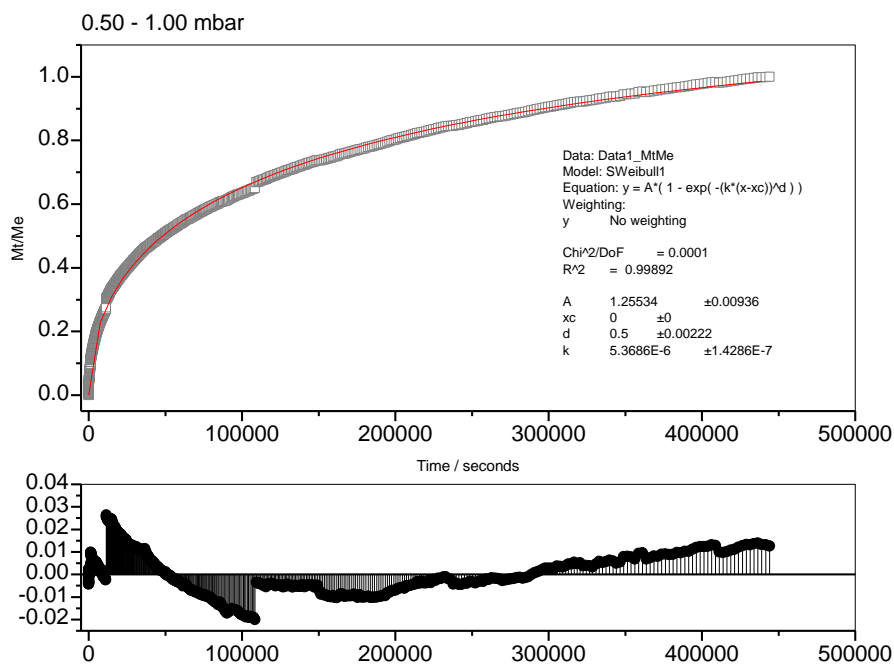


**Figure 7-20:** EtOAc adsorption on Cage 1 $\alpha$ # at 303 K 0.50 – 1.00 mbar step SE kinetic analysis

**Table 7-2:** Table of stretched exponential kinetic analysis parameter for ethyl acetate adsorption on Cage 1 $\beta$  at 303 K

Pressure / mbar	SE $\beta$ Parameter	Rate constant, $k / s^{-1}$
0.25	$0.566 \pm 0.00093$	$2.40 \times 10^{-4} \pm 1.22 \times 10^{-6}$
0.50	$0.620 \pm 0.00083$	$3.80 \times 10^{-4} \pm 1.39 \times 10^{-6}$
1.00	$0.693 \pm 0.0012$	$7.30 \times 10^{-4} \pm 2.86 \times 10^{-6}$
2.22	$0.713 \pm 0.0035$	$3.07 \times 10^{-3} \pm 3.00 \times 10^{-5}$
5.47	$0.827 \pm 0.0057$	$6.88 \times 10^{-3} \pm 5.00 \times 10^{-5}$
10.42	$0.916 \pm 0.0077$	$1.13 \times 10^{-2} \pm 7.00 \times 10^{-5}$
15.40	$0.983 \pm 0.0094$	$1.40 \times 10^{-2} \pm 9.00 \times 10^{-5}$
20.41	$1.000 \pm 0.0130$	$1.46 \times 10^{-2} \pm 1.30 \times 10^{-4}$
24.34	$0.867 \pm 0.0120$	$7.25 \times 10^{-3} \pm 8.00 \times 10^{-5}$
27.99	$0.978 \pm 0.0011$	$3.80 \times 10^{-4} \pm 2.44 \times 10^{-7}$
30.41	$0.935 \pm 0.0125$	$1.36 \times 10^{-2} \pm 1.20 \times 10^{-4}$
35.46	$1.000 \pm 0.0169$	$3.31 \times 10^{-2} \pm 3.40 \times 10^{-4}$

Chapter 7 Structural Change Induced by Adsorption of Gases and Vapours on  
Porous Cage Materials

**Table 7-3:** Table of stretched exponential kinetic analysis parameter for ethyl acetate adsorption on Cage 1 $\alpha$ # at 303 K

Pressure / mbar	SE $\beta$ Parameter	Rate constant, $k / s^{-1}$
0.10	$0.500 \pm 0.000940$	$4.00 \times 10^{-5} \pm 4.43 \times 10^{-7}$
0.25	$0.567 \pm 0.00108$	$5.55 \times 10^{-6} \pm 4.37 \times 10^{-8}$
0.50	$0.574 \pm 0.00977$	$7.80 \times 10^{-4} \pm 6.00 \times 10^{-5}$
1.00	$0.500 \pm 0.00222$	$5.37 \times 10^{-6} \pm 1.43 \times 10^{-7}$
4.99	$0.500 \pm 0.00877$	$5.00 \times 10^{-5} \pm 1.11 \times 10^{-6}$
14.99	$0.500 \pm 0.00892$	$2.00 \times 10^{-5} \pm 5.68 \times 10^{-7}$
24.00	$0.500 \pm 0.01767$	$1.30 \times 10^{-4} \pm 2.00 \times 10^{-5}$
34.99	$0.500 \pm 0.01301$	$1.00 \times 10^{-5} \pm 2.65 \times 10^{-6}$

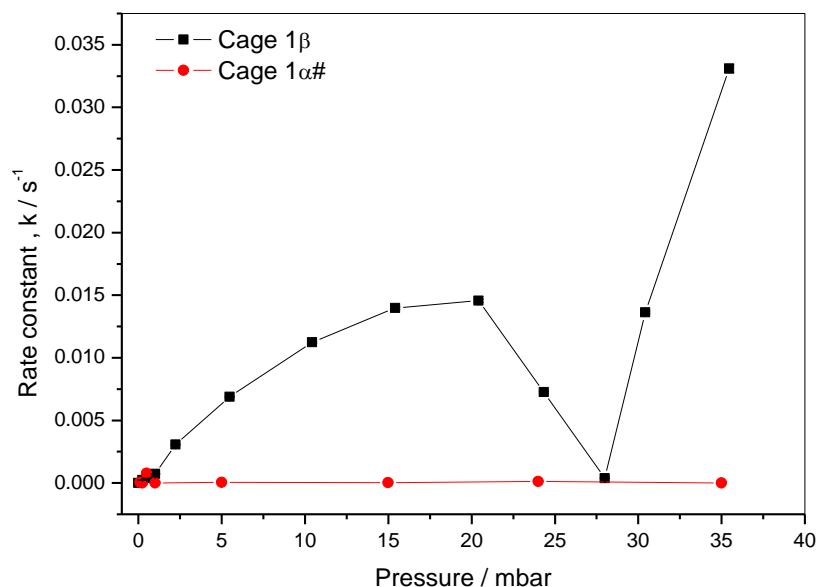


**Figure 7-21:** Comparison of rate constant,  $k$  for EtOAc adsorption on Cage 1 $\beta$  and Cage 1 $\alpha$ # at 303 K

Chapter 7 Structural Change Induced by Adsorption of Gases and Vapours on  
Porous Cage Materials

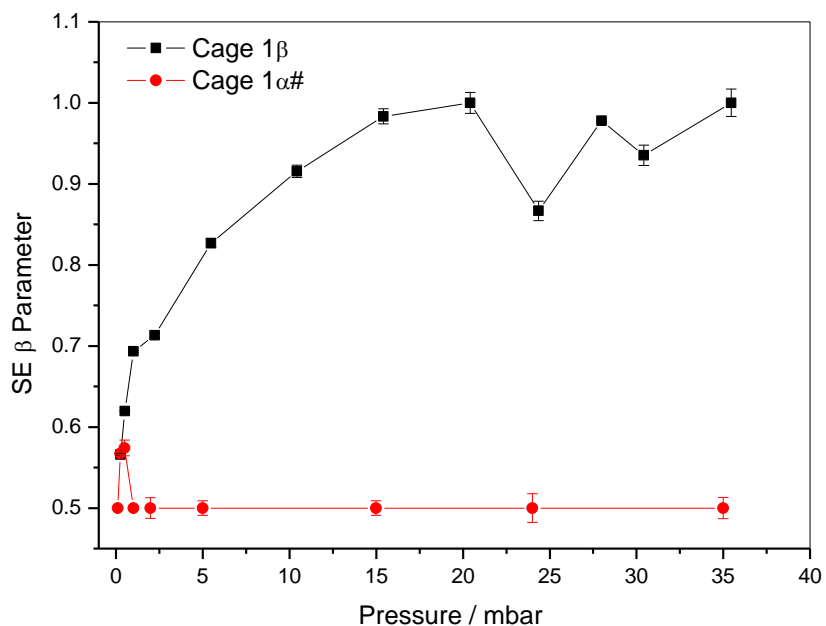


**Figure 7-22:** Comparison of SE  $\beta$  parameter for EtOAc adsorption on Cage 1 $\beta$  and Cage 1 $\alpha$ # at 303 K

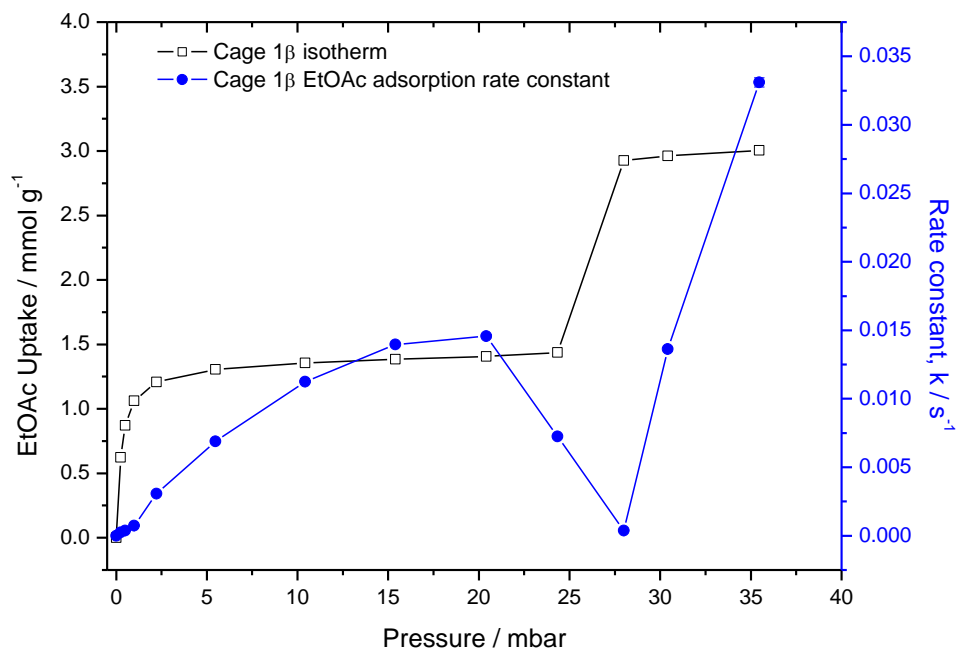


**Figure 7-23:** Comparison of EtOAc adsorption isotherm and rate constant,  $k$ , for EtOAc adsorption on Cage 1 $\beta$  at 303 K



Chapter 7 Structural Change Induced by Adsorption of Gases and Vapours on  
Porous Cage Materials

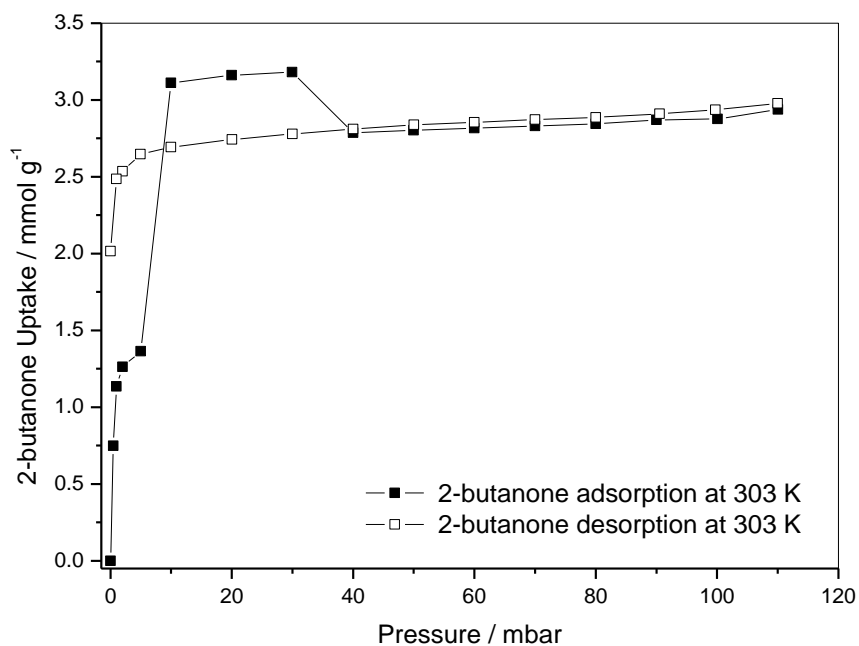


Figure 7-24: 2-butanone adsorption on Cage 1 $\beta$  at 298 K

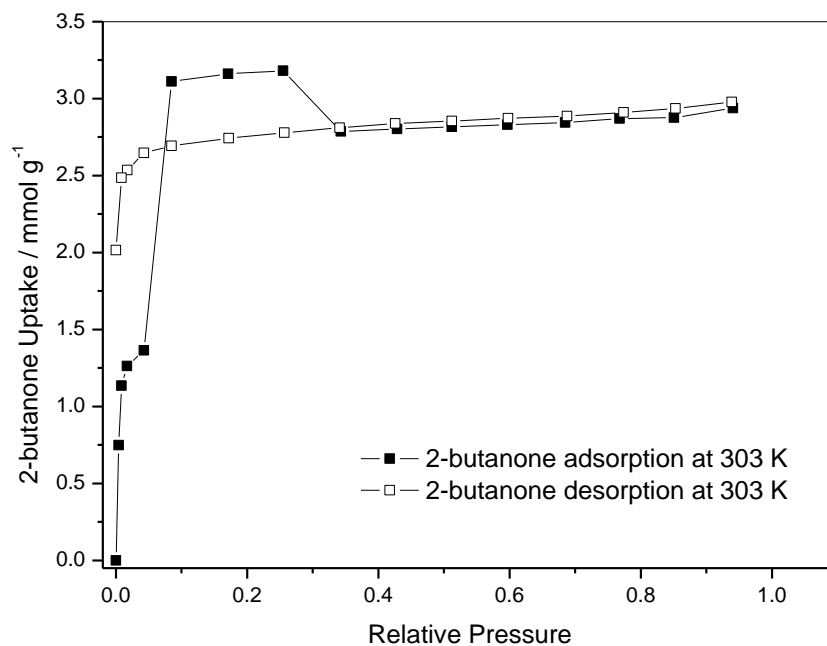


Figure 7-25: 2-butanone adsorption on Cage 1 $\beta$  at 298 K on a relative pressure basis

Chapter 7 Structural Change Induced by Adsorption of Gases and Vapours on  
Porous Cage Materials

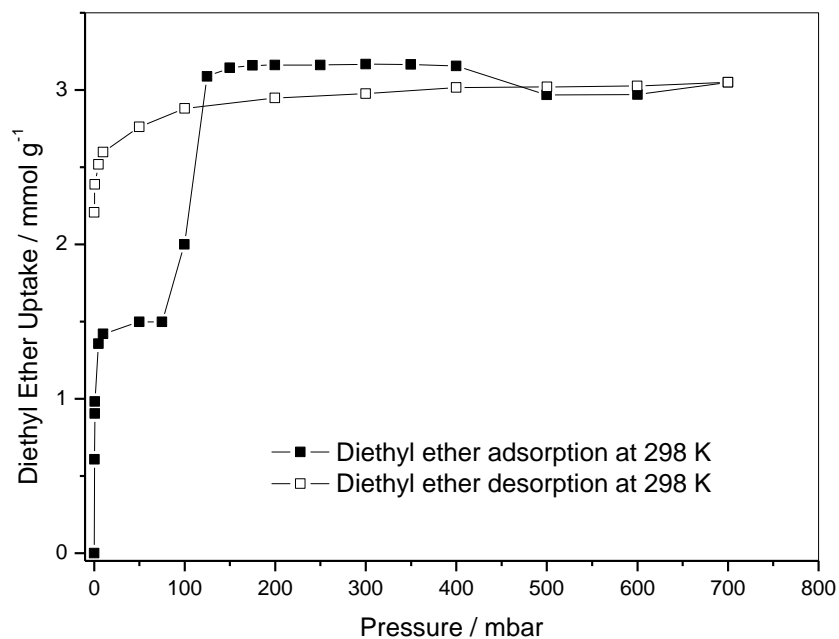


Figure 7-26: Diethyl ether adsorption on Cage 1 $\beta$  at 298 K

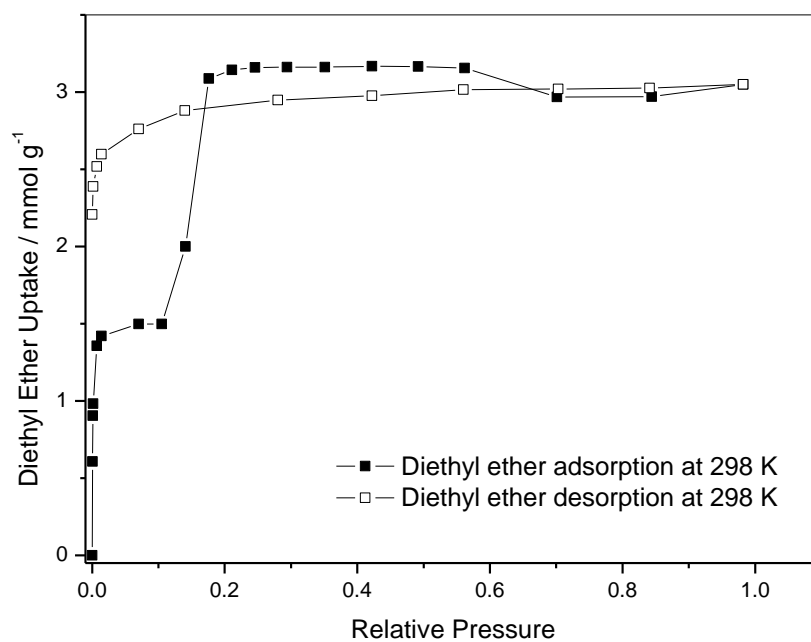
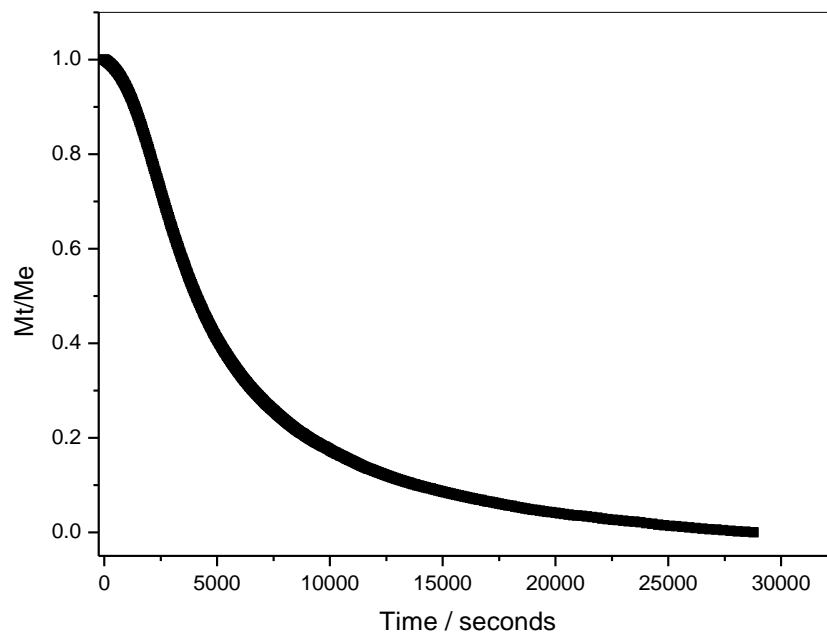
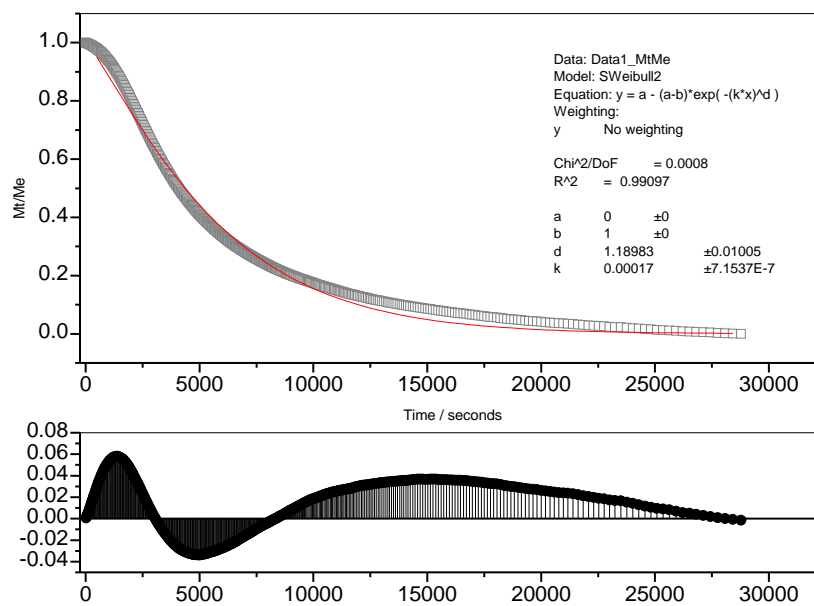


Figure 7-27: Diethyl ether adsorption on Cage 1 $\beta$  at 298 K on a relative pressure basis

Chapter 7 Structural Change Induced by Adsorption of Gases and Vapours on  
Porous Cage Materials



**Figure 7-28:** Desorption of 2 - butanone for the pressure step 30 to 40 mbar at 298 K



**Figure 7-29:** Cage 1 $\beta$  2-butanone desorption step 30 to 40 mbar at 298 K Avrami analysis

Chapter 7 Structural Change Induced by Adsorption of Gases and Vapours on  
Porous Cage Materials

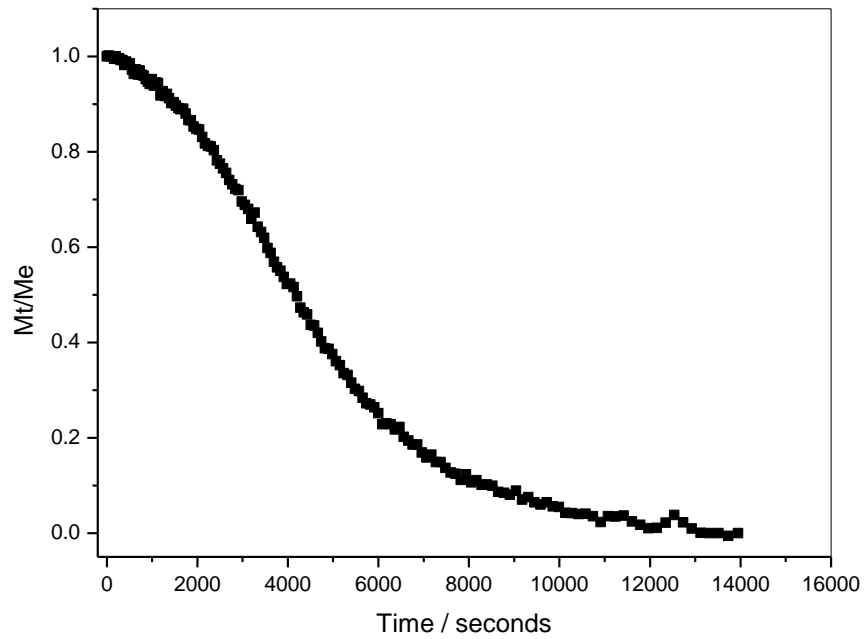


Figure 7-30: Desorption of diethyl ether for the pressure step 400 to 500 mbar 298 K

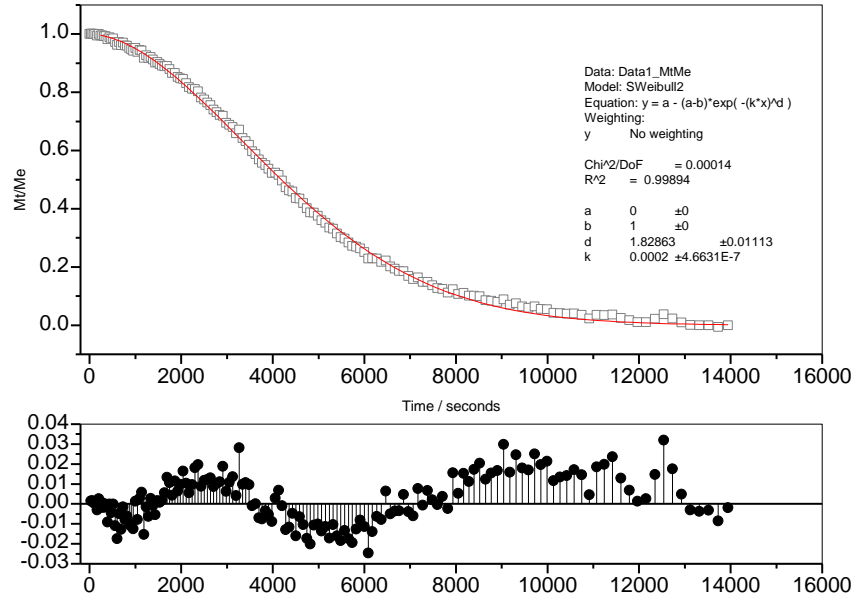
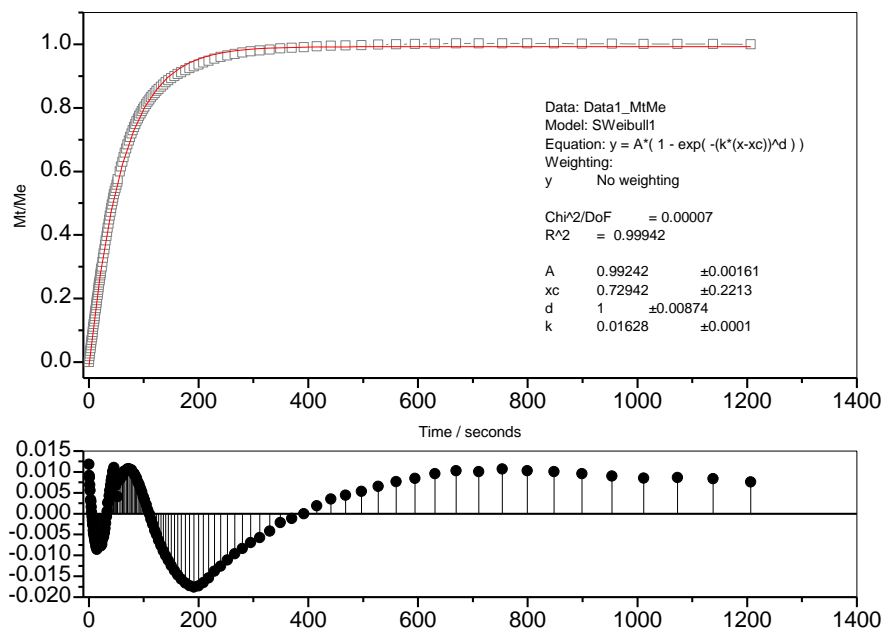


Figure 7-31: Cage 1  $\beta$  diethyl ether desorption step 400 – 500 mbar at 298 K  
Avrami analysis

Chapter 7 Structural Change Induced by Adsorption of Gases and Vapours on Porous Cage Materials



**Figure 7-32:** 2-butanone adsorption on Cage  $\beta$  at 298 K 2.00 – 5.00 mbar step SE kinetic analysis

**Table 7-4:** Table of stretched exponential kinetic analysis parameter for 2-butanone adsorption on Cage  $1\beta$  at 298 K

Pressure / mbar	SE $\beta$ Parameter	Rate constant, $k / s^{-1}$
0.10	$0.745 \pm 0.00132$	$7.00 \times 10^{-4} \pm 9.27 \times 10^{-7}$
2.02	$0.893 \pm 0.00671$	$5.66 \times 10^{-3} \pm 5.00 \times 10^{-5}$
5.01	$1.000 \pm 0.00874$	$1.63 \times 10^{-2} \pm 1.00 \times 10^{-4}$
9.98	$1.000 \pm 0.00536$	$7.56 \times 10^{-3} \pm 4.00 \times 10^{-5}$
19.99	$0.890 \pm 0.0200$	$3.33 \times 10^{-2} \pm 6.00 \times 10^{-4}$

Chapter 7 Structural Change Induced by Adsorption of Gases and Vapours on  
Porous Cage Materials

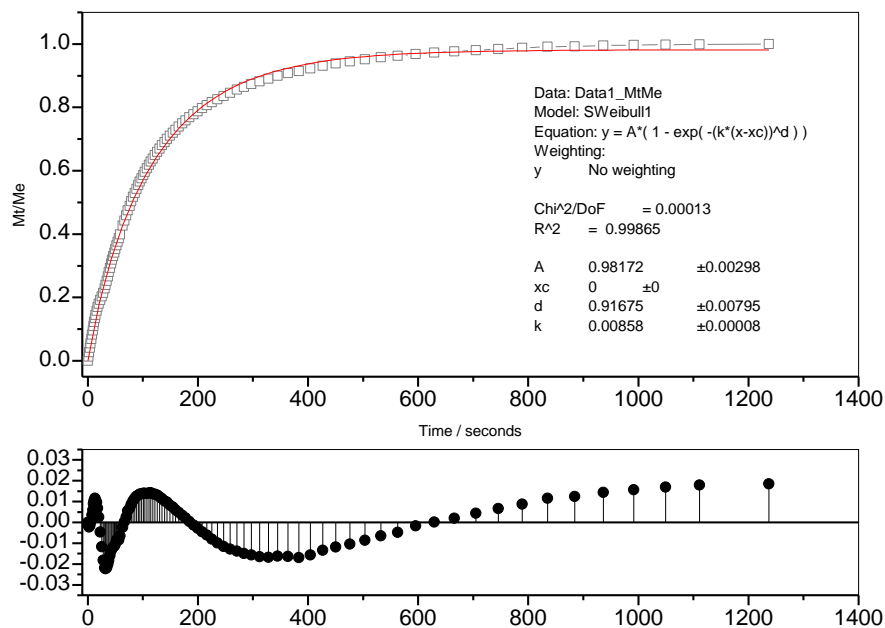


**Figure 7-33:** Diethyl ether adsorption on Cage 1 $\beta$  at 298 K 5.00 – 10.00 mbar step SE kinetic analysis

**Table 7-5:** Table of stretched exponential kinetic analysis parameter for diethyl ether adsorption on Cage 1 $\beta$  at 298 K

Pressure / mbar	SE $\beta$ Parameter	Rate constant, $k / s^{-1}$
<b>0.40</b>	$0.637 \pm 0.00242$	$5.30 \times 10^{-4} \pm 5.30 \times 10^{-6}$
<b>0.80</b>	$0.694 \pm 0.00421$	$6.80 \times 10^{-4} \pm 8.68 \times 10^{-6}$
<b>1.00</b>	$0.709 \pm 0.00486$	$1.02 \times 10^{-3} \pm 1.00 \times 10^{-4}$
<b>5.00</b>	$0.755 \pm 0.00269$	$2.21 \times 10^{-3} \pm 6.09 \times 10^{-6}$
<b>9.97</b>	$0.917 \pm 0.00795$	$8.58 \times 10^{-3} \pm 8.00 \times 10^{-5}$
<b>49.99</b>	$1.000 \pm 0.0469$	$1.29 \times 10^{-2} \pm 4.30 \times 10^{-4}$
<b>99.82</b>	$1.000 \pm 0.00332$	$1.28 \times 10^{-2} \pm 4.47 \times 10^{-6}$
<b>124.99</b>	$0.920 \pm 0.00241$	$3.30 \times 10^{-3} \pm 5.43 \times 10^{-6}$
<b>150.02</b>	$1.000 \pm 0.0190$	$3.00 \times 10^{-2} \pm 4.30 \times 10^{-4}$
<b>174.94</b>	$0.812 \pm 0.0276$	$2.85 \times 10^{-2} \pm 8.50 \times 10^{-4}$

Chapter 7 Structural Change Induced by Adsorption of Gases and Vapours on  
Porous Cage Materials

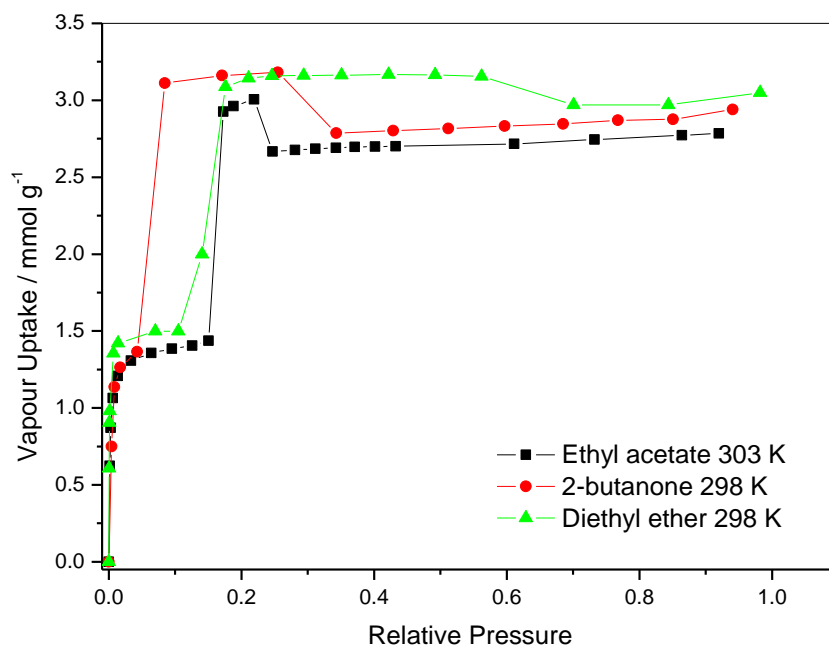


**Figure 7-34:** Comparison of ethyl acetate, 2-butanone and diethyl ether adsorption isotherms on Cage 1 $\beta$  on a relative pressure basis

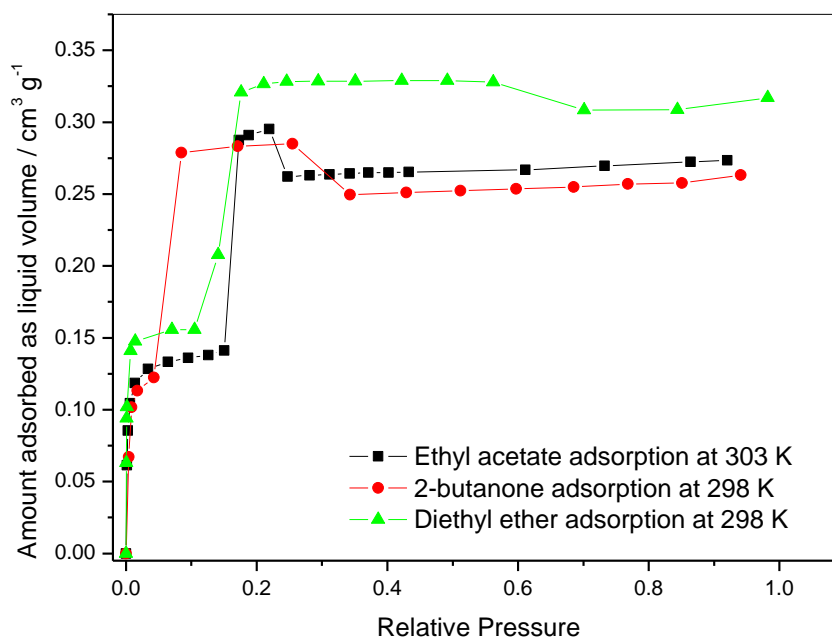


**Figure 7-35:** Comparison of ethyl acetate, 2-butanone and diethyl ether vapour amount adsorbed on a vapour volume basis on Cage 1 $\beta$

Chapter 7 Structural Change Induced by Adsorption of Gases and Vapours on  
Porous Cage Materials

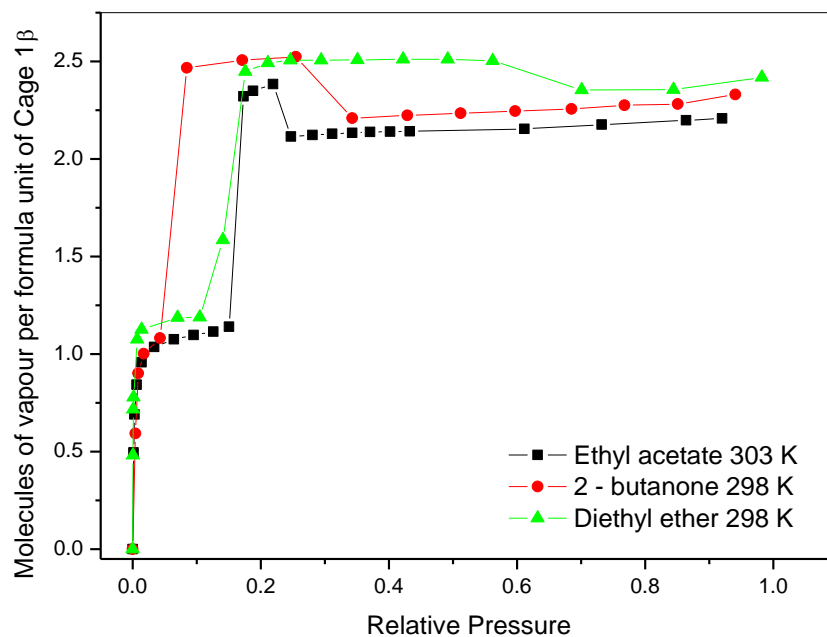


**Figure 7-36:** Comparison of ethyl acetate, 2-butanone and diethyl ether number of molecules per formula unit of Cage 1 $\beta$  on a relative pressure basis



Chapter 7 Structural Change Induced by Adsorption of Gases and Vapours on  
Porous Cage Materials

**Table 7-6:** Isotherm data for ethyl acetate, 2-butanone, and diethyl ether adsorption on Cage 1 $\beta$

<b>Section of Isotherm</b>	<b>Vapour</b>	<b>Relative Pressure</b>	<b>Uptake / mmol g<sup>-1</sup></b>	<b>Vapour Volume / cm<sup>3</sup> g<sup>-1</sup></b>	<b>No. of molecules per formula unit</b>
<b>First plateau</b>	EtOAc	0.150	1.437	0.141	1.14
	2-butanone	0.043	1.365	0.122	1.08
	Diethyl ether	0.105	1.500	0.156	1.19
<b>Before desorption</b>	EtOAc	0.219	3.006	0.295	2.38
	2-butanone	0.255	3.182	0.285	2.52
	Diethyl ether	0.562	3.156	0.328	2.50
<b>After desorption</b>	EtOAc	0.247	2.668	0.262	2.16
	2-butanone	0.343	2.786	0.250	2.21
	Diethyl ether	0.701	2.969	0.308	2.35
<b>At maximum pressure</b>	EtOAc	0.920	2.784	0.273	2.21
	2-butanone	0.941	2.939	0.263	2.33
	Diethyl ether	0.982	3.050	0.317	2.42

Chapter 7 Structural Change Induced by Adsorption of Gases and Vapours on Porous Cage Materials

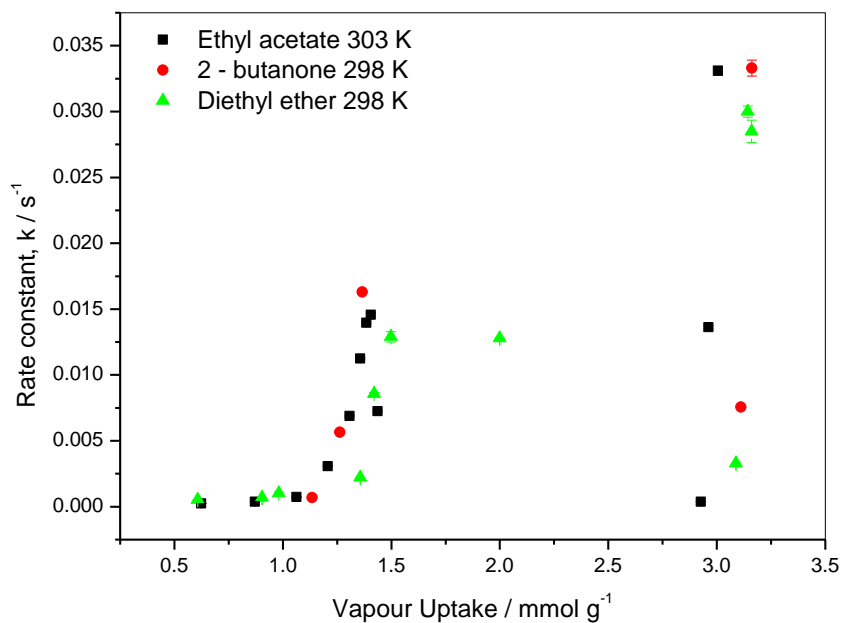


Figure 7-37: Comparison of ethyl acetate, 2-butanone and diethyl ether rate constant,  $k$  for adsorption on Cage  $1\beta$ , on a vapour uptake basis

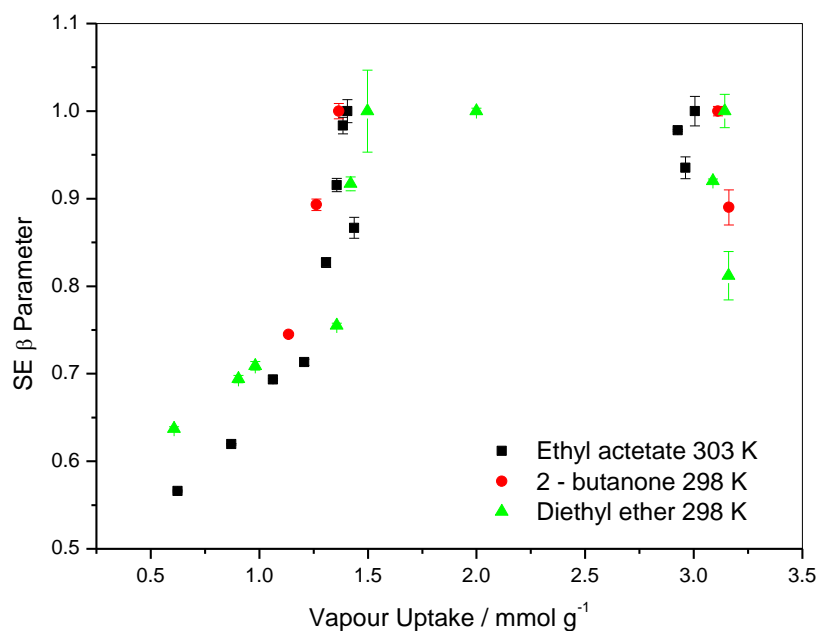
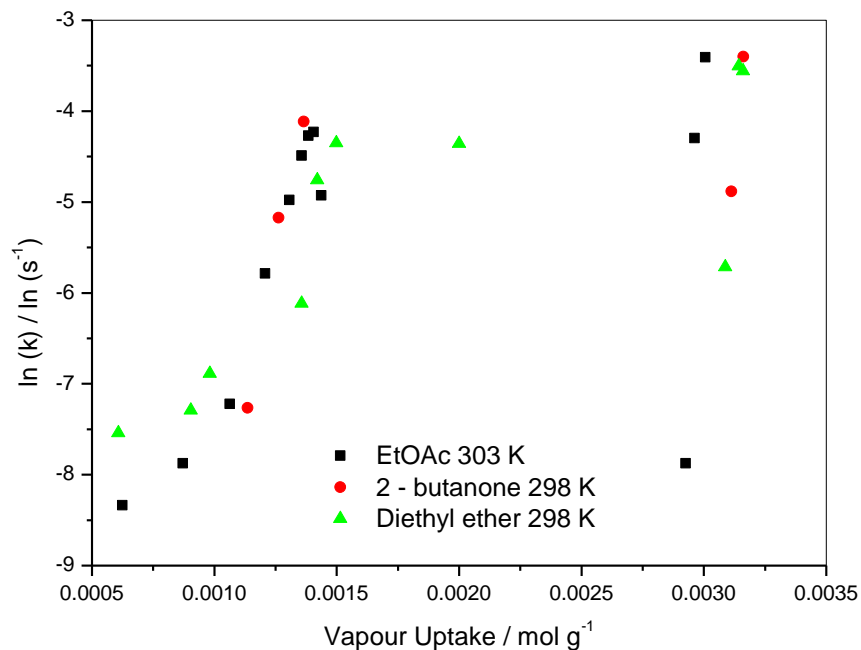
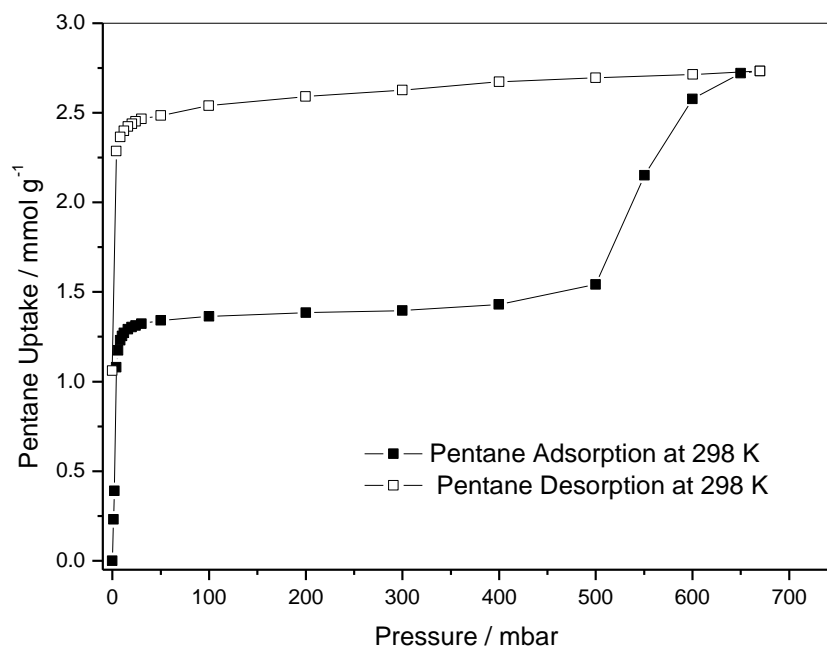


Figure 7-38: Comparison of ethyl acetate, 2-butanone and diethyl ether SE  $\beta$  parameter for adsorption on Cage  $1\beta$ , on a vapour uptake basis

Chapter 7 Structural Change Induced by Adsorption of Gases and Vapours on  
Porous Cage Materials



**Figure 7-39:** Comparison of ethyl acetate, 2-butanone and diethyl ether  $\ln(k)$  for adsorption on Cage 1 $\beta$



**Figure 7-40:** Pentane adsorption on Cage 1 $\beta$  at 298 K

Chapter 7 Structural Change Induced by Adsorption of Gases and Vapours on  
Porous Cage Materials

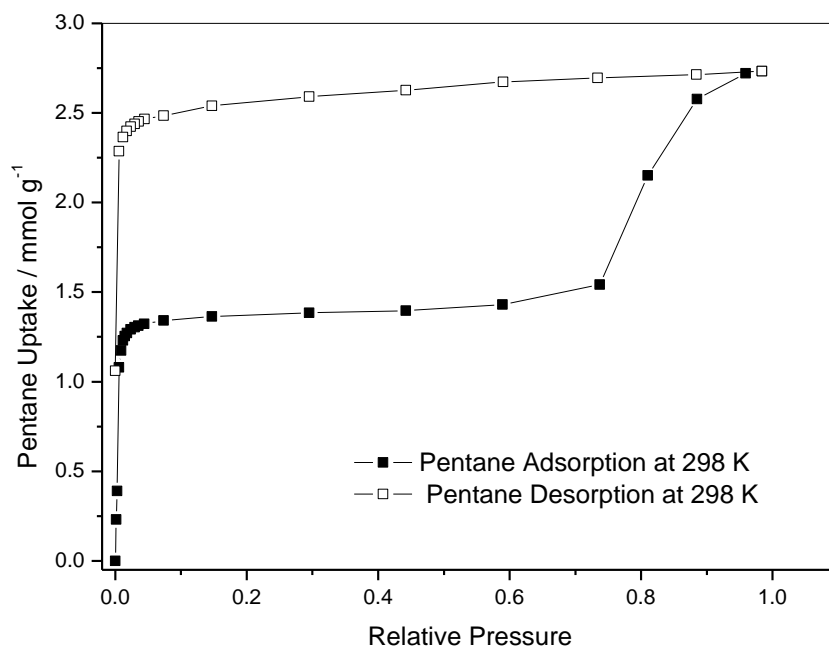


Figure 7-41: Pentane adsorption on Cage 1 $\beta$  at 298 K on a relative pressure basis

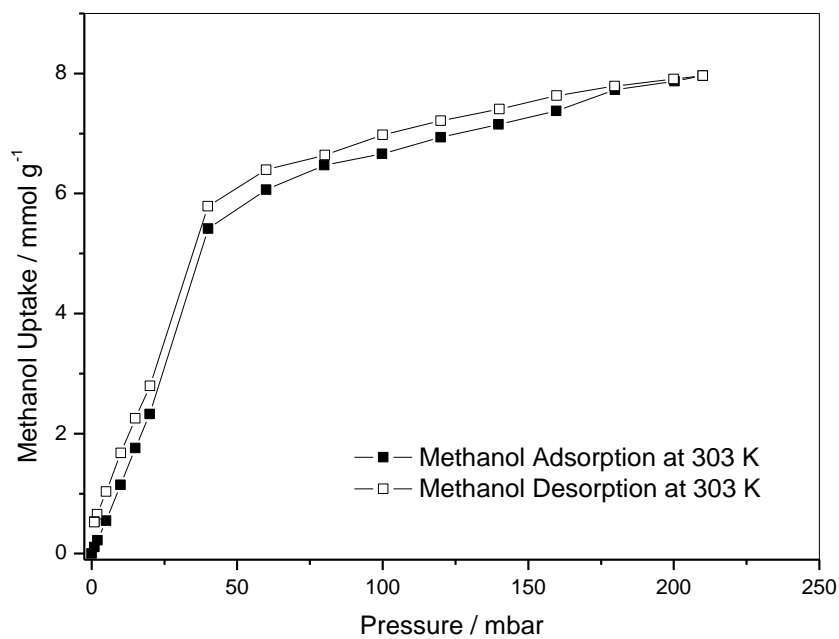


Figure 7-42: Methanol adsorption on Cage 1 $\beta$  at 303 K

Chapter 7 Structural Change Induced by Adsorption of Gases and Vapours on  
Porous Cage Materials

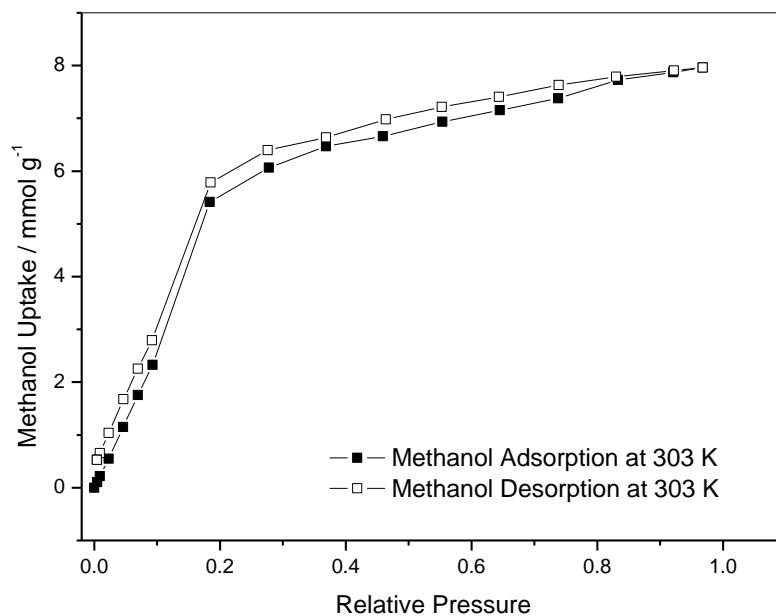


Figure 7-43: Methanol adsorption on Cage 1 $\beta$  at 303 K on a relative pressure basis

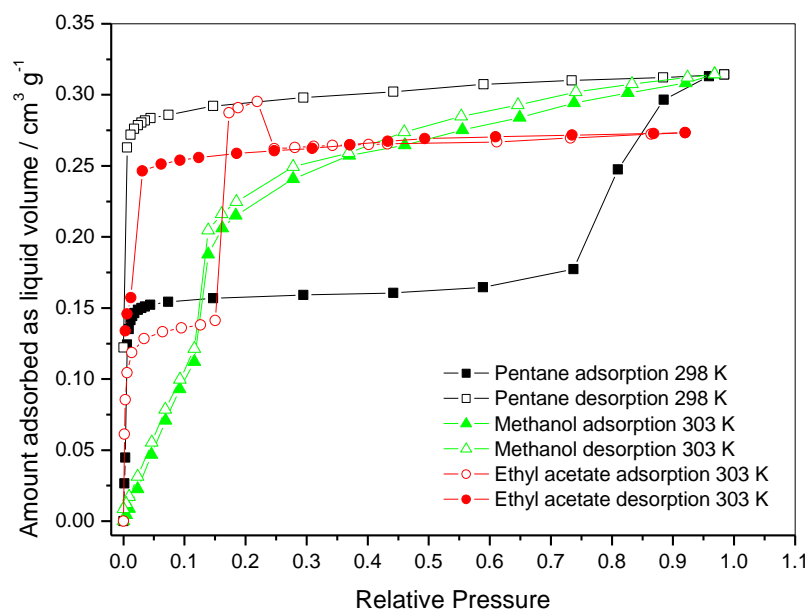
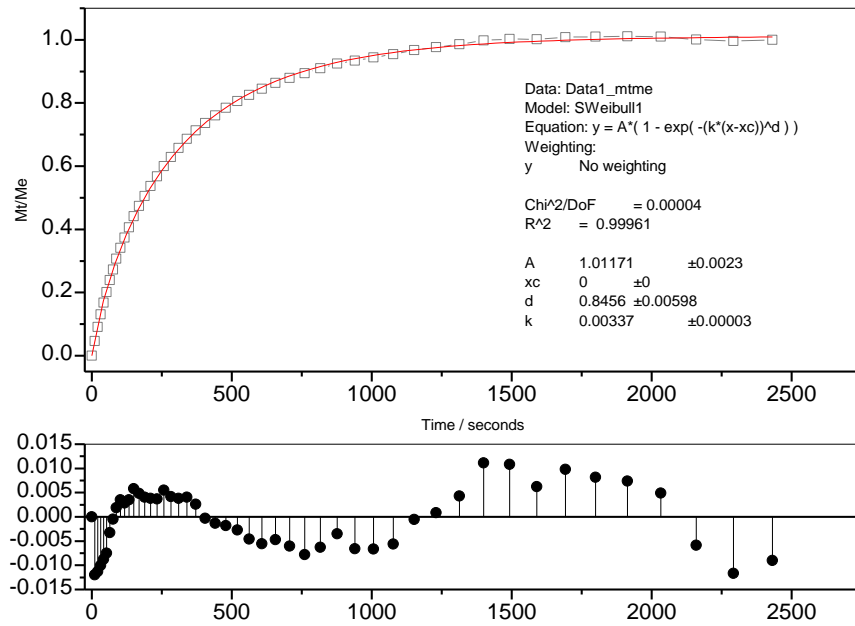
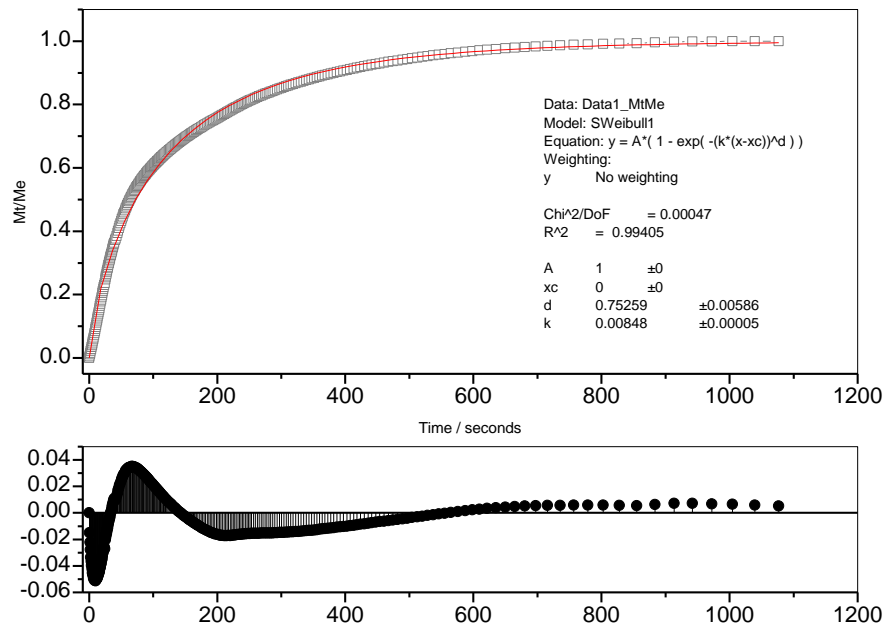


Figure 7-44: Comparison of pentane, methanol and ethyl acetate adsorption on Cage 1 $\beta$

Chapter 7 Structural Change Induced by Adsorption of Gases and Vapours on Porous Cage Materials



**Figure 7-45:** Pentane adsorption on Cage 1 $\beta$  at 298 K 50.0 – 100.0 mbar step SE kinetic analysis



**Figure 7-46:** Methanol adsorption on Cage 1 $\beta$  at 303 K 20.00 – 25.00 mbar step SE kinetic analysis

Chapter 7 Structural Change Induced by Adsorption of Gases and Vapours on  
Porous Cage Materials

**Table 7-7:** Table of stretched exponential kinetic analysis parameter for pentane adsorption on Cage 1 $\beta$  at 298 K

Pressure / mbar	SE $\beta$ Parameter	Rate constant, $k / s^{-1}$
<b>6.00</b>	$0.625 \pm 0.00629$	$4.70 \times 10^{-5} \pm 1.93 \times 10^{-6}$
<b>8.06</b>	$0.635 \pm 0.00520$	$6.00 \times 10^{-5} \pm 1.88 \times 10^{-6}$
<b>10.01</b>	$0.964 \pm 0.00165$	$2.20 \times 10^{-4} \pm 3.12 \times 10^{-6}$
<b>12.07</b>	$1.000 \pm 0.0305$	$3.20 \times 10^{-4} \pm 6.42 \times 10^{-6}$
<b>16.03</b>	$0.692 \pm 0.00945$	$3.10 \times 10^{-4} \pm 8.96 \times 10^{-6}$
<b>19.96</b>	$0.649 \pm 0.00827$	$5.40 \times 10^{-4} \pm 2.00 \times 10^{-4}$
<b>24.05</b>	$0.642 \pm 0.0144$	$5.30 \times 10^{-4} \pm 4.00 \times 10^{-4}$
<b>30.01</b>	$0.813 \pm 0.00709$	$1.33 \times 10^{-3} \pm 1.00 \times 10^{-6}$
<b>50.00</b>	$0.833 \pm 0.00564$	$1.82 \times 10^{-3} \pm 1.00 \times 10^{-4}$
<b>99.90</b>	$0.846 \pm 0.00598$	$3.37 \times 10^{-3} \pm 3.00 \times 10^{-4}$
<b>200.18</b>	$0.785 \pm 0.0199$	$6.87 \times 10^{-3} \pm 1.60 \times 10^{-4}$
<b>399.83</b>	$0.645 \pm 0.00187$	$5.00 \times 10^{-5} \pm 5.54 \times 10^{-6}$
<b>649.97</b>	$0.836 \pm 0.00504$	$3.00 \times 10^{-5} \pm 4.16 \times 10^{-7}$

Chapter 7 Structural Change Induced by Adsorption of Gases and Vapours on  
Porous Cage Materials

**Table 7-8:** Table of stretched exponential kinetic analysis parameter for methanol adsorption on Cage 1 $\beta$  at 303K

<b>Pressure / mbar</b>	<b>SE <math>\beta</math> Parameter</b>	<b>Rate constant, <math>k / s^{-1}</math></b>
<b>2.01</b>	$1.000 \pm 0.00309$	$2.60 \times 10^{-2} \pm 5.00 \times 10^{-5}$
<b>5.00</b>	$0.981 \pm 0.0104$	$1.98 \times 10^{-2} \pm 1.30 \times 10^{-4}$
<b>10.01</b>	$0.814 \pm 0.00906$	$1.41 \times 10^{-2} \pm 1.20 \times 10^{-4}$
<b>14.99</b>	$0.766 \pm 0.00633$	$1.08 \times 10^{-2} \pm 7.00 \times 10^{-5}$
<b>19.99</b>	$0.754 \pm 0.00486$	$9.18 \times 10^{-3} \pm 5.00 \times 10^{-5}$
<b>24.99</b>	$0.753 \pm 0.00586$	$8.48 \times 10^{-3} \pm 5.00 \times 10^{-5}$
<b>29.99</b>	$0.820 \pm 0.0232$	$4.50 \times 10^{-4} \pm 8.50 \times 10^{-7}$
<b>35.00</b>	$0.803 \pm 0.00319$	$7.26 \times 10^{-3} \pm 2.00 \times 10^{-5}$
<b>40.02</b>	$0.753 \pm 0.00872$	$1.00 \times 10^{-2} \pm 1.10 \times 10^{-4}$
<b>60.03</b>	$0.804 \pm 0.00523$	$8.22 \times 10^{-3} \pm 4.00 \times 10^{-5}$
<b>80.02</b>	$0.790 \pm 0.00579$	$9.17 \times 10^{-3} \pm 6.00 \times 10^{-5}$
<b>119.90</b>	$0.853 \pm 0.0102$	$1.35 \times 10^{-2} \pm 1.30 \times 10^{-4}$
<b>139.92</b>	$0.772 \pm 0.0105$	$1.20 \times 10^{-2} \pm 1.40 \times 10^{-4}$
<b>199.59</b>	$0.782 \pm 0.0127$	$1.31 \times 10^{-2} \pm 1.70 \times 10^{-4}$



Chapter 7 Structural Change Induced by Adsorption of Gases and Vapours on  
Porous Cage Materials

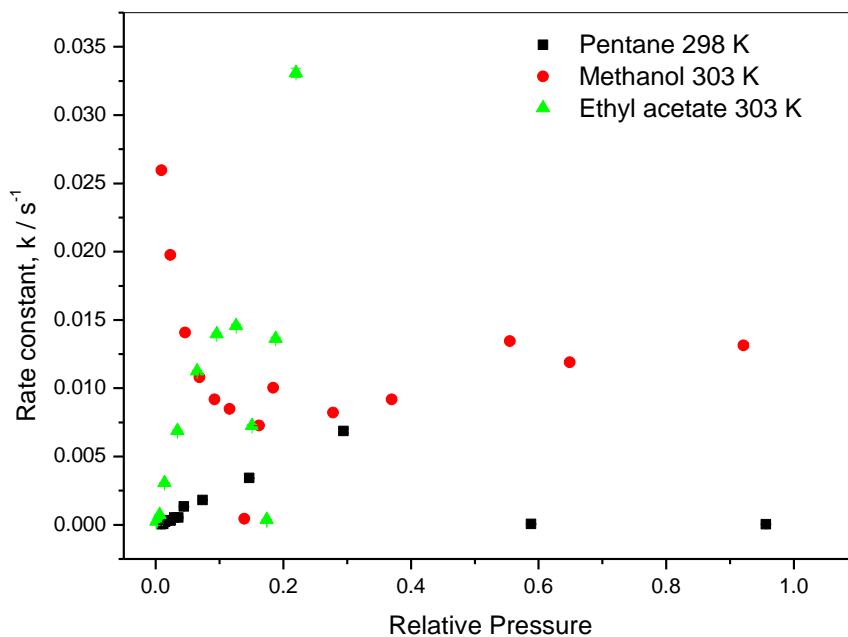


**Figure 7-47:** Comparison of pentane, methanol and ethyl acetate adsorption on Cage  $1\beta$  SE rate constant,  $k$ .

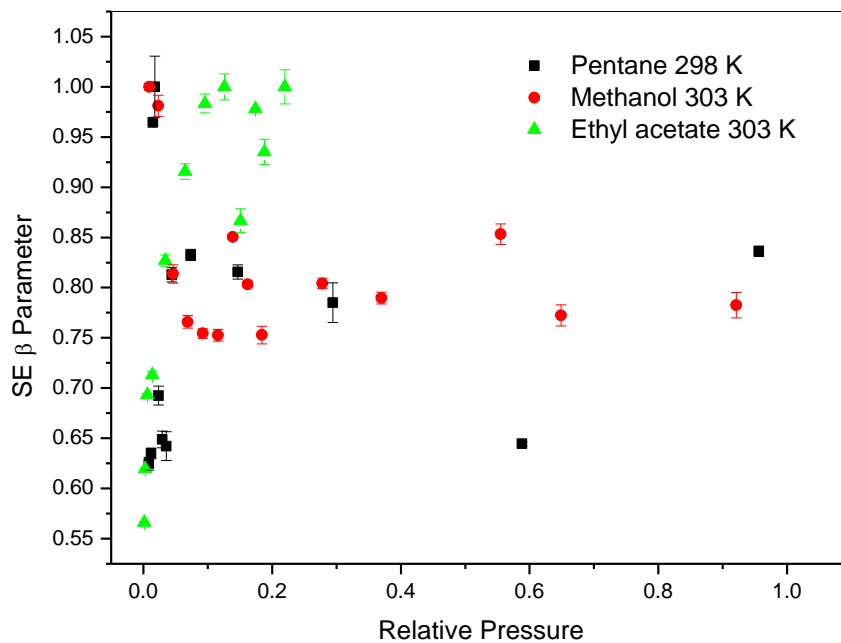


**Figure 7-48:** Comparison of pentane, methanol and ethyl acetate adsorption on Cage  $1\beta$  SE  $\beta$  parameter

Chapter 7 Structural Change Induced by Adsorption of Gases and Vapours on  
Porous Cage Materials

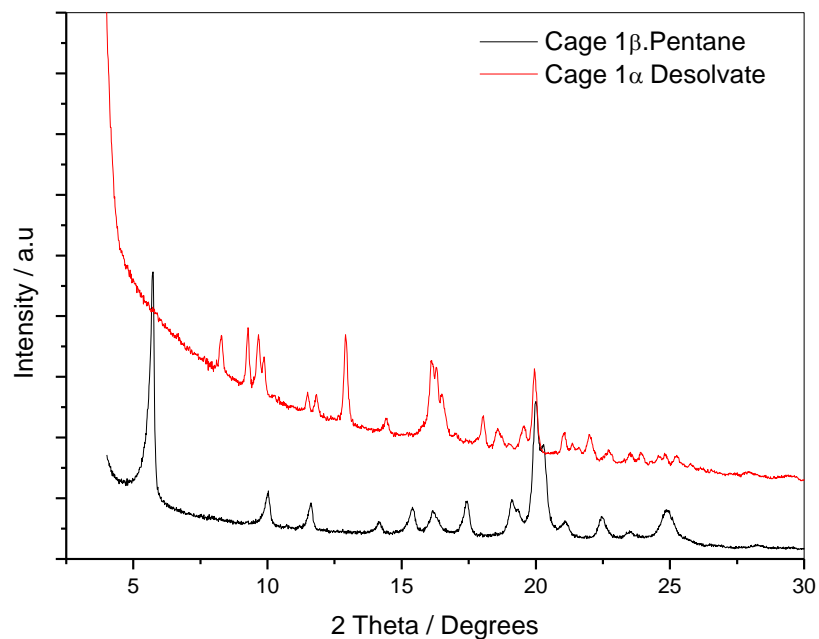


**Figure 7-49:** PXRD comparison of Cage 1 $\beta$  after pentane adsorption and Cage 1 $\alpha$  desolvate

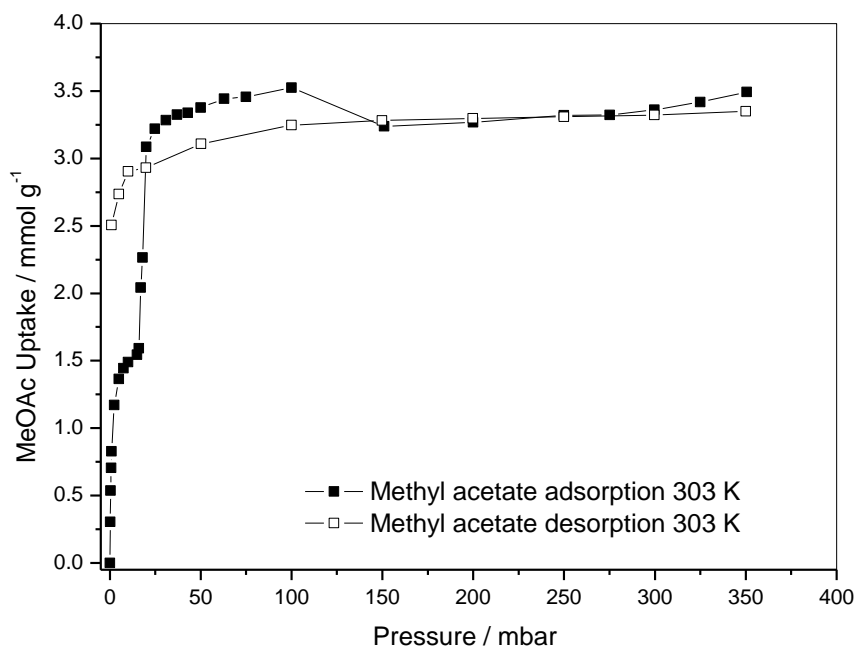


**Figure 7-50:** Methyl acetate isotherm on Cage 1 $\beta$  at 303 K

Chapter 7 Structural Change Induced by Adsorption of Gases and Vapours on Porous Cage Materials

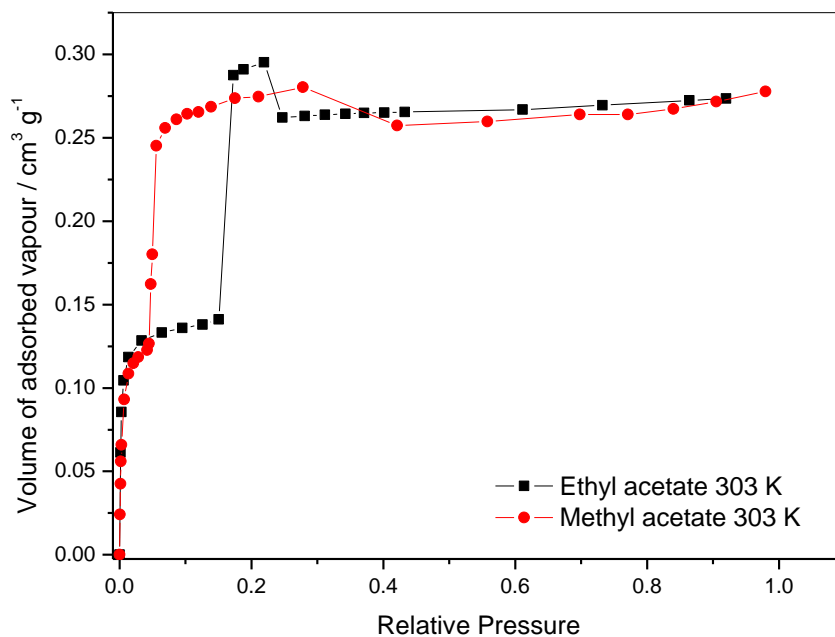


Figure 7-51: Comparison of methyl acetate and ethyl acetate adsorption isotherms at 303 K on Cage 1β

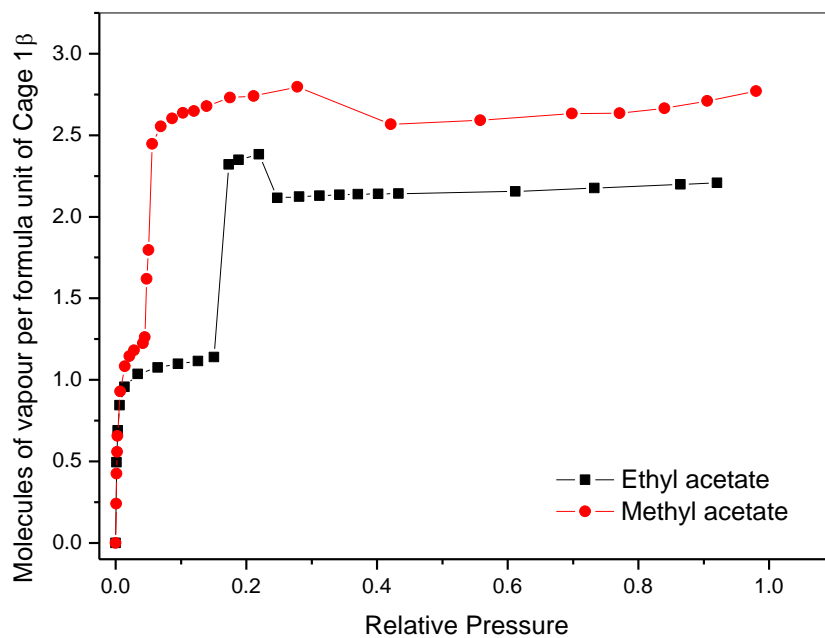
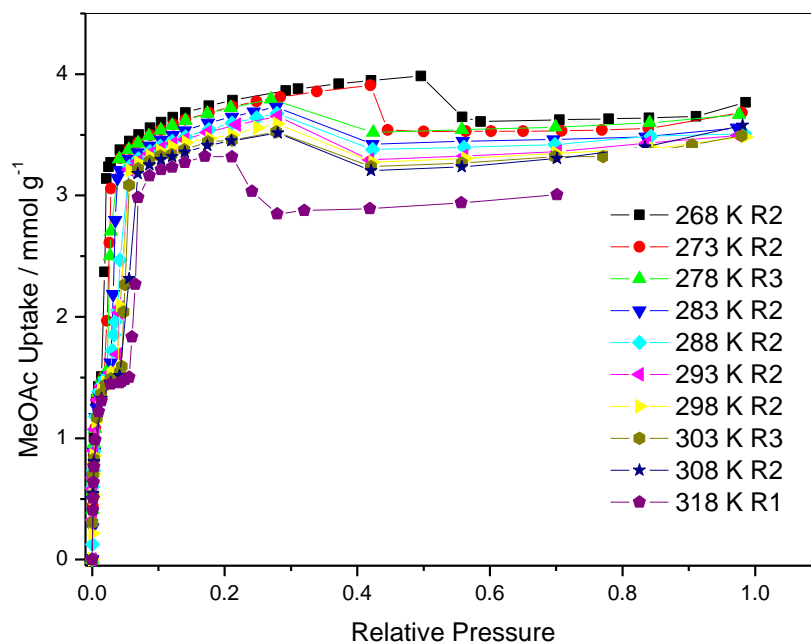
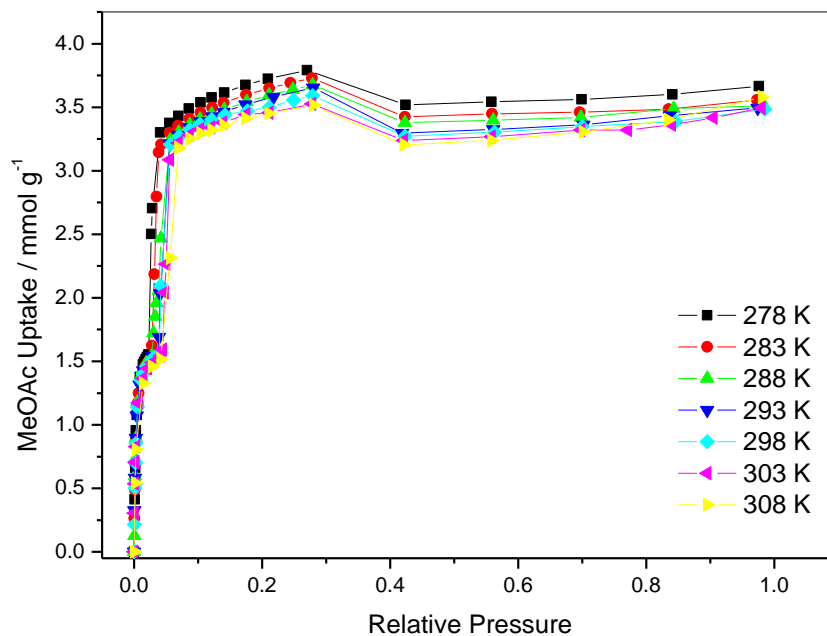


Figure 7-52: Comparison of methyl acetate and ethyl acetate number of molecules adsorbed per formula unit of Cage 1β at 303 K

Chapter 7 Structural Change Induced by Adsorption of Gases and Vapours on  
Porous Cage Materials



**Figure 7-53:** Methyl acetate adsorption isotherms on Cage 1 $\beta$  for the temperature range 268 – 318 K



**Figure 7-54:** Methyl acetate adsorption isotherms on Cage 1 $\beta$  for the temperature range 283 - 308 K

Chapter 7 Structural Change Induced by Adsorption of Gases and Vapours on  
Porous Cage Materials

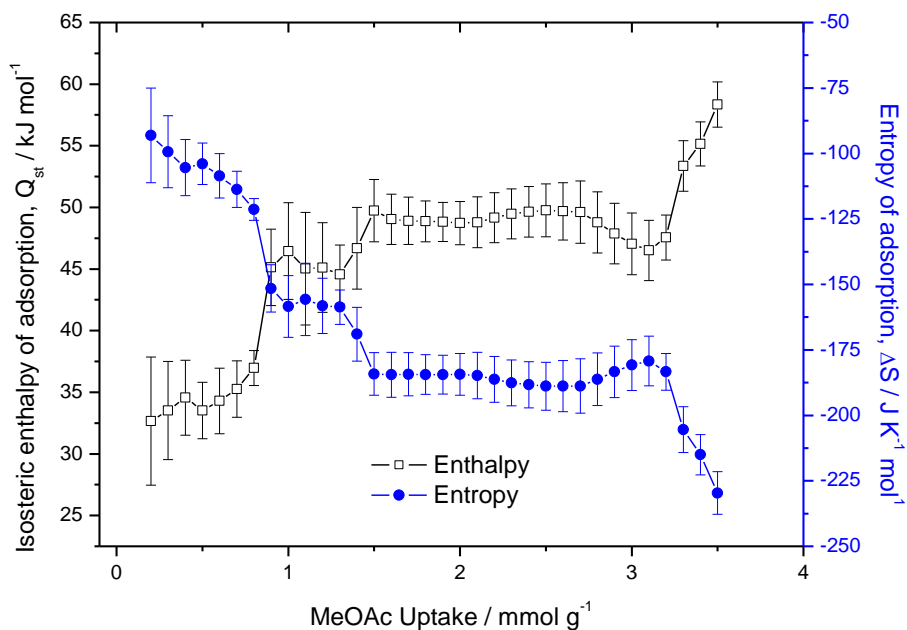


**Figure 7-55:** Enthalpy and entropy graph for methyl acetate adsorption on Cage 1 $\beta$  for the temperature range 278 - 308 K

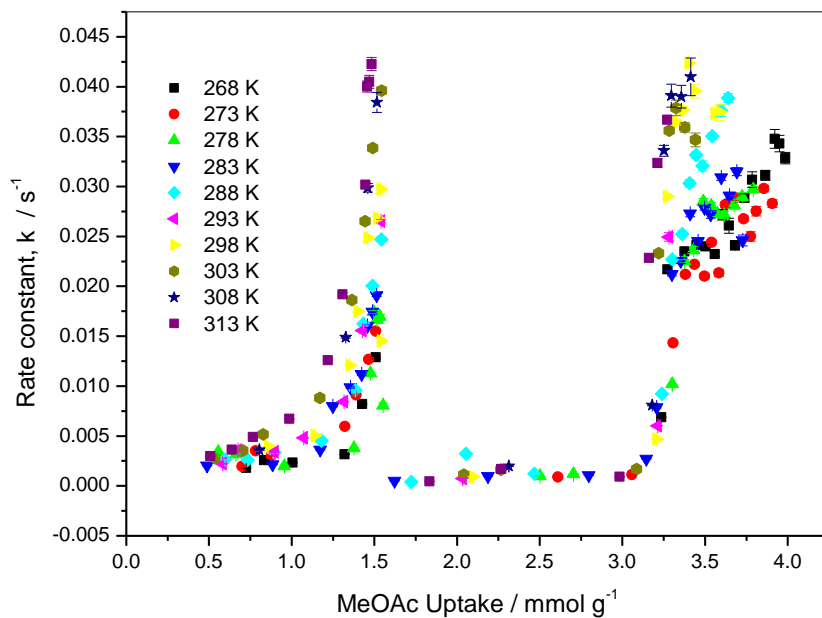


**Figure 7-56:** Graph of rate constant,  $k$ , versus MeOAc uptake on Cage 1 $\beta$  for the temperature range 268 – 313 K

Chapter 7 Structural Change Induced by Adsorption of Gases and Vapours on  
Porous Cage Materials

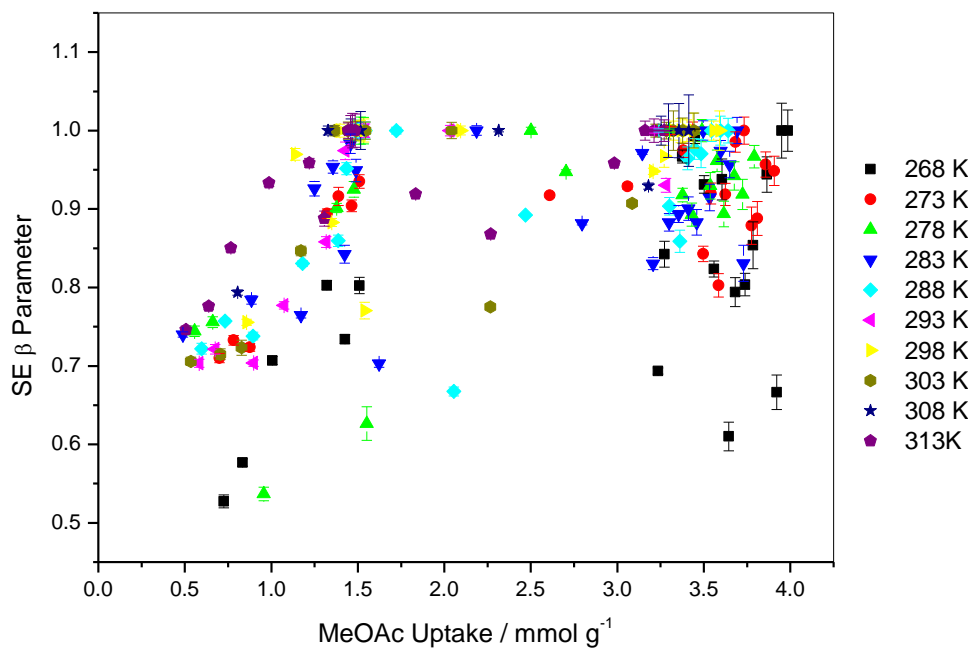


**Figure 7-57:** Graph of SE parameter,  $\beta$ , versus MeOAc uptake on Cage 1 $\beta$  for the temperature range 268 – 313 K

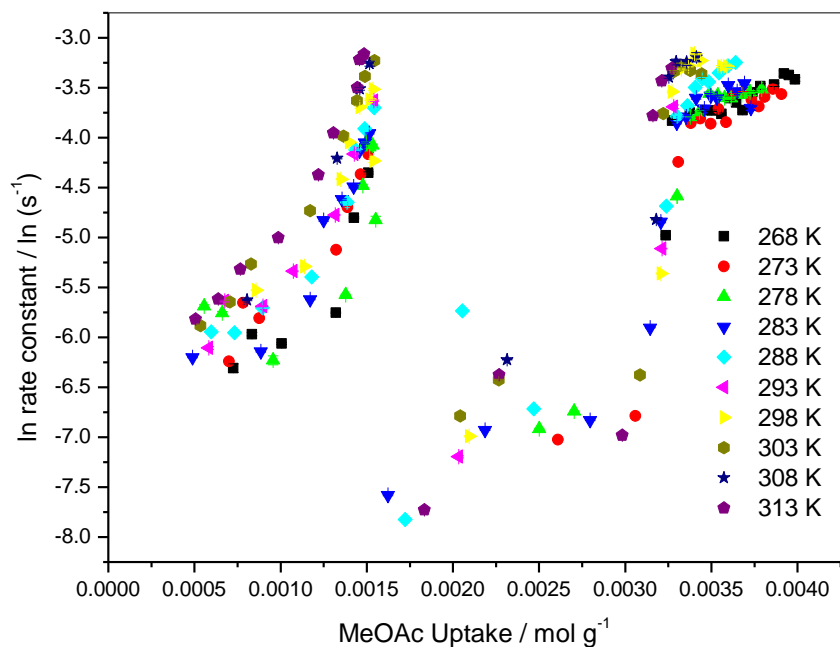


**Figure 7-58:** Graph of  $\ln k$  versus MeOAc uptake /  $\text{mol g}^{-1}$  for MeOAc uptake on Cage 1 $\beta$  for the temperature range 268 - 313 K

Chapter 7 Structural Change Induced by Adsorption of Gases and Vapours on Porous Cage Materials

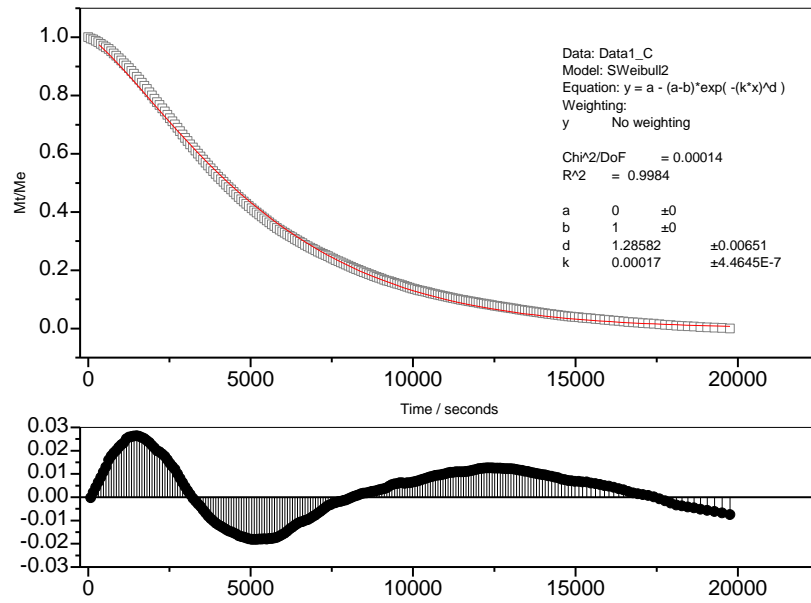


Figure 7-59: Cage 1β MeOAc desorption step at 278 K Avrami analysis

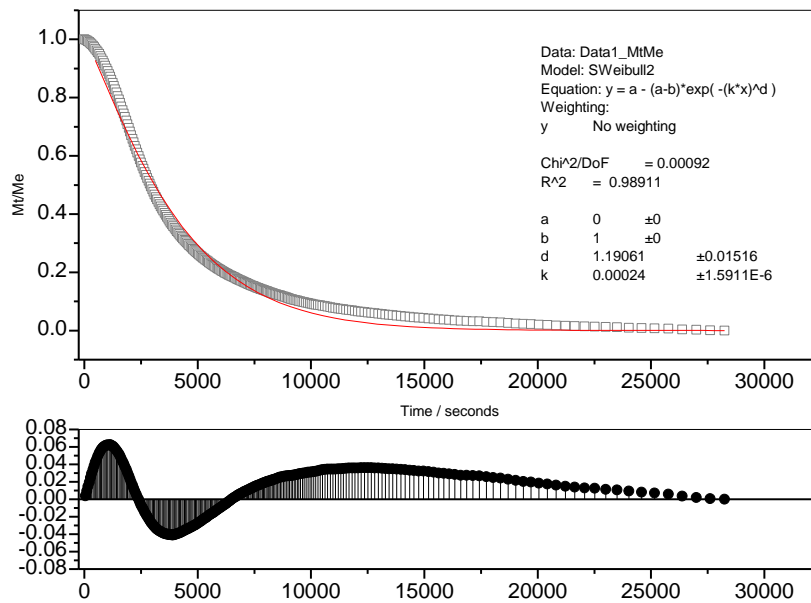


Figure 7-60: Cage 1β MeOAc desorption step at 283 K Avrami analysis

Chapter 7 Structural Change Induced by Adsorption of Gases and Vapours on Porous Cage Materials

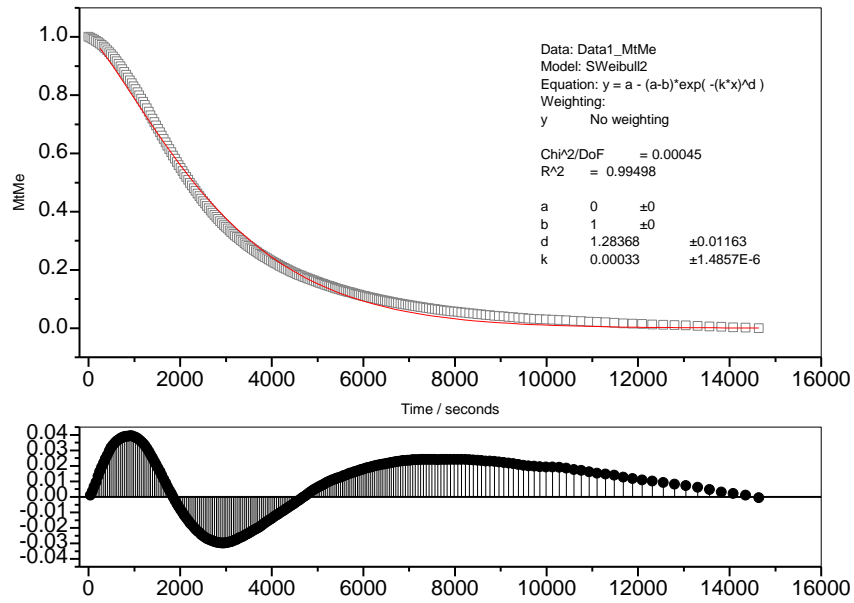


Figure 7-61: Cage 1β MeOAc desorption step at 288 K Avrami analysis

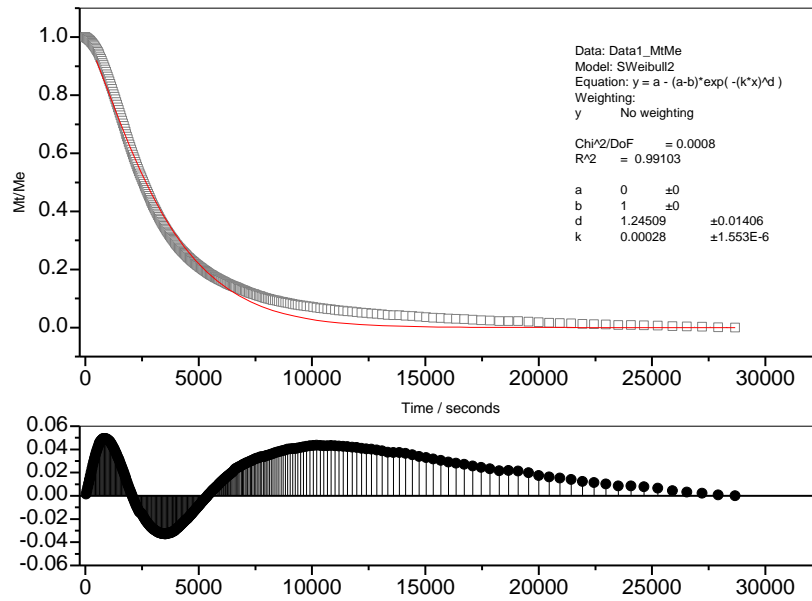


Figure 7-62: Cage 1β MeOAc desorption step at 293 K Avrami analysis



Chapter 7 Structural Change Induced by Adsorption of Gases and Vapours on Porous Cage Materials

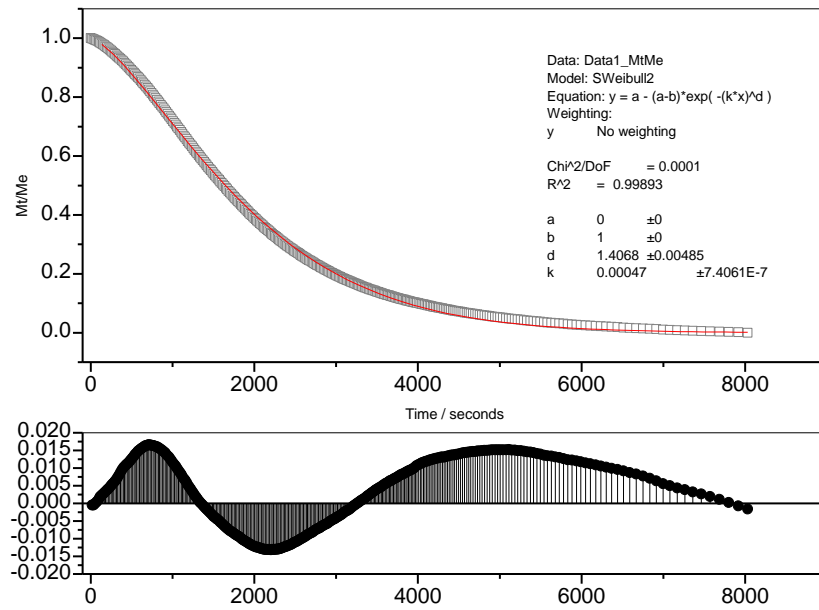


Figure 7-63: Cage 1β MeOAc desorption step at 298 K Avrami analysis

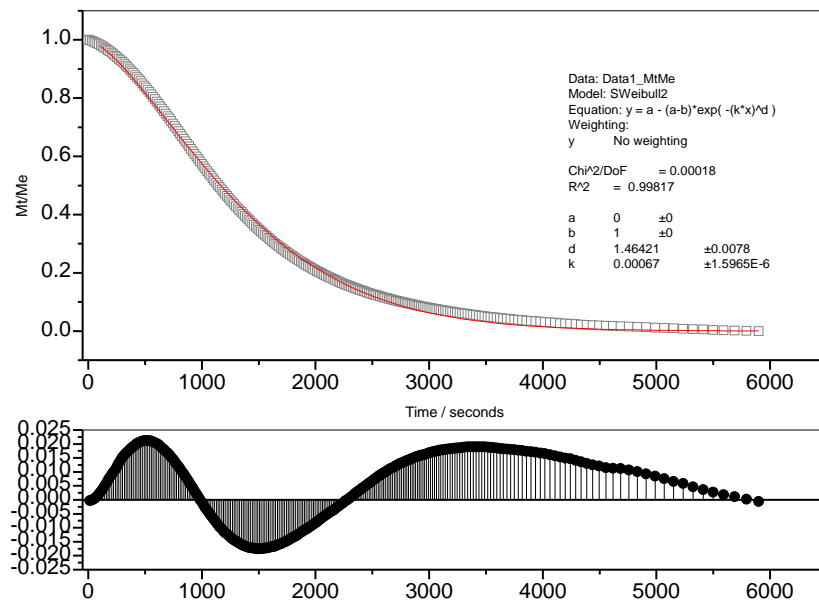
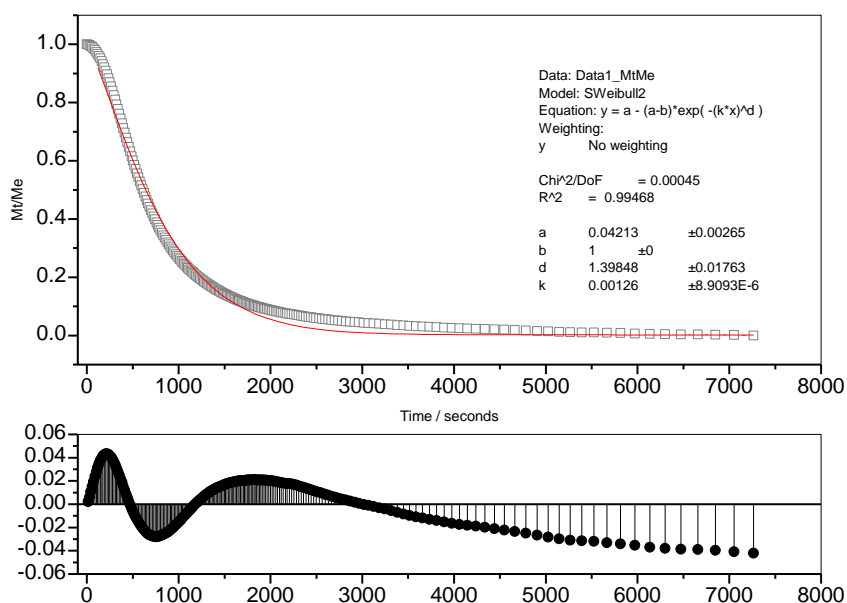


Figure 7-64: Cage 1β MeOAc desorption step at 303 K Avrami analysis

## Chapter 7 Structural Change Induced by Adsorption of Gases and Vapours on Porous Cage Materials



**Figure 7-65:** Cage 1 $\beta$  MeOAc desorption step at 308 K Avrami analysis

**Table 7-9:** Cage 1 $\beta$  MeOAc desorption step kinetics Avrami analysis parameters

Temperature / K	Rate constant / s <sup>-1</sup>	Avrami $\beta$ parameter
283	$2.4 \times 10^{-4} \pm 1.59 \times 10^{-6}$	$1.19 \pm 0.015$
288	$3.3 \times 10^{-4} \pm 1.49 \times 10^{-6}$	$1.28 \pm 0.012$
293	$2.8 \times 10^{-4} \pm 1.55 \times 10^{-6}$	$1.25 \pm 0.014$
298	$4.7 \times 10^{-4} \pm 7.41 \times 10^{-7}$	$1.41 \pm 0.0049$
303	$6.7 \times 10^{-4} \pm 1.60 \times 10^{-6}$	$1.46 \pm 0.0078$
308	$1.26 \times 10^{-3} \pm 8.91 \times 10^{-6}$	$1.34 \pm 0.018$

Chapter 7 Structural Change Induced by Adsorption of Gases and Vapours on  
Porous Cage Materials

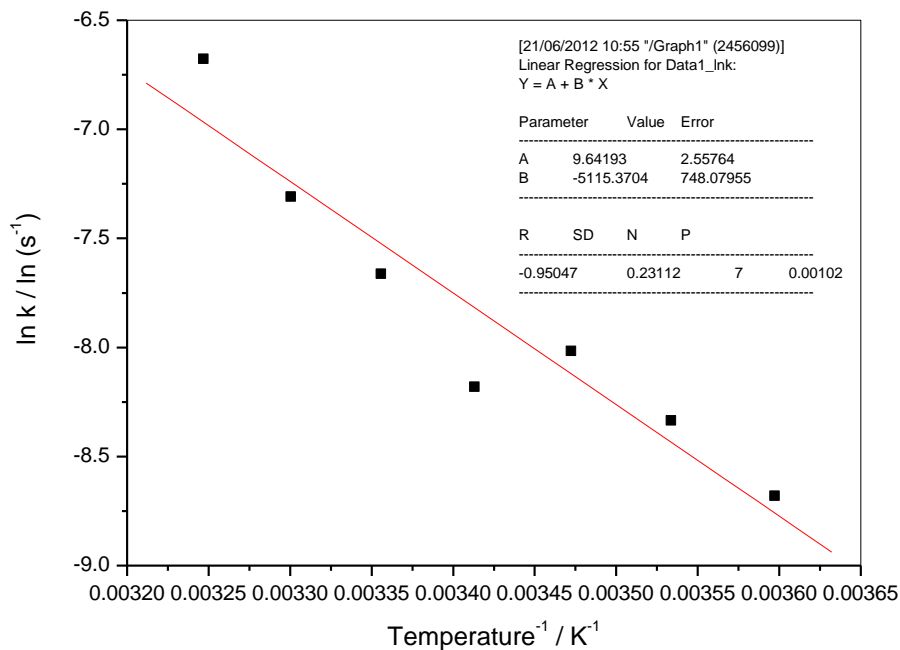


**Figure 7-66:** Graph on ln (k) against reciprocal temperature for MeOAc desorption steps on Cage 1 $\beta$  for the temperature range 278 – 308 K

## Chapter 7 Structural Change Induced by Adsorption of Gases and Vapours on Porous Cage Materials

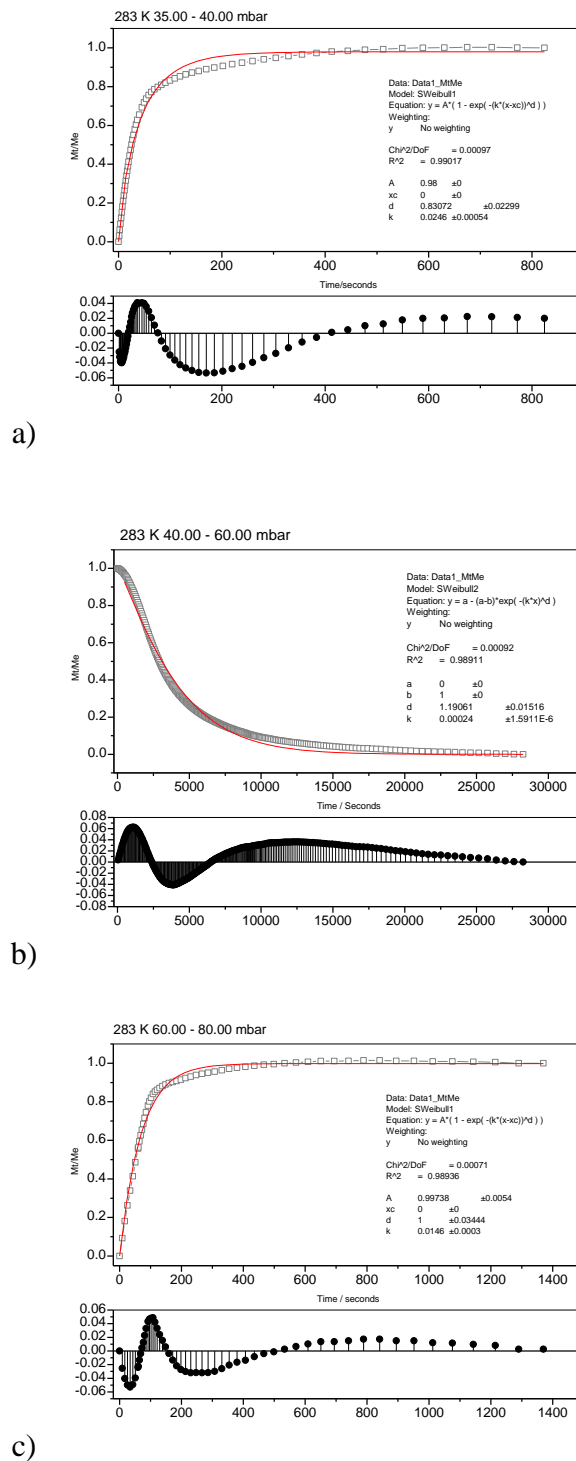


**Figure 7-67:** MeOAc profiles for a) 35 -40 mbar, b) 40 – 60 mbar and c) 60 – 80 mbar showing profiles before, during and after desorption step on Cage 1β at 283 K

Chapter 7 Structural Change Induced by Adsorption of Gases and Vapours on  
Porous Cage Materials

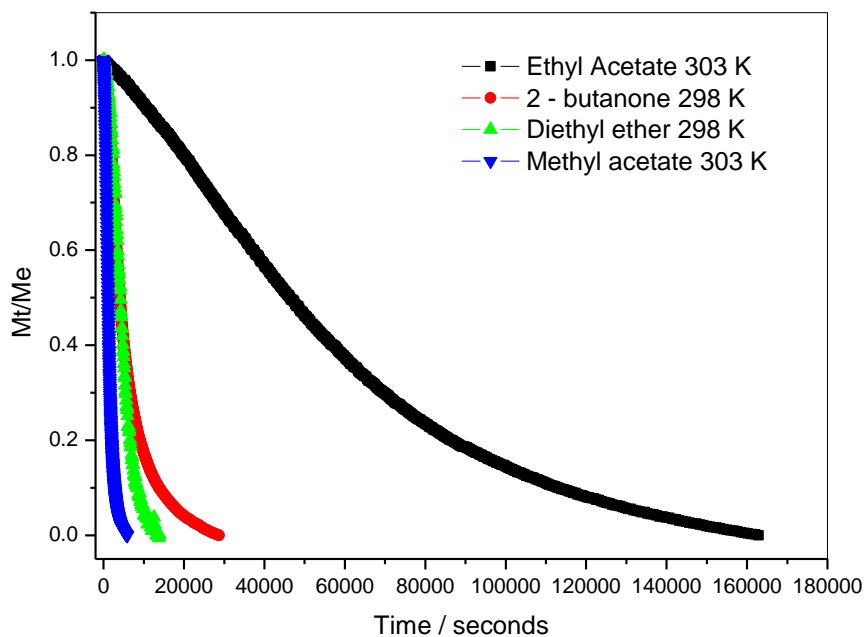


**Figure 7-68:** Comparison of the desorption steps in the ethyl acetate, 2-butanone, diethyl ether and methyl acetate adsorption isotherms

**Table 7-10:** Parameters for desorption step from Cage 1 $\beta$  Avrami analysis

Adsorptive	Rate constant, $k / s^{-1}$	Avrami $\beta$ Parameter
<b>EtOAc 303 K</b>	$2.00 \times 10^{-5} \pm 2.73 \times 10^{-8}$	$1.37 \pm 0.0033$
<b>2-butanone 298 K</b>	$1.70 \times 10^{-4} \pm 7.15 \times 10^{-7}$	$1.19 \pm 0.010$
<b>Diethyl ether 298 K</b>	$2.00 \times 10^{-4} \pm 4.66 \times 10^{-7}$	$1.82 \pm 0.011$
<b>MeOAc</b>	$4.7 \times 10^{-4} \pm 7.41 \times 10^{-7}$	$1.41 \pm 0.0049$

Chapter 7 Structural Change Induced by Adsorption of Gases and Vapours on  
Porous Cage Materials

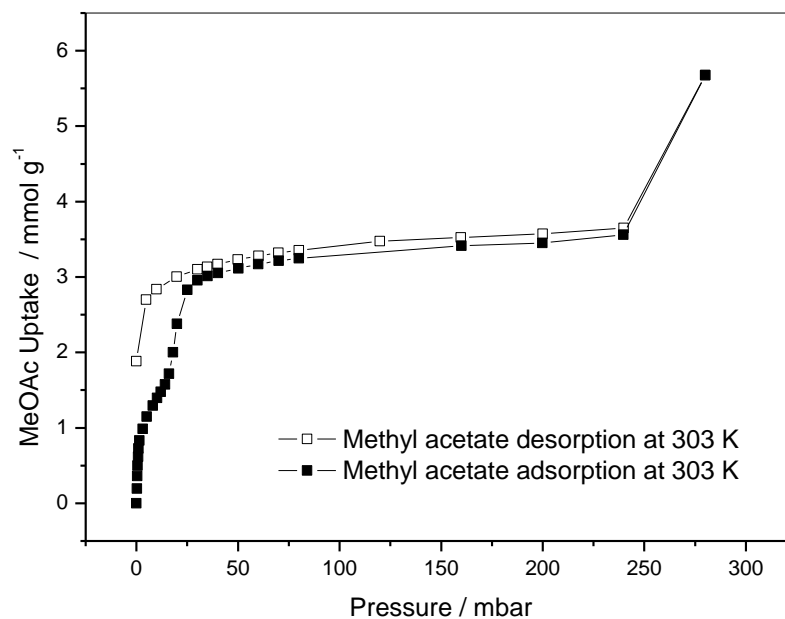


Figure 7-69: Methyl acetate isotherm on Cage 1 $\alpha$ # at 303 K

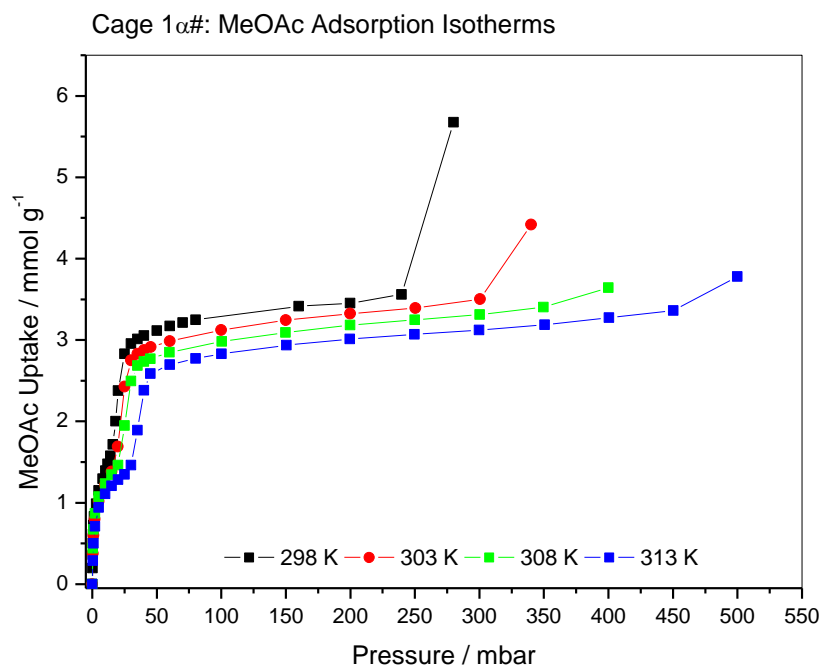
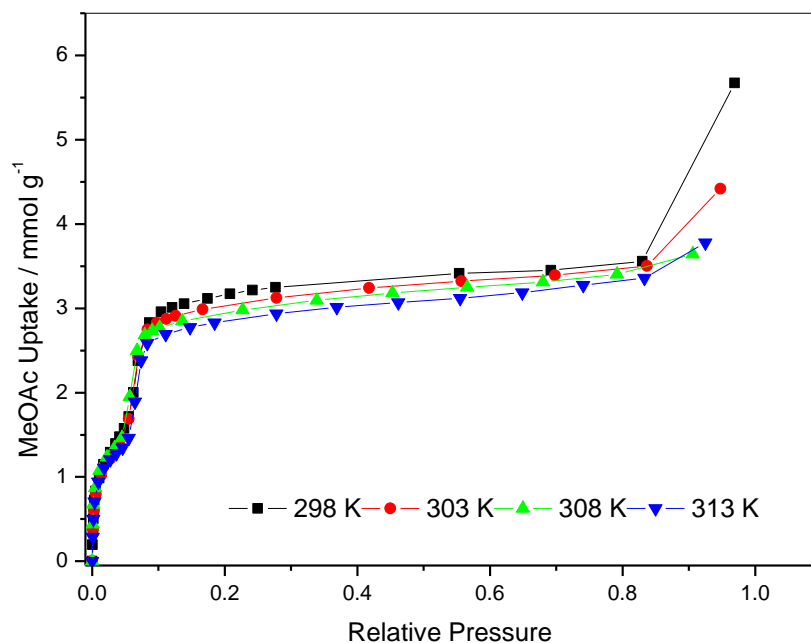
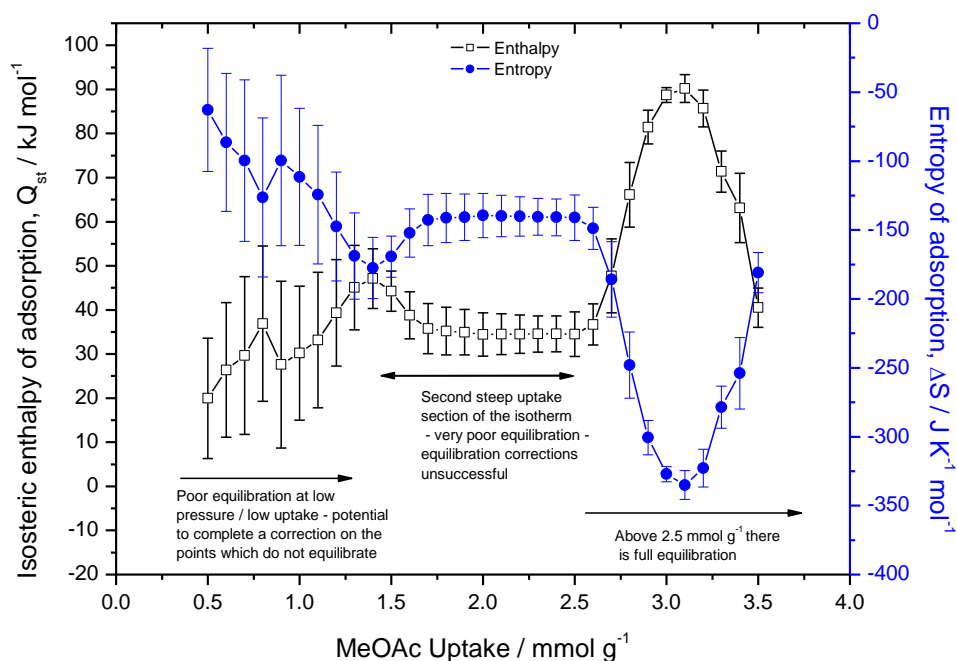


Figure 7-70: Methyl acetate adsorption isotherms on Cage 1 $\alpha$ # for the temperature range 298 - 313 K

Chapter 7 Structural Change Induced by Adsorption of Gases and Vapours on  
Porous Cage Materials



**Figure 7-71:** Methyl acetate adsorption isotherms on Cage 1a# for the temperature range 298 - 313 K on a relative pressure basis



**Figure 7-72:** Enthalpy and entropy variation with uptake graph for methyl acetate adsorption on Cage 1a# for the temperature range 298 - 313 K

Chapter 7 Structural Change Induced by Adsorption of Gases and Vapours on  
Porous Cage Materials

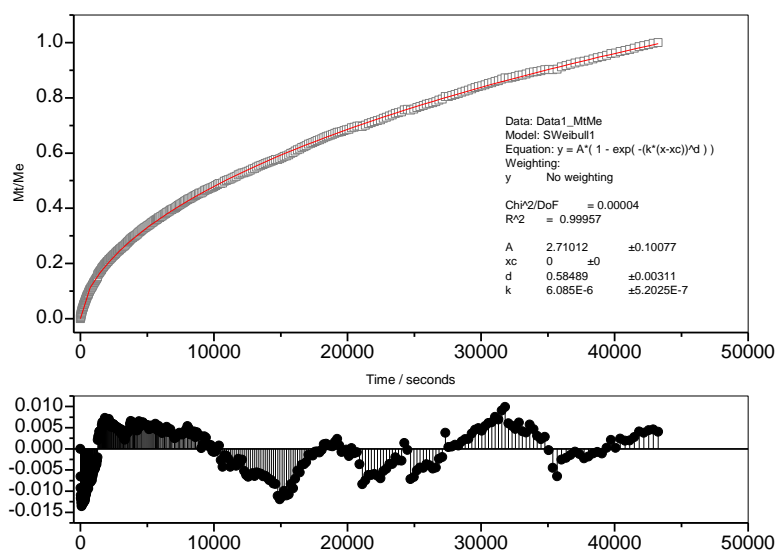


**Figure 7-73:** MeOAc on Cage 1 $\alpha$ # at 303 K 1.22 mmol g<sup>-1</sup> uptake, 5 – 10 mbar pressure step SE kinetic analysis showing poor equilibration

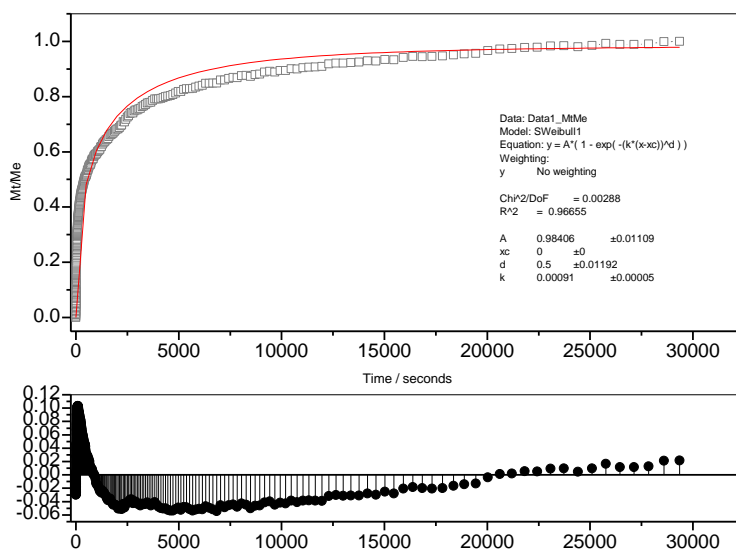


**Figure 7-74:** MeOAc on Cage 1 $\alpha$ # at 298 K 3.42 mmol g<sup>-1</sup> uptake, 80 – 160 mbar pressure step SE kinetic analysis showing good equilibrium



Chapter 7 Structural Change Induced by Adsorption of Gases and Vapours on  
Porous Cage Materials

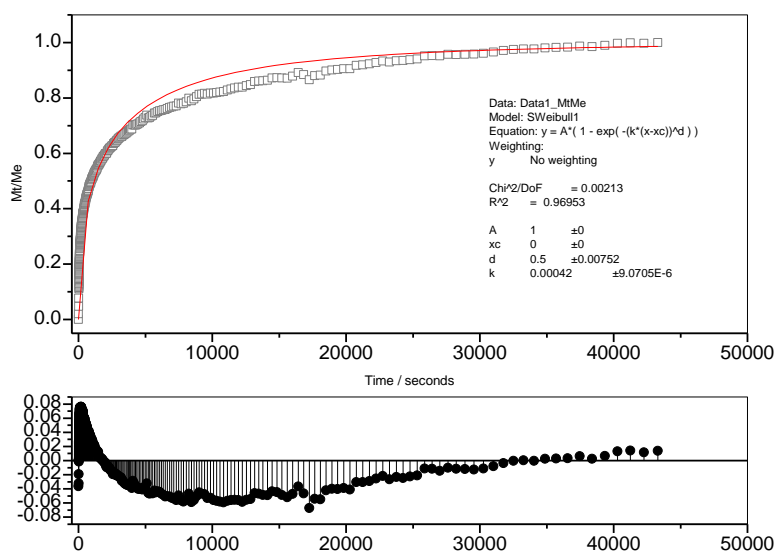


**Figure 7-75:** MeOAc on Cage 1 $\alpha$ # at 303 K 3.12 mmol g<sup>-1</sup> uptake, 60 – 100 mbar pressure step SE kinetic analysis showing good equilibrium

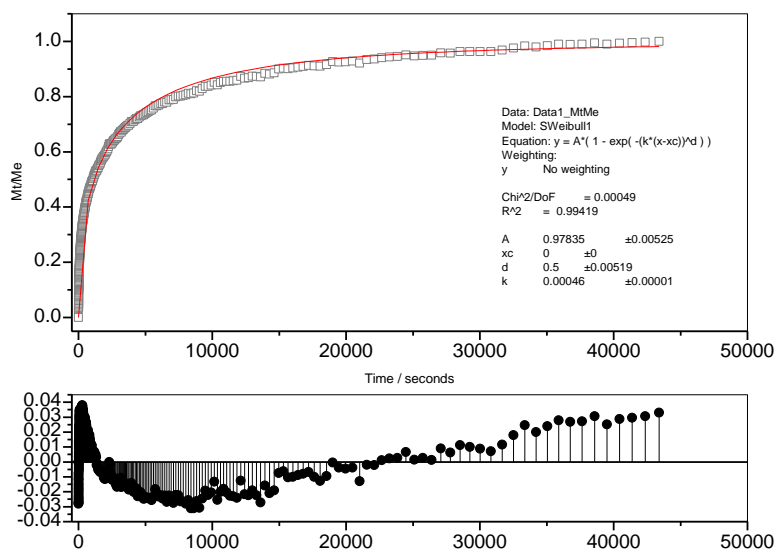


**Figure 7-76:** MeOAc on Cage 1 $\alpha$ # at 308 K 3.00 mmol g<sup>-1</sup> uptake, 60 – 100 mbar pressure step SE kinetic analysis showing good equilibrium

Chapter 7 Structural Change Induced by Adsorption of Gases and Vapours on Porous Cage Materials

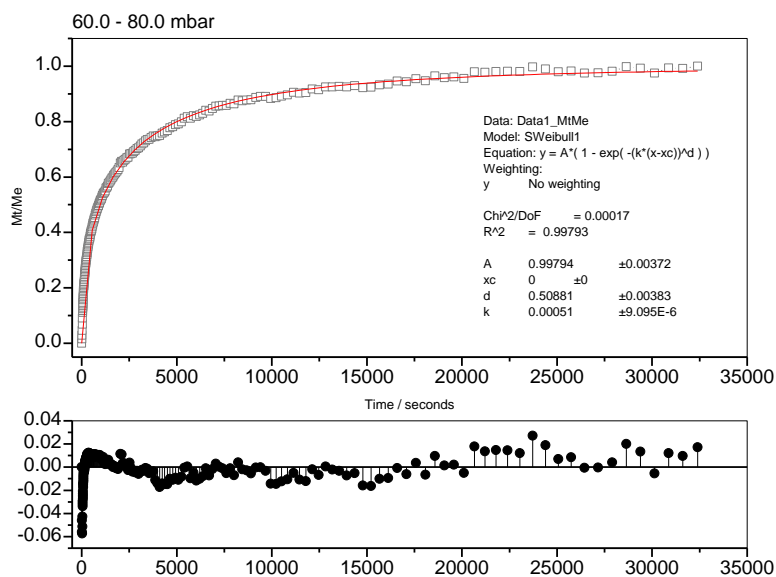


**Figure 7-77:** MeOAc on Cage 1 $\alpha$ # at 313 K 2.77 mmol g<sup>-1</sup> uptake, 60 – 80 mbar pressure step SE kinetic analysis showing good equilibrium

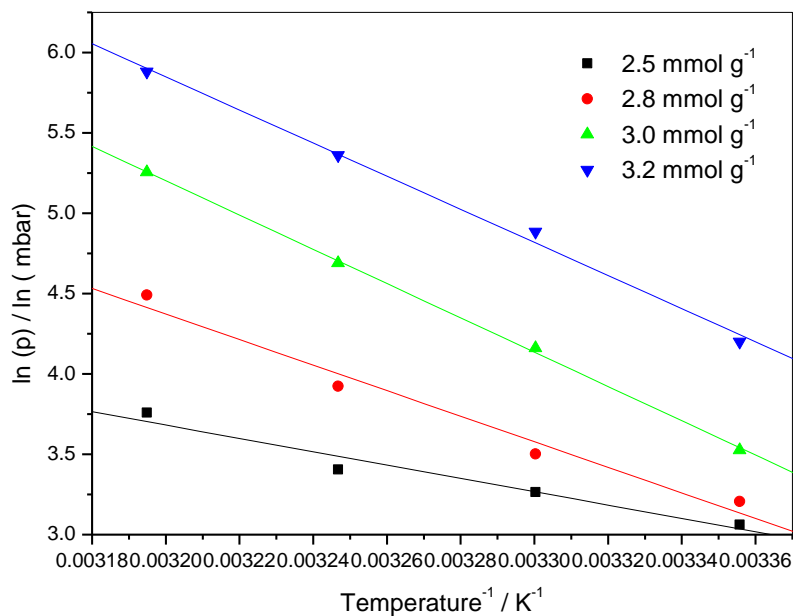


**Figure 7-78:** van't Hoff plots for MeOAc uptakes of 2.5, 2.8, 3.0 and 3.2 mmol g<sup>-1</sup> on Cage 1 $\alpha$ # for the temperature range 298 – 313 K

Chapter 7 Structural Change Induced by Adsorption of Gases and Vapours on  
Porous Cage Materials

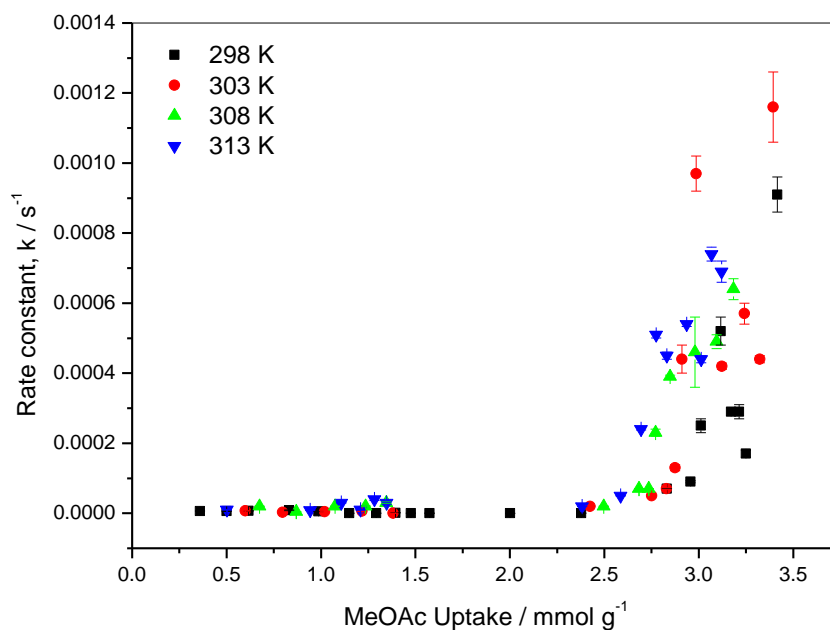


**Figure 7-79:** Graph of rate constant,  $k$ , versus MeOAc uptake on Cage 1 $\alpha$ # for the temperature range 298 – 313 K

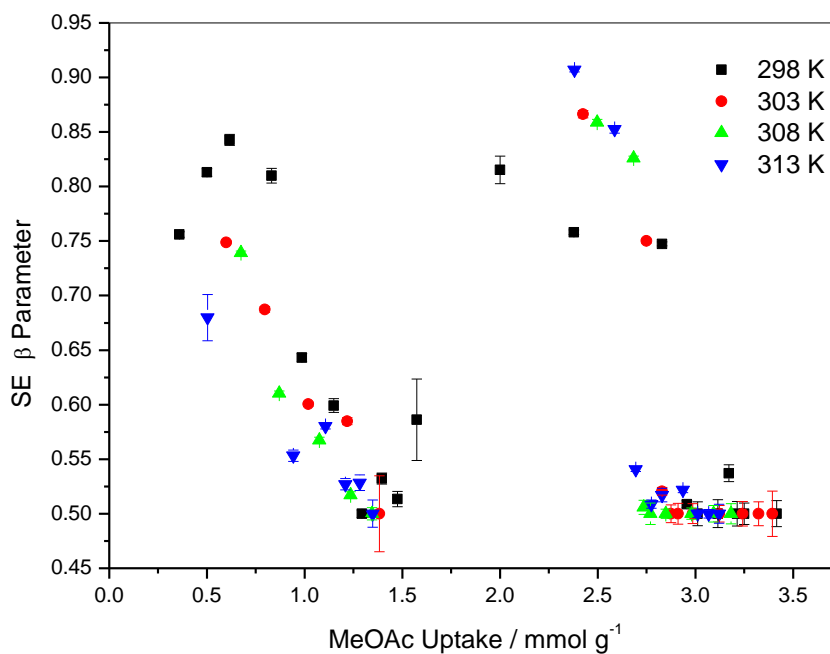


**Figure 7-80:** Graph of SE parameter,  $\beta$ , versus MeOAc uptake on Cage 1 $\alpha$ # for the temperature range 268 – 313 K

Chapter 7 Structural Change Induced by Adsorption of Gases and Vapours on Porous Cage Materials

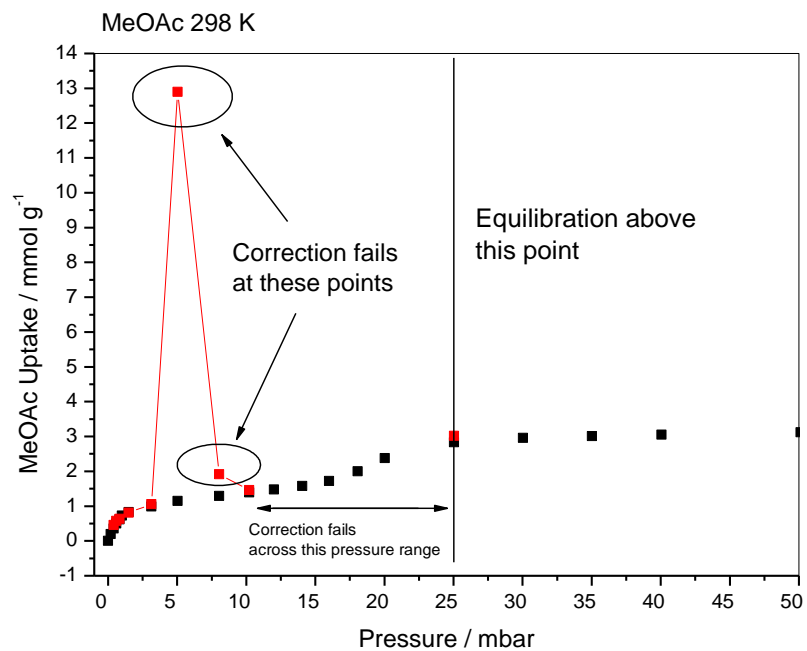


Figure 7-81: Corrected and original isotherm points for methyl acetate adsorption on Cage 1 $\alpha$ # at 298 K for the pressure range 0 – 50 mbar

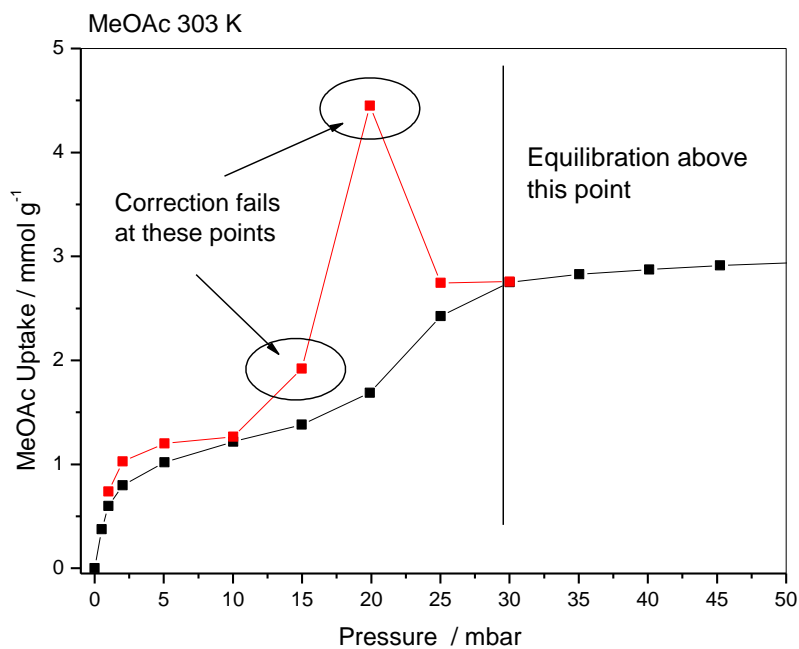
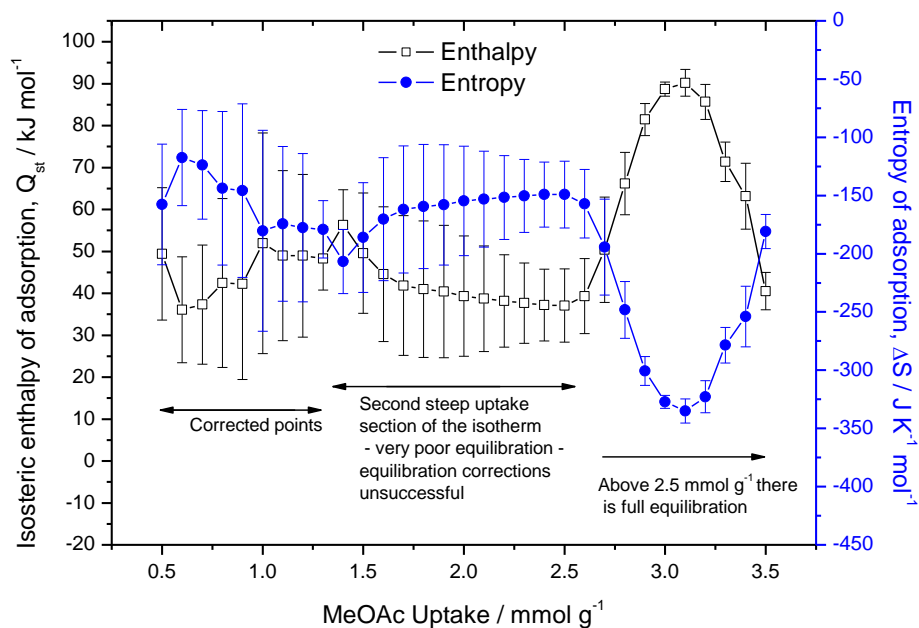
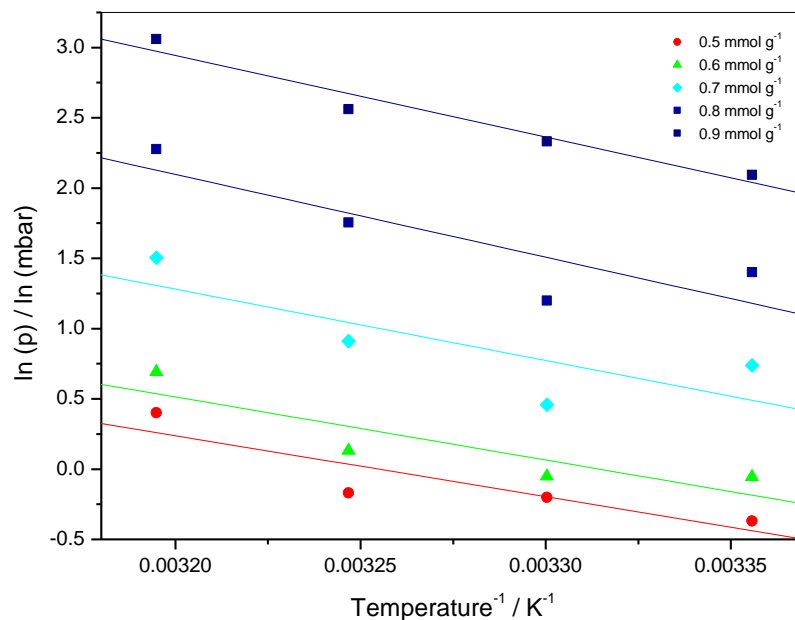


Figure 7-82: Corrected and original isotherm points for methyl acetate adsorption on Cage 1 $\alpha$ # at 303 K for the pressure range 0 – 50 mbar

Chapter 7 Structural Change Induced by Adsorption of Gases and Vapours on  
Porous Cage Materials



**Figure 7-83:** Corrected isosteric enthalpy of adsorption and entropy of adsorption profiles for methyl acetate adsorption on Cage 1a#



**Figure 7-84:** van't Hoff plots for MeOAc uptakes of 0.5, 0.6, 0.7, 0.8 and 0.9 mmol g<sup>-1</sup> on Cage 1a# for the temperature range 298 – 313 K

Chapter 7 Structural Change Induced by Adsorption of Gases and Vapours on  
Porous Cage Materials

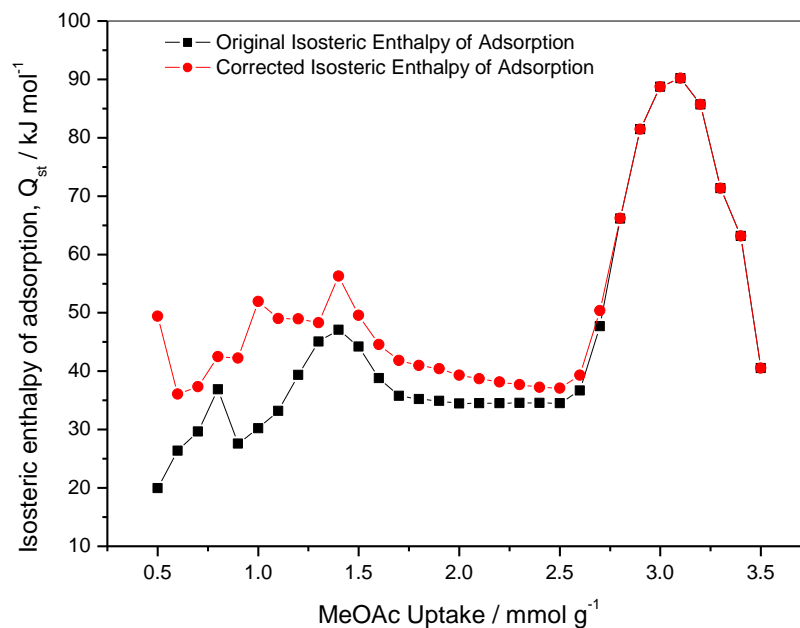


**Figure 7-85:** Comparison of original and corrected isosteric enthalpy of adsorption for methyl acetate adsorption on Cage 1 $\alpha$ #, with error bars omitted for clarity, for the temperature range 298 – 313 K

Chapter 7 Structural Change Induced by Adsorption of Gases and Vapours on  
Porous Cage Materials

**Table 7-11:** Comparison of the corrected and original isosteric enthalpy of adsorption and entropy of adsorption values for methyl acetate adsorption on Cage 1 $\alpha$ #

MeOAc Uptake / mmol g <sup>-1</sup>	Original Q <sub>st(ADS)</sub> / kJ mol <sup>-1</sup>	Corrected Q <sub>st(ADS)</sub> / kJ mol <sup>-1</sup>	Original $\Delta S_{(ADS)}$ / J K <sup>-1</sup> mol <sup>-1</sup>	Corrected $\Delta S_{(ADS)}$ / J K <sup>-1</sup> mol <sup>-1</sup>
0.5	19.97 ± 13.65	49.41 ± 15.82	-62.85 ± -44.70	-157.75 ± -51.80
0.6	26.39 ± 15.25	36.07 ± 12.64	-86.42 ± -49.95	-117.39 ± -41.40
0.7	29.68 ± 17.89	37.33 ± 14.22	-99.68 ± -58.60	-123.71 ± -46.56
0.8	36.88 ± 17.62	42.48 ± 20.15	-126.4 ± -57.73	-143.74 ± -65.98
0.9	27.6 ± 18.88	42.25 ± 22.78	-99.63 ± -61.83	-145.84 ± -74.61
1	30.2 ± 15.2	51.94 ± 26.35	-111.45 ± -49.77	-180.37 ± -86.28
1.1	33.2 ± 15.36	49.00 ± 20.28	-124.26 ± -50.29	-174.24 ± -66.43
1.2	39.37 ± 12.07	48.98 ± 19.41	-147.49 ± -39.52	-177.62 ± -63.58
1.3	45.07 ± 9.58	48.32 ± 7.52	-168.88 ± -31.38	-179.1 ± -24.62
1.4	47.1 ± 6.76	56.28 ± 8.41	-177.56 ± -22.14	-206.75 ± -27.53

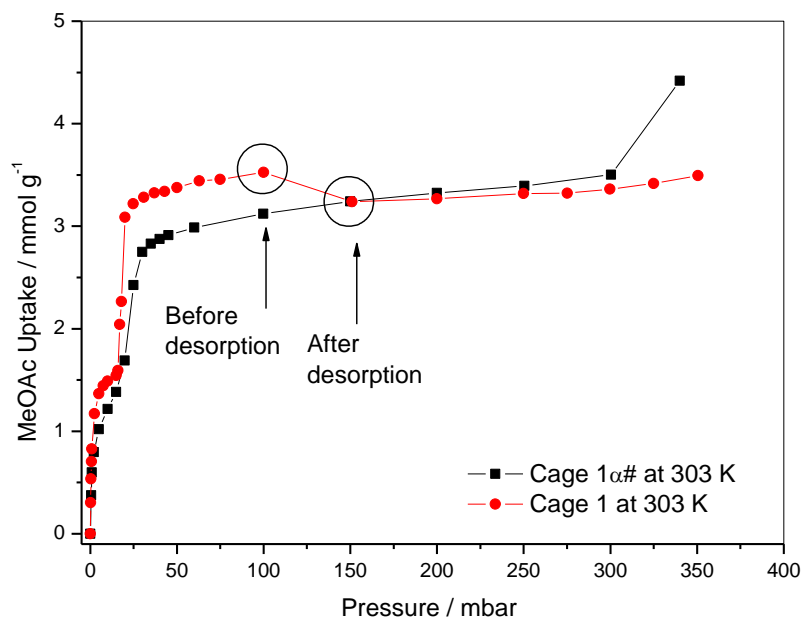


**Figure 7-86:** Comparison of methyl acetate adsorption on Cage 1 $\beta$  and Cage 1 $\alpha$ # at 303 K

Chapter 7 Structural Change Induced by Adsorption of Gases and Vapours on  
Porous Cage Materials

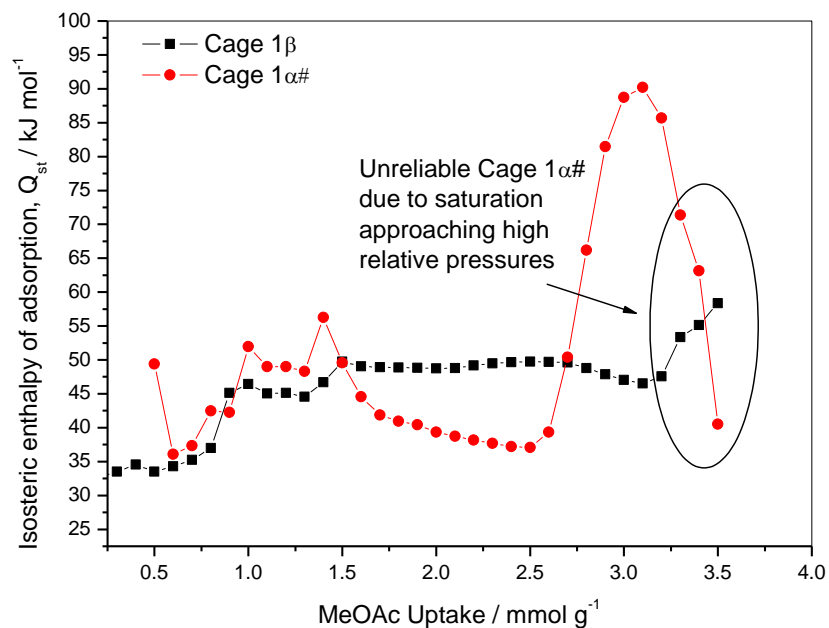


**Figure 7-87:** Comparison of methyl acetate isosteric enthalpy of adsorption on Cage 1 $\beta$  and Cage 1 $\alpha\#$

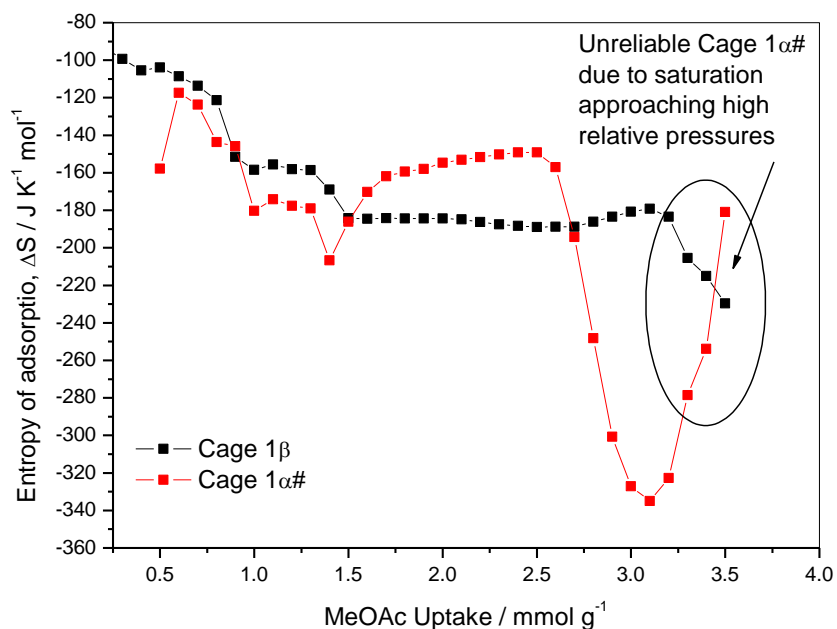


**Figure 7-88:** Comparison of methyl acetate isosteric entropy of adsorption on Cage 1 $\beta$  and Cage 1 $\alpha\#$



Chapter 7 Structural Change Induced by Adsorption of Gases and Vapours on  
Porous Cage Materials

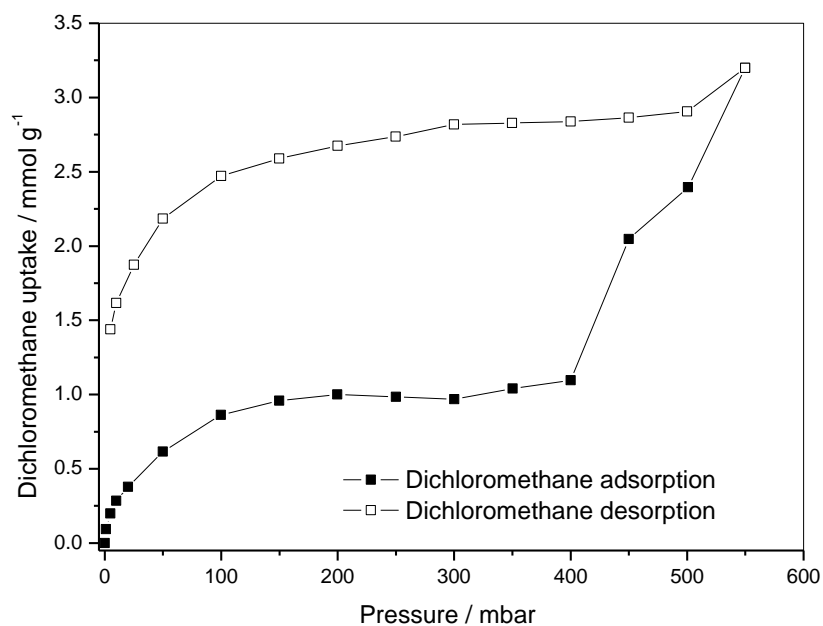


Figure 7-89: Dichloromethane adsorption on Cage 1a at 298 K

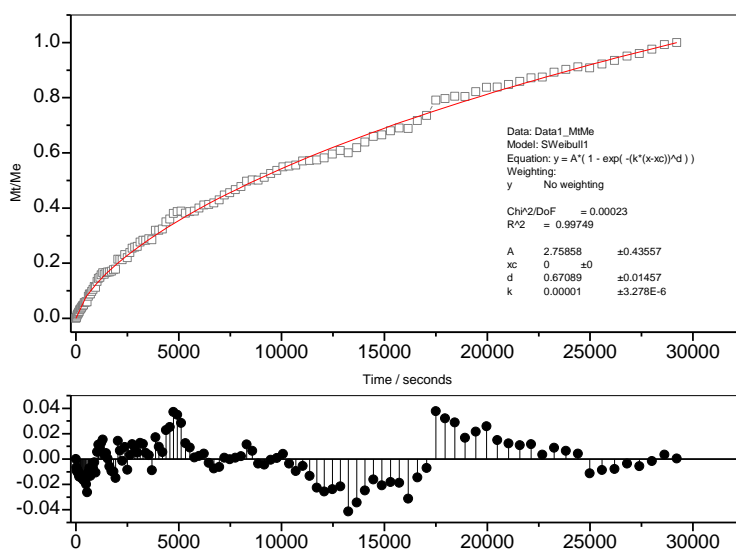
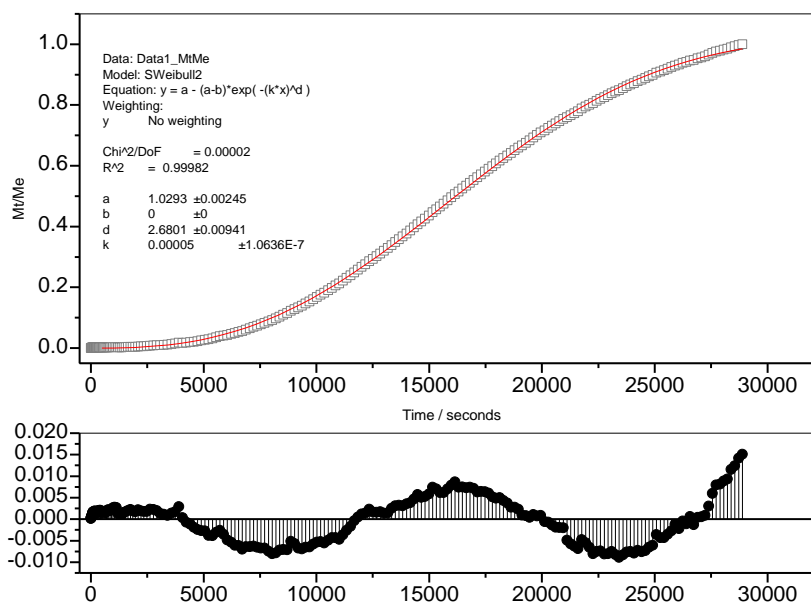


Figure 7-90: Stretched exponential kinetic analysis of dichloromethane adsorption on Cage 1a for the pressure step 5 – 10 mbar

Chapter 7 Structural Change Induced by Adsorption of Gases and Vapours on  
Porous Cage Materials

**Table 7-12:** Dichloromethane adsorption at 298 K stretched exponential kinetic analysis parameters

Pressure / mbar	SE $\beta$ Parameter	Rate constant, $k / s^{-1}$
1.00	$0.743 \pm 0.00981$	$5.00 \times 10^{-5} \pm 3.00 \times 10^{-6}$
4.92	$0.746 \pm 0.00598$	$4.00 \times 10^{-5} \pm 2.00 \times 10^{-6}$
10.012	$0.671 \pm 0.0146$	$1.00 \times 10^{-5} \pm 3.00 \times 10^{-6}$
20.01	$0.502 \pm 0.00642$	$5.00 \times 10^{-9} \pm 4.00 \times 10^{-10}$
50.02	$0.500 \pm 0.00698$	$2.00 \times 10^{-5} \pm 3.00 \times 10^{-6}$
99.88	$0.500 \pm 0.00351$	$9.00 \times 10^{-5} \pm 4.00 \times 10^{-6}$
149.95	$0.742 \pm 0.00983$	$3.00 \times 10^{-5} \pm 2.00 \times 10^{-6}$
199.74	$0.876 \pm 0.0254$	$8.00 \times 10^{-5} \pm 6.00 \times 10^{-6}$



**Figure 7-91:** Dichloromethane adsorption pressure step 400 – 450 mbar Avrami kinetic analysis

Chapter 7 Structural Change Induced by Adsorption of Gases and Vapours on Porous Cage Materials

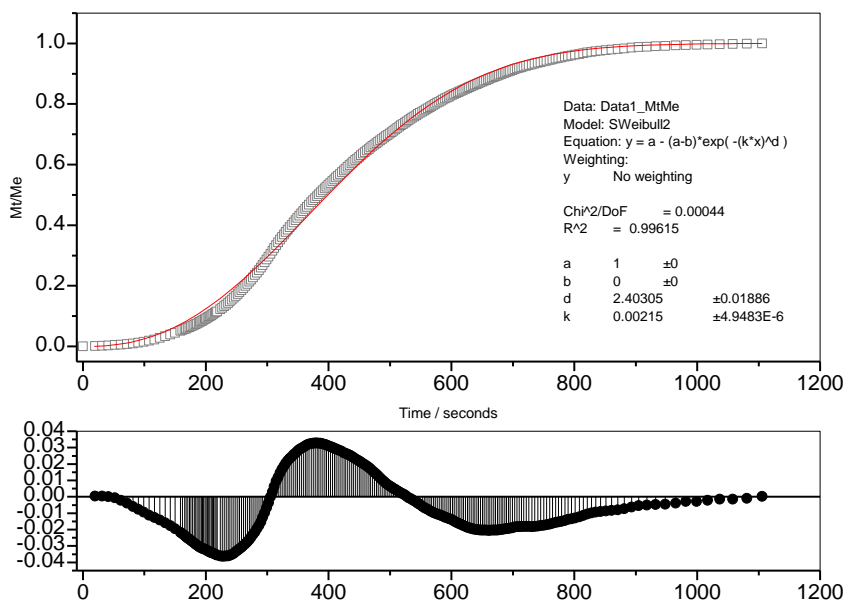


Figure 7-92: Dichloromethane adsorption pressure step 450 – 500 mbar Avrami kinetic analysis

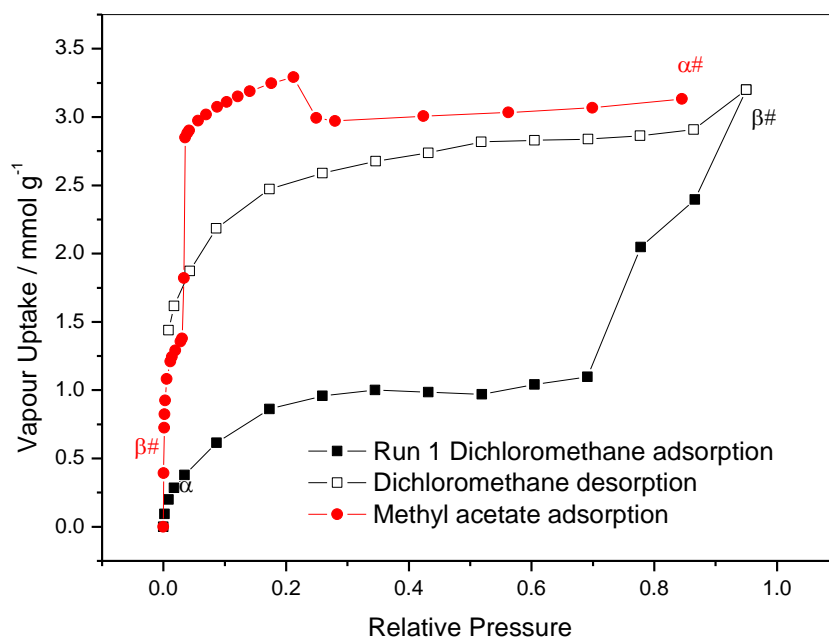


Figure 7-93: Cage 1 $\alpha$  dichloromethane → methyl acetate cycle

Chapter 7 Structural Change Induced by Adsorption of Gases and Vapours on  
Porous Cage Materials

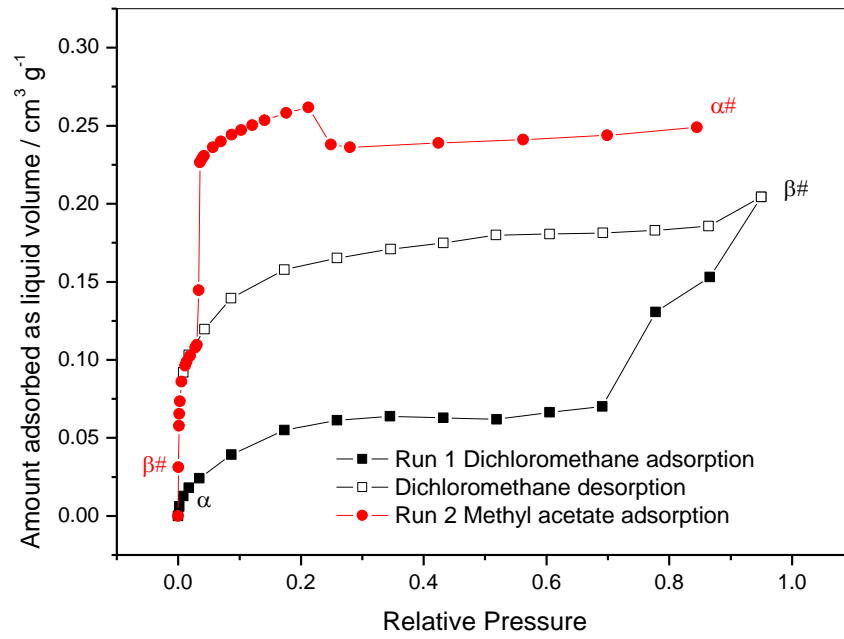


Figure 7-94: Cage 1 $\alpha$  dichloromethane  $\rightarrow$  methyl acetate cycle on a vapour volume basis

Chapter 7 Structural Change Induced by Adsorption of Gases and Vapours on  
Porous Cage Materials

7.9 References

- <sup>1</sup> T. Tomokazu, J. T. A. Jones, S. I. Swamy, S. Jiang, D. J. Adams, S. Shakespeare, R. Clowes, D. Bradshaw, T. Hasell, S. Y. Chong, C. Tang, S. Thompson, J. Parker, A. Trewin, J. Bacsá, A. M. Z. Slawin, A. Steiner, A. I. Cooper, *Nat. Mat.*, **2009**, 8, 973
- <sup>2</sup> J. T. A. Jones, D. Holden, T. Mitra, T. Hasell, D. J. Adams, K. E. Jelfs, A. Trewin, D. J. Willock, G. M. Day, J. Bacsá, A. Steiner, A. I. Cooper, *Angew. Chem. Int. Ed.*, **2010**, 50, 749
- <sup>3</sup> I. Langmuir, *J. Amer. Chem. Soc.*, 1916, **38**, 2219
- <sup>4</sup> I. Langmuir, *J. Amer. Chem. Soc.*, 1918, **40**, 1361
- <sup>5</sup> K. S. W. Sing, D. H. Everett, R. W. Haul, L. Moscou, R. A. Pierotti, J. Rouquerol, T. Siemieniewska, *Pure & Applied Chem.*, **1985**, 57, 603
- <sup>6</sup> M. M. Dubinin, *Carbon* **1984**, 22, 221
- <sup>7</sup> E. M. Freeman, T. Siemieniewska, H. Marsh, B. Rand, *Carbon*, **1967**, 8, 7
- <sup>8</sup> M. Avrami, *Journal of Chemical Physics*, **1939**, 7, 1103
- <sup>9</sup> M. Avrami, *Journal of Chemical Physics*, **1940**, 8, 212
- <sup>10</sup> M. Avrami, *Journal of Chemical Physics*, **1941**, 9, 177
- <sup>11</sup> R. J. Young, P. A. Lovell, *Introduction to Polymers 2<sup>nd</sup> Edition*, Chapman and Hall, London, **1991**
- <sup>12</sup> A. N. Wilkinson, A. J. Ryan, *Polymer Processing and Structure Development*, Kluwer Academic Publishers, **1998**
- <sup>13</sup> J. Klafter, M. F. Shlesinger, *Proc. Natl. Acad. Sc., USA*, **1986**, 83, 848
- <sup>14</sup> J. R. Barrante, *Applied Mathematics for Physical Chemistry*, Pearson Education Ltd, London, **2004**
- <sup>15</sup> G. Buckton, P. Darcy, *Int. J. Pharma.*, **1995**, 123, 265
- <sup>16</sup> D. Das, T. A. G. Langrish, *J. Food Eng.*, **2012**, 109, 691
- <sup>17</sup> Y. D. Chen, R. T. Yang, *Carbon*, **1998**, 36, 1525

Chapter 8 Kinetic Molecular Sieving of Oxygen and Nitrogen by  
Organic Cage Materials Cage 1 $\alpha$  and Cage 1 $\alpha$ #

8.1 Introduction

The separation of oxygen and nitrogen is achieved commercially using carbon molecular sieves and the pressure swing adsorption technique (PSA) – see **Chapter 3 – Separation of Gases and Vapours**. The pressure swing adsorption separation of oxygen and nitrogen by carbon molecular sieves is based upon the difference in the adsorption kinetics of oxygen and nitrogen, as the amount of each gas that is adsorbed is similar. The difference in the kinetics of adsorption of the two gases is related to the relatively small differences in molecular dimensions with oxygen (2.930 x 2.985 x 4.052 Å) being slightly smaller than nitrogen (2.991 x 3.054 x 4.046Å).<sup>1</sup> Although the differences in size are small, they can make a large difference in the rate of adsorption, with oxygen adsorbing up to 25 times faster than nitrogen on carbon molecular sieve.<sup>2</sup> Previous studies of the kinetic molecular sieving of oxygen and nitrogen by commercially available carbon molecular sieves have shown that the kinetic molecular sieving is achieved by the heterogeneous deposition of a hydrocarbon layer on the surface of the carbon molecular sieve.<sup>3</sup> Deposition across the entrance to the pore is highly desirable as this allows a constriction in the entrance to the pores, without reducing the available pore volume. In these cases the kinetics fit the linear driving force model as there is only one rate determining step for diffusion into the pores, which is diffusion through the constriction at the entrance to the pore caused by the hydrocarbon deposition layer.<sup>4,5</sup> The kinetic selectivity of the carbon molecular sieves is defined as the ratio of the linear driving force rate constants for oxygen and nitrogen adsorption:

$$\frac{k_{O_2}}{k_{N_2}} = \text{selectivity} \quad 8.1$$

Cage 1 $\alpha$ # is formed *in situ* under vacuum from the exposure of Cage 1 $\beta$  to ethyl acetate, as described in **Chapter 7 – Structural Change Induced by Adsorption of Gases and Vapours on Porous Cage Materials**. The kinetic molecular sieving properties for these materials was analysed, and compared with the Cage 1 $\alpha$  material formed from the crystallisation of Cage 1 from ethyl acetate.

## 8.2 Characterisation of Cage 1 $\alpha$ #

A comparison of the scanning electron micrograph at 150 x magnification for Cage 1 $\alpha$ #, Cage 1 $\beta$  and Cage 1 $\alpha$  is given in **Figure 8-2**. The micrograph of Cage 1 $\alpha$  shows long, thin rectangular crystals. The micrograph for Cage 1 $\beta$  shows smaller, hexagonal shaped crystals. The Cage 1 $\alpha$  crystals are of a smaller size to Cage 1 $\beta$ , and have aggregated into clusters. **Figure 8-2** shows the micrographs for Cage 1 $\alpha$ # and Cage 1 $\beta$  at 1000 and 1500 x magnification respectively, of individual crystals not aggregated into clusters. Cage 1 $\alpha$ # shows similar individual crystal shape to that of Cage 1 $\beta$ , with a reduction in size of the crystals during the transformation from Cage 1 $\beta$  to Cage 1 $\alpha$ #, and an aggregation of the individual units. This was also shown to occur by Jones *et al* during successive “vial in vial” methods of structural rearrangement.<sup>6</sup> Jones *et al* showed that although the size of the crystals is reduced through successive transformation, long range order is retained, as shown by PXRD analysis.<sup>6</sup>

The PXRD of the Cage 1 $\alpha$  and Cage 1 $\alpha$ # are shown in **Figure 8-3**. The PXRD shows significant differences between these two polymorphs. The Cage materials are susceptible to hydration from water in the atmosphere. Although these samples were fully desolvated, small amounts of moisture can produce vastly different PXRD patterns. The exposure of the sample to water vapour in the atmosphere before analysis by PXRD through transport to Liverpool University for analysis is suspected to be the reason for the difference in the PXRD patterns.

Analysis by Fourier-Transform Infra-Red Spectroscopy (FTIR) for Cage 1 $\alpha$ , Cage 1 $\alpha$ # and Cage 1 $\beta$  is shown in **Figure 8-4**. The FTIR spectra are very similar. The FTIR spectrum for Cage 1 $\beta$  shows a broad peak at 3375 cm<sup>-1</sup>, which is not present in the spectrum for Cage 1 $\alpha$ #. This is attributed to the presence of atmospheric water hydrogen bonded to the sample.

The adsorption of carbon dioxide at 195 K and 273 K was used to characterise the porous structure of Cage 1 $\alpha$ #. The carbon dioxide adsorption isotherms at 195 K and 273 K for Cage 1 $\alpha$ , Cage 1 $\alpha$ # and Cage 1 $\beta$ , and the subsequent Langmuir, DR and Virial analysis are shown in **Figure 8-5** to **Figure 8-9**. The resulting Langmuir pore

volumes, DR micropore volumes and Virial parameters are shown in **Table 8-1** and **Table 8-2**.

**Table 8-1:** Langmuir and DR data for carbon dioxide adsorption on Cage 1 $\alpha$ , Cage 1 $\alpha$ # and Cage 1 $\beta$  at 273 K (using CO<sub>2</sub> liquid density 1.023 g cm<sup>3</sup>)

Material	Langmuir capacity / mmol g <sup>-1</sup>	Langmuir pore volume / cm <sup>3</sup> g <sup>-1</sup>	DR micropore volume / cm <sup>3</sup> g <sup>-1</sup>
Cage 1 $\alpha$ #	5.03 ± 0.0884	0.216 ± 3.78 x 10 <sup>-3</sup>	0.108 ± 3.44 x 10 <sup>-3</sup>
Cage 1 $\alpha$	4.55 ± 0.0445	0.170 ± 1.66 x 10 <sup>-3</sup>	0.108 ± 1.16 x 10 <sup>-3</sup>
Cage 1 $\beta$	5.80 ± 0.0570	0.255 ± 2.50 x 10 <sup>-3</sup>	0.187 ± 4.54 x 10 <sup>-4</sup>

**Table 8-2:** Virial data for carbon dioxide adsorption on Cage 1 $\alpha$ , Cage 1 $\alpha$ # and Cage 1 $\beta$  at 273 K

Material	A <sub>0</sub> / ln (mol g <sup>-1</sup> Pa <sup>-1</sup> )	A <sub>1</sub> / g mol <sup>-1</sup>
Cage 1 $\alpha$ #	-15.369 ± 0.0035	-1693.417 ± 26.458
Cage 1 $\alpha$	-15.396 ± 0.0075	-1692.374 ± 5.789
Cage 1 $\beta$	-16.108 ± 0.025	-703.181 ± 14.822

From the carbon dioxide adsorption at 195 K data, it is apparent that there is a reduction in the Langmuir pore volume on conversion from Cage 1 $\beta$  to Cage 1 $\alpha$ #. The Langmuir pore volume for Cage 1 $\alpha$ # remains higher than that observed for Cage 1 $\alpha$ . From the carbon dioxide at 273 K data it is also apparent that there is a reduction in the micropore volume on conversion of Cage 1 $\beta$  to Cage 1 $\alpha$ #, the micropore volume for Cage 1 $\alpha$  and Cage 1 $\alpha$ # are not statistically different, indicating that the structures have a similar microporous structure. Virial analysis of carbon dioxide adsorption at 273 K show that Cage 1 $\alpha$  and Cage 1 $\alpha$ # have very similar A<sub>1</sub> values, of -1692.374 ± 5.789 and -1693.417 ± 26.458 g mol<sup>-1</sup> respectively; and Cage 1 $\beta$  has a value of -703.181 ± 14.822 g mol<sup>-1</sup>. This difference indicates that there are stronger adsorbate-adsorbate interactions and narrower pores in both Cage 1 $\alpha$  and Cage 1 $\alpha$ # than in Cage 1 $\beta$ .

The PXRD and FTIR analysis shows that the cages may be susceptible to structural change on exposure to atmospheric water; therefore it is apparent that any transformation from Cage 1 $\beta$  to Cage 1 $\alpha$ # would be more reliable under vacuum,



with no exposure to water, and to keep the sample sealed throughout any gas adsorption experiments. As Cage 1 $\alpha$ # is formed under vacuum, and can be kept under vacuum throughout gas adsorption experiments, it is the more reliable sample to work with. Carbon dioxide adsorption indicates a decrease in pore and micropore volume upon the transformation from Cage 1 $\beta$  to Cage 1 $\alpha$ #, showing a narrowing of the pores and increased adsorbate-adsorbate interaction. This narrowing of the pores could lead to kinetic molecular sieving of oxygen and nitrogen in Cage 1 $\alpha$ # and Cage 1 $\alpha$  that would not be present in Cage 1 $\beta$ .

### 8.3 Kinetic Molecular Sieving of Oxygen and Nitrogen by Cage 1 $\alpha$ # and Cage 1 $\alpha$

The kinetic molecular sieving properties of Cage 1 $\alpha$  and Cage 1 $\alpha$ # were investigated. Cage 1 $\alpha$ # is the product of the exposure of Cage 1 $\beta$  to ethyl acetate through the adsorption isotherm as discussed in **Chapter 7 – Structural Change Induced by Adsorption of Gases and Vapours on Porous Cage Materials**. Upon repetition of ethyl acetate adsorption on cage 1 $\alpha$ # it was found that although the amount of ethyl acetate adsorbed did not change, the rate of adsorption was much slower –indicating a reduction in the size of the entrance to the porous structure, which could potentially lead to the ability to separate different molecules. To investigate this, oxygen and nitrogen adsorption isotherms on Cage 1 $\alpha$ # were collected, and compared to Cage 1 $\alpha$ , which is the pure form produced by ethyl acetate vapour diffusion by the research group at Liverpool University, the synthetic procedure for which is outlined in **Chapter 5 – Experimental**.

### 8.4 Cage 1 $\alpha$ # Oxygen and Nitrogen Adsorption

#### 8.4.1 Oxygen and Nitrogen Isotherm Analysis Cage 1 $\alpha$ #

The oxygen and nitrogen adsorption isotherms on Cage 1 $\alpha$ # for the temperature range 273 K to 298 K on Cage 1 $\alpha$ # are shown in **Figure 8-10** and **Figure 8-11**. The isotherms for both oxygen and nitrogen adsorption are consistent with Type I in the IUPAC classification scheme.<sup>7</sup> The isotherms show a similar uptake for both oxygen and nitrogen, with values between 0.15 and 0.35 mmol g<sup>-1</sup> for the temperature range 273 K to 298 K. The isotherms show a decrease in uptake with increasing temperatures as is expected for physisorption systems.

The isotherms were analysed using the virial equation in the following form:

$$\ln\left(\frac{n}{p}\right) = A_0 + A_1n + A_2n^2 \dots \quad 8.2$$

Where:

$n$  = the amount adsorbed (mol g<sup>-1</sup>)

$p$  = pressure (Pa)

$A_0$  and  $A_1$  = parameters are indicative of the interaction between the adsorbate-adsorbent at zero coverage and adsorbate-adsorbate interactions, respectively<sup>8</sup>

The virial equation can be used to determine the isosteric enthalpy of adsorption. By plotting  $\ln(n/p)$  against  $n$  at series of temperatures, it is then possible to estimate the enthalpy of adsorption at zero surface coverage by plotting values of  $A_0$  against  $1/T$ . The gradient of this plot would be equal to  $\Delta H/R$ , allowing calculation of  $\Delta H$  in kJ mol<sup>-1</sup>.

The virial graphs for oxygen and nitrogen adsorption on Cage 1 $\alpha$ # are shown in **Figure 8-12** and **Figure 8-13**, respectively, with all the graphs showing good linearity. The virial parameters for oxygen and nitrogen adsorption on Cage 1 $\alpha$ # are shown in **Table 8-3** and **Table 8-4**. The tables show that  $A_1$  values cover the range  $-440.1 \pm 21.0$  to  $-1102.2 \pm 47.1$  g mol<sup>-1</sup>. These values fit well with the range obtained for carbon molecular sieves of  $-684$  to  $-1077$  g mol<sup>-1</sup> over the temperature range 303 - 343 K.<sup>9,10</sup>

The corresponding isosteric enthalpies of adsorption at zero surface coverage ( $Q_{st, n=0}$ ) values were derived from a graph of  $A_0$  versus  $1/T$ . The graph for oxygen adsorption is given in **Figure 8-14**; the graph for nitrogen adsorption is given in **Figure 8-15**. Both graphs show good linearity. The  $Q_{st, n=0}$  value can be obtained from the gradient of the graph. The  $Q_{st, n=0}$  value for oxygen adsorption was  $16.9 \pm 1.7$  kJ mol<sup>-1</sup>, the  $Q_{st, n=0}$  value for nitrogen adsorption was  $18.8 \pm 1.1$  kJ mol<sup>-1</sup>. These values are similar and also similar to the values obtained for carbon molecular sieves.<sup>9, 10</sup>

#### 8.4.2 Oxygen and Nitrogen Kinetic Analysis Cage 1 $\alpha$ #

The oxygen and nitrogen adsorption kinetics on Cage 1 $\alpha$ # were analysed using the stretched exponential (SE) model in the following form (equation 8.3).<sup>11</sup>

$$\frac{M_t}{M_e} = A_0 \left( 1 - e^{-(kt)^\beta} \right) \quad 8.3$$

Where:

$M_t$  = the amount adsorbed (g) at time  $t$  (s)

$M_e$  = the equilibrium uptake (g)

$k$  = rate constant ( $s^{-1}$ )

$t$  = time (s)

$\beta$  = the exponential parameter

$A_0$  = a parameter used for fitting purposes

All kinetic profiles of oxygen and nitrogen adsorption analysed by the stretched exponential model can be found in **CD Appendix C – Kinetic Molecular Sieving of Oxygen and Nitrogen by Organic Cage Materials**. Typical oxygen and nitrogen profiles for the stretched exponential fit at 283 K for the pressure increment 800 – 900 mbar are shown in **Figure 8-16** and **Figure 8-17**. It is apparent from the profiles that nitrogen is much more slowly adsorbed than oxygen, with the oxygen adsorption reaching equilibrium after ~ 250 seconds and nitrogen adsorption reaching equilibrium after ~ 2000 seconds. All stretched exponential profiles fit the experimental data within 4%, showing that the model provides a good description of the data. Analysis of the kinetic data using the stretched exponential model provides values for the rate constant and the  $\beta$  parameter.

The rate constant and  $\beta$  parameters for oxygen adsorption on Cage 1 $\alpha$ # are shown in **Figure 8-18** and **Figure 8-19**. From **Figure 8-18** it is apparent that the rate constant for oxygen adsorption increases with increasing temperature, ranging between 0.015  $s^{-1}$  and 0.040  $s^{-1}$  for the temperature range 278 – 298 K. For this temperature range the stretched exponential  $\beta$  parameter varies between 0.5 and 1 as shown in **Figure 8-19**, with the parameter approaching 1 with increased temperature. When  $\beta = 1$  this indicates a single relaxation time, where the rate determining step of adsorption is diffusion through a barrier at the pore entrance.<sup>11</sup>

The rate constant and  $\beta$  parameters for nitrogen adsorption on Cage 1 $\alpha$ # are shown in **Figure 8-20** and **Figure 8-21**. **Figure 8-20** shows that the rate constant for nitrogen adsorption is much slower than that for oxygen adsorption, with the rate constant varying between  $0.001 \text{ s}^{-1}$  and  $0.008 \text{ s}^{-1}$  increasing for the temperature range 273 – 298 K. For this temperature range the stretched exponential  $\beta$  parameter varies between 0.5 and 1, as shown in **Figure 8-21**. The  $\beta$  parameter at 298 K approaches the value of 1, however most values are between 0.6 and 1, averaging around 0.7 – 0.8 which indicates a distribution of relaxation times, where the rate determining step is both diffusion through a barrier at the pore entrance and surface diffusion.<sup>11</sup>

The variation of the natural log of the rate constant,  $\ln(k)$ , is shown for oxygen adsorption in **Figure 8-22** and for nitrogen in **Figure 8-23**. It is evident from the graphs that there is a linear correlation. These graphs can be used to calculate the activation energy for the diffusion of oxygen and nitrogen into the porous structure of Cage 1 $\alpha$ #. Extrapolation of the  $\ln(k)$  against amount adsorbed graphs to zero surface coverage gives the values shown in **Table 8-5** for oxygen and **Table 8-6** for nitrogen adsorption. The activation energy at zero surface coverage,  $E_{a(n=0)}$ , can then be calculated from graphs of  $\ln(k)$  at zero surface coverage against reciprocal temperature as shown in **Figure 8-24** for oxygen adsorption and **Figure 8-25** for nitrogen adsorption. The activation energies at zero surface coverage were  $30.4 \pm 3.6 \text{ kJ mol}^{-1}$  for oxygen and  $40.9 \pm 3.5 \text{ kJ mol}^{-1}$  for nitrogen. As the activation energy at zero surface coverage for oxygen and nitrogen adsorption is much greater than the isosteric enthalpy of adsorption at zero surface coverage, diffusion through a barrier from constrictions at the entrance to the porous structure is the rate determining step for the adsorption of these two gases rather than the diffusion of the gas molecules across the surface of the porous structure.

The kinetic profiles for the pressure step 200 – 300 mbar for nitrogen, carbon dioxide and oxygen adsorption on Cage 1 $\alpha$ # at 273 K is given in **Figure 8-26**. This figure illustrates the difference in equilibration times for the three gases on Cage 1 $\alpha$ #, nitrogen has the longest equilibration time, followed by carbon dioxide then oxygen. A comparison of the  $\ln(k)$  against uptake is shown in **Figure 8-27** for nitrogen, carbon dioxide and oxygen adsorption on Cage 1 $\alpha$ #. This shows that carbon dioxide

has an intermediate rate of adsorption between oxygen and nitrogen. This follows the same trend as shown by carbon molecular sieves.<sup>10</sup>

### 8.4.3 Diffusion Coefficients for Oxygen and Nitrogen Adsorption on Cage 1 $\alpha$ #

The diffusion coefficient can be calculated using Ficks second law, and is shown in equation 8.4 to model the amount of diffusing substance entering and leaving a spherical particle.<sup>12</sup>

$$\frac{M_t}{M_e} = 1 - \frac{6}{\pi^2} \sum_{n=1}^{\infty} \frac{1}{n^2} \exp\left(\frac{-Dn^2\pi^2t}{a^2}\right) \quad 8.4$$

For long time scales equation 8.4 can be solved as follows:

$$1 - \frac{M_t}{M_e} = \frac{6}{\pi^2} \left[ \exp\left(\frac{-D\pi^2t}{a^2}\right) \right] \quad 8.5$$

Where:

$M_t$  = uptake (g) at time  $t$  (s)

$M_e$  = uptake at equilibrium (g)

$D$  = gas diffusion coefficient ( $\text{cm}^2 \text{s}^{-1}$ )

$a$  = radius of particle (cm)

To illustrate the long term behaviour of diffusion, a plot of  $\ln(1 - M_t/M_e)$  against time will give a linear plot of gradient  $\frac{-D\pi^2}{a^2}$ . This equation is valid for long timescales where  $M_t/M_e > 60\%$ . This equation has been used to analysis kinetics of gas adsorption on carbon molecular sieves.<sup>13</sup> This equation is valid when the kinetics fit the stretched exponential model. If a linear driving force model is followed, adjustment of the equation allows the conversion of the linear driving force rate constant  $k$  to the diffusion coefficient  $D$ ,<sup>14</sup> as shown in equation 8.6:

$$1 - \frac{M_t}{M_e} = \frac{6}{\pi^2} \left[ \exp\left(\frac{-D15t}{a^2}\right) \right] \quad 8.6$$

Cage 1 $\alpha$ # crystals are needle-like crystals, and as such an approximation of spherical radius is given. The crystals are of varying length but have approximately the same radius, which for these diffusion coefficient calculations is approximated as 10 $\mu\text{m}$ , based on SEM (**Figure 8-2**).

Selected plots of  $\ln (1 - M_t/M_e)$  against time for oxygen and nitrogen adsorption on Cage 1 $\alpha$ # are given in **CD Appendix C – Kinetic Molecular Sieving of Oxygen and Nitrogen by Organic Cage Materials**. The range of diffusion coefficients is calculated as  $7.18 \times 10^{-11} - 3.58 \times 10^{-10} \text{ cm}^2\text{s}^{-1}$  for nitrogen adsorption and  $6.47 \times 10^{-10} - 3.14 \times 10^{-9} \text{ cm}^2\text{s}^{-1}$  for oxygen adsorption on Cage 1 $\alpha$ #.

#### 8.5 Comparison of O<sub>2</sub>/N<sub>2</sub> Adsorption Kinetics on Cage 1 $\alpha$ # and Cage 1 $\beta$

The oxygen and nitrogen adsorption isotherms at 298 K for both Cage 1 $\alpha$ # and Cage 1 $\beta$  are shown in **Figure 8-28**. Both cages show similar uptakes for these gases. All kinetic profiles can be found in **CD Appendix C – Kinetic Molecular Sieving of Oxygen and Nitrogen by Organic Cage Materials**. A comparison of the rate constant and SE  $\beta$  parameter for Cage 1 $\alpha$ # and Cage 1 $\beta$  oxygen and nitrogen adsorption at 298 K are given in **Figure 8-29** and **Figure 8-30** respectively. The rate constants for oxygen and nitrogen adsorption on Cage 1 $\beta$  are very similar, and are similar to that of the rate constant for oxygen adsorption on Cage 1 $\alpha$ #, while the rate constants for nitrogen adsorption on Cage 1 $\alpha$ # are considerably smaller. Both cages display similar SE  $\beta$  parameters of approximately 1, indicating a single relaxation time, where the rate determining step is diffusion through a barrier due to a constriction in the pore structure. The variation of  $\ln$  (rate constant) with gas uptake graph is shown in **Figure 8-31**. It is apparent from this graph that there is a significant difference in the rate of adsorption of oxygen and nitrogen on Cage 1 $\alpha$ #, whereas the rates of adsorption for Cage 1 $\beta$  are similar and do not vary greatly with amount adsorbed. This indicates that the kinetic molecular sieving properties of the Cages is limited to Cage 1 $\alpha$ #, and is not present in Cage 1 $\beta$ .

#### 8.6 Cage 1 $\alpha$ Oxygen and Nitrogen Adsorption

Cage 1 $\alpha$ #, formed *in situ* under vacuum from exposure of Cage 1 $\beta$  to ethyl acetate, has been shown to kinetically molecular sieve oxygen and nitrogen. The kinetic molecular sieving properties of Cage 1 $\alpha$ , formed through the condensation reaction of 1,3,5-triformylbenzene with 1,2-ethylenediamine, and crystallised from ethyl acetate were also investigated.<sup>15</sup>

### 8.6.1 Oxygen and Nitrogen Isotherm Analysis Cage 1 $\alpha$

The oxygen and nitrogen adsorption isotherms for Cage 1 $\alpha$  are shown in **Figure 8-32** and **Figure 8-33**, respectively. The isotherms for both oxygen and nitrogen adsorption are consistent with Type I in the IUPAC classification scheme.<sup>7</sup> The isotherms for Cage 1 $\alpha$  show an uptake at the maximum pressure reached of 1000 mbar of 0.25 mmol g<sup>-1</sup> for oxygen at 273 K and values from 0.15 – 0.30 mmol g<sup>-1</sup> for nitrogen for the temperature range 293 – 273 K. The nitrogen adsorption isotherms show a decrease in uptake with increasing temperature as expected for physisorption systems. The isotherms were again analysed by the virial equation given in equation 9.2. The virial graph for oxygen adsorption is shown in **Figure 8-34**, the virial graphs for nitrogen adsorption for the temperature range 273 – 293 K are given in **Figure 8-35**. The graphs all show good linearity. The  $A_1$  value for oxygen adsorption at 273 K is  $-1788.1 \pm 5.6$  g mol<sup>-1</sup> and the  $A_0$  value is  $-19.299 \pm 0.0012$  ln (mol g<sup>-1</sup> Pa<sup>-1</sup>). The  $A_1$  and  $A_0$  values for nitrogen adsorption on Cage 1 $\alpha$  are given in **Table 8-7**. These values cover the range  $-19.170 \pm 0.0055$  to  $-19.771 \pm 0.0072$  ln (mol g<sup>-1</sup> Pa<sup>-1</sup>) for  $A_0$  and  $-1433.7 \pm 9.8$  to  $-1792.8 \pm 50.3$  g mol<sup>-1</sup> for  $A_1$ . The  $A_0$  values are slightly larger than that obtained for carbon molecular sieves for the temperature range 303 – 343 K.<sup>9,10</sup>

The isosteric enthalpy of adsorption at zero surface coverage,  $Q_{st, n=0}$  for nitrogen adsorption can again be obtained from a graph of  $A_0$  against reciprocal temperature. The graph for nitrogen adsorption is shown in **Figure 8-36**, showing good linearity. The  $Q_{st, n=0}$  value for nitrogen adsorption on Cage 1 $\alpha$  was  $20.2 \pm 0.3$  kJ mol<sup>-1</sup>.

### 8.6.2 Oxygen and Nitrogen Kinetic Analysis Cage 1 $\alpha$

The oxygen and nitrogen adsorption kinetics for adsorption on Cage 1 $\alpha$  were again analysed using the stretched exponential equation, equation 8.3. All kinetic profiles can be found in **CD Appendix C – Kinetic Molecular Sieving of Oxygen and Nitrogen by Organic Cage Materials**.

Typical oxygen and nitrogen profiles for the stretched exponential fit at 273 K for the pressure increment 600 -700 mbar are shown in **Figure 8-37** and **Figure 8-38**, respectively. The stretched exponential profiles fit the data within 4%, showing that the model is again a good description of the data.

The rate constants and the stretched exponential  $\beta$  parameters for oxygen adsorption at 273 K are shown in **Figure 8-39** and **Figure 8-40**. The rate constant increases with pressure from  $0.020 \pm 3.4 \times 10^{-4}$  to  $0.022 \pm 0.0015 \text{ s}^{-1}$ . The stretched exponential  $\beta$  parameter remains at approximately 1 throughout the isotherm.

The rate constants and the stretched exponential  $\beta$  parameters for nitrogen adsorption on Cage 1 $\alpha$  for the temperature range 273 – 293 K are shown in **Figure 8-41** and **Figure 8-42**. **Figure 8-41** shows that the rate constant for nitrogen adsorption varies between  $0.00124 \pm 2 \times 10^{-5}$  and  $0.00497 \pm 9 \times 10^{-5} \text{ s}^{-1}$  for the temperature range 273 – 293 K. For this temperature range the stretched exponential  $\beta$  parameter varies between 0.6 and 0.8 indicating a distribution of relaxation times.

The variation of the natural log of the rate constant,  $\ln(k)$  with uptake is shown in **Figure 8-44** for nitrogen for the temperature range 273 – 293 K and in **Figure 8-43** for oxygen uptake at 273 K. The graphs show a linear correlation and the nitrogen data can be used to calculate the activation energy for the diffusion of nitrogen into the porous structure of Cage 1 $\alpha$ . Extrapolation of the  $\ln(k)$  against amount of nitrogen adsorbed graphs to zero surface coverage gives the values shown in **Table 8-8**. A graph of  $\ln(k)$  at zero surface coverage against reciprocal temperature allows the calculation of activation energy at zero surface coverage; the graph is shown in **Figure 8-45** and the value of  $E_{a(n=0)} = 32.4 \pm 3.6 \text{ kJ mol}^{-1}$  for nitrogen adsorption. The activation energy at zero surface coverage is larger than the isosteric enthalpy of adsorption at zero surface coverage, showing that diffusion through a barrier from constrictions in the porosity is most likely the rate determining step for nitrogen adsorption into Cage 1 $\alpha$ .

### 8.6.3 Diffusion Coefficients for Oxygen and Nitrogen Adsorption on Cage 1 $\alpha$

The diffusion coefficients for the adsorption of oxygen and nitrogen on Cage 1 $\alpha$  can also be estimated using equation 8.6. The radius of the Cage 1 $\alpha$  needles is estimated to be on average 15 $\mu\text{m}$  based on SEM (see **Figure 8-1**).

Selected plots of  $\ln(1 - M_t/M_e)$  against time for oxygen and nitrogen adsorption on Cage 1 $\alpha$ # are given in **CD Appendix C – Kinetic Molecular Sieving of Oxygen and Nitrogen by Organic Cage Materials**. The range of diffusion coefficients is calculated as  $1.65 \times 10^{-10} - 2.14 \times 10^{-10} \text{ cm}^2\text{s}^{-1}$  for nitrogen adsorption for the



temperature range 273 – 293 K and  $1.79 \times 10^{-9} - 7.70 \times 10^{-10} \text{ cm}^2\text{s}^{-1}$  for oxygen adsorption at 273 K on Cage 1 $\alpha$ .

The diffusion coefficients for nitrogen and oxygen adsorption in Cage 1 $\alpha$  and Cage 1 $\alpha$ # are of similar order of magnitude. There is a degree of uncertainty in the calculations due to the needle shape of the crystals and the variation of the radii of the crystals. However, the values do fit within an accepted range of diffusion coefficients.

### 8.7 Comparison of the Kinetic Molecular Sieving Properties of Cage 1 $\alpha$ # and Cage 1 $\alpha$

The oxygen and nitrogen uptakes for Cage 1 $\alpha$ # are similar at maximum uptakes of  $0.35 \text{ mmol g}^{-1}$ , and are also similar to the uptakes for nitrogen on Cage 1 $\alpha$  at a maximum pressure of 1000 mbar. A comparison of the virial parameters  $A_0$  and  $A_1$  for nitrogen adsorption on Cage 1 $\alpha$ # and Cage 1 $\alpha$  are shown in **Figure 8-46**. The graph shows that the  $A_0$  parameters for both cages are similar. When comparing  $A_1$  values, both oxygen and nitrogen for Cage 1 $\alpha$ # are similar, covering the range  $-440.1 \pm 21.0$  to  $-1102.2 \pm 47.1 \text{ g mol}^{-1}$ . The values for Cage 1 $\alpha$  are however larger, with nitrogen adsorption covering the range  $-1433.7 \pm 9.8$  to  $-1792.8 \pm 50.3 \text{ g mol}^{-1}$  and oxygen adsorption at 273 K at  $-1788.1 \pm 5.6 \text{ g mol}^{-1}$ . These values also sit outside the range obtained for carbon molecular sieves of  $-684$  to  $-1077 \text{ g mol}^{-1}$  over the temperature range 303 - 343 K.<sup>9, 10</sup> The more negative the value of  $A_1$ , the stronger the interaction between the adsorbate and other adsorbate molecules. The more negative  $A_1$  values for oxygen and nitrogen adsorption on Cage 1 $\alpha$  suggest a stronger interaction within the pores of Cage 1 $\alpha$  than within in the pores of Cage 1 $\alpha$ #, indicating a constriction in the size of the pores in Cage 1 $\alpha$  compared to Cage 1 $\alpha$ #.

For Cage 1 $\alpha$ # nitrogen adsorption is much slower than oxygen adsorption, with nitrogen adsorption rate constants varying between  $0.001 \text{ s}^{-1}$  and  $0.008 \text{ s}^{-1}$  increasing for the temperature range 273 – 298 K, whereas for oxygen adsorption the rate constant ranges between  $0.015 \text{ s}^{-1}$  and  $0.040 \text{ s}^{-1}$ , approximately 10 times faster than nitrogen adsorption. The rate of nitrogen adsorption into Cage 1 $\alpha$  varies between  $0.00124 \pm 2 \times 10^{-5}$  and  $0.00497 \pm 9 \times 10^{-5} \text{ s}^{-1}$ , and oxygen adsorption at 273 K is approximately  $0.0216 \pm 0.0015 \text{ s}^{-1}$ . This shows that nitrogen adsorption into the two cages occurs at a similar rate, both much slower than oxygen adsorption. Oxygen

## Chapter 8 Kinetic Molecular Sieving of Oxygen and Nitrogen by Organic Cage Materials Cage 1 $\alpha$ and Cage 1 $\alpha$ #

adsorption into Cage 1 $\alpha$  at 273 K is slightly faster than oxygen adsorption on Cage 1 $\alpha$ # at 273 K. A comparison of  $\ln(k)$  against reciprocal temperature for nitrogen and oxygen adsorption on Cage 1 $\alpha$ # and nitrogen adsorption on Cage 1 $\alpha$  is shown in **Figure 8-47**, where it is apparent that the  $\ln(k)$  values for nitrogen on the two different cages are similar, as are the oxygen  $\ln(k)$  values.

A comparison of the isosteric enthalpy of adsorption at zero surface coverage and activation energy at zero surface coverage values are given in **Table 8-9**. For both materials the activation energy at zero surface coverage for nitrogen were higher than the isosteric enthalpy of adsorption at zero surface coverage, indicating that the rate determining step is diffusion through a barrier due to constrictions at the entrance to the porosity.<sup>16</sup>

The kinetic selectivity values are shown in a graph of kinetic selectivity against pressure in **Figure 8-48**. From this graph it is apparent that the selectivity values for Cage 1 $\alpha$ # are slightly lower than that for Cage 1 $\alpha$ . There is no trend in selectivity with temperature for Cage 1 $\alpha$ #, with selectivity values ranging between 5.0 and 8.5 for the temperature range 278 – 298 K. The selectivity for Cage 1 $\alpha$  at 273 K is slightly higher, ranging from 8.75 to 11.75 across the pressure range.

### 8.8 Conclusions

The conversion between the polymorphs of cage 1 $\alpha$  and  $\beta$  is shown in **Figure 8-49**. Cage 1 $\beta$  exists in a helical channel structure. Upon desolvation of the dichloromethane solvent, a structure is formed consisting of disconnected cage voids, Cage 1 $\beta$ '. **Figure 8-49** shows that Cage 1 $\beta$ ' has available pore space in the channels between the cages as well as within the cages themselves. Exposure of the structure to ethyl acetate results in the formation of Cage 1 $\alpha$ . This causes the disconnected cages to stack in parallel layers. Upon desolvation of the ethyl acetate, these layers move closer together, showing a reduction of 12% in the PLATON pore volume, through the loss of pore space in the channels between the cages.<sup>17</sup>

Cage 1 $\alpha$ # was successfully synthesised under vacuum through the low-pressure adsorption of ethyl acetate vapour. The structural characteristics of Cage 1 $\alpha$ # were compared to those of Cage 1 $\beta$  and Cage 1 $\alpha$ , and it was found that Cage 1 $\alpha$ # has similar properties to Cage 1 $\alpha$ , and contains a smaller pore volume and micropore

volume than Cage 1 $\beta$ , consistent with the crystallographic data and PLATON pore volume reduction. Cage 1 $\alpha$  and Cage 1 $\alpha$ # show stronger adsorbate – adsorbate interactions through virial analysis of carbon dioxide adsorption at 273 K. This indicates a narrowing of the pores in Cage 1 $\alpha$  and Cage 1 $\alpha$ # compared to Cage 1 $\beta$ .

The kinetic molecular sieving properties of Cage 1 $\alpha$ #, Cage 1 $\alpha$  and Cage 1 $\beta$  were investigated by analysis of adsorption of oxygen and nitrogen. The smaller porosity found in Cage 1 $\alpha$  and Cage 1 $\alpha$ # allows the effective separation of oxygen and nitrogen due to the differences in molecular diameter. This is not seen in Cage 1 $\beta$ . Kinetic molecular sieving is introduced when Cage 1 $\beta$  undergoes structural transformation to Cage 1 $\alpha$  or Cage 1 $\alpha$ #. For both Cage 1 $\alpha$  and Cage 1 $\alpha$ # the activation energy at zero surface coverage for nitrogen were higher than the isosteric enthalpy of adsorption at zero surface coverage, indicating that the rate determining step is diffusion through a barrier due to constrictions at the entrance to the porosity. The structure of Cage 1 $\beta$  has wider pore constrictions than Cage 1 $\alpha$ , with very narrow constrictions in the porosity introduced upon rearrangement of Cage 1 $\beta$  to Cage 1 $\alpha$ . Kinetic molecular sieving occurs when the molecule cross-section is similar in size to the pore constriction resulting in an activated diffusion process taking place. Cage 1 $\alpha$ # has similar virial parameters to that of carbon molecular sieves; whereas Cage 1 $\alpha$  shows slightly higher values indicating that a stronger interaction between adsorbate molecules is induced within the pores of Cage 1 $\alpha$ . Both cages have very similar kinetic properties, with oxygen adsorption occurring at 10 times faster rate than nitrogen. Cage 1 $\alpha$  has a higher selectivity than Cage 1 $\alpha$ #, due to constrictions in the porosity being greater for Cage 1 $\alpha$  than Cage 1 $\alpha$ #. Selectivity values for oxygen and nitrogen separation on carbon molecular sieves have been previously shown to be in the region of 5 - 25 depending on the type of deposition present in the material.<sup>3</sup> The selectivity values for Cage 1 $\alpha$ # and Cage 1 $\alpha$  are of similar values as carbon molecular sieves. The difference in the selectivity and the  $A_I$  parameters between Cage 1 $\alpha$  and Cage 1 $\alpha$ # could be attributed to the differences in preparation of the two materials. Cage 1 $\alpha$  is crystallised from ethyl acetate and therefore forms an initially more stable structure. It is not the product of a transformation and therefore is a more pure sample. As Cage 1 $\alpha$ # is formed from the exposure of Cage 1 $\beta$  to ethyl acetate, there is the possibility of a mixed phase

Chapter 8 Kinetic Molecular Sieving of Oxygen and Nitrogen by Organic Cage  
Materials Cage 1 $\alpha$  and Cage 1 $\alpha$ #

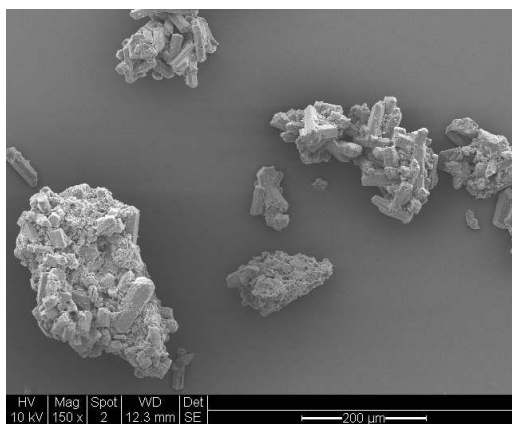
present, where complete conversion to Cage 1 $\alpha$ # does not occur. Cage 1 $\alpha$ # remains a stable structure under vacuum, with very repeatable adsorption characteristics. Cage 1 $\alpha$  reacts with water vapour in the atmosphere. As this does not occur for Cage 1 $\alpha$ #, as it is made under vacuum and remains sealed from the atmosphere throughout the adsorption work, Cage 1 $\alpha$ # provides more repeatable and reliable adsorption data. The PXRD data for Cage 1 $\alpha$ # before and after nitrogen and oxygen separation studies are shown in **Figure 8-50**, showing that the structure of Cage 1 $\alpha$ # before and after adsorption is similar, and that the separation of oxygen and nitrogen causes no structural transition in Cage 1 $\alpha$ #, and that the long range crystallographic order remains intact.

The data shows that the two cages, Cage 1 $\alpha$  and Cage 1 $\alpha$ #, although prepared differently, both show the potential to separate oxygen and nitrogen on a scale which is similar to carbon molecular sieves. As far as is currently known, this is the first example of a porous cage material to kinetically separate oxygen and nitrogen.

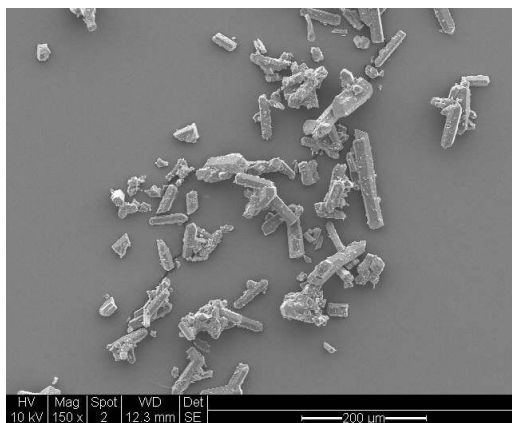
Chapter 8 Kinetic Molecular Sieving of Oxygen and Nitrogen by Organic Cage  
Materials Cage 1 $\alpha$  and Cage 1 $\alpha$ #

8.9 Figures

a)



b)



c)

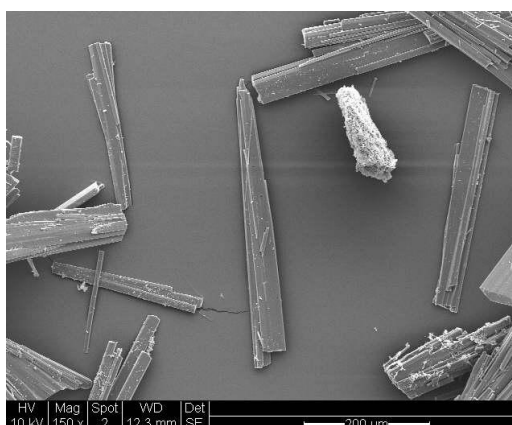
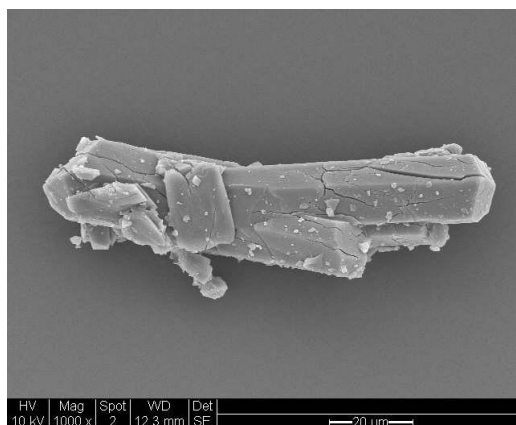


**Figure 8-1:** Scanning electron micrographs at 150 x magnification a) Cage 1 $\alpha$ # b) Cage 1 $\beta$  c) Cage 1 $\alpha$

Chapter 8 Kinetic Molecular Sieving of Oxygen and Nitrogen by Organic Cage  
Materials Cage 1 $\alpha$  and Cage 1 $\alpha$ #

a)



b)

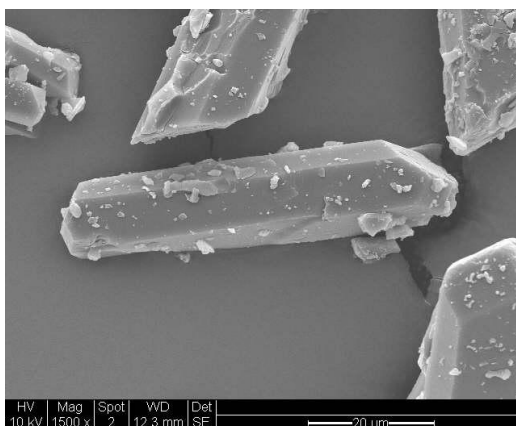


**Figure 8-2:** Scanning electron micrograph (SEM) image of **a)** Cage 1 $\alpha$ # at 1000 x magnification **b)** Cage 1 $\beta$  crystals at 1500x magnification

Chapter 8 Kinetic Molecular Sieving of Oxygen and Nitrogen by Organic Cage  
Materials Cage 1 $\alpha$  and Cage 1 $\alpha$ #

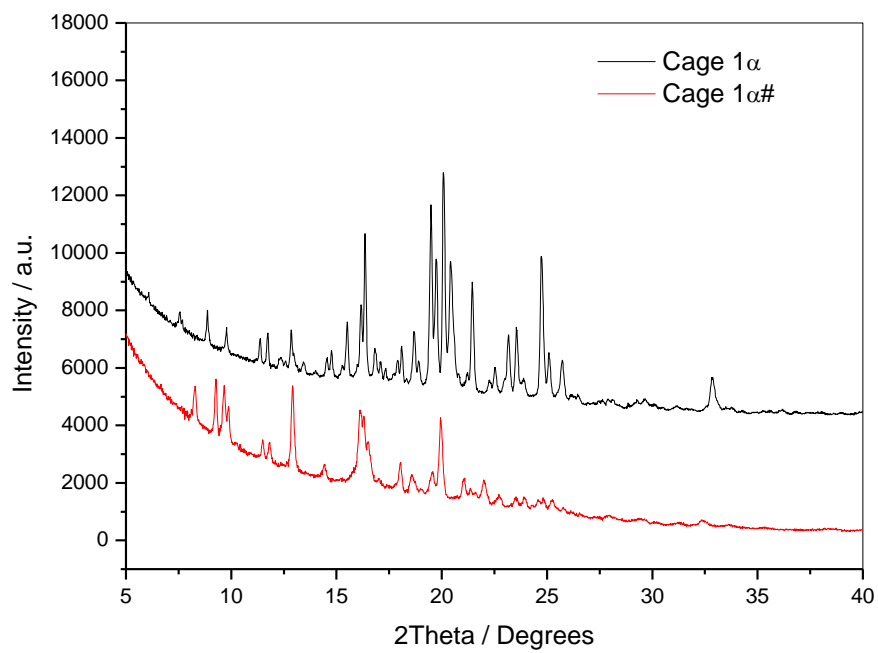


**Figure 8-3:** PXRD comparison of Cage 1 $\alpha$  and Cage 1 $\alpha$ #

Chapter 8 Kinetic Molecular Sieving of Oxygen and Nitrogen by Organic Cage  
Materials Cage 1 $\alpha$  and Cage 1 $\alpha$ #

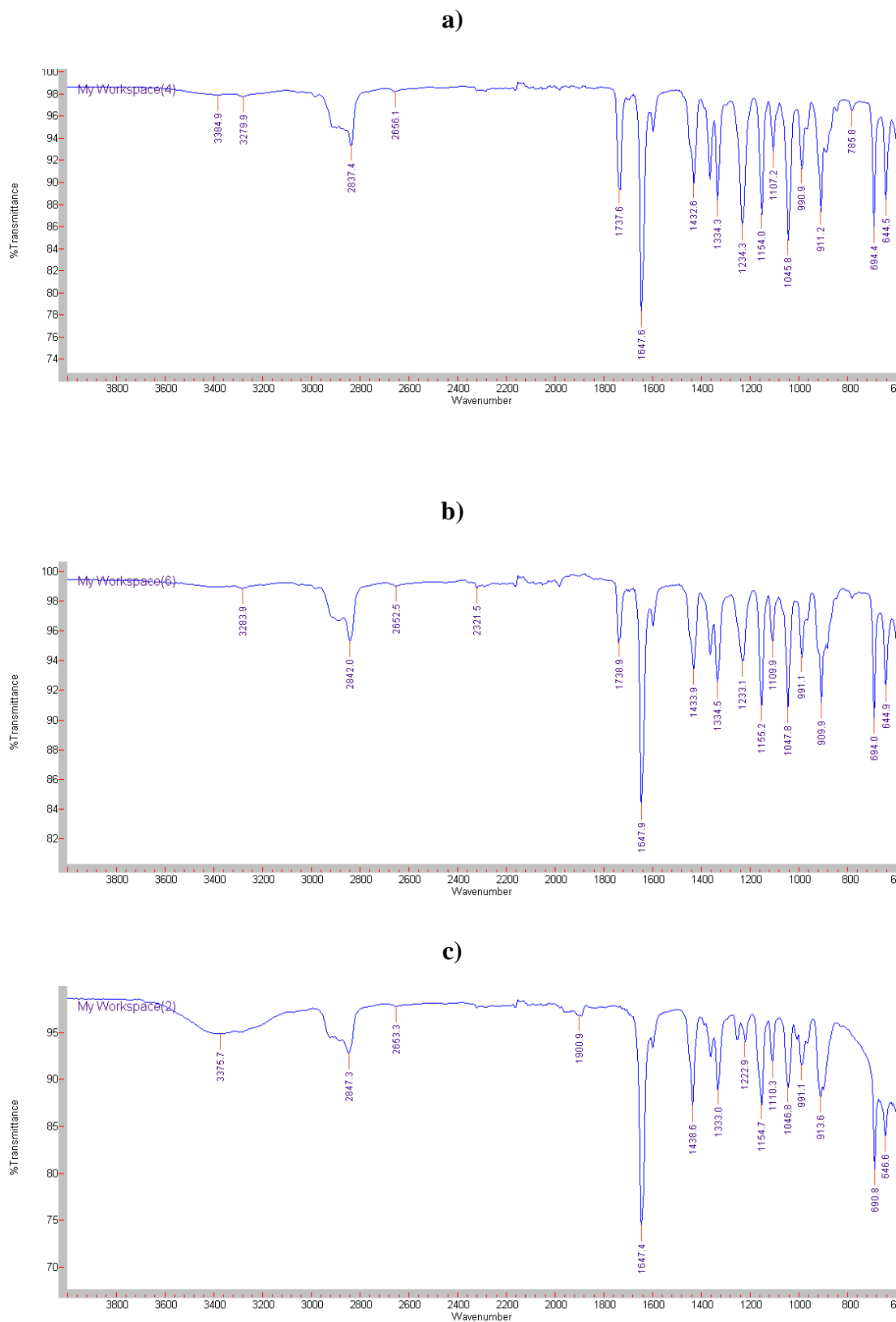


Figure 8-4: FTIR spectra of a) Cage 1 $\alpha$  b) Cage 1 $\alpha$ # c) Cage 1 $\beta$



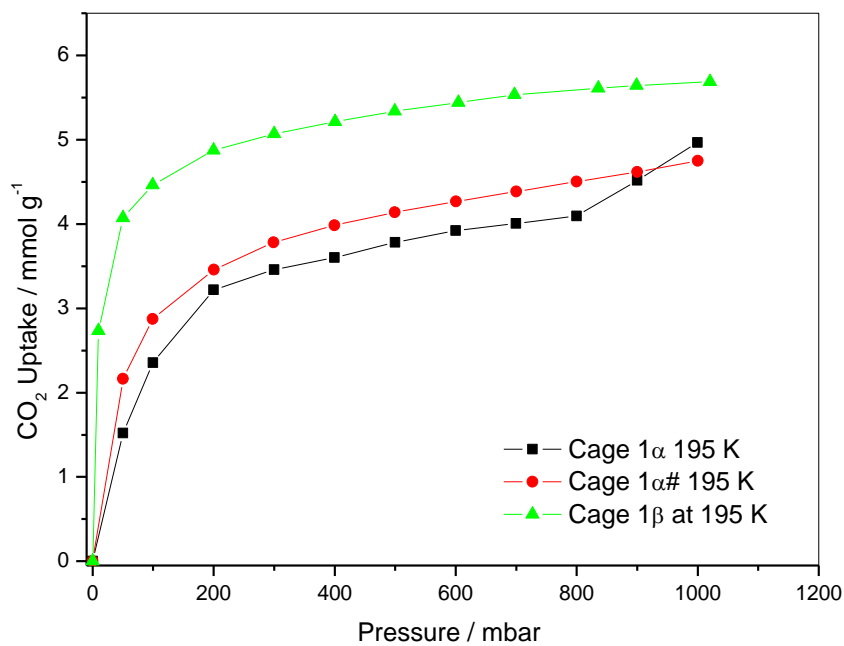


Figure 8-5: Carbon dioxide adsorption on Cage 1 $\alpha$ , Cage 1 $\alpha$ # and Cage 1 $\beta$  at 195 K

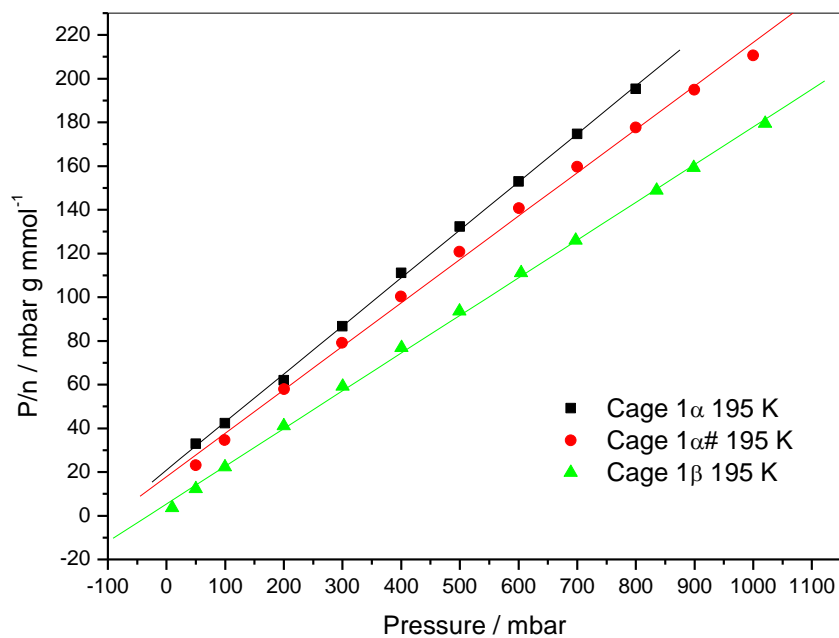


Figure 8-6: Langmuir analysis of carbon dioxide adsorption on Cage 1 $\alpha$ , Cage 1 $\alpha$ # and Cage 1 $\beta$  at 195 K

Chapter 8 Kinetic Molecular Sieving of Oxygen and Nitrogen by Organic Cage  
Materials Cage 1 $\alpha$  and Cage 1 $\alpha$ #

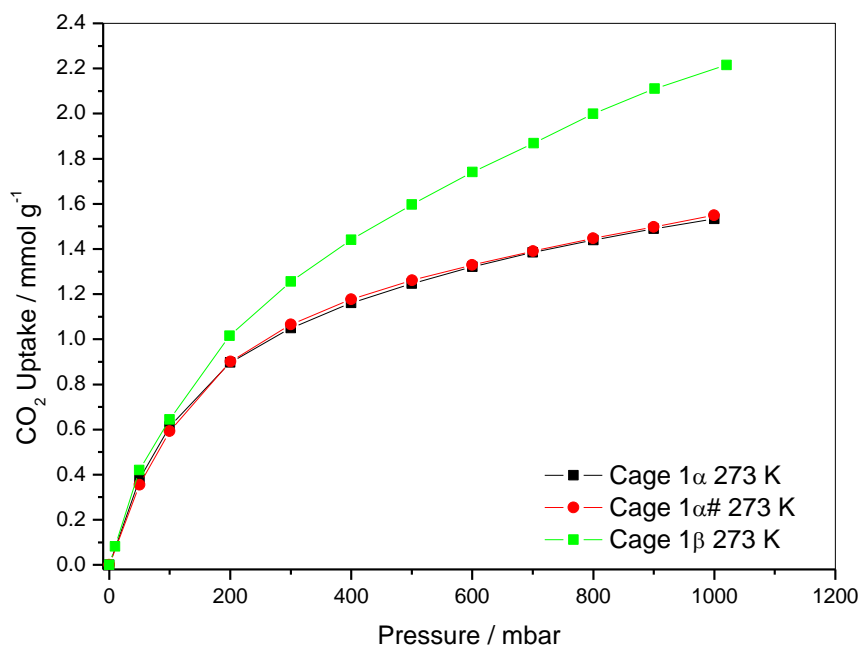


Figure 8-7: Carbon dioxide adsorption on Cage 1 $\alpha$ , Cage 1 $\alpha$ # and Cage 1 $\beta$  at 273 K

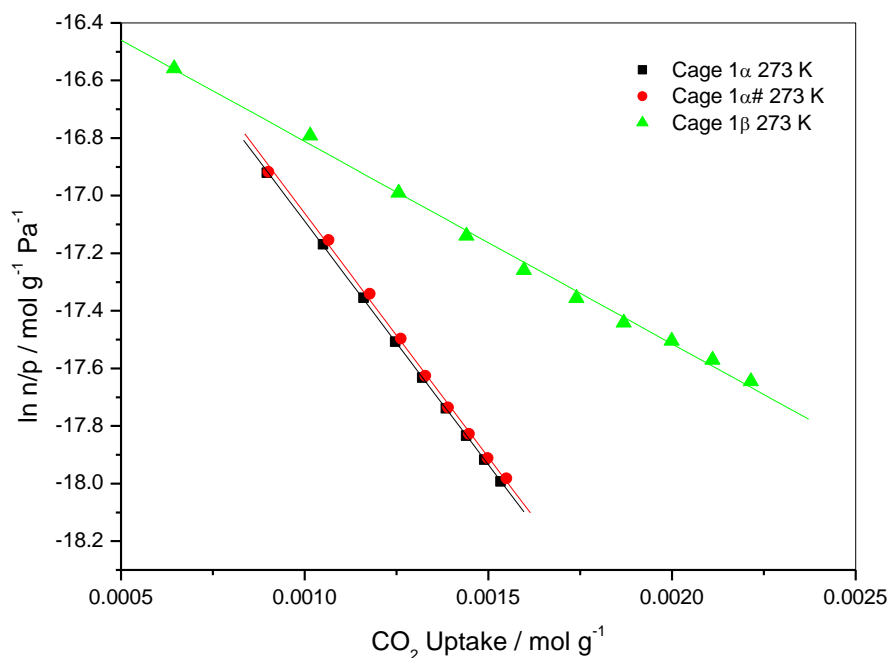
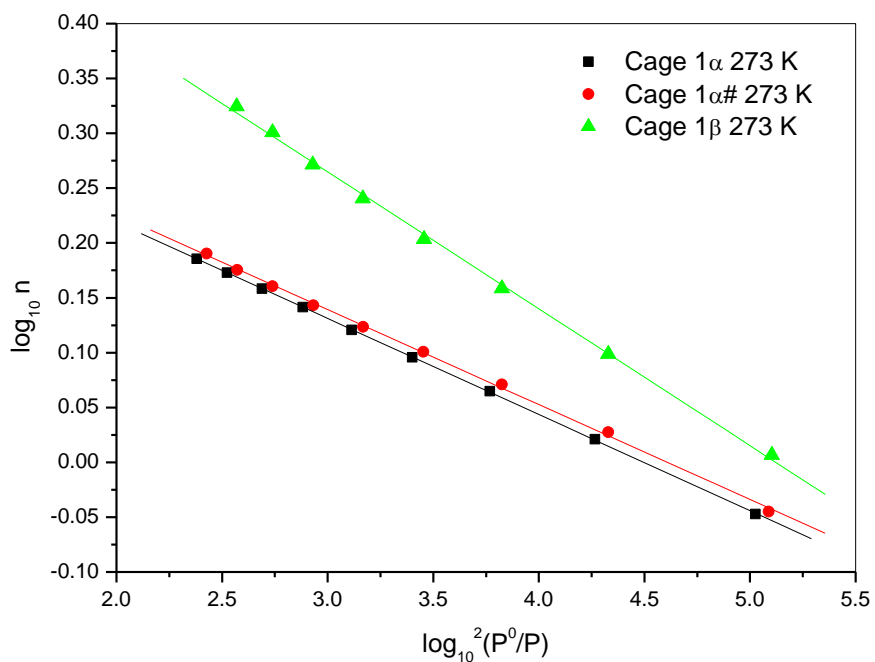
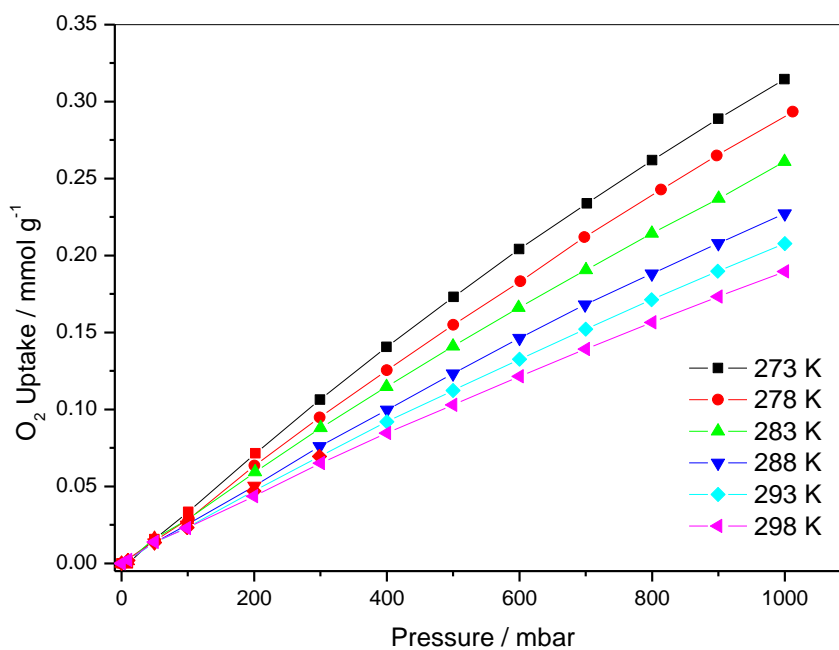


Figure 8-8: Virial analysis of carbon dioxide adsorption on Cage 1 $\alpha$ , Cage 1 $\alpha$ # and Cage 1 $\beta$  at 273 K

Materials Cage 1 $\alpha$  and Cage 1 $\alpha$ #

**Figure 8-9:** DR analysis of carbon dioxide adsorption on Cage 1 $\alpha$ , Cage 1 $\alpha$ # and Cage 1 $\beta$  at 273 K



**Figure 8-10:** Oxygen adsorption isotherms for Cage 1 $\alpha$ # for temperature range 273 – 298 K

Chapter 8 Kinetic Molecular Sieving of Oxygen and Nitrogen by Organic Cage  
Materials Cage 1 $\alpha$  and Cage 1 $\alpha$ #

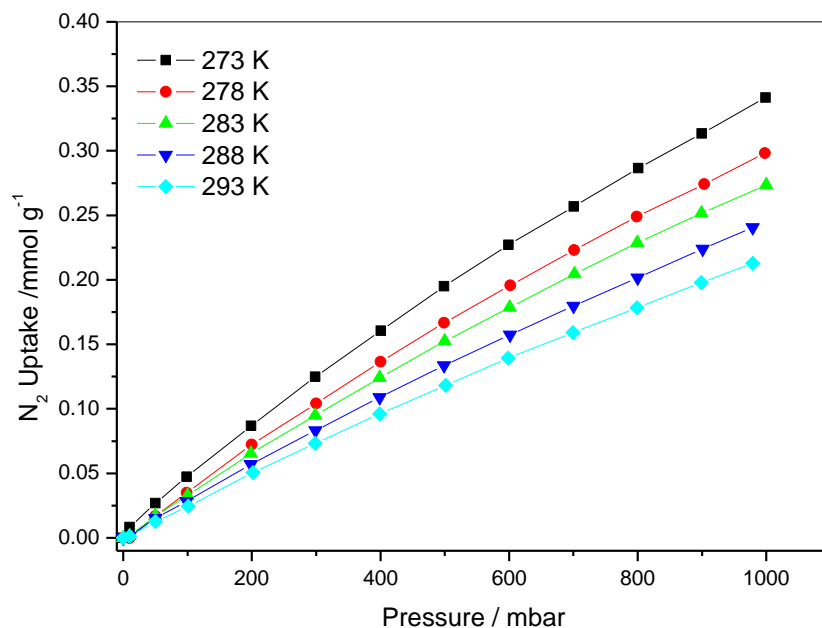


**Figure 8-11:** Nitrogen adsorption isotherms for Cage 1 $\alpha$ # for temperature range 273 – 293 K

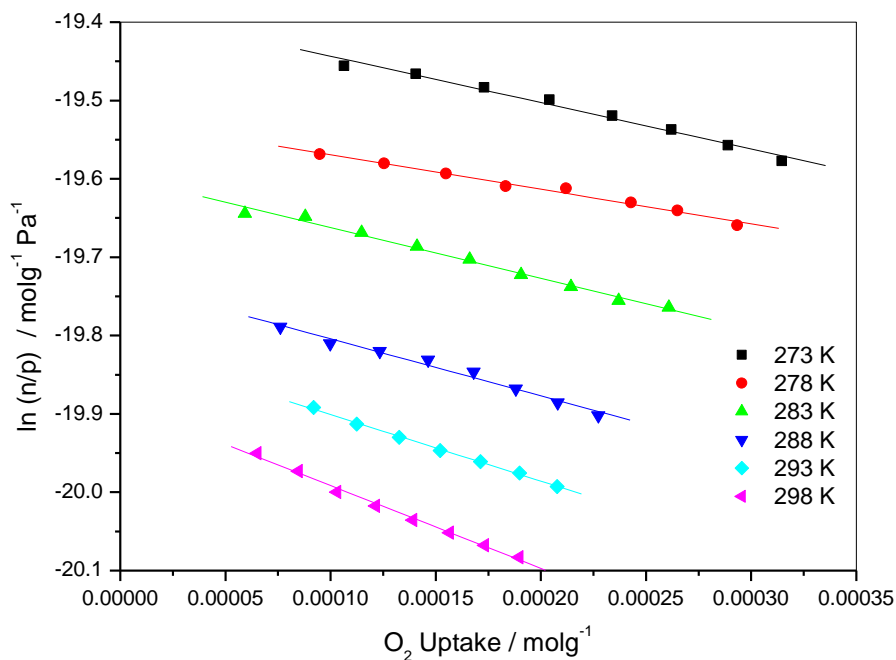


**Figure 8-12:** Virial graphs for oxygen adsorption on Cage 1 $\alpha$ # for temperature range 273 – 298 K

Chapter 8 Kinetic Molecular Sieving of Oxygen and Nitrogen by Organic Cage  
Materials Cage 1 $\alpha$  and Cage 1 $\alpha$ #

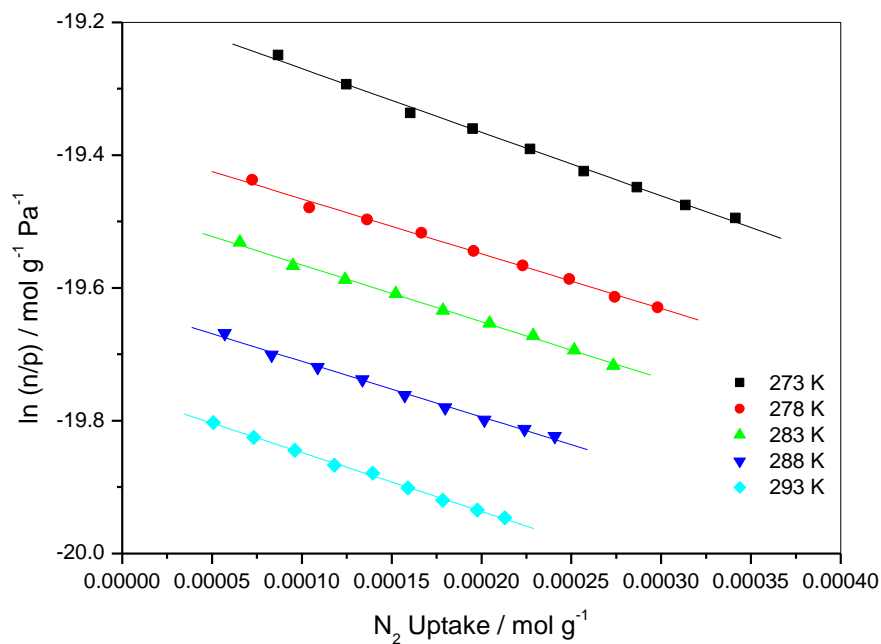


**Figure 8-13:** Virial graphs for nitrogen adsorption on Cage 1 $\alpha$ # for temperature range 273 – 293 K

**Table 8-3:** Virial constants for the adsorption of oxygen on Cage 1 $\alpha$ # for temperature range 273 – 298 K

Temperature / K	$A_0 / \ln (\text{mol g}^{-1} \text{ Pa}^{-1})$	$A_1 / \text{g mol}^{-1}$
273	$-19.253 \pm 0.009$	$-746.2 \pm 36.3$
278	$-19.525 \pm 0.004$	$-440.1 \pm 21.0$
283	$-19.597 \pm 0.004$	$-648.2 \pm 24.8$
288	$-19.731 \pm 0.006$	$-728.1 \pm 39.6$
293	$-19.819 \pm 0.002$	$-848.5 \pm 16.0$
298	$-19.918 \pm 0.002$	$-954.3 \pm 15.9$

Chapter 8 Kinetic Molecular Sieving of Oxygen and Nitrogen by Organic Cage  
Materials Cage 1 $\alpha$  and Cage 1 $\alpha$ #

**Table 8-4:** Virial constants for the adsorption of nitrogen on Cage 1 $\alpha$ # for temperature range 273 – 293K

Temperature / K	$A_0 / \ln (\text{mol g}^{-1} \text{Pa}^{-1})$	$A_1 / \text{g mol}^{-1}$
273	$-19.174 \pm 0.0051$	$-957.7 \pm 14.5$
278	$-19.383 \pm 0.0046$	$-825.6 \pm 22.6$
283	$-19.480 \pm 0.0033$	$-856.1 \pm 17.4$
288	$-19.627 \pm 0.0037$	$-835.9 \pm 22.3$
293	$-19.760 \pm 0.0021$	$-886.1 \pm 21.6$

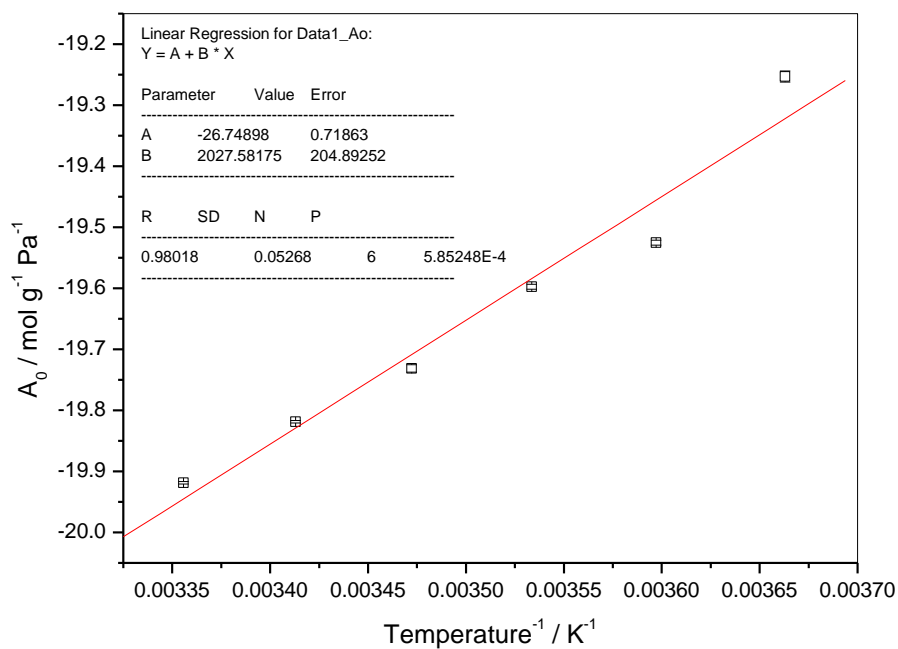


**Figure 8-14:** Graph of  $A_0$  versus  $1/T$  for oxygen adsorption on Cage 1 $\alpha$ # for temperature range 273 – 298 K

Chapter 8 Kinetic Molecular Sieving of Oxygen and Nitrogen by Organic Cage  
Materials Cage 1 $\alpha$  and Cage 1 $\alpha$ #

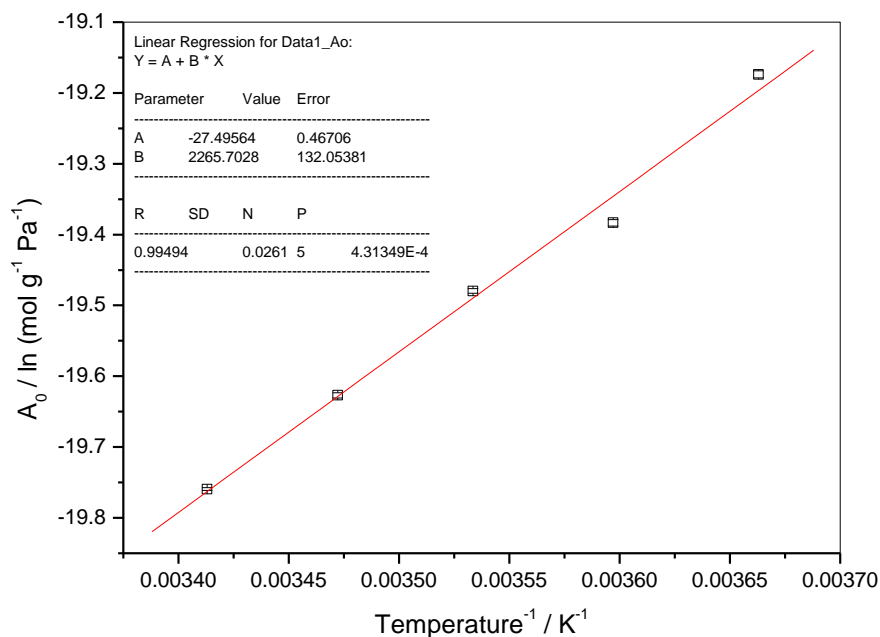


**Figure 8-15:** Graph of  $A_0$  versus  $1/T$  for nitrogen adsorption on Cage 1 $\alpha$ # for temperature range 273 – 293 K

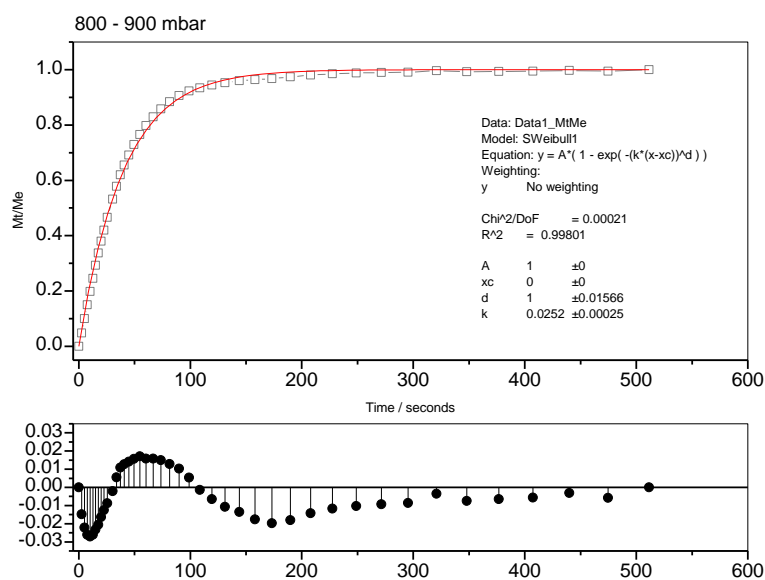


**Figure 8-16:** Oxygen adsorption on Cage 1 $\alpha$ # at 283 K 800 - 900 mbar step SE analysis

Chapter 8 Kinetic Molecular Sieving of Oxygen and Nitrogen by Organic Cage  
Materials Cage 1a and Cage 1a#

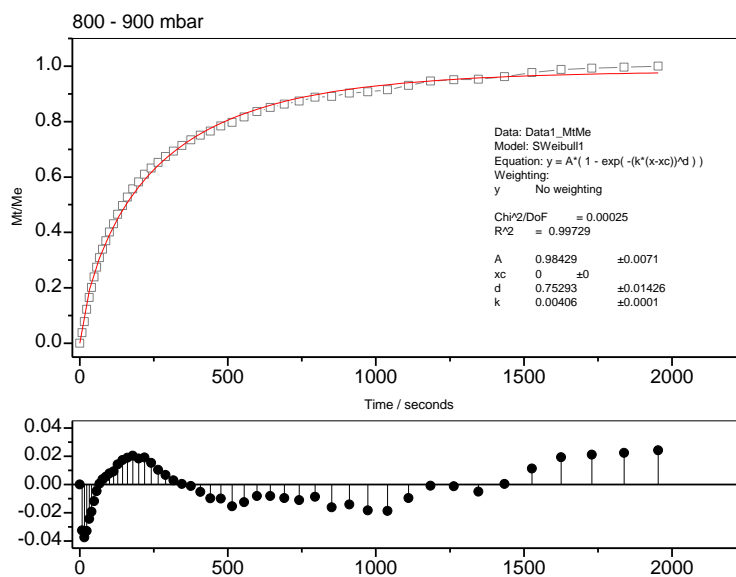


**Figure 8-17:** Nitrogen adsorption on Cage 1a# at 283 K 800 - 900 mbar step SE analysis

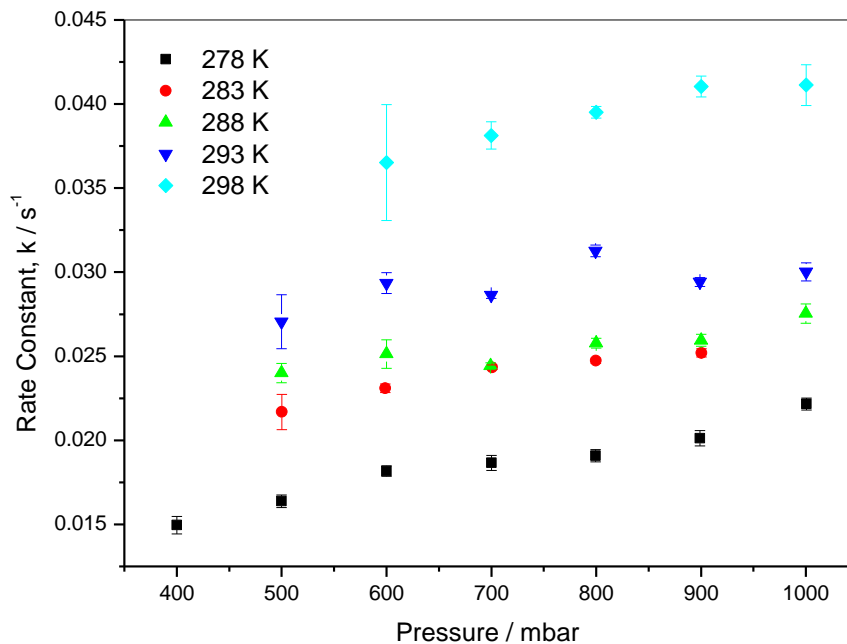


**Figure 8-18:** Graph of rate constant,  $k$ , versus pressure for oxygen adsorption on Cage 1a# for temperature range 278 – 298 K



Chapter 8 Kinetic Molecular Sieving of Oxygen and Nitrogen by Organic Cage  
Materials Cage 1 $\alpha$  and Cage 1 $\alpha$ #

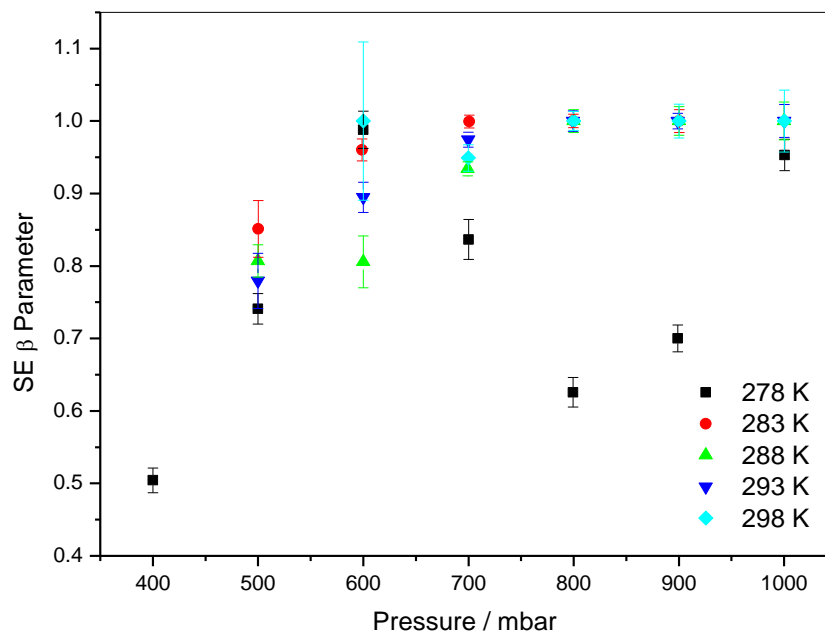


**Figure 8-19:** Graph of SE parameter,  $\beta$ , versus pressure for oxygen adsorption on Cage 1 $\alpha$ # for temperature range 278 – 298 K

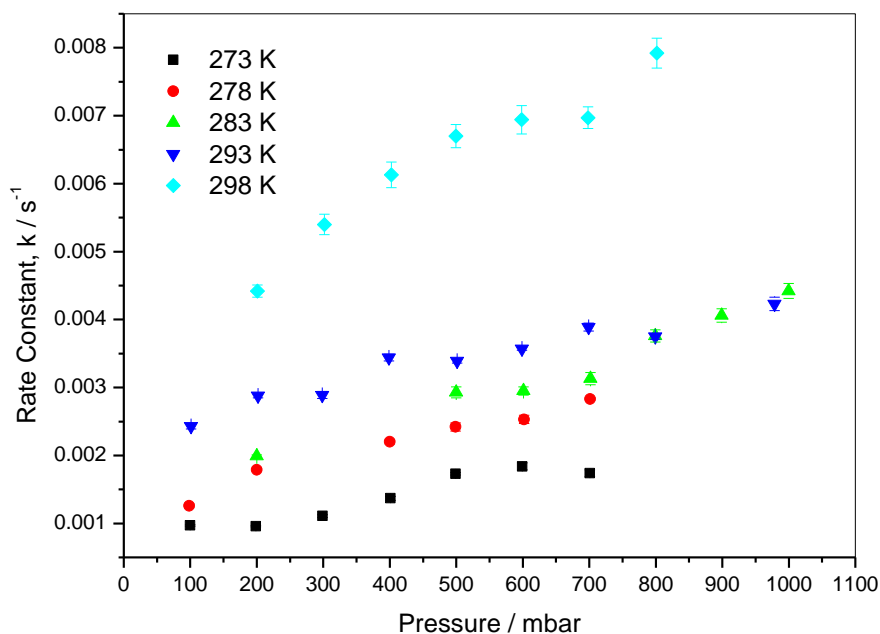


**Figure 8-20:** Graph of rate constant,  $k$ , versus pressure for nitrogen adsorption on Cage 1 $\alpha$ # for temperature range 273 – 298 K

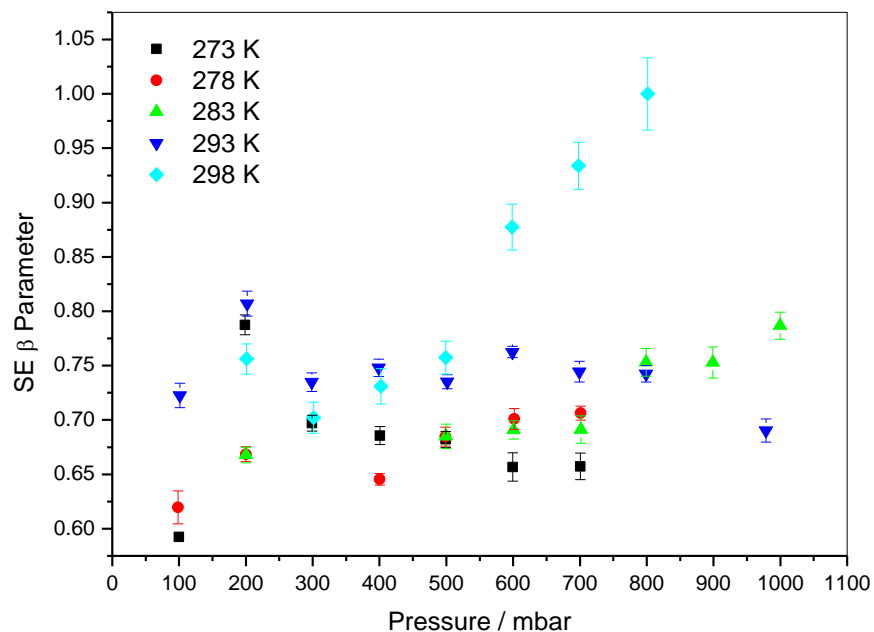


**Figure 8-21:** Graph of SE parameter,  $\beta$ , versus pressure for nitrogen adsorption on Cage 1 $\alpha$ # for temperature range 273 – 298 K

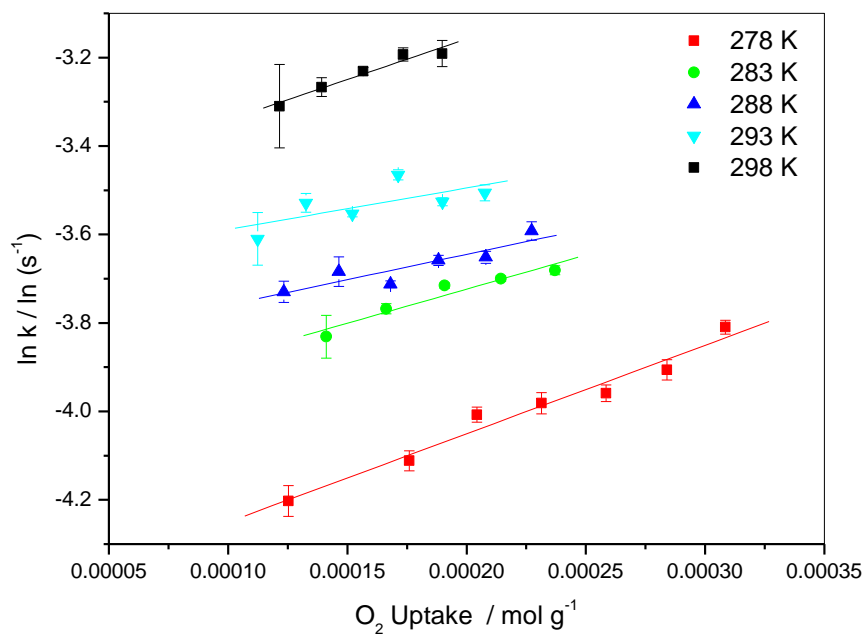


**Figure 8-22:** Graphs of  $\ln k$  versus oxygen uptake / mol g<sup>-1</sup> for oxygen adsorption on Cage 1 $\alpha$ # for temperature range 278 – 298 K

Chapter 8 Kinetic Molecular Sieving of Oxygen and Nitrogen by Organic Cage  
Materials Cage 1 $\alpha$  and Cage 1 $\alpha$ #

**Table 8-5:**  $\ln k / \ln (s^{-1})$  values at zero surface coverage for oxygen adsorption on Cage 1 $\alpha$ # for temperature range 278 – 298 K

Temperature / K	$\ln k / \ln (s^{-1})$
278	$-4.450 \pm 0.038$
283	$-4.032 \pm 0.047$
288	$-3.874 \pm 0.049$
293	$-3.682 \pm 0.080$
298	$-3.525 \pm 0.038$

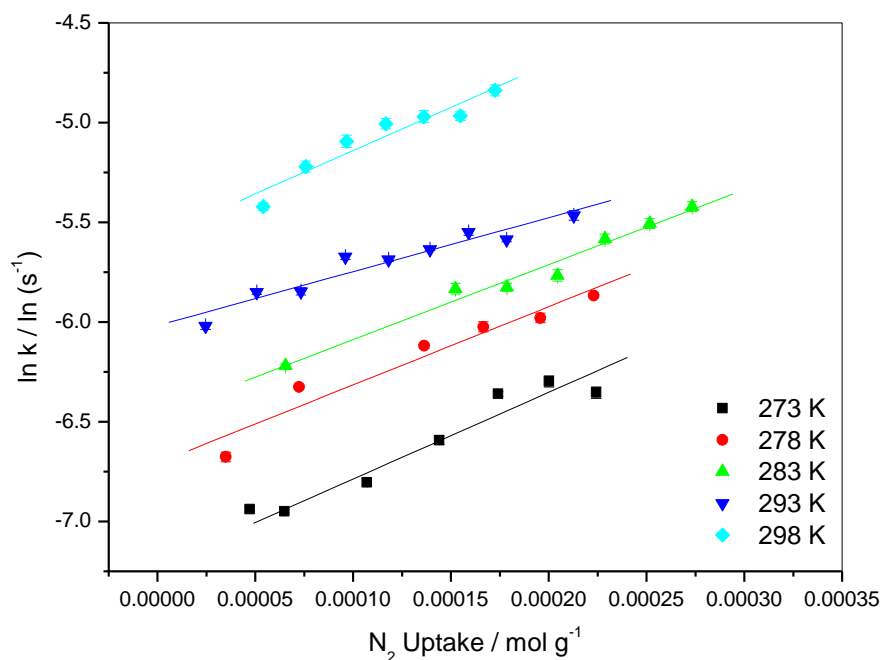
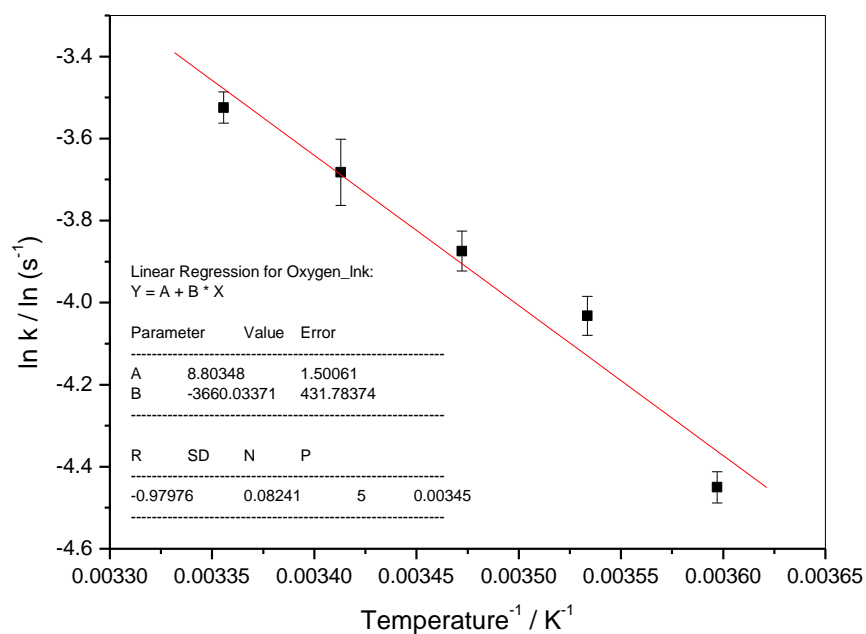


**Figure 8-23:** Graphs of  $\ln k$  versus nitrogen uptake /  $\text{mol g}^{-1}$  for nitrogen adsorption on Cage 1 $\alpha$ # for temperature range 273 – 298 K

Chapter 8 Kinetic Molecular Sieving of Oxygen and Nitrogen by Organic Cage  
Materials Cage 1 $\alpha$  and Cage 1 $\alpha$ #

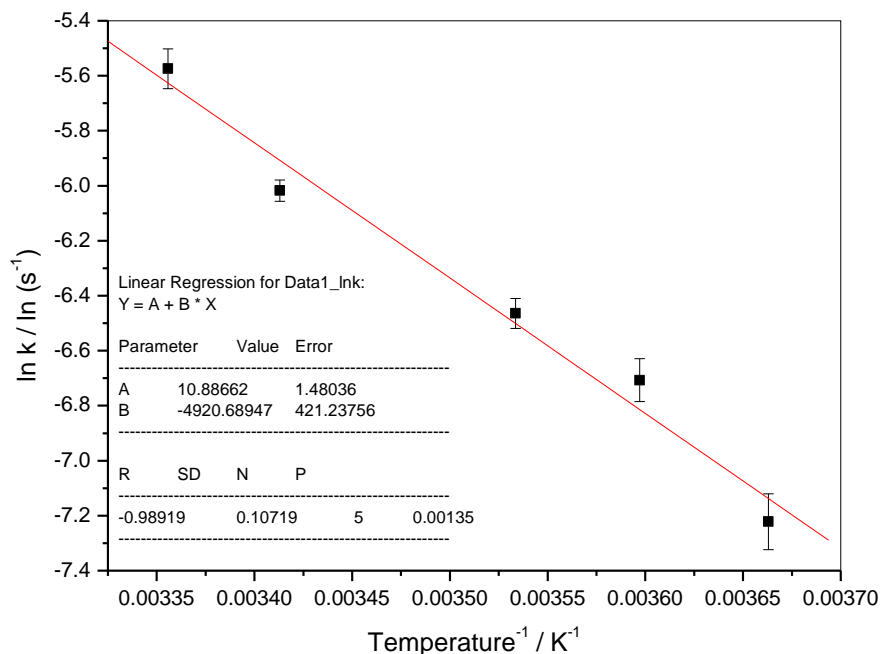
**Table 8-6:**  $\ln k / \ln (s^{-1})$  values at zero surface coverage for nitrogen adsorption on Cage 1 $\alpha$ # for temperature range 273 – 298 K

Temperature / K	$\ln k / \ln (s^{-1})$
273	$-7.221 \pm 0.101$
278	$-6.707 \pm 0.078$
283	$-6.465 \pm 0.054$
293	$-6.018 \pm 0.038$
298	$-5.574 \pm 0.072$

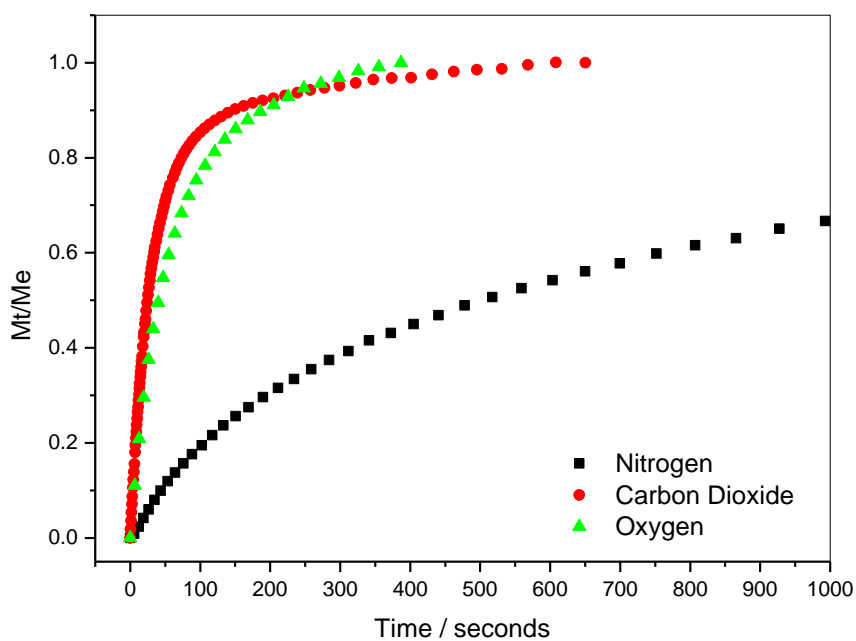


**Figure 8-24:**  $\ln k$  versus  $1/T$  for oxygen adsorption on Cage 1 $\alpha$ # for temperature range 273 – 298 K

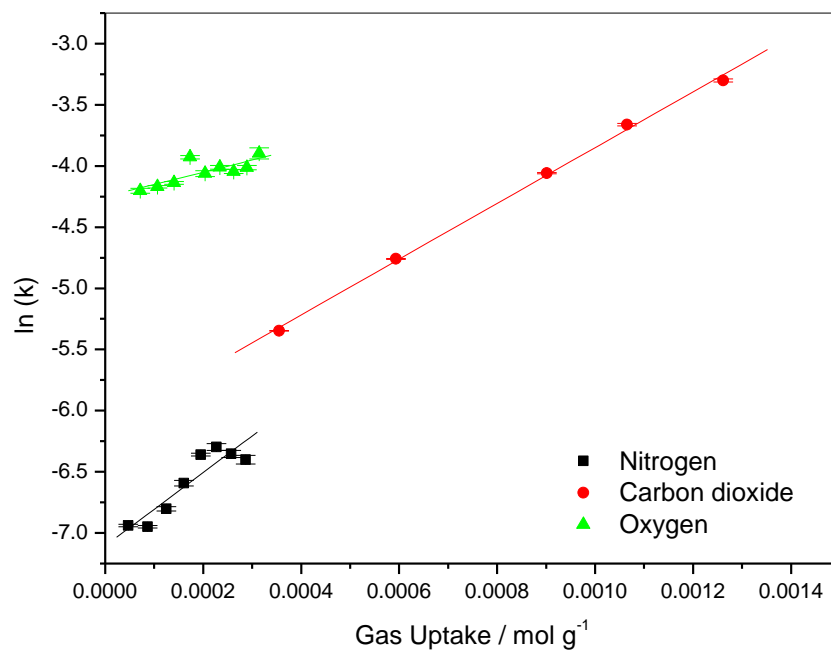
Chapter 8 Kinetic Molecular Sieving of Oxygen and Nitrogen by Organic Cage  
Materials Cage 1 $\alpha$  and Cage 1 $\alpha$ #



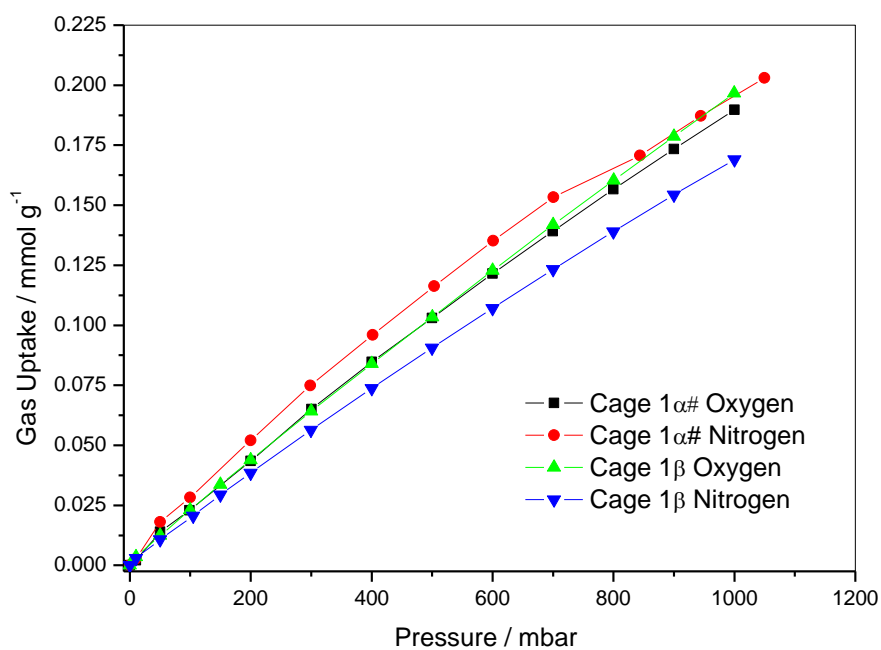
**Figure 8-25:**  $\ln k$  versus  $1/T$  for nitrogen adsorption on Cage 1 $\alpha$ # for temperature range 273 – 298 K



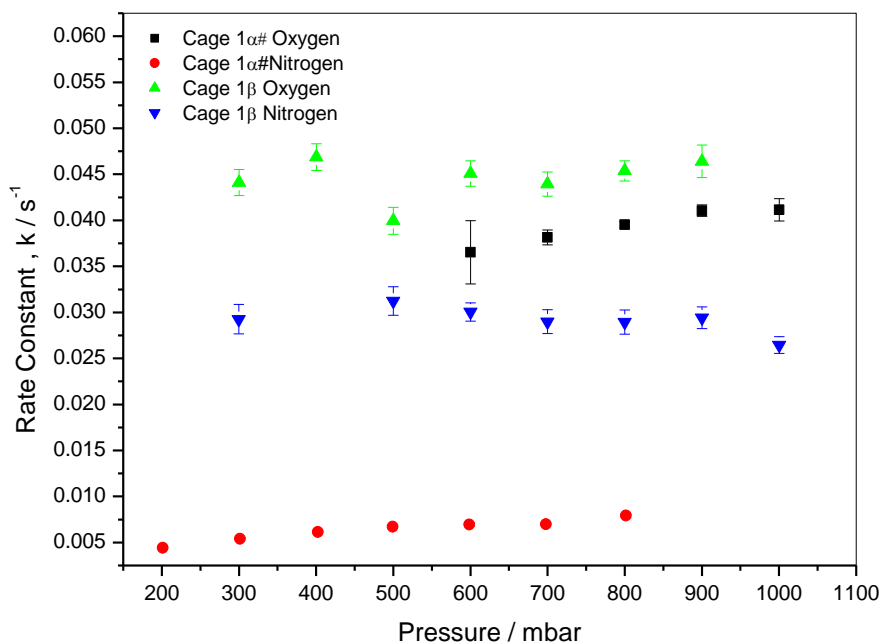
**Figure 8-26:** Comparison of the kinetic profiles for the pressure step 200 – 300 mbar for nitrogen, carbon dioxide and oxygen adsorption on Cage 1 $\alpha$ # at 273 K

Materials Cage 1 $\alpha$  and Cage 1 $\alpha$ #

**Figure 8-27:** Comparison of  $\ln k$  against amount adsorbed for nitrogen, carbon dioxide and oxygen adsorption on Cage 1 $\alpha$ # at 273 K



**Figure 8-28:** Oxygen and nitrogen adsorption by Cage 1 $\alpha$ # and Cage 1 $\beta$  at 298 K

Materials Cage 1 $\alpha$ # and Cage 1 $\beta$ #

**Figure 8-29:** Graph of rate constant,  $k$ , versus pressure for oxygen and nitrogen adsorption by Cage 1 $\alpha$ # and Cage 1 $\beta$  at 298 K

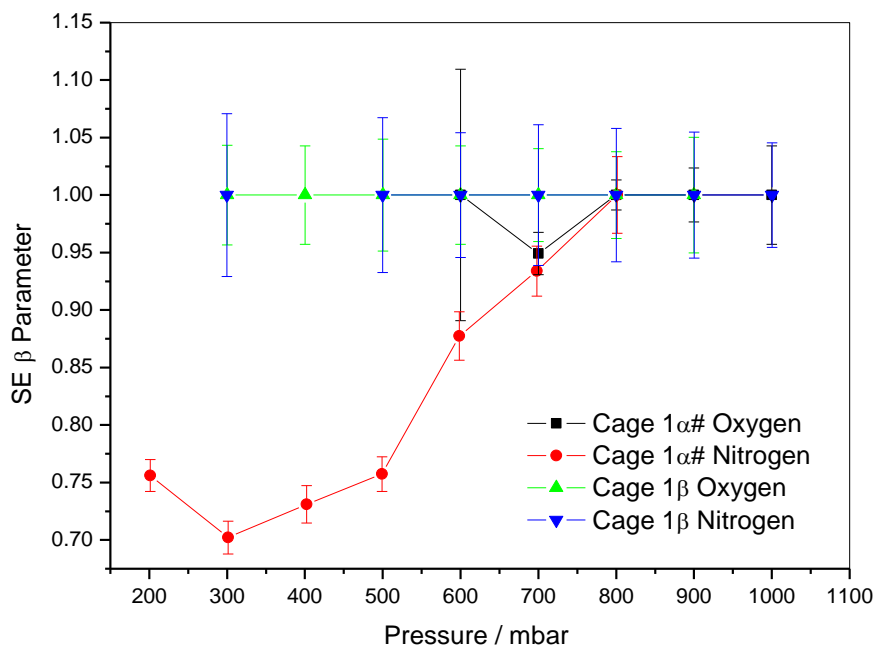


**Figure 8-30:** Graph of SE  $\beta$  parameter versus pressure for oxygen and nitrogen adsorption by Cage 1 $\alpha$ # and Cage 1 $\beta$  at 298 K

Materials Cage 1 $\alpha$ # and Cage 1 $\beta$ #

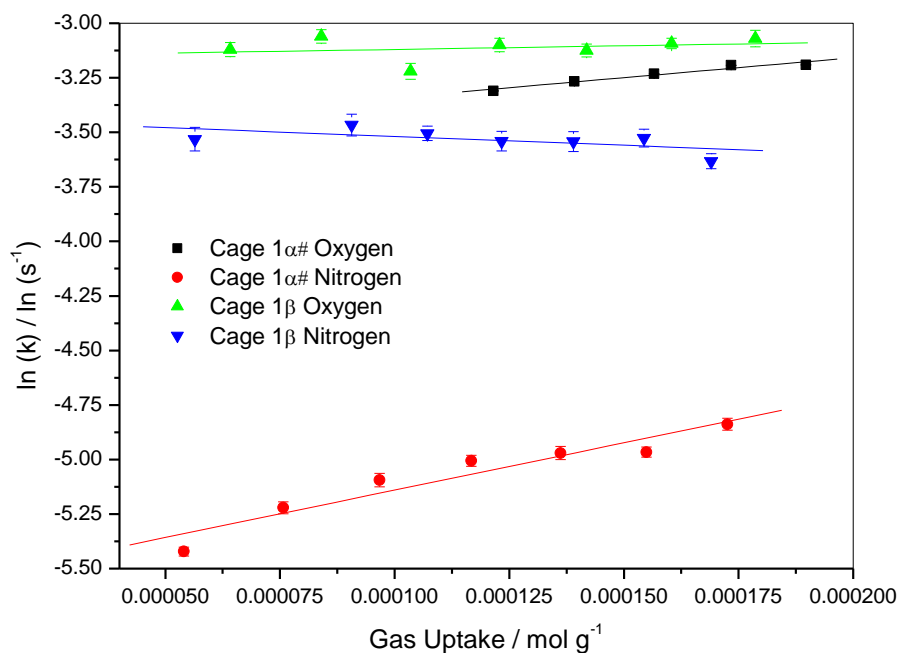


**Figure 8-31:** Graph of  $\ln(k)$  versus gas uptake for oxygen and nitrogen adsorption by Cage 1 $\alpha$ # and Cage 1 $\beta$  at 298 K

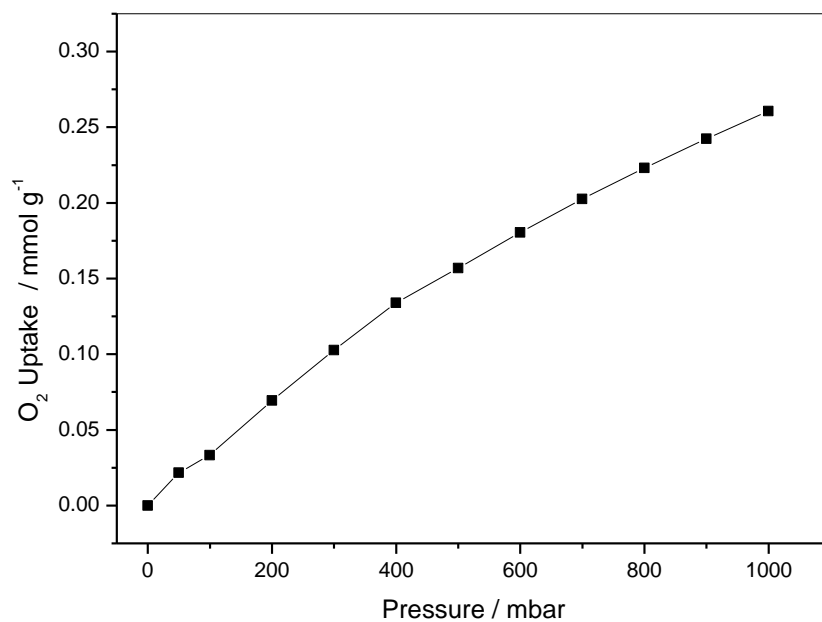


**Figure 8-32:** Oxygen adsorption isotherms for Cage 1 $\alpha$  at 273 K



Chapter 8 Kinetic Molecular Sieving of Oxygen and Nitrogen by Organic Cage  
Materials Cage 1 $\alpha$  and Cage 1 $\alpha$ #

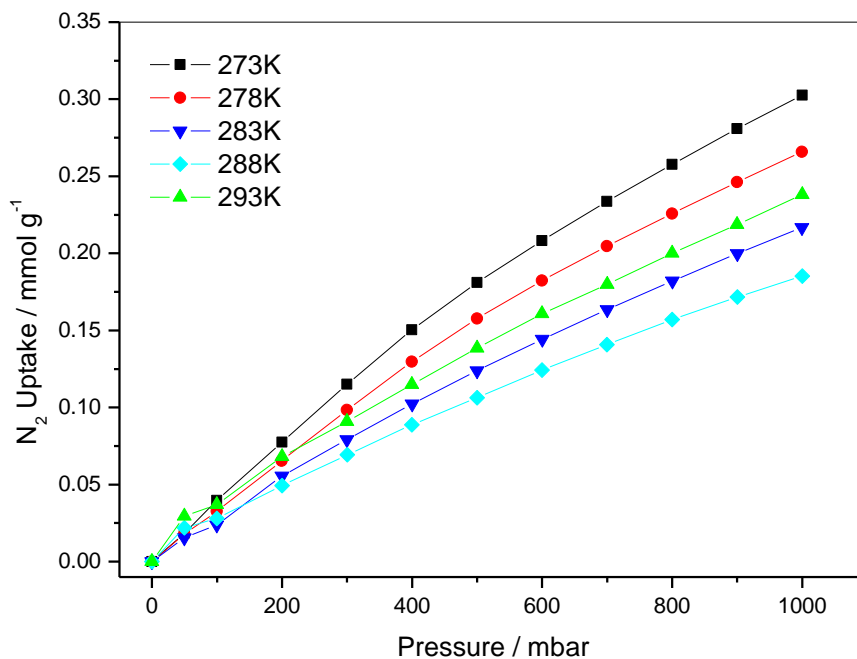


**Figure 8-33:** Nitrogen adsorption isotherms for Cage 1 $\alpha$  for temperature range 273 – 293 K

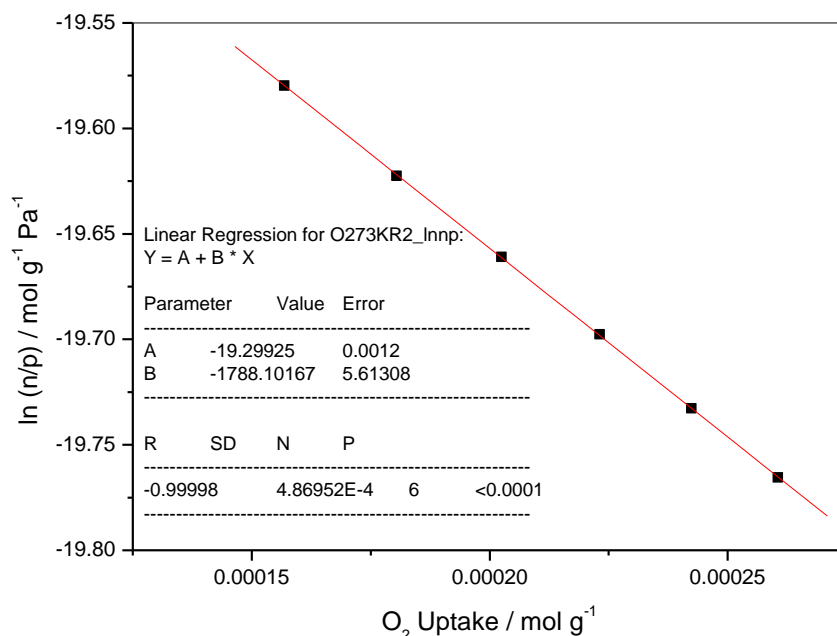


**Figure 8-34:** Virial graph for oxygen adsorption on Cage 1 $\alpha$  at 273 K

Chapter 8 Kinetic Molecular Sieving of Oxygen and Nitrogen by Organic Cage  
Materials Cage 1 $\alpha$  and Cage 1 $\alpha$ #

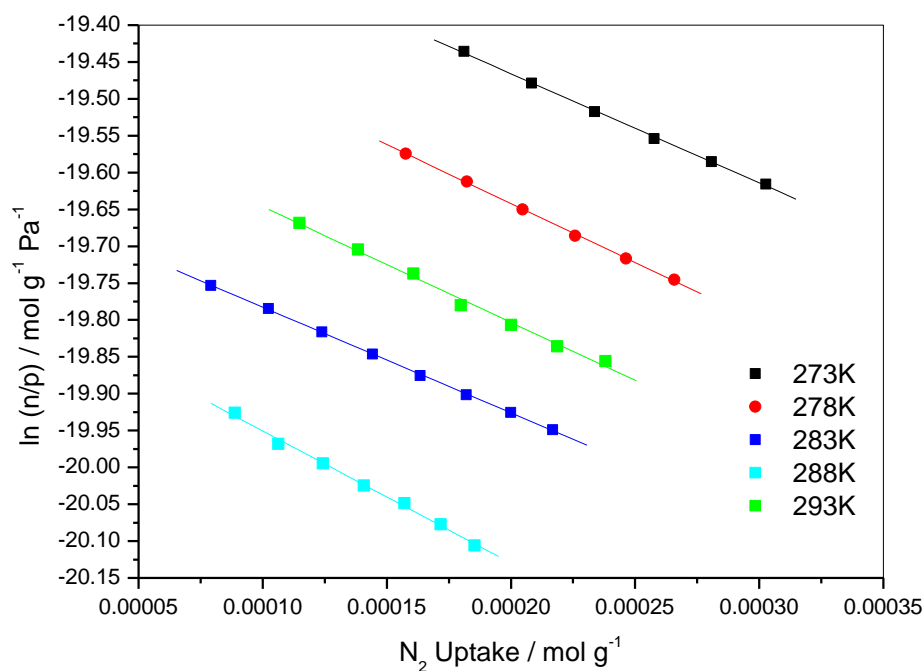


**Figure 8-35:** Virial graphs for nitrogen adsorption on Cage 1 $\alpha$  for temperature range 273 – 293 K

**Table 8-7:** Virial constants for the adsorption of nitrogen on Cage 1 $\alpha$  for temperature range 273 – 293 K

Temperature / K	$A_0 / \ln (\text{mol g}^{-1} \text{Pa}^{-1})$	$A_1 / \text{g mol}^{-1}$
273	$-19.170 \pm 0.0055$	$-1480.9 \pm 22.3$
278	$-19.322 \pm 0.0042$	$-1598.19 \pm 19.5$
283	$-19.489 \pm 0.010$	$-1570.3 \pm 54.5$
288	$-19.639 \pm 0.0015$	$-1433.7 \pm 9.8$
293	$-19.771 \pm 0.0072$	$-1792.8 \pm 50.3$

Chapter 8 Kinetic Molecular Sieving of Oxygen and Nitrogen by Organic Cage  
Materials Cage 1 $\alpha$  and Cage 1 $\alpha$ #

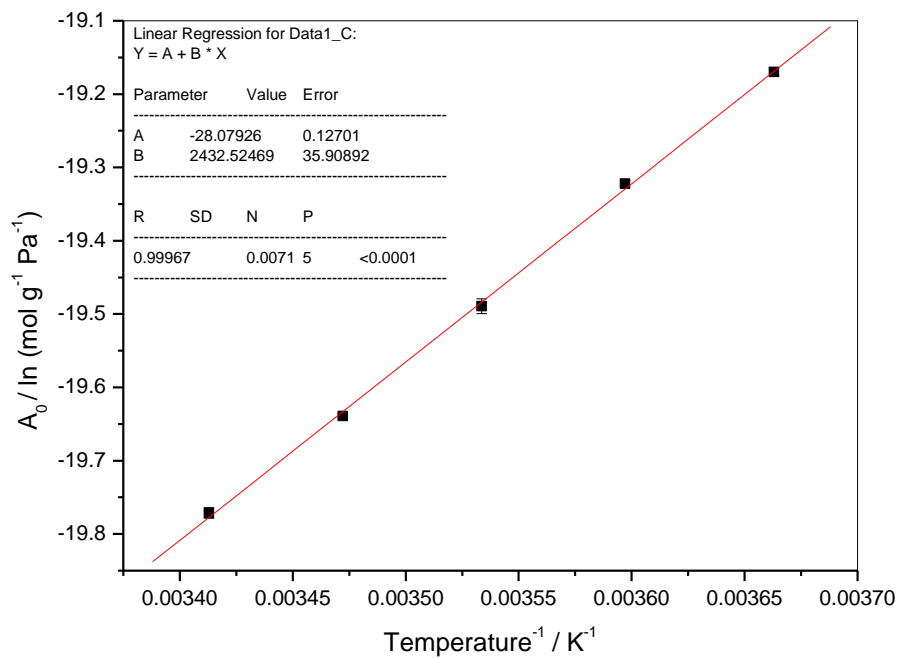


**Figure 8-36:** Graph of  $A_0$  versus  $1/T$  for nitrogen adsorption on Cage 1 $\alpha$  for temperature range 273 – 298 K

Materials Cage 1 $\alpha$  and Cage 1 $\alpha$ #

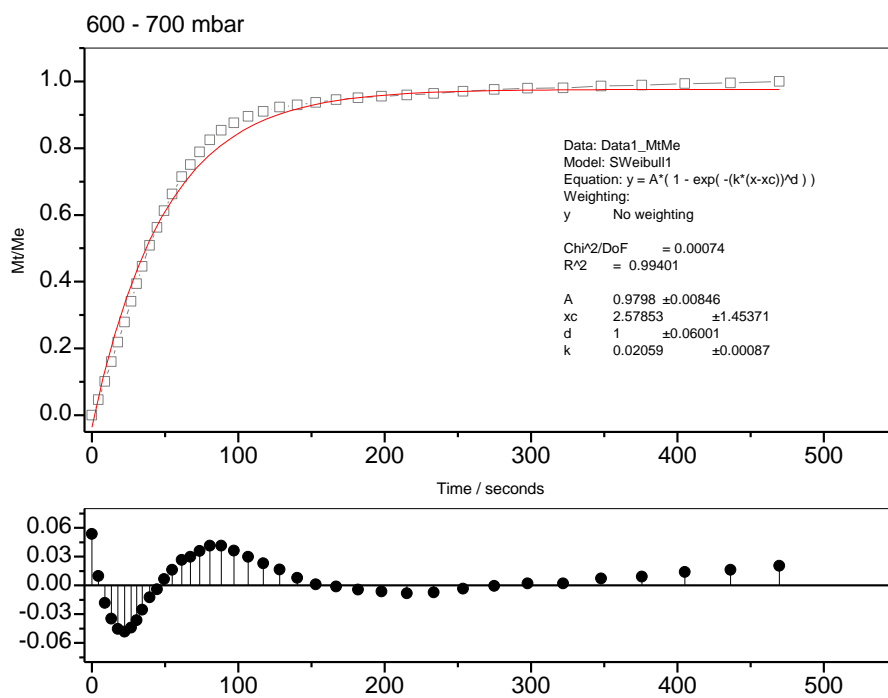


**Figure 8-37:** Oxygen adsorption on Cage 1 $\alpha$  at 273 K 600 – 700 mbar step SE analysis

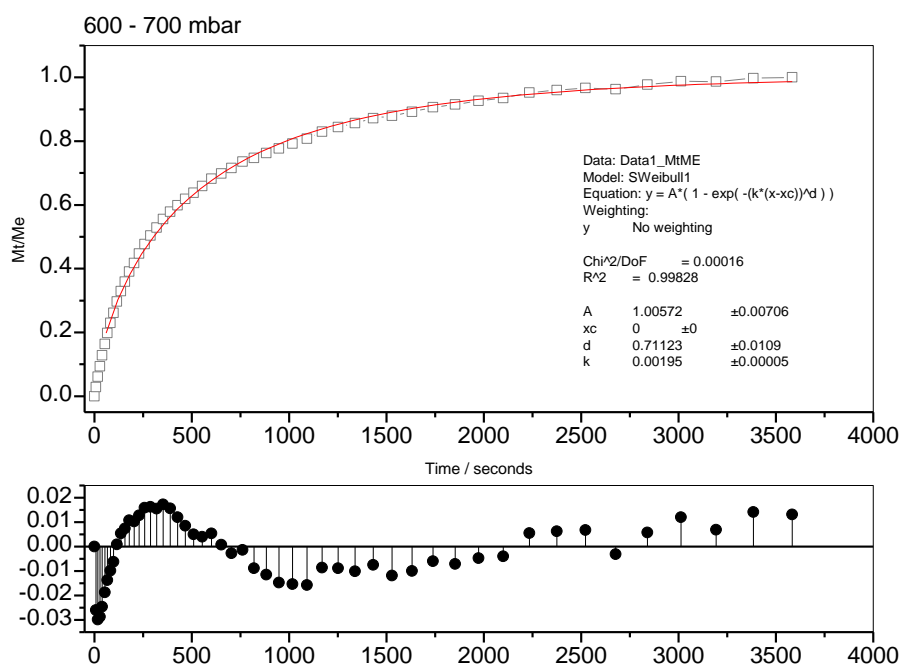


**Figure 8-38:** Nitrogen adsorption on Cage 1 $\alpha$  at 273 K 600 - 700 mbar step SE analysis

Chapter 8 Kinetic Molecular Sieving of Oxygen and Nitrogen by Organic Cage  
Materials Cage 1 $\alpha$  and Cage 1 $\alpha$ #

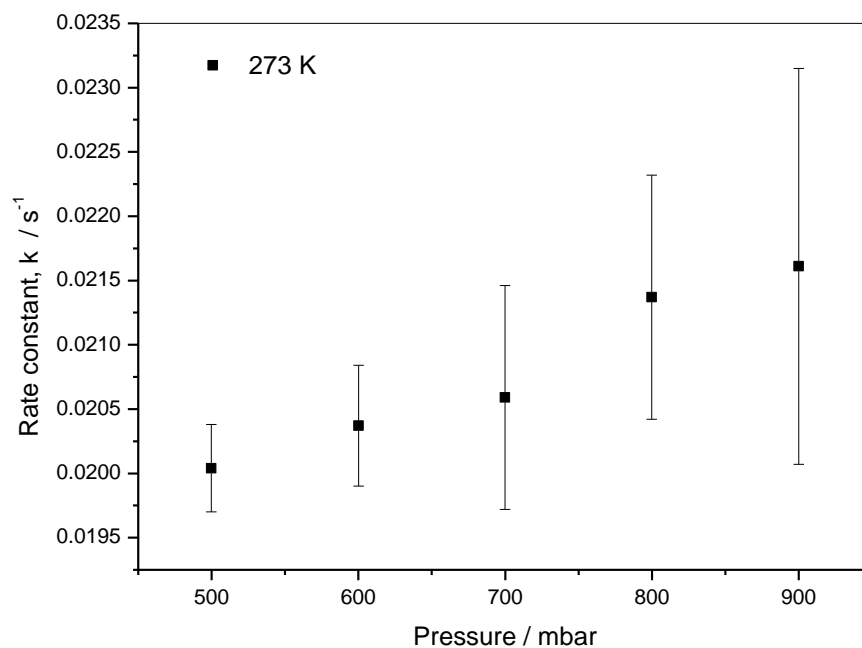


**Figure 8-39:** Graph of rate constant,  $k$ , versus pressure for oxygen adsorption on Cage 1 $\alpha$  at 273 K

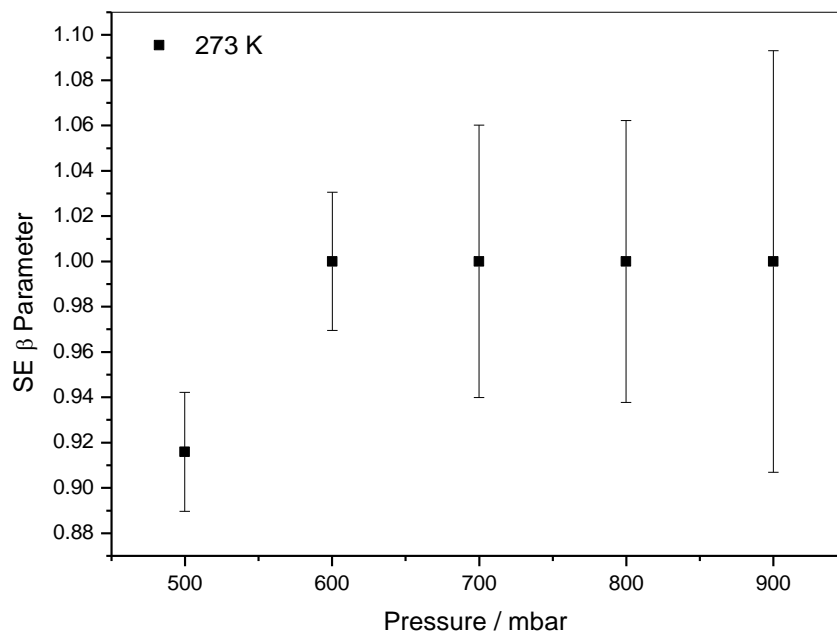


**Figure 8-40:** Graph of SE parameter,  $\beta$ , versus pressure for oxygen adsorption on Cage 1 $\alpha$  at 273 K

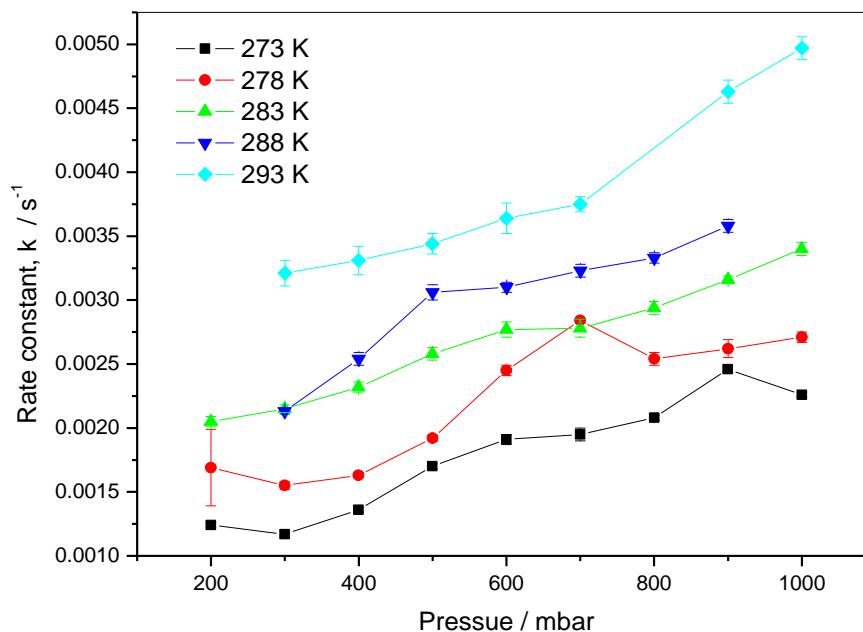


**Figure 8-41:** Graph of rate constant,  $k$ , versus pressure for nitrogen adsorption on Cage 1 $\alpha$  for the temperature range 273 – 293 K

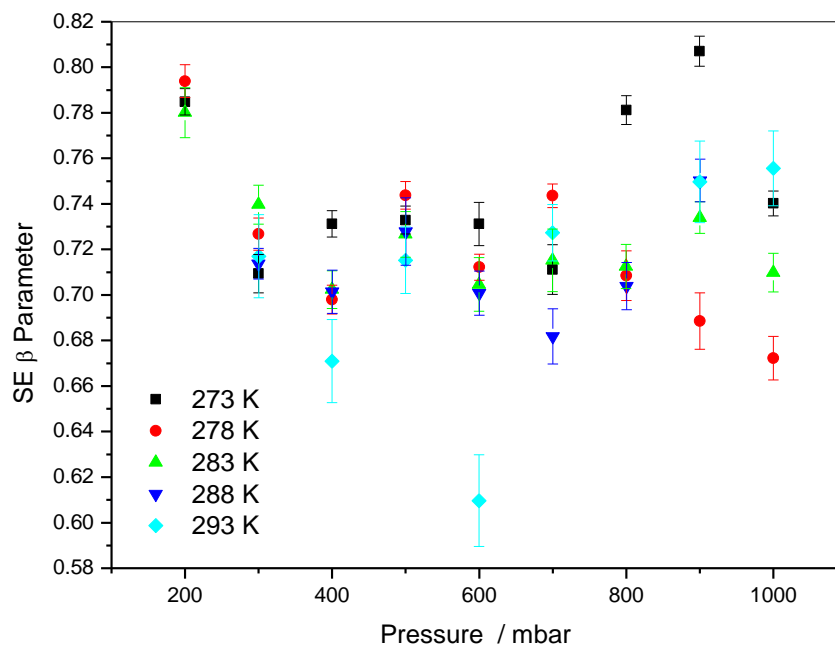


**Figure 8-42:** Graph of SE parameter,  $\beta$ , versus pressure for nitrogen adsorption on Cage 1 $\alpha$  for the temperature range 273 – 293 K

Chapter 8 Kinetic Molecular Sieving of Oxygen and Nitrogen by Organic Cage  
Materials Cage 1 $\alpha$  and Cage 1 $\alpha$ #

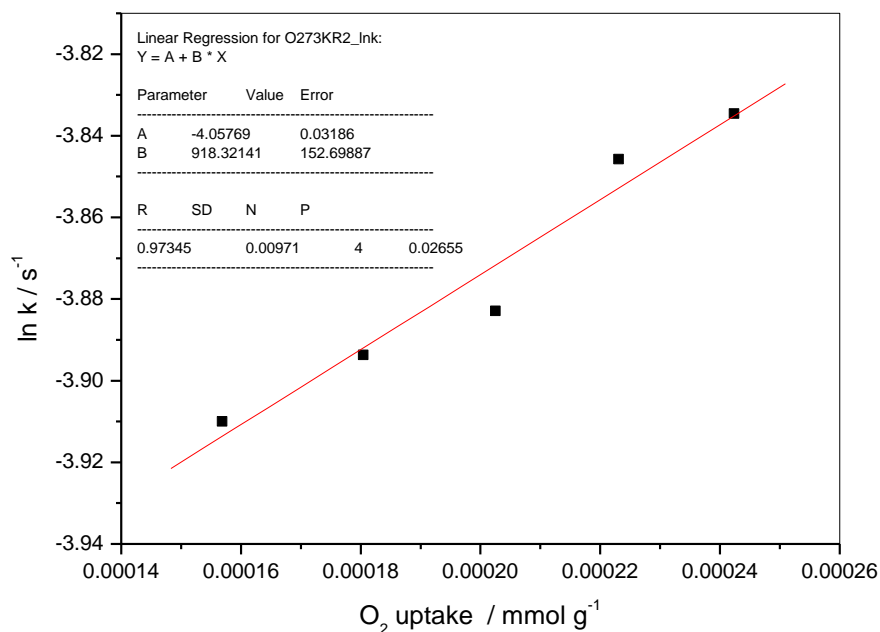


**Figure 8-43:** Graph of  $\ln k$  versus oxygen uptake / mol  $\text{g}^{-1}$  for oxygen adsorption on Cage 1 $\alpha$  at 273 K

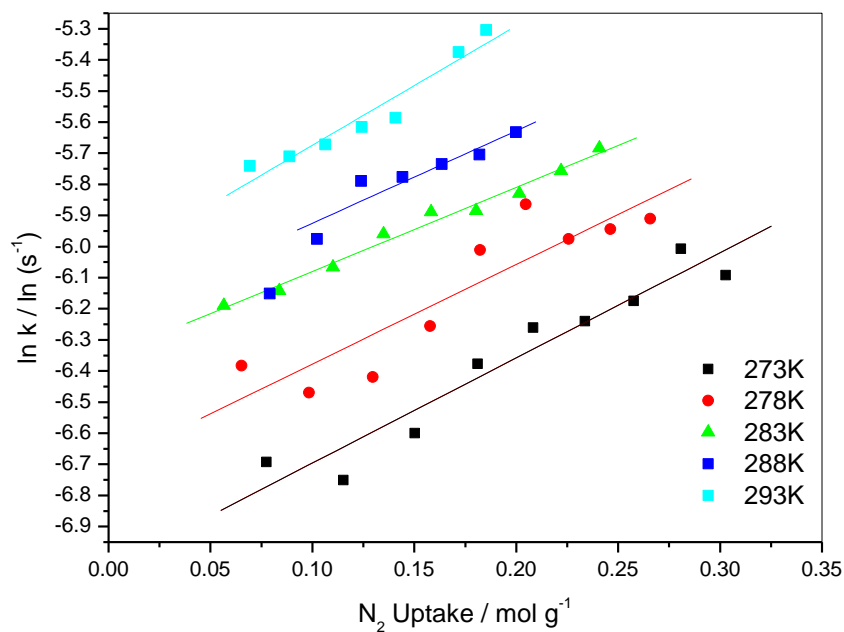


**Figure 8-44:** Graphs of  $\ln k$  versus nitrogen uptake / mol  $\text{g}^{-1}$  for nitrogen adsorption on Cage 1 $\alpha$  for temperature range 273 – 293 K

Chapter 8 Kinetic Molecular Sieving of Oxygen and Nitrogen by Organic Cage  
Materials Cage 1 $\alpha$  and Cage 1 $\alpha$ #

**Table 8-8:**  $\ln k / \ln (s^{-1})$  values at zero surface coverage for nitrogen adsorption on Cage 1 $\alpha$  for temperature range 273 – 293 K

Temperature / K	$\ln k / \ln (s^{-1})$
273	$-7.034 \pm 0.077$
278	$-6.698 \pm 0.11$
283	$-6.350 \pm 0.021$
288	$-6.222 \pm 0.088$
293	$-6.058 \pm 0.061$

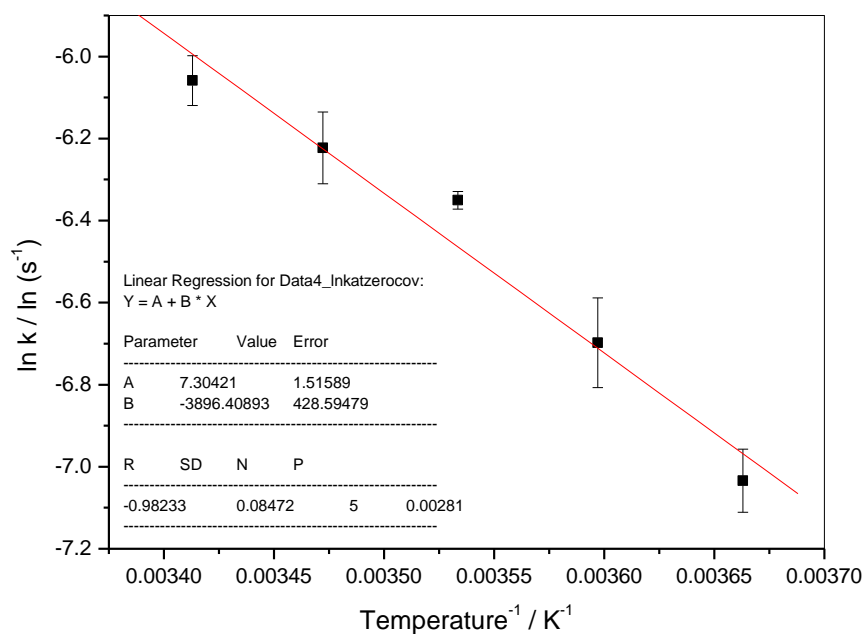


**Figure 8-45:**  $\ln k$  versus  $1/T$  for nitrogen adsorption on Cage 1 $\alpha$  for temperature range 273 – 293 K



Chapter 8 Kinetic Molecular Sieving of Oxygen and Nitrogen by Organic Cage  
Materials Cage 1 $\alpha$  and Cage 1 $\alpha$ #

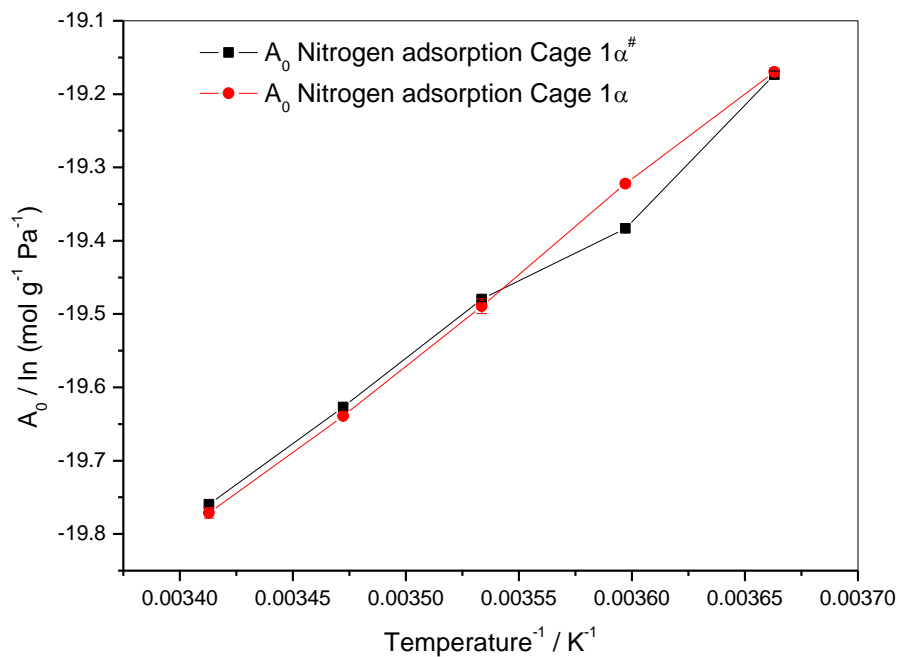


**Figure 8-46:** Comparison of virial parameter  $A_0$  for nitrogen adsorption on Cage 1 $\alpha$ # and Cage 1 $\alpha$  for the temperature range 273 – 293 K

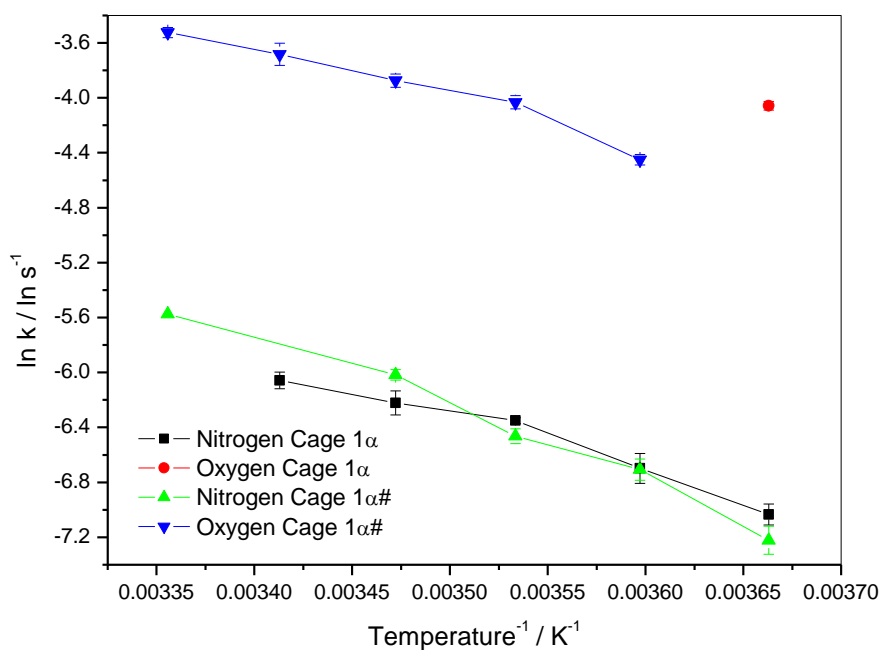


**Figure 8-47:** Variation of  $\ln(k)$  with reciprocal temperature for oxygen and nitrogen adsorption on Cage 1 $\alpha$ # and Cage 1 $\alpha$  for the temperature range 273 – 298 K

Chapter 8 Kinetic Molecular Sieving of Oxygen and Nitrogen by Organic Cage  
Materials Cage 1 $\alpha$  and Cage 1 $\alpha$ #

**Table 8-9:** Comparison of  $Q_{st}$  and  $E_a$  values for Cage 1 $\alpha$  and Cage 1 $\alpha$ # for oxygen and nitrogen adsorption

	Cage 1 $\alpha$		Cage 1 $\alpha$ #	
	Oxygen	Nitrogen	Oxygen	Nitrogen
$Q_{st} / \text{kJ mol}^{-1}$	-	$20.2 \pm 0.3$	$16.9 \pm 1.7$	$18.8 \pm 1.1$
$E_a / \text{kJ mol}^{-1}$	-	$32.4 \pm 3.6$	$30.4 \pm 3.6$	$40.9 \pm 3.5$

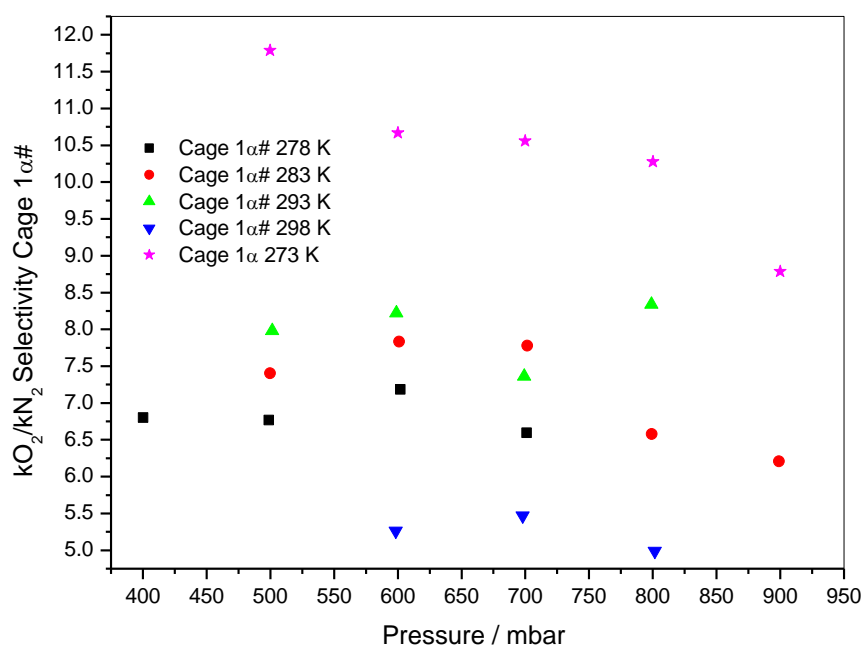


**Figure 8-48:** Comparison of the  $k_{O_2}/k_{N_2}$  kinetic selectivity of Cage 1 $\alpha$ # for the temperature range 278 – 298 K and Cage 1 $\alpha$  at 273 K

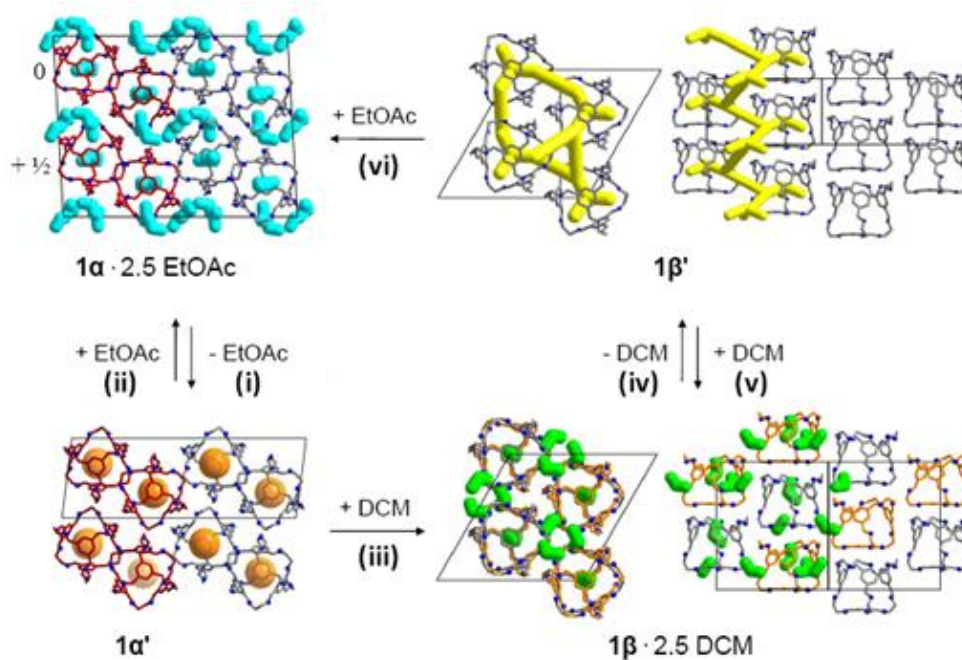


**Figure 8-49:** Conversion between various polymorphs (1 $\alpha$  and 1 $\beta$ ) accessible to the cage one structure, where 1 $\alpha$ ' and 1 $\beta$ ' indicate desolvated structures<sup>17</sup>

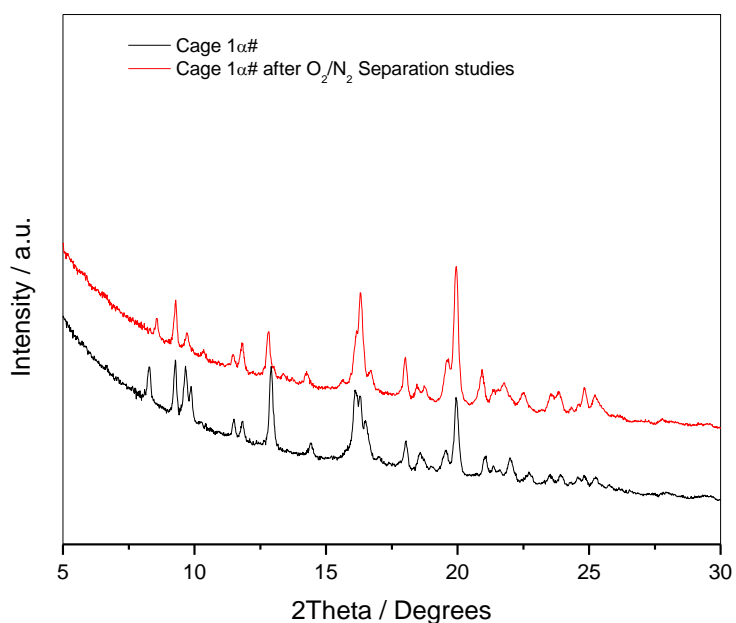


**Figure 8-50:** PXRD data for Cage 1 $\alpha$ # before and after N<sub>2</sub>/O<sub>2</sub> separation studies

8.10 References

- <sup>1</sup> C. E. Webster, R. S. Drago, M. C. Zemer, *J. Am. Chem. Soc.* **1998**, *120*, 5509
- <sup>2</sup> I. P. O’Koye, M. Benham, K. M. Thomas, *Langmuir* **1997**, *13*, 4054
- <sup>3</sup> H. K. Chagger, F. E. Ndaji, M. L. Sykes, K. M. Thomas, *Carbon*, **1995**, *33*, 1405
- <sup>4</sup> Y. Kawabuchi, H. Oka, S. Kawano, I. Mochida, N. Yoshizawa, *Carbon*, **1998**, *36*, 377
- <sup>5</sup> S. Villar-Rodil, R. Navarrete, R. Denoyel, A. Albinia, J. I. Paredes, A. Martinez-Alonso, J. M. D. Tascón, *Meso. Micro. Mater.*, **2005**, *77*, 109
- <sup>6</sup> J. T. A. Jones, D. Holden, T. Mitra, T. Hasell, D. J. Adams, K. E. Jelfs, A. Trewin, D. J. Willock, G. M. Day, J. Bacsá, A. Steiner, A. I. Cooper, *Angew. Chem. Int. Ed.*, **2010**, *50*, 749
- <sup>7</sup> K. S. W. Sing, D. H. Everett, R. W. Haul, L. Moscou, R. A. Pierotti, J. Rouquerol, T. Siemieniewska, *Pure & Applied Chem.*, **1985**, *57*, 603
- <sup>8</sup> J. H. Cole, D. H. Everett, C. T. Marshall, A. R. Paniago, J. C. Powl, F. Rodriguez – Reinoso, *J. Chem. Soc. Faraday Transactions*, **1974**, *70*, 2154
- <sup>9</sup> C. R. Reid, I. P. O’Koye, K. M. Thomas, *Langmuir*, **1998**, *14*, 2415
- <sup>10</sup> C. R. Reid, K. M. Thomas, *Langmuir*, **1999**, *15*, 3206.
- <sup>11</sup> J. Klafter, M. F. Shlesinger, *Proc. Natl. Acad. Sc., USA*, **1986**, *83*, 848
- <sup>12</sup> J. Crank, *The Mathematics of Diffusion*, Clarendon Press, Oxford, **1975**.
- <sup>13</sup> C. R. Reid, K. M. Thomas, *Langmuir*, **1999**, *15*, 3206
- <sup>14</sup> M. D. LeVan, *Adsorption Science and Technology*, Kluwer, The Netherlands, **1989**
- <sup>15</sup> T. Tomokazu, J. T. A. Jones, S. I. Swamy, S. Jiang, D. J. Adams, S. Shakespeare, R. Clowes, D. Bradshaw, T. Hasell, S. Y. Chong, C. Tang, S. Thompson, J. Parker, A. Trewin, J. Bacsá, A. M. Z. Slawin, A. Steiner, A. I. Cooper., *Nat. Mat.*, **2009**, *8*, 973
- <sup>16</sup> Y. D. Chen, R. T. Yang, *Carbon*, **1998**, *36*, 1525
- <sup>17</sup> J. T. A. Jones, D. Holden, T. Mitra, T. Hasell, D. J. Adams, K. E. Jelfs, A. Trewin, D. J. Willock, G. M. Day, J. Bacsá, A. Steiner, A. I. Cooper., *Angew. Chem. Int. Ed.*, **2010**, *50*, 749

## Chapter 9      Overall Conclusions

Over the past decade there has been a rapid increase in the development of novel nanoporous materials, and extensive investigations into the applicability of these materials for gas storage, separation and purification process. Materials such as activated carbon<sup>1</sup>, carbon molecular sieves and zeolites<sup>2</sup> have predominantly been used for industrial applications such as gas separation, catalysis and removal of trace impurities. While these are traditional materials that have a successful history for such applications, there is always a drive for new materials to improve the efficiency of these processes and for potential new applications, for example, hydrogen storage, drug delivery and sensor technology. Any material which is developed has to compete with existing adsorbents such as zeolites and activated carbons in industrial process. New materials must have 1) high adsorption capacity, 2) suitable kinetics, 3) stability over multiple cycles of use and 4) be economic and cost effective.<sup>3</sup>

Porous coordination polymers and porous organic cage molecules are at the forefront of current research into new materials for adsorption processes. Metal organic frameworks have been discussed in the literature for applications in gas storage, separation and purification, clean energy applications, and catalysis.<sup>4</sup> The surface chemistry of metal organic frameworks can be tailored through the introduction of functional groups, creating the ability to control the size of the pores and the specific interaction with target molecules, often through simple one-step synthesis reactions. Metal organic frameworks were initially synthesised in rigid frameworks, analogous to that of zeolites. Recently, the effects of introducing flexibility through pore reformation, shrinkage and breathing of pores and crystal to crystal structural change have been investigated.<sup>5</sup>

One such flexible metal organic framework was investigated in this thesis. A 2D framework showed conversion to a 3D framework induced by a coordination change upon desolvation facilitated by the flexibility of carboxylate groups. The 3D framework of Zn(TBAPy) was tailored for the adsorption of xylene molecules through the inclusion of the pyrene polyaromatic core, designed to enhance interactions with aromatic species. This metal organic framework was used to investigate the challenging separation of the *p*-xylene and *m*-xylene isomers, an important industrial separation currently achieved using simulated moving bed

technology based on a *p*-xylene shape selective zeolite adsorbent. The framework showed a structural change on the adsorption of *m*-xylene, leading to slower rate of adsorption of this isomer over the *p*-xylene at higher pressures.<sup>6</sup> The investigations into the metal organic framework highlighted a particular problem associated with this type of porous material, and that is the inherent instability of these materials. The Zn (TBAPy)', the desolvated 3D network, was especially susceptible to structural degradation upon exposure to atmospheric water vapour. Although relatively stable metal organic frameworks have been published in the literature, such as HKUST and the IR MOF series, the stability of these materials still poses a major issue in the use of these materials in industrial applications.

Zhang<sup>7</sup>, Mastalerz<sup>8</sup> and Cooper<sup>9</sup> have been leading research into the development of porous organic cages, which contain inherent flexibility through weak interactions between the cages, allowing potential flexibility through reorientation of discrete cage units within the crystal lattice. The polymorphism of Cage 1 can be demonstrated through structural rearrangement on the exposure of the cage to various organic vapours/solvents, showing inter conversion between two stable structures, Cage 1 $\alpha$  and Cage 1 $\beta$ . The conversion of Cage 1 $\beta$  to Cage 1 $\alpha$ # displays an unprecedented shape of adsorption isotherm, which included desorption of adsorbed vapour with increasing pressure during the adsorption isotherms. The unprecedented isotherm shape and the structural transformation have been shown for a selection of gases/vapours, including ethyl acetate, methyl acetate, 2-butanone and diethyl ether, but not methanol and pentane. This shows a response to selected solvent vapour molecules. Methyl acetate adsorption on Cage 1 $\beta$  allowed the characterisation of the kinetics and thermodynamics of the structural change from Cage 1 $\beta$  to Cage 1 $\alpha$ #. The adsorption of methyl acetate on Cage 1 $\beta$  was also compared with the adsorption of methyl acetate on Cage 1 $\alpha$ # in order to establish the thermodynamic effects on the conversion of Cage 1 $\beta$  to Cage 1 $\alpha$ #. Comparison of the isosteric enthalpy and entropy of adsorption before transformation on Cage 1 $\beta$  and after transformation on Cage 1 $\alpha$ # show that the structural change, which occurs during desorption of methyl acetate, is driven by the enthalpy of adsorption. The desorption kinetics for the structural change show that it is an activated process. The product, Cage 1 $\alpha$ #, has narrower pores, and hence an increased interaction between the adsorbate and adsorbent, leading to a larger isosteric enthalpy of adsorption. This structural change

also results in more negative entropy of adsorption, showing ordering of the system as methyl acetate is removed and the crystalline to crystalline transformation occurs. The reverse transformation from Cage 1 $\alpha$  to Cage 1 $\beta$ # has been shown to be induced through exposure to dichloromethane. The transformations lead to the formation of stable polymorphs, which can interconvert without the loss of long range crystallographic order.

Cage 1 $\alpha$  has voids between the cages, which are connected by very narrow constrictions that allow the kinetic molecular sieving of oxygen, carbon dioxide and nitrogen, a property which is not present in the polymorph Cage 1 $\beta$ . It was found that oxygen adsorbs approximately ten times faster than nitrogen on Cage 1 $\alpha$ #, with selectivity and rate constants similar to those observed for carbon molecular sieves. This material was found to be extremely stable, and repeatable isotherms of carbon dioxide, oxygen and nitrogen adsorption were collected after over 30 cycles of adsorption, heating to 120°C and desorption, with isotherms collected over a pressure range of 0 - 1000 mbar.

This thesis has investigated the adsorption characteristics and properties of two different types of porous materials. Metal organic frameworks are often unstable and this leads to limitations in their use. They have the potential for many industrial applications, but as yet have not been able to compete with the more traditional adsorbents such as zeolites and carbon molecular sieves. The more recent developments into porous organic cages show considerable potential for these materials. The study of vapour adsorption on Cage 1 polymorphs has shown the ability to introduce structural responses to selected molecules, which can be measured and quantified. The stability and narrow pores in Cage 1 $\alpha$ # gives this cage the ability to separate oxygen and nitrogen by kinetic molecular sieving with characteristics that are similar to commercially available carbon molecular sieves.

9.1 References

- <sup>1</sup> S. Sircar, T. C. Golden, M. B. Pao, *Carbon*, **1996**, *34*, 1
- <sup>2</sup> H. H. Funke, M. G. Kovalchick, J. L. Falconer, R. D. Noble, *Ind. Eng. Chem. Res.*, **1996**, *35*, 1575
- <sup>3</sup> D. D. Do, *Adsorption Analysis: Equilibria and Kinetics*, Imperial College, London, **1998**
- <sup>4</sup> A. U. Czaja, N. Trukhan, U. Müller, *Chem. Soc. Rev.*, **2009**, *38*, 1284
- <sup>5</sup> S. Kitigawa, R. Kitaura, S. Noro, *Angew. Chem. Int. Ed.*, **2004**, *43*, 2334
- <sup>6</sup> K. C. Stylianou, J. Rabone, S. Y. Chong, R. Heck, J. Armstrong, P. V. Wiper, K. E. Jelfs, S. Zlatogorsky, J. Bacsa, A. G. McLennan, C. P. Ireland, Y. Z. Khimyak, K. M. Thomas, D. Bradshaw, M. J. Rosseinsky, *J. Am. Chem. Soc.*, **2012**, *134*, 20466
- <sup>7</sup> Y. Jin, B. A. Voss, R. D. Noble, W. Zhang, *Angew. Chem. Int. Ed.*, **2010**, *49*, 6348
- <sup>8</sup> M. Mastalerz, M.W. Schneider, I. M. Opiel, O. Presly, *Angew. Chem. Int. Ed.*, **2011**, *50*, 1046
- <sup>9</sup> T. Tomokazu, J. T. A. Jones, S. I. Swamy, S. Jiang, D. J. Adams, S. Shakespeare, R. Clowes, D. Bradshaw, T. Hasell, S. Y. Chong, C. Tang, S. Thompson, J. Parker, A. Trewin, J. Bacsa, A. M. Z. Slawin, A. Steiner, A. I. Cooper, *Nat. Mat.*, **2009**, *8*, 973



Chapter 10      Further Work

The remaining work to be completed is mainly focused on the investigations into the adsorption induced structural rearrangement of the different polymorphs of Cage 1. The structural change from Cage 1 $\beta$  to Cage 1 $\alpha$  induced by exposure to the methyl acetate has been fully assessed both thermodynamically and kinetically, with isosteric enthalpies of adsorption and the activation energy of adsorption calculated, as well as the activation energy for the desorption of vapour. The kinetics of desorption of methyl acetate were found to follow the Avrami model of crystallisation kinetics. The adsorption of dichloromethane results in the reverse structural transition from Cage 1 $\alpha$  to Cage 1 $\beta$ . The key question that needs to be answered is – What are the solvent-cage interactions, which trigger the transformation of Cage 1 $\beta$  to Cage 1 $\alpha$  and vice versa?

The structural change of Cage 1 $\beta$  to Cage 1 $\alpha$  could be monitored using powder X-ray diffraction data. This would give information on the structural changes produced during the adsorption process, in particular around the first step at  $\sim$  1:1 solvent: cage stoichiometry and the structural change around 2.5:1 solvent: cage stoichiometry.

The extension of the current probe molecule adsorption study on Cage 1 $\beta$ , to include determination of enthalpies of adsorption and activation energy for 2-butanone and diethyl ether adsorption would lead to more detailed understanding of the factors which influence structural change.

The initial investigations into the reverse transformation of Cage 1 $\alpha$  to Cage 1 $\beta$  through exposure to dichloromethane showed very interesting adsorption kinetics, which changed from a stretched-exponential model to an Avrami model at high pressure. This suggests that dichloromethane also induces a crystallisation effect whilst undergoing structural transformation. This cycle of transformations for Cage 1 $\alpha$  and Cage 1 $\beta$  requires further investigation, with measurement of dichloromethane adsorption isotherms for a range of temperatures to give thermodynamic and kinetic parameters to answer the following specific questions:

- What is the isosteric enthalpy and activation energy of dichloromethane adsorption on Cage 1 $\alpha$ ?

## Chapter 10 Further Work

- Is dichloromethane adsorption induced rearrangement an activated process?
- Is a higher enthalpy required to transform Cage 1 $\beta$  to Cage 1 $\alpha$  through dichloromethane adsorption than the reverse transformation with methyl acetate adsorption?
- The structural changes induced by dichloromethane adsorption could also be monitored using powder X-ray diffraction studies.
- How many cycles of transformations can be achieved before degradation of the sample?

Chapter 11      Publications

K. C. Stylianou, J. Rabone, S. Y. Chong, R. Heck, **J. Armstrong**, P. V. Wiper, K. E. Jelfs, S. Zlatogorsky, J. Bacsa, A. G. McLennan, C. P. Ireland, Y. Z. Khimyak, K. M. Thomas, D. Bradshaw, M. J. Rosseinsky, *Dimensionality Transformation through Paddlewheel Reconfiguration in a Flexible and Porous Zn-Based Metal-Organic Framework*, *J. Am. Chem. Soc.*, **2012**, *134*, 20466 – 20478

**J. Armstrong**, J. Bell, J. Jones, T. Hassell, S. Y. Chong, K. E. Jelfs, A. I. Cooper, K. M. Thomas, *Kinetic Molecular Sieving of Oxygen and Nitrogen by Porous Cage Materials*, Pending Publication

Chapter 12      Appendix

CD Appendix

CD Appendix A – Xylene Separation by Zn (TBAPy) 1' Metal Organic Framework

CD Appendix B – Molecular Cage Materials

CD Appendix C – Kinetic Molecular Sieving of Oxygen and Nitrogen by Organic Cage Material